

Impedance-Based Structural Health Monitoring to Detect Corrosion

by

Garnett E. Simmers Jr.

Thesis Submitted to the Faculty of the
Virginia Polytechnic Institute and State University
in partial fulfillment of the requirements for the degree of
Master of Science

in

Mechanical Engineering

Dr. Daniel J. Inman, Chair
Dr. Donald J. Leo
Dr. Harry Robertshaw

May 6, 2005

Blacksburg, Virginia

Keywords: structural, health, monitoring, corrosion, detection, impedance, damage, NDE,
SHM, evaluation

Impedance-Based Structural Health Monitoring to Detect Corrosion

Garnett E. Simmers Jr.

Abstract

Corrosion begins as moisture penetrates the protective barrier of a surface, starting an electrochemical process which over time leads to surface pitting. The combined action of mechanical stresses and corrosion induced pitting reduces structural integrity as the pits enlarge to form nucleation sites for surface cracks, which propagate into through-thickness cracks. In most cases, the total mass loss due to corrosion within the structure is small; however, significant reductions in mechanical strength and fatigue life can occur in the corroded material leading to advanced crack growth rates or fast fracture. Since the structural damage due to localized corrosion pitting is small and the crack growth rates may be large, traditional inspections methods and “find it and fix it” maintenance approaches may lead to catastrophic mechanical failures.

Therefore, precise structural health monitoring of pre-crack surface corrosion is paramount to understanding and predicting the effect corrosion has on the fatigue life and integrity of a structure. In this first third of this study, the impedance method was experimentally tested to detect and the onset and growth of the earliest stages of pre-crack surface corrosion in beam and plate like structures. Experimental results indicate the impedance method is an effective detection tool for corrosion induced structural damage in plates and beams. For corrosion surface coverages less than 1.5% and pit depths of less than 25 microns (light corrosion), the impedance method could successfully detect corrosion on plates and beams at distances up to 150 cm from the sensor location.

Since the impedance method is a proven tool for corrosion detection, it makes sense to determine how well the method can quantify and track key corrosion variables like location, pit depth, and surface coverage. In order to make fatigue life adjustments for corroded structures it is necessary to quantify those variables. Thus, the second portion of this study uses the impedance method to quantify corrosion location, pit depth, and location. Three separate tests are conducted

on beam-like structures to determine how well the damage metrics from the impedance method correlate to the key corrosion variables. From the three tests, it is found that the impedance method correlates best with the changes in corrosion pit depth, so if combined with data from routine maintenance it would be possible to use the impedance method data in a predictive or tracking manner. The impedance method can be correlated to location and surface coverage changes, but the relationship is not as strong. Other NDE techniques like Lamb Waves could use the same sensors to quantify corrosion location, and perhaps surface coverage.

The impedance method can detect and quantify pre-crack surface corrosion which leads to shortened fatigue life in structures; however, the sensors must be robust enough to withstand corrosive environments. The last portion of this study tests the following: corrosive effect on Lead Zirconate Titanate (PZT) and Macro Fiber Composites (MFC) sensors, Kapton protected MFC actuators for corrosion detection, and determines if corrosion damage can be sensed on the side of the structure opposite the damage. Sensor recommendations regarding the use of piezoelectric sensors in corrosive environments are made.

Acknowledgments

First I would like to extend my sincerest thanks to my advisor Dr. Daniel J. Inman for welcoming me into the Center for Intelligent Materials Systems and Structures (CIMSS) as an undergraduate, and for continuing to support me through the graduate program. Dr. Inman is very good at relating to students, so his classes were always enjoyable and there was always laughter in the halls of CIMSS. Second I would like to thank Los Alamos National Laboratory (LANL) and Dr. Chuck Farrar for accepting me into the Dynamics Summer School Program in the summer of 2003, and for sponsoring my graduate work through the National Physical Science Consortium Fellowship. I would like to thank Dr. Gyuhae Park and Dr. Henry Sodano for serving as selfless, tireless mentors who taught me to be a successful researcher. I would also like to thank my CIMSS colleagues who helped me to learn my way around the lab and provided me with an endless supply of much-needed distractions. Without the professional assistance and encouragement of each these individuals my research would have been less successful and enjoyable. As I move to an industry position, I will continue learning, working, and publishing in the structural health monitoring field, so I look forward to working with each of you in the future. Please feel free to call on me if I can ever be of assistance to you.

Next, I would like to thank my parents who taught me the most important lessons in life. They always valued learning and encouraging me to pursue higher education. Finally, I would like to thank my wife for her endless support and encouragement throughout my graduate program. She spent many late nights in the lab watching me set up experiments, and she never complained. Even when I thought I was in over my head, she put things into perspective and encouraged me to push on. Without her support, I doubt I could have escaped graduate school with no gray hairs.

Table of Contents

Chapter 1 - Introduction

1.1	Corrosion, Costs, and Effect on Structural Health	1
1.1.1	Corrosion in Terms of Business Costs.....	1
1.1.2	Corrosion’s Effect on Structural Health.....	2
1.1.3	Understanding Corrosion Development.....	3
1.2	Corrosion Cost and Effect on Aircraft	7
1.2.1	How Corrosion Has Become Such a Challenge for the Aircraft Industry.....	7
1.2.2	The Nature of Aircraft Corrosion.....	8
1.2.3	The Structural Effect and Implications of Corrosion on Aircraft.....	9
1.3	Corrosion Detection Methods for Aircraft	10
1.3.1	Aircraft Corrosion Detection Methods.....	10
1.3.2	The Advantages and Disadvantages of Corrosion Detection Methods.....	12
1.4	Introduction to the Impedance Method	14
1.4.1	Mechanical Impedance.....	15
1.4.2	Important Properties Piezoelectric Materials.....	17
1.4.3	Impedance Method.....	19
1.5	Literature Review	20
1.5.1	Impedance-Based Corrosion Detection.....	21
1.6	Thesis Overview	23
1.6.1	Chapter 1 Summary.....	23
1.6.2	Chapter 2 Summary & Contributions.....	23
1.6.3	Chapter 3 Summary & Contributions.....	24
1.6.4	Chapter 4 Summary & Contributions.....	25
1.6.5	Chapter 5 Summary & Contributions.....	25

Chapter 2 - Detecting Corrosion Damage in Beams

2.1	Introduction	27
------------	---------------------------	-----------

2.2	Testing Procedure & Experimental Setup	27
2.2.1	Impedance Terminology and Definitions.....	27
2.2.2	Experimental Setup & Sensitivity Testing.....	28
2.2.3	Introducing Corrosion Damage.....	30
2.2.4	Managing Ambient Variation Not Associated With Damage.....	30
2.2.5	Converting Impedance Data to a Useable Form.....	33
2.3	Beam Corrosion Detection Results for All Frequencies	37
2.3.1	Corrosion Detection Relative to Baseline #1 for All Frequencies.....	37
2.3.2	Corrosion Detection Relative to Previous Baselines.....	39
2.4	Improved Beam Detection Results	40
2.4.1	Improved Corrosion Detection Relative to Baseline #1.....	40
2.4.2	Improved Corrosion Detection Relative to Previous Baselines.....	40
2.5	Corrosion Detection Patterns	44
2.5.1	Patterns Conducive to Corrosion Detection.....	44
2.5.2	Patterns Not Conducive to Corrosion Detection.....	45

Chapter 3 - Quantifying Beam Corrosion Damage

3.1	Introduction	47
3.2	Testing Procedure & Experimental Setup	48
3.2.1	Pit Depth Testing Experimental Procedure.....	48
3.2.2	Location Testing Experimental Procedure.....	48
3.2.3	Surface Coverage Tracking Experimental Procedure.....	49
3.3	Corrosion Quantification Results	50
3.3.1	Corrosion Pit Depth/Mass Loss Tracking.....	50
3.3.2	Corrosion Location Tracking Results.....	54
3.3.3	Corrosion Surface Coverage Tracking Results.....	56
3.4	Corrosion Quantification Conclusions	59

Chapter 4 - Corrosion Detection in Plates

4.1	Introduction	61
4.2	Testing Procedure & Experimental Setup	61
4.2.1	Beam and Plate Differences.....	61
4.2.2	Sensitivity Testing and Frequency Selection in Plates.....	64

4.2.3	Plate Corrosion Testing Procedure.....	65
4.3	Plate Corrosion Detection Results.....	67
4.3.1	Corrosion Detection Results for Damage #1.....	67
4.3.2	Corrosion Detection Results for Damage #2.....	70
4.3.3	Corrosion Detection Patterns in Plates.....	73

Chapter 5 - Impedance Sensor Corrosion

5.1	Introduction.....	76
5.2	How Corrosion Affects PZT & MFC Sensors.....	76
5.2.1	Initial Observations on PZT Sensor Corrosion.....	76
5.2.2	Experimental Setup for Sensor Corrosion Testing.....	77
5.2.3	Experimental Results of Sensor Corrosion Testing.....	80
5.3	Macro-Fiber Composites Used for Corrosion Detection.....	82
5.3.1	MFC and PZT Corrosion Detection Setup.....	82
5.3.2	Experimental Results MFC and PZT Same-Side Corrosion Detection.....	85
5.3.3	Through-Structure Corrosion Detection Results for MFCs and PZT.....	87
5.3.4	High Frequency Detection Results.....	89

Chapter 6 - Conclusions

6.1	Brief Summary of Thesis.....	92
6.2	Contributions.....	94
6.3	Future Work.....	96

Bibliography	97
---------------------	-----------

Appendix A Beam Corrosion Detection Plots and Figures	102
--	------------

Appendix B Corrosion Pit Depth, Location, and Surface Coverage Plots and Figures	115
---	------------

Appendix C Plate Corrosion Impedance and Damage Metric Plots	137
---	------------

Appendix D Sensor Corrosion Impedance and Damage Metric Plots	162
--	------------

Vita	181
-------------	------------

List of Tables

1.1.1	The most common corrosion forms, how each forms, and diagram.....	4
1.2.1	The aircraft corrosion classification index sets a standard based on pit depth.....	8
1.3.1	NDE and NDI techniques used to corrosion detection in aircraft.....	11
1.3.2	The advantages and disadvantage of each corrosion detection methods.....	12
2.2.1	Common corrosion reactions for corroding aluminum.....	30
2.2.2	Nomenclature definitions for the experimental system.....	36
2.4.1	Impedance based corrosion detection results for an aluminum beam.....	43
3.3.1	Results of the corrosion pit depth tracking test.....	50
3.3.2	Corrosion location results for a beam-like structure.....	54
3.3.3	Corrosion surface coverage detection results.....	57
4.3.1	Impedance based corrosion detection results for damage #1.....	68
4.3.2	Damage algorithms used for damage #2.....	70
4.3.3	Corrosion detection results for damage #2.....	71
4.3.4	Plate corrosion results compiled by sensing location and frequency.....	74
5.3.1	Same side corrosion detection results for an MFC D_{33}	86
5.3.2	Same side corrosion detection results for PZT #1.....	86
5.3.3	Same side corrosion detection results for an MFC D_{31}	86
5.3.4	Opposite side corrosion detection results for an MFC D_{31}	87
5.3.5	Opposite side corrosion detection results for an MFC D_{33}	87
5.3.6	Opposite side corrosion detection results for PZT.....	88

List of Figures

1.1.1	An industry sector analysis on the non-extrapolated corrosion cost in 1998.....	2
1.1.2	Corrosion induced in-flight failure in an Aloha Airlines 737.....	3
1.1.3	Initially, damage size is corrosion dominated, and influences the time until cracks form [42].....	6
1.4.1	Schematic diagram of an ideal mechanical damper.....	16
1.4.2	Schematic diagram of an ideal mechanical spring.....	16
1.4.3	Schematic diagram of an ideal mechanical mass.....	17
1.4.4	Pictures of several commercially available piezoelectric materials.....	18
1.4.5	An electrometrical model of the admittance.....	20
2.2.1	Sensitivity tests aid frequency selection by showing areas of high sensitivity.....	29
2.2.2	An aluminum beam after the corrosion detection tests with squares marking the damage and an oval marking the sensor.....	29
2.2.3	Dielectric constant versus temperature for piezoelectrics.....	32
2.2.4	Coupling coefficient versus temperature for piezoelectrics.....	32
2.2.5	The baseline measurements show changes in the impedance signatures due to damage in beams.....	34
2.3.1:	Beam corrosion detection results for the beam for all tested frequencies measured relative to the baseline #1.....	37
2.3.2	Beam corrosion results measured relative to previous instances of damage.....	39
2.4.1	Beam corrosion damage detection for impedances sweeps from 20-22 kHz.....	41
2.4.2	Corrosion detection results for beam impedance testing between 103-105 kHz.....	42
2.4.3	Corrosion detection results for beam impedance testing between 71-73 kHz.....	42
2.4.4	All five levels of corrosion damage are distinguishable for 71-73 kHz.....	43
2.5.1	Impedance signatures from 20.25-21.00 kHz.....	44
2.5.2	Average damage metrics versus frequency plot identifies which individual impedance peaks are sensitive to damage.....	45
2.5.3	Impedance signatures from 71.4-72 kHz.....	46

2.5.4	Average damage metrics versus frequency plot identifies which individual impedance peaks are sensitive to damage but can't distinguish damage	46
3.2.1	The beam used for pit depth detection after 5 levels of corrosion damage	48
3.2.2	The aluminum beam used in the corrosion coverage test in its final damage state	49
3.3.1	For 22-106 kHz, corrosion pit depth changes are detectable and distinguishable	51
3.3.2	For 20-22 kHz, corrosion pit depth changes are detectable and distinguishable	52
3.3.3	The relationship between damage metrics and cumulative corrosion mass loss	53
3.3.4	Relationship between damage metrics versus corrosion induced mass loss	53
3.3.5	For damage metrics calculated across all six frequencies the damage is detectable	55
3.3.6	From 20-22 kHz, three levels of damage are distinguishable	55
3.3.7	Damage metric values versus corrosion damage location in beams	56
3.3.8	The results of the surface coverage test for all of the test frequencies combined	57
3.3.9	The results of the surface coverage for all for 20-22 kHz show all are detectable	58
3.3.10	Plots of the damage metric versus surface coverage correlation for each frequency	59
4.2.1	The peak density for beam-like structures is low relative to plate-like structures	62
4.2.2	The peak density and real magnitudes for plate-like structures is large	62
4.2.3	The peak magnitudes are lower and appear to be more damped in beams	63
4.2.4	The peak magnitudes are larger and the less damped in plates	64
4.2.5	A sensitivity test on a plate with the damage metric difference overlaid	65
4.2.6	Ovals mark the PZT locations and squares mark the corrosion damage locations	66
4.3.1	Corrosion detection results from PZT #2 at 52-53.2 kHz	69
4.3.2	Corrosion detection results from PZT #2 at 230-231.2 kHz	69
4.3.3	Corrosion detection results from PZT #4 at 7.5-8.7 kHz	70
4.3.4	At 230-231.2 kHz the corrosion damage #2 is distinguishable from PZT#2	71
4.3.5	Damage #2 is distinguishable from PZT #4 at 52-53.1 kHz	72
4.3.6	Damage #2 is distinguishable from PZT #4 at 230-231.2 kHz	73
4.2.7	Impedance signatures with distinguishable damage overlaid for PZT #3	75
4.2.8	Impedance signatures with distinguishable damage overlaid for PZT #2	75
5.2.1	The impedance change in PZT #1, were black is 43 undamaged signatures and the blue to green colormap is the 33 signatures for damage #1 measured with a corrosion damaged sensor	78

5.2.2	Over a narrow frequency band, it is easy to see the time dependant shift in the impedance signature caused by the corrosion damaged sensor	78
5.2.3	Impedance versus time plot for a damage PZT sensor show definite trends	79
5.2.4	Capacitance versus time plot for a damage PZT sensor show definite trends	80
5.2.5	The test structure for sensor corrosion testing	81
5.3.1	Both sides of the test structure with all sensors and levels of damage shown	83
5.3.2	Sensitivity test results show the impedance response differences between PZT MFC D_{31} , and MFC D_{33}	84
5.3.3	MFC D_{31} can detect and distinguish both levels of damage at 3-5 kHz	88
5.3.4	MFC D_{33} can detect and distinguish both levels of damage at 33-35 kHz	88
5.3.5	PZT #1 can detect and distinguish same-side corrosion damage at 70.5-72.5 kHz	89
5.3.6	PZT can detect and distinguish through-structure corrosion damage at 50-52 kHz	89
5.3.7	Impedance signatures for PZT A4 from 206-208 kHz	90
5.3.8	Impedance signatures for MFC D_{31} from 206-208 kHz	90
5.3.9	Impedance signatures for MFC D_{33} from 206-208 kHz	91
A.1	Impedance signatures for beam corrosion damage from 20-20 kHz	103
A.2	Average damage metrics for beam corrosion damage from 20-20 kHz	103
A.3	Corrosion damage plots relative to baseline #1 from 20-20 kHz	104
A.4	Corrosion damage plots relative to previous baselines from 20-20 kHz	104
A.5	Impedance signatures for beam corrosion damage from 54-56 kHz	105
A.6	Average damage metrics for beam corrosion damage from 54-56 kHz	105
A.7	Corrosion damage plots relative to baseline #1 from 54-56 kHz	106
A.8	Corrosion damage plots relative to previous baselines from 54-56 kHz	106
A.9	Impedance signatures for beam corrosion damage from 71-73 kHz	107
A.10	Average damage metrics for beam corrosion damage from 71-73 kHz	107
A.11	Corrosion damage plots relative to baseline #1 from 71-73 kHz	108
A.12	Corrosion damage plots relative to previous baselines from 71-73 kHz	108
A.13	Impedance signatures for beam corrosion damage from 96.5-98.5 kHz	109
A.14	Average damage metrics for beam corrosion damage from 96.5-98.5 kHz	109
A.15	Corrosion damage plots relative to baseline #1 from 96.5-98.5 kHz	110
A.16	Corrosion damage plots relative to previous baselines from 96.5-98.5 kHz	110
A.17	Impedance signatures for beam corrosion damage from 103-105 kHz	111
A.18	Average damage metrics for beam corrosion damage from 103-105 kHz	111
A.19	Corrosion damage plots relative to baseline #1 from 103-105 kHz	112

A.20	Corrosion damage plots relative to previous baselines from 103-105 kHz.....	112
A.21	Impedance signatures for beam corrosion damage from 126-128 kHz.....	113
A.22	Average damage metrics for beam corrosion damage from 126-128 kHz.....	113
A.23	Corrosion damage plots relative to baseline #1 from 126-128 kHz.....	114
A.24	Corrosion damage plots relative to previous baselines from 126-128 kHz.....	114
B.1	Pit depth damage metric plot relative to initial baseline for all frequencies.....	116
B.2	Pit depth damage metric plot relative to previous baseline for all frequencies.....	116
B.3	Pit depth damage metric plot relative to initial baseline from 20-22 kHz.....	117
B.4	Pit depth damage metric plot relative to initial baseline from 44-46 kHz.....	117
B.5	Pit depth damage metric plot relative to initial baseline from 54-56 kHz.....	117
B.6	Pit depth damage metric plot relative to initial baseline from 72-74 kHz.....	118
B.7	Pit depth damage metric plot relative to initial baseline from 97-99 kHz.....	118
B.8	Pit depth damage metric plot relative to initial baseline from 104-106 kHz.....	118
B.9	Pit depth damage metric plot relative to previous baseline from 20-22 kHz.....	119
B.10	Pit depth damage metric plot relative to previous baseline from 44-46 kHz.....	119
B.11	Pit depth damage metric plot relative to previous baseline from 54-56 kHz.....	119
B.12	Pit depth damage metric plot relative to previous baseline from 72-74 kHz.....	120
B.13	Pit depth damage metric plot relative to previous baseline from 97-99 kHz.....	120
B.14	Pit depth damage metric plot relative to previous baseline from 104-106 kHz.....	120
B.15	Pit depth impedance signatures from 20-22 kHz.....	121
B.16	Pit depth impedance signatures from 44-46 kHz.....	121
B.17	Pit depth impedance signatures from 54-56 kHz.....	121
B.18	Pit depth impedance signatures from 72-74 kHz.....	122
B.19	Pit depth impedance signatures from 97-99 kHz.....	122
B.20	Pit depth impedance signatures from 104-106 kHz.....	122
B.21	Location test damage metric plot relative to initial baseline for all frequencies.....	123
B.22	Location test damage metric plot relative to previous baseline for all frequencies.....	123
B.23	Location test damage metric plot relative to baseline 1 from 20-22 kHz.....	124
B.24	Location test damage metric plot relative to baseline 1 from 54-56 kHz.....	124
B.25	Location test damage metric plot relative to baseline 1 from 71-73 kHz.....	124
B.26	Location test damage metric plot relative to baseline 1 from 96.5-98.5 kHz.....	125
B.27	Location test damage metric plot relative to baseline 1 from 103-105 kHz.....	125
B.28	Location test damage metric plot relative to baseline 1 from 126-128 kHz.....	125
B.29	Location test damage metric plot relative to previous baseline from 20-22 kHz.....	126

B.30	Location test damage metric plot relative to previous baseline from 54-56 kHz.....	126
B.31	Location test damage metric plot relative to previous baseline from 71-73 kHz.....	126
B.32	Location test damage metric plot relative to previous baseline from 96.5-98.5 kHz.....	127
B.33	Location test damage metric plot relative to previous baseline from 103-105 kHz.....	127
B.34	Location test damage metric plot relative to previous baseline from 126-128 kHz.....	127
B.35	Location impedance signatures from 20-22 kHz.....	128
B.36	Location impedance signatures from 54-56 kHz.....	128
B.37	Location impedance signatures from 71-73 kHz.....	128
B.38	Location impedance signatures from 96.5-98.5 kHz.....	129
B.39	Location impedance signatures from 103-105 kHz.....	129
B.40	Location impedance signatures from 126-128 kHz.....	129
B.41	Coverage damage metric plot relative to initial baseline for all frequencies.....	130
B.42	Coverage damage metric plot relative to previous baseline for all frequencies.....	130
B.43	Coverage damage metric plot relative to initial baseline from 20-22 kHz.....	131
B.44	Coverage damage metric plot relative to initial baseline from 54-66 kHz.....	131
B.45	Coverage damage metric plot relative to initial baseline from 71-73 kHz.....	131
B.46	Coverage damage metric plot relative to initial baseline from 96.5-98.5 kHz.....	132
B.47	Coverage damage metric plot relative to initial baseline from 103-105 kHz.....	132
B.48	Coverage damage metric plot relative to initial baseline from 126-128 kHz.....	132
B.49	Coverage damage metric plot relative to previous baseline from 20-22 kHz.....	133
B.50	Coverage damage metric plot relative to previous baseline from 54-66 kHz.....	133
B.51	Coverage damage metric plot relative to previous baseline from 71-73 kHz.....	133
B.52	Coverage damage metric plot relative to previous baseline from 96.5-98.5 kHz.....	134
B.53	Coverage damage metric plot relative to previous baseline from 103-105 kHz.....	134
B.54	Coverage damage metric plot relative to previous baseline from 126-128 kHz.....	134
B.55	Corrosion surface coverage impedance signatures from 20-22 kHz.....	135
B.56	Corrosion surface coverage impedance signatures from 46-48 kHz.....	135
B.57	Corrosion surface coverage impedance signatures from 57-59 kHz.....	135
B.58	Corrosion surface coverage impedance signatures from 72-74 kHz.....	136
B.59	Corrosion surface coverage impedance signatures from 104-106 kHz.....	136
B.60	Corrosion surface coverage impedance signatures from 130-132 kHz.....	136
C.1	Plate impedance signatures measured with PZT #2.....	138
C.2	Plate impedance signatures measured with PZT #2.....	138
C.3	Plate impedance signatures measured with PZT #2.....	138

C.4	Plate damage plots for PZT #2.....	139
C.5	Plate damage plots for PZT #2.....	139
C.6	Plate damage plots for PZT #2.....	139
C.7	Plate impedance signatures measured with PZT #2.....	140
C.8	Plate impedance signatures measured with PZT #2.....	140
C.9	Plate impedance signatures measured with PZT #2.....	140
C.10	Plate damage plots for PZT #2.....	141
C.11	Plate damage plots for PZT #2.....	141
C.12	Plate damage plots for PZT #2.....	141
C.13	Plate impedance signatures measured with PZT #2.....	142
C.14	Plate impedance signatures measured with PZT #2.....	142
C.15	Plate impedance signatures measured with PZT #2.....	142
C.16	Plate damage plots for PZT #2.....	143
C.17	Plate damage plots for PZT #2.....	143
C.18	Plate damage plots for PZT #2.....	143
C.19	Plate impedance signatures measured with PZT #2.....	144
C.20	Plate impedance signatures measured with PZT #2.....	144
C.21	Plate impedance signatures measured with PZT #2.....	144
C.22	Plate damage plots for PZT #2.....	145
C.23	Plate damage plots for PZT #2.....	145
C.24	Plate damage plots for PZT #2.....	145
C.25	Plate impedance signatures measured with PZT #3.....	146
C.26	Plate impedance signatures measured with PZT #3.....	146
C.27	Plate impedance signatures measured with PZT #3.....	146
C.28	Plate damage plots for PZT #3.....	147
C.29	Plate damage plots for PZT #3.....	147
C.30	Plate damage plots for PZT #3.....	147
C.31	Plate impedance signatures measured with PZT #3.....	148
C.32	Plate impedance signatures measured with PZT #3.....	148
C.33	Plate impedance signatures measured with PZT #3.....	148
C.34	Plate damage plots for PZT #3.....	149
C.35	Plate damage plots for PZT #3.....	149
C.36	Plate damage plots for PZT #3.....	149
C.37	Plate impedance signatures measured with PZT #3.....	150

C.38	Plate impedance signatures measured with PZT #3.....	150
C.39	Plate impedance signatures measured with PZT #3.....	150
C.40	Plate damage plots for PZT #3.....	151
C.41	Plate damage plots for PZT #3.....	151
C.42	Plate damage plots for PZT #3.....	151
C.43	Plate impedance signatures measured with PZT #3.....	152
C.44	Plate impedance signatures measured with PZT #3.....	152
C.45	Plate impedance signatures measured with PZT #3.....	152
C.46	Plate damage plots for PZT #3.....	153
C.47	Plate damage plots for PZT #3.....	153
C.48	Plate damage plots for PZT #3.....	153
C.49	Plate impedance signatures measured with PZT #4.....	154
C.50	Plate impedance signatures measured with PZT #4.....	154
C.51	Plate impedance signatures measured with PZT #4.....	154
C.52	Plate damage plots for PZT #4.....	155
C.53	Plate damage plots for PZT #4.....	155
C.54	Plate damage plots for PZT #4.....	155
C.55	Plate impedance signatures measured with PZT #4.....	156
C.56	Plate impedance signatures measured with PZT #4.....	156
C.57	Plate impedance signatures measured with PZT #4.....	156
C.58	Plate damage plots for PZT #4.....	157
C.59	Plate damage plots for PZT #4.....	157
C.60	Plate damage plots for PZT #4.....	157
C.61	Plate impedance signatures measured with PZT #4.....	158
C.62	Plate impedance signatures measured with PZT #4.....	158
C.63	Plate impedance signatures measured with PZT #4.....	158
C.64	Plate damage plots for PZT #4.....	159
C.65	Plate damage plots for PZT #4.....	159
C.66	Plate damage plots for PZT #4.....	159
C.67	Plate impedance signatures measured with PZT #4.....	160
C.68	Plate impedance signatures measured with PZT #4.....	160
C.69	Plate impedance signatures measured with PZT #4.....	160
C.70	Plate damage plots for PZT #4.....	161
C.71	Plate damage plots for PZT #4.....	161

C.72	Plate damage plots for PZT #4.....	161
D.1	Impedance signatures for MFC D ₃₁ from 3-5 kHz.....	163
D.2	Impedance signatures for MFC D ₃₁ from 13.9-15.9 kHz.....	163
D.3	Impedance signatures for MFC D ₃₁ from 19.9-21.9 kHz.....	163
D.4	Damage metric plots for MFC D ₃₁ from 3-5 kHz.....	164
D.5	Damage metric plots for MFC D ₃₁ from 13.9-15.9 kHz.....	164
D.6	Damage metric plots for MFC D ₃₁ from 19.9-21.9 kHz.....	164
D.7	Impedance signatures for MFC D ₃₁ from 33-35 kHz.....	165
D.8	Impedance signatures for MFC D ₃₁ from 50-52 kHz.....	165
D.9	Impedance signatures for MFC D ₃₁ from 72.5-74.5 kHz.....	165
D.10	Damage metric plots for MFC D ₃₁ from 33-35 kHz.....	166
D.11	Damage metric plots for MFC D ₃₁ from 52-54 kHz.....	166
D.12	Damage metric plots for MFC D ₃₁ from 72.5-74.5 kHz.....	166
D.13	Impedance signatures for MFC D ₃₃ from 3-5 kHz.....	167
D.14	Impedance signatures for MFC D ₃₃ from 13.9-15.9 kHz.....	167
D.15	Impedance signatures for MFC D ₃₃ from 19.9-21.9 kHz.....	167
D.16	Damage metric plots for MFC D ₃₃ from 3-5 kHz.....	168
D.17	Damage metric plots for MFC D ₃₃ from 13.9-15.9 kHz.....	168
D.18	Damage metric plots for MFC D ₃₃ from 19.9-21.9 kHz.....	168
D.19	Impedance signatures for MFC D ₃₃ from 33-35 kHz.....	169
D.20	Impedance signatures for MFC D ₃₃ from 50-52 kHz.....	169
D.21	Impedance signatures for MFC D ₃₃ from 72.5-74.5 kHz.....	169
D.22	Damage metric plots for MFC D ₃₃ from 33-35 kHz.....	170
D.23	Damage metric plots for MFC D ₃₃ from 50-52 kHz.....	170
D.24	Damage metric plots for MFC D ₃₃ from 72.5-74.5 kHz.....	170
D.25	Impedance signatures for PZT A4 from 3-5 kHz.....	171
D.26	Impedance signatures for PZT A4 from 13.9-15.9 kHz.....	171
D.27	Impedance signatures for PZT A4 from 19.9-21.9 kHz.....	171
D.28	Damage metric plots for PZT A4 from 3-5 kHz.....	172
D.29	Damage metric plots for PZT A4 from 13.9-15.9 kHz.....	172
D.30	Damage metric plots for PZT A4 from 19.9-21.9 kHz.....	172
D.31	Impedance signatures for PZT A4 from 33-35 kHz.....	173
D.32	Impedance signatures for PZT A4 from 50-52 kHz.....	173
D.33	Impedance signatures for PZT A4 from 72.5-74.5 kHz.....	173

D.34	Damage metric plots for PZT A4 from 33-35 kHz.....	174
D.35	Damage metric plots for PZT A4 from 50-52 kHz.....	174
D.36	Damage metric plots for PZT A4 from 72.5-74.5 kHz.....	174
D.37	Impedance signatures for PZT A4 from 100-102 kHz.....	175
D.38	Impedance signatures for PZT A4 from 125-127 kHz.....	175
D.39	Impedance signatures for PZT A4 from 134.5-136.5 kHz.....	175
D.40	Impedance signatures for PZT A4 from 158-160 kHz.....	176
D.41	Impedance signatures for PZT A4 from 173-175 kHz.....	176
D.42	Impedance signatures for PZT A4 from 206-208 kHz.....	176
D.43	Impedance signatures for MFC D ₃₁ from 100-102 kHz.....	177
D.44	Impedance signatures for MFC D ₃₁ from 125-127 kHz.....	177
D.45	Impedance signatures for MFC D ₃₁ from 134.5-136.5 kHz.....	177
D.46	Impedance signatures for MFC D ₃₁ from 158-160 kHz.....	178
D.47	Impedance signatures for MFC D ₃₁ from 173-175 kHz.....	178
D.48	Impedance signatures for MFC D ₃₁ from 206-208 kHz.....	178
D.49	Impedance signatures for MFC D ₃₃ from 100-102 kHz.....	179
D.50	Impedance signatures for MFC D ₃₃ from 125-127 kHz.....	179
D.51	Impedance signatures for MFC D ₃₃ from 134.5-136.5 kHz.....	179
D.52	Impedance signatures for MFC D ₃₃ from 158-160 kHz.....	180
D.53	Impedance signatures for MFC D ₃₃ from 173-175-127 kHz.....	180
D.54	Impedance signatures for MFC D ₃₃ from 206-208 kHz.....	180

Nomenclature

F = force

j = imaginary component

ω = driving frequency

F_0 = magnitude of driving force

t = time

v = velocity

v_0 = magnitude of velocity

φ = phase angle

Z = impedance

c = damping constant

k = stiffness constant

m = mass

Y = electrical admittance

V = voltage

I = current

δ = dielectric loss of PZT

a = geometric constant of PZT

ε = dielectric permittivity

d = strain coefficient

Y^E = Young's modulus

Re = real

Im = imaginary

$B1$ = baseline #1 – calculated damage metrics for “healthy” impedance signatures

Bx = baseline #x – calculated damage metrics for impedance signatures of damage level x

Dyz = calculated damage metrics for impedance signatures between baseline y and baseline z

Chapter 1

Introduction

1.1 Corrosion, Costs, and Effect on Structural Health

The formation of corrosion plays a major role in the health and long-term maintenance cost of structures. In this section, the business cost of corrosion will be presented to make a case for the economic need to detect, control, and prevent corrosion. To better understand the costly nature of corrosion, the methods of corrosion formation and the effect on structural health will be discussed.

1.1.1 Corrosion in Terms of Business Costs

Corrosion is an extremely costly problem for industries and business sectors throughout the world, and it has a major impact on world economies. In 1998, Congress funded the Department of Transportation (DOT) and the Federal Highway Administration (FHWA) to estimate the total cost of corrosion on the U.S. economy and provide corrosion prevention guidelines. The final results of the survey estimated the extrapolated total direct corrosion cost to be \$278 billion per year, which was 3.14% of the gross domestic product in the United States [40]. A breakdown of the corrosion cost per analyzed business sector may be found in Figure 1 [40]. Clearly, corrosion prevention, maintenance, and losses due to downtime are very costly and should not be underestimated. Additionally, the potential benefits of corrosion awareness, preventive measures during design, better predictive models, prevention policies, and improved detection and monitoring techniques could yield large cost savings while providing for safer structures with longer service lives [20]. Based on safety, structural effect, and potential benefits, one of the

industries that could benefit most from better corrosion detection techniques is the aerospace industry. This study focuses on a non-destructive corrosion detection method for the types of corrosion that plague aircraft, and the unique costs and challenges posed by aircraft corrosion.

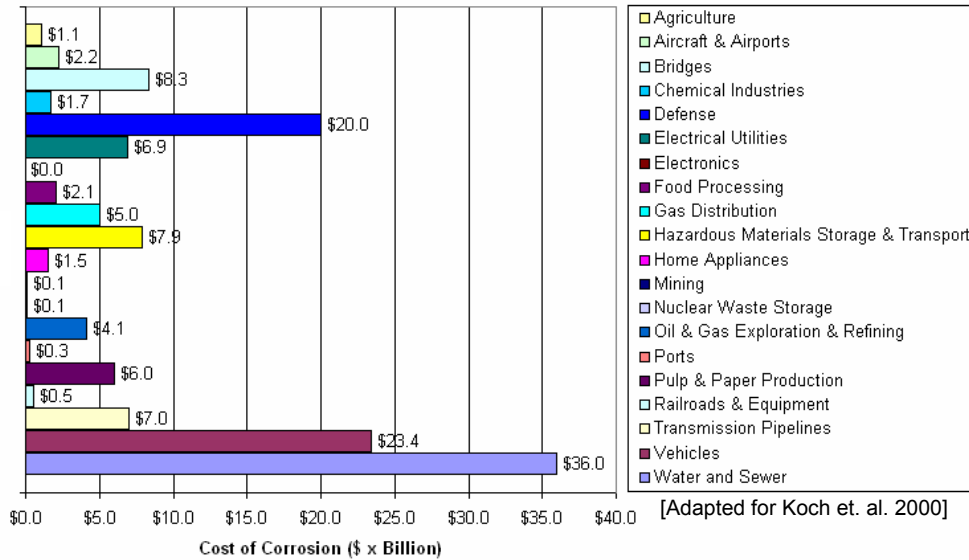


Figure 1.1.1: An industry sector analysis on the non-extrapolated corrosion cost in 1998 [40].

1.1.2 Corrosion’s Effect on Structural Health

At first glance, one may think of the corrosive effect on structures as one that is simply cosmetic in nature. For many people, the image of corrosion on structures that most quickly comes to mind is the unsightly rusting of a once beautiful late-model car. Initially this appears to be true, corrosion on most structures including aircraft is a cosmetic problem, and it can be very expensive to remove the old anti-corrosion coatings (paint), blend out the corrosion pits or replace the damage, and then reapply paint.

However, in the time it takes for aircraft corrosion to become visually observable to an untrained eye, the real structural damage is done and maybe irreversible. Even under careful examination by well-trained maintenance personnel, corrosion can lead to structural deficiencies which go unnoticed until mechanical failure is reached. Figure 1.1.2 shows an Aloha Airlines 737 after corrosion accelerated fatigue failure caused the aircraft to lose the upper half of the fuselage during flight at 24000 ft [1]. According to a National Transportation Safety Board report, the operator’s maintenance program failed to detect the corrosion damage that led to the failure [1]. The Aloha Airlines flight is an extreme but by no means isolated case of corrosion induced

in-flight failure that graphically conveys the fact that the structural effects of corrosion are significant and must be detectable and understandable. Even after the post-Aloha incident inspection and maintenance reforms and the development of nondestructive inspection (NDI) tools, aircraft corrosion detection still relies heavily on “find and fix” maintenance approaches [20]. To improve safety it is imperative to further improve existing NDI techniques and develop new NDI techniques to detect smaller hidden corrosion defects earlier and more economically [20].



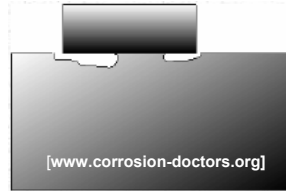







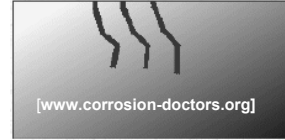
Figure 1.1.2: Corrosion induced in-flight failure in an Aloha Airlines 737 [1].

1.1.3 Understanding Corrosion Development

Corrosion has an adverse effect on the structures that it forms on, but it is important to understand why. Understanding why requires a basic knowledge of how corrosion forms and how it interacts with material properties and loads to reduce the life of structures. The electrochemistry of corrosion is beyond the scope of this manuscript, so only a brief summary of corrosion formation and interactions will be presented. There are three types of corrosion: auto, contact and externally induced [1], and almost all forms belong to one of those groups. The main corrosion forms are: uniform, pitting, crevice, galvanic, intergranular, selective leaching, erosion, stress corrosion cracking (SCC), and corrosion fatigue [37, 1]. Table 1.1.1 lists the main forms of corrosion, gives an explanation for how each forms and affects the structure, and shows a cross sectional diagram of the material after corrosion.

Table 1.1.1: The most common corrosion forms, how each develops, and diagrams.

Corrosion Forms	Description	Cross Section Diagram
Uniform [37, 44, 1]	Corrosion occurs at nearly the same rate over the exposed surface usually due to a chemical reaction. The material thins till failure. The most predictable and common form of corrosion.	 <p>[www.corrosion-doctors.org]</p>
Pitting [14, 37, 44, 1]	Corrosion normally caused by chloride and chlorine ions creating very small pinholes in the material. Pitting can lead to premature failure with only a small percentage of weight loss. Tends to be localized, hard to detect, and unpredictable. When combined with stress the pits serve a nucleation sites for crack formation. Common in aircraft.	 <p>[www.corrosion-doctors.org]</p>
Crevice [37, 44, 1]	Corrosion occurs when a corrosive liquid is confined to a tight space with poor drainage. Once a stagnation zone is established there is an incubation period. When the reaction starts it progresses at an increasing rate. Common in aircraft.	 <p>[www.corrosion-doctors.org]</p>
Galvanic [37, 44, 1]	Corrosion occurs when dissimilar metals with different electrical potentials are placed in conductive contact the one with another, the material with the lower potential acts as a cathode and corrodes. Causes cathode pitting and anode pillowing. Common in older aircraft.	 <p>[www.corrosion-doctors.org]</p>
Intergranular [5, 37, 44, 1]	Corrosion occurs when material grain boundaries contain impurities, enriched alloys, or depleted alloys have dissimilar electrical potentials causing some grains to dissolve or disintegrate forming pits. When it occurs across grains it is called exfoliation. Common in aircraft.	 <p>[www.corrosion-doctors.org]</p>
Selective Leaching [37, 44, 1]	Corrosion where one element of an alloy is removed, usually by aqueous acids containing the same element. Zinc, aluminum, iron, cobalt, and chromium tend to leach.	 <p>[www.corrosion-doctors.org]</p>

<p>Erosion [37, 44, 1]</p>	<p>Corrosion where a movement of one material removes the protective layer. For a solid to liquid interaction it is called erosion. For a solid to solid interaction through a load it is called fretting. Often induced by vibration or thermal expansion. May also include cavitation.</p>	
<p>Stress Corrosion Cracking [400, 14, 37, 44, 1]</p>	<p>Corrosion occurs when a corroded materials interacts with mechanical stress leading to premature cracking. Works in conjunction with other types of corrosion and hydrogen embrittlement. Causes loss of strength and reduces time till crack formation and failure for stresses just 10% of yield. Can even lead to fast fracture. Not easily detectable or predictable.</p>	
<p>Corrosion Fatigue [7, 8, 14, 37, 1]</p>	<p>When corrosion and cyclic stress are combined the mean time till cracks form significantly decreases and a significant loss of fatigue life can result.</p>	

All corroding systems require the following conditions to be present: two materials or elements with different electrical potentials, an electrolyte, and a metallic connection between the anode and cathode [25]. In general, corroding systems experience a chemical reaction created when water or corrosive fluid penetrates a protective barrier (usually at a joint or fastener) and creates a reaction site [43]. One material acts as a cathode while the other serves as an anode; as the reaction progresses one material loses mass (pitting) and the other material gains mass (pillowing) [4]. Corrosion induced pitting and pillowing creates mechanical defects similar to surface roughness effects accounted for in machine design equations. Even though the associated mass loss due to the pitting is small, the surface roughness of the material is increased which changes the stress concentration factors. Pitting serves as nucleation sites for surface cracks because they increase the stress concentrations significantly over the very small area occupied by the pit [39, 43]. Before cracks form on a structure (pre-crack), damage growth is corrosion dominated, and corrosion damage size influences the mean time till cracks form as seen in Figure 1.1.3 [43].

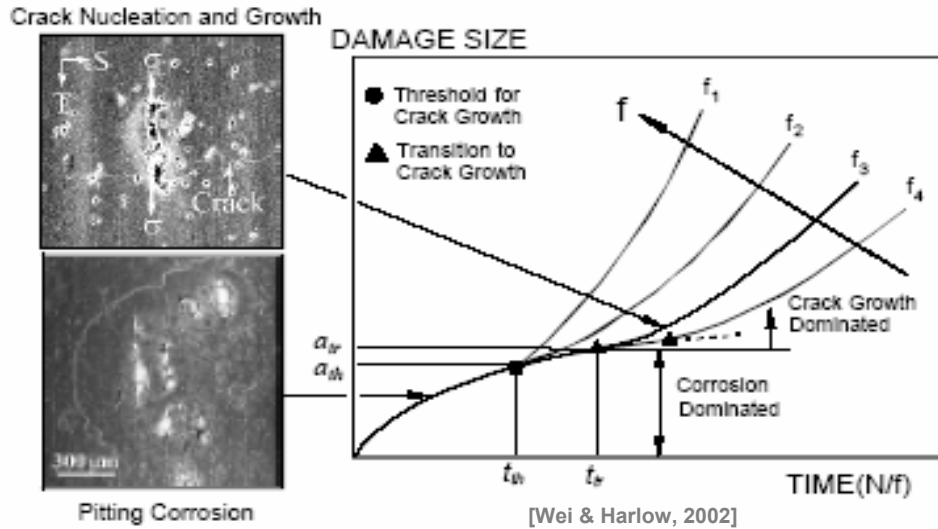


Figure 1.1.3: Initially, damage size is corrosion dominated, and influences the time until cracks form [42].

When the pitted material is exposed to static or dynamic stresses, the areas of high stress concentrations around the pits lead to surface cracking which can grow to form through-the-thickness cracks [44]. Thus, corrosion pit depths of only tens or hundreds of microns can significantly accelerate crack growth and reduce fatigue life of the structure at all stress levels [7, 39, 43, 45]. Additionally, pit formation in aluminum usually results in a corrosion by-product that can have a volume increase of 6.5 times [44]. When by-product that created the pit is trapped between surfaces the volume change causes pillowing which leads to increased stress levels [44]. Researchers have tried to model and/or predict the effect of corrosion on structures using deterministic, non-deterministic, fuzzy, and probability models with varying amounts of success [24, 35, 42, 43, 44]. However, stress corrosion cracking and corrosion fatigue can lead to complicated failure mechanisms which are geometry, material, environment, and load dependant, so it can be nearly impossible to model or predict the effects of those corrosion forms [5, 8, 20, 1]. Therefore, precise structural health monitoring of pre-crack surface corrosion is critical to understanding and predicting the effect corrosion has on fatigue life and the integrity of a structure.

1.2 Corrosion Cost and Effect on Aircraft

To more narrowly define the scope of the research, the economic and structural challenges corrosion presents for aircraft will be discussed. Of all the industries affected by corrosion, the aircraft industry could perhaps benefit the most from better corrosion detection and prevention techniques. All industries suffer similar corrosion design, prevention, and maintenance challenges; however, corrosion problem tends to be exaggerated in aircraft for reasons that will be discussed in the following sections.

1.2.1 How Corrosion Has Become Such a Challenge for the Aircraft Industry

The first generation of commercial (B-707, DC-8, DC-9, B727, L-1010, DC-10) and military (C/KC-135, B52H, C-5A, C-130) jet aircraft from the 1950s and 1960s did not address corrosion control during design, and those aircraft had design service lives of 20-30 years [14, 20]. Second generation aircraft (B-737, 747, 757, 767, MD-81, 82, 88, 11, and F-100) from the 1970s and 1980s only incorporated corrosion tolerance into designs [20]. Since 1990, third generation aircraft like the B-777s and new B-737s were designed with corrosion prevention and control in mind. From a design standpoint, the first two generations of aircraft were never built to control or prevent corrosion, in fact, many of the corrosion resistant materials and practices that are common today did not even exist then. However, based on the design service objective of 20-30 years and regular maintenance, the aircraft were adequate assuming the service objective was adhered to.

Economic times changed for commercial airlines in the 1960s and 1970s, and the need to make a profit pressured airlines to extend the service lives of aging aircraft [20]. Many of the first two generations of aircraft are still in service today, and have exceeded the expected design service life of 20 years. In 1992, Boeing had produced 6660 aircraft since the late 1950s and 5300 were still in service [25]. Of those 5300 aircraft, 1100 had exceeded 100% of the design life, flight hours, or landings [25]. Similarly, in the late 1980s, the U.S. military was facing defense budget cuts and increasing aircraft costs, so service lives of C/KC-135s, B52Hs, C-5As, and C-130s were extended [14, 44]. The average age of those aircraft was 40-50 years in 1997 [14]. Many of those same aircraft will be expected to serve through 2010 and will reach service lives of 60-80 years [14]. Corrosion induced fatigue could be the life limiting factor for many of these aircraft, so it has become increasingly important to monitor, track, and quantify corrosion on these aircraft [14].

1.2.2 The Nature of Aircraft Corrosion

There are thousands of aging aircraft not designed to limit and control corrosion that are flying up to 4 times the initial design service life, so corrosion has a major effect on aircraft. Aircraft corrosion most often takes the form of intergranular or crevice corrosion in 2000 and 7000 series aluminum used in aircraft construction materials [5, 20, 39]. Crevice corrosion is caused when corrosive fluid becomes trapped between two surfaces setting up a chemical reaction which weakens areas with poor drainage or inadequate cleanouts. Intergranular corrosion is a result of local dissolution of the matrix due to a galvanic couple between the particles in the alloy [43]. Intergranular pitting corrosion has high penetration rates, and tends to weaken the airframe in localized areas. Failure can occur when corrosion is combined with static and dynamic stresses leading to stress corrosion cracking (SCC) or corrosion fatigue.

These types of corrosion produce very little mass loss; however, large losses in mechanical strength and fatigue life result [20]. Stress corrosion cracking and corrosion fatigue are difficult to detect by casual observation, yet can lead to mechanical fast fracture and catastrophic failure [8]. The reduction in strength and fatigue life result from localized pits which serve as nucleation sites for surface cracks and leads to through thickness cracks [43]. Experimental testing on aircraft components made from 2024 T3 aluminum indicate corrosion pits of just 5-10 microns can reduce fatigue life by a factor of two, and can decrease the mean time till crack formation by factors of 10 or more [7]. Based on the aircraft corrosion classification index shown in Table 1.2.1, 5-10 micron corrosion pits would be considered “light” corrosion damage, yet those pits have a significant effect on mean time till crack formation and fatigue life. It is estimated that atmospheric corrosion (material interaction with air and impurities) alone may penetrate aluminum at rates of 0.81 microns per year in industrial environments [1].

Table 1.2.1: The aircraft corrosion classification index sets a standard based on pit depth [14].

Corrosion Classification Index		
Classification	Corrosion Depth (in)	Corrosion Depth (microns)
Light	0.001 or less	25.4 or less
Light to Moderate	0.001 to 0.003	25.4 to 76.2
Moderate	0.001 to 0.01	25.4 to 254
Moderate to Severe	0.008 to 0.012	203 to 305
Severe	Greater than 0.01	254

1.2.3 The Structural Effect and Implications of Corrosion on Aircraft

Corrosion induced fatigue can lead to dangerous in-flight fatigue failures when visual inspection techniques do not identify corrosion damage. The most well-known example was the 1988 Aloha Airlines flight mentioned previously. Even after the post accident industry reforms, corrosion related accidents are still a problem. US Navy, Canadian Forces, and RAAF F-18s have lost trailing edge flaps during flight [17]. The aluminum hinge components experience corrosion accelerated fatigue which reduces the service life of the hinge pin by a factor of 10 [17]. Corrosion and fretting has been a factor in 687 accidents in aircraft between 1975 and 1994 [17]. The lap joints on C/KC-135s have been observed to contain corrosion pits that penetrate through the skin of the aircraft [44]. Rapid loss of cabin pressure could have resulted, and static deflection of the skin in the air stream could have caused fuselage skin loss. These are just a few of the corrosion related structural failures in aircraft listed in the literature.

For commercial and military aircraft, maintenance checks are tailored to the aircraft based on age and flight hours. For the average aircraft the “newness” phase lasts 5-6 years, and the “mature” stage lasts till 25000 flight hours [20]. Then, the aircraft goes through a D-Check where the aircraft is completely stripped and inspected. When corrosion damage is detected, metal is replaced before returning to service in the “aging” phase [20]. The modifications to the airframe reduce fatigue resistance, so the number of future non-routine repairs are increased [20]. Therefore, these aging aircraft have many corrosion problems, and it is very expensive to inspect, detect, and repair those aircraft. In 1996, the U.S. spent \$1.7 billion on commercial aircraft maintenance, and lost \$0.3 billion due to corrosion maintenance downtime [40]. In 1990, the USAF spent \$110,000 per aircraft per year on corrosion maintenance for the 7500 aircraft in the fleet [19]. In 2001, the USAF spent \$170,000 per aircraft per year on corrosion maintenance for the 5500 aircraft in the fleet, and the cost was rising 7% per year [10, 19].

Since corrosion and its effects are often unpredictable, the commercial and military aircraft industries have adopted find and fix maintenance approaches to corrosion detection. The find and fix maintenance practices of the airline industry are costly and in some cases inadequate [14, 20]. Those practices must be replaced by understanding corrosion processes and developing methods to predict and monitor corrosion behavior before cracking occurs. Using the impedance method and other nondestructive evaluation and inspection techniques (NDE & NDI) to detect corrosion should be part of next generation maintenance practices.

1.3 Corrosion Detection Methods for Aircraft

Corrosion detection techniques within the aircraft industry are similar to those used in any industry. However, the utilization of those techniques is more widespread in the aircraft industry due to the scope and nature of the challenge corrosion presents for aircraft. In this section, the current state-of-the-art in aircraft corrosion detection will be presented. The operating principles of each corrosion detection method and technique will be described, and the advantages and disadvantages of each method will be presented.

1.3.1 Aircraft Corrosion Detection Methods

Several corrosion and crack monitoring techniques have been developed, and the detection methods fall into two major categories. First, there are corrosion detection devices and techniques used to supplement visual inspection at routine maintenance intervals. Those techniques include Visual, Eddy Current, Ultrasonics, Electrochemical Impedance Spectroscopy (EIS), Color Visual Imaging (CVI), Radiography, and Infrared Imaging (IRI) [11, 38]. Some of these techniques are used throughout the aircraft industry and many have been automated to speed detection; however, most still require skilled operators with knowledge of where to focus the detection. Additionally, these devices are only used at maintenance intervals, so damage arising between routine service intervals is problematic. Several methods do not directly detect corrosion, but instead detect the presence of moisture which is an indicator of corrosive environments.

The second group of corrosion and crack monitoring tools is sensors and/or actuators integrated into automated Structural Health Monitoring (SHM) systems. The sensors subgroup passively measures at discrete predetermined locations: acceleration, pH, humidity, acoustic emission, ion concentration, linear polarization resistance, and chemical potential detectors. The self-sensing actuator subgroup uses the properties of piezoelectric smart materials to actively generate high frequency nondestructive vibrations to inspect a structure for cracks and/or corrosion using Lamb Wave or impedance methods. The advantage of the second group of corrosion and crack detectors is the ability to do real-time monitoring and alert maintenance technicians as the structure changes. Group two methods are not as widely used, but that is changing. The goal of this research is to evaluate the impedance method for structural health

monitoring of pre-crack corrosion. A listing of the corrosion and crack detection methods and how they work may be seen in Figure 1.3.1.

Table 1.3.1: NDE and NDI techniques used to corrosion detection in aircraft.

Detection Technique	How the detection method works
Visual & Enhanced Visual	Routine reviews of the structure by a human observer usually at scheduled service and maintenance intervals to detect cracks and corrosion [11, 37].
Eddy Current	After calibration on similar materials, a probe containing a coil is passed close to a conductive surface. AC current flows through the coil producing circulating magnetic fields (eddy currents) in the structure. The phase and magnitude of the eddy currents affect the coil impedance. Cracks and corrosion disrupt the eddy current flows and change the coil impedance as described by [15, 44, 11, 37].
Ultrasonics	Ultrasound is passed into the structure and the reflection is measured used to create a 2-D map of the surface to detect cracks and corrosion [11, 23, 37].
Radiography	X-Ray beams attenuate when passed through aluminum; therefore, a loss of material can be detected by increased intensity of the radiograph [11, 37].
Electrochemical Impedance Spectroscopy (EIS)	Corrosive reactions produce an anodic (i_a) and cathodic (i_c) current, and i_a is proportional to the corrosion rate. Only the net current can be directly measured. In EIS an AC voltage is applied to the metal, and the magnitude and phase of the impedance are measured for various frequencies to determine the anode current. The system can be modeled as a system of resistors and capacitors which produce a similar FRF [8, 9, 12, 26, 47].
Color Visible Imaging (CVI)	High resolution color cameras photograph the surface and a pixel by pixel analysis algorithm evaluates the surface of the structure for pitting, pillowing, or cracking [12, 37].
Infrared Imaging (IRI)/ Thermography	The structure is heated or cooled rapidly to create a thermal gradient. Thermal cameras monitor the change in the temperature gradient to determine areas with different thermal conductivity. Conductivity changes result from defects or the presence of moisture [11, 12, 37].
Lamb Waves	Nondestructive high frequency surface waves are generated by piezoelectrics, and those surface waves pass through the material. Reflections occur at surface boundaries and are recorded by the piezoelectrics. As cracks or corrosion occurs on the structure, the reflection patterns or the energy absorbed changes [6, 18, 21, 41, 46].

Impedance Method	When piezoelectric materials are bonded to a structure the mechanical impedance of the structure couples with the electrical impedance of the piezoelectric. As cracks or corrosion occur on the structure, the mechanical impedance changes, and is measured as a corresponding electrical impedance change in the piezoelectric [28, 34].
------------------	---

1.3.2 The Advantages and Disadvantages of Corrosion Detection Methods

Each of the corrosion detection methods listed above has unique properties that make them useful for detecting certain types of corrosion. As of yet, no one method can detect and quantify all types and forms of corrosion in all types of joints, fasteners, and materials. Thus, it requires multiple techniques to detect aircraft corrosion. The advantages and disadvantages of each method may be seen in Table 1.1.4.

Table 1.3.2: The advantages and disadvantages of each corrosion detection methods.

Detection Technique	Advantage	Disadvantage
Visual & Enhanced Visual [11, 37]	<ul style="list-style-type: none"> • Humans are very good at identifying patterns associated with damage. • Large coverage areas in accessible regions. • Relatively fast, inexpensive, and portable. 	<ul style="list-style-type: none"> • Can be subjective. • Limited to visually accessible areas. • Time intensive. • Can be imprecise.
Eddy Current [15, 44, 11, 37]	<ul style="list-style-type: none"> • Good for detecting cracks, intergranular, and pitting corrosion in thin plates and fasteners • Has been automated for quick fastener examination with humans guiding the probe. • Can detect damage in multiple layers. 	<ul style="list-style-type: none"> • Must be calibrated. • Skilled operators required to interpret data. • Localized detection requires knowledge of possible damaged areas.
Ultrasonics [11, 23, 37]	<ul style="list-style-type: none"> • Works well on aluminum. • Detects material loss. • Good for corrosion, delaminations, and voids. • Relatively time-intensive. 	<ul style="list-style-type: none"> • Rough surfaces may have weak reflections which make thickness gauging difficult. • May require a gel between probe and structure. • Does not work well on multiple layers.

<p>Radiography [11, 37]</p>	<ul style="list-style-type: none"> • Good for localized detection. • Layers do not affect the outcome. • Water absorbs the radiation, so it can detect moisture. • Produces an image of the damage. 	<ul style="list-style-type: none"> • Requires a minimum intensity difference. • Requires a material loss, so remaining corrosion products obscure detection. • High cost and safety concerns.
<p>Electrochemical Impedance Spectroscopy (EIS) [8, 9, 12, 26, 47]</p>	<ul style="list-style-type: none"> • Direct measurement of corrosion rate and degree of moisture content. • Can detect non-visible corrosion • Models the corrosive system may be developed. • Possibility of prediction based on models. 	<ul style="list-style-type: none"> • Localized detection requires knowledge of damaged areas. • Less than 1 sq ft detection area.
<p>Color Visible Imaging (CVI) [12, 37]</p>	<ul style="list-style-type: none"> • Direct replacement for visible inspection with greater sensitivity. • A way to automate the visual inspection process. 	<ul style="list-style-type: none"> • Only detects the effects of corrosion. • Damage must be visible. • Image processing can be computationally intensive.
<p>Infrared Imaging (IRI)/ Thermograph [11, 12, 37]</p>	<ul style="list-style-type: none"> • Can identify damage missed by CVI. • Produces an image of the damage. • Good for surface corrosion. • Large scan area. 	<ul style="list-style-type: none"> • Only detects the effects of corrosion. • Requires heating and cooling of the system. • Active nature requires more operator skill. • Not good for layered materials.
<p>Lamb Waves [13, 18, 21, 41,46].</p>	<ul style="list-style-type: none"> • Good for locating damage. • Baselines are not always required. • Arrays of sensors aid detections. • Some commercial products are now available. 	<ul style="list-style-type: none"> • Can only detect surface damage • Can require very high sampling rates (greater than 1 MHz). • In some cases waves must pass through the damage to be detectable. • The time signals must be post-processed.

Impedance Method [28, 34].	<ul style="list-style-type: none"> • Detection is based on the structural response. • Reduces required sensors by allowing self-sensing actuation (SSA). • No bridge circuits are required for SSA. • Damage metrics allow for quick data reduction with minimal post-processing. • Very sensitive to damage and changes in damage. • Can identify the same damage as ultrasound and eddy current. 	<ul style="list-style-type: none"> • Not as useful for locating damage • Maintaining sensor health and bonding is important. • Requires knowledge of a healthy structure.
-------------------------------	--	--

Routine aircraft maintenance occurs at defined service intervals, so structural damage like corrosion occurring between service intervals is not monitored even though it may be detrimental to the immediate health of the aircraft. Additionally, with no structural information being recorded between service intervals, maintenance technicians and personnel may only make experienced guesses or rely on historical data to determine areas on the aircraft to focus corrosion detection during the routine service intervals. Thus, significant structural changes related to damage may be missed during the inspection process.

The newest generation of autonomous structural health monitoring systems with active sensors (Lamb Wave and Impedance) could remedy the lack of between-service structural data. This would allow maintenance technicians to more accurately focus routine service to areas already defined as problem areas. Plus, between-service data could also alert pilots of immediate structural changes that might preclude catastrophic in-flight failures, so that immediate action could be taken.

1.4 Introduction to the Impedance Method

Lamb waves and the impedance methods are two active damaged detection techniques which utilized the self-sensing capabilities of smart materials to non-destructively inspect and evaluate the health of structures. As an added benefit, both methods have recently been integrated into autonomous SHM devices, such that the same self-sensing actuator can perform both detection techniques [28].

The goal of this research is to evaluate the impedance method as a corrosion detection and quantification tool. In this section, the following topics will be discussed: the mechanical

impedance of structures, piezoelectric materials, and how piezoelectric material can electrically be coupled with the mechanical impedance of structures. Finally, the impedance method will be presented, and how it is used as a SHM tool will be explained.

1.4.1 Mechanical Impedance

Typically, impedance is a parameter used to characterize electric circuits and components, and most people are accustomed to seeing impedance from that perspective. To understand the impedance method it is important to understand the concepts of electrical impedance (V/I) and mechanical impedance (F/v). The two relationships are exactly the same, so the mechanical impedance will be discussed to develop some background for a discussion of the impedance method.

For any single point in a vibrating system the mechanical impedance (Z) is the ratio of the harmonic driving force (F) and the velocity (v). For a sinusoidal driving force with a magnitude F_0 and angular frequency ω , the force is defined as

$$F = F_0 e^{j\omega t} \quad (1.1)$$

When the driving force is applied, the velocity

$$v = v_0 e^{j(\omega t + \phi)} \quad (1.2)$$

results where v_0 is the magnitude and ϕ is the phase angle between the force and velocity. Thus, the mechanical impedance (Z)

$$Z = \frac{F(j\omega)}{v(j\omega)} \quad (1.3)$$

is the ratio of equation 1 and 2, and is a function of ($j\omega$) [3, 15].

Like the electrical relationships, combinations of mechanical elements like dampers, springs, and masses comprise mechanical systems. By knowing the mechanical impedances of the three basic mechanical elements we can see how they combine to form more complex systems. The first mechanical element is a damper, and a schematic diagram may be seen in Figure 1.4.1. For dampers, the relative velocities of the endpoints are proportional to the force applied to one end. For a damper the velocity of point 1 (v_a) with respect to point 2 (v_b) is

$$v = (v_a - v_b) = \frac{F_1}{c} \quad (1.4)$$

where c is the proportionality constant (damping constant). The mechanical impedance of a damper is

$$Z_c = \frac{F(j\omega)}{v(j\omega)} = c \quad (1.5)$$

which acts like a mechanical resistance [3, 15].

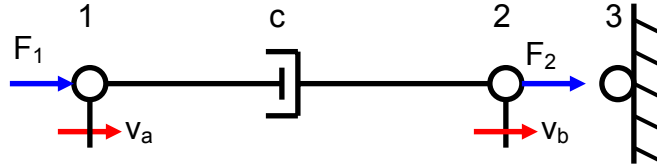


Figure 1.4.1: Schematic diagram of an ideal mechanical damper [15].

For an ideal linear spring, the relative displacement between the ends is proportional to the force applied to one end as seen in Figure 1.4.2. From the diagram, the relative displacement is

$$x_a - x_b = \frac{F_1}{k} \quad (1.6)$$

where k is the spring constant. Knowing that F_1 & F_2 are equal, substituting in equation 1, and differentiating with respect to time yields the mechanical impedance of a spring [3, 15].

$$Z_k = \frac{-jk}{\omega} \quad (1.7)$$

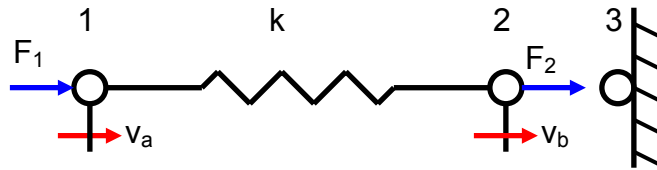


Figure 1.4.2: Schematic diagram of an ideal mechanical spring [15].

For an ideal mass shown in Figure 1.4.3, the acceleration is proportional to F and inversely proportional to the mass (m) such that

$$\ddot{x}_1 = \frac{F_1}{m} \quad (1.8)$$

where \ddot{x}_1 is the second time derivative of position. Substituting equation 1 into equation 8, and integrating with respect to time yields the mechanical impedance

$$Z = j\omega m \quad (1.9)$$

of an ideal mass [3, 15].

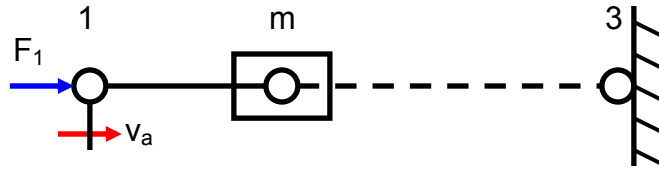


Figure 1.4.3: Schematic diagram of an ideal mechanical mass [15].

For the previous derivations the elements were assumed to be ideal, meaning the springs are considered to be linear with no energy loss and the dampers and springs were considered to be massless. In reality, those assumptions are likely not true, but they will be assumed so for the purposes of this discussion.

A healthy structure (like an aircraft panel) may be thought of as a multiple degree of freedom system composed many mechanical elements with different mass, spring, and damper elements. If all the basic elements are known, then all of the mechanical impedance elements could be combined using Kirchhoff's Laws, Thevenin's equivalents, Norton's equivalence, reciprocity theorems, and superposition theorems. The result would be a single impedance equation which would describe the input (Force) output (velocity) relationship for the structure. The equation would define the frequency dependant structural response of the system. It would be very useful to know such a relationship for the system for many reasons, but for SHM such an equation would define the healthy mechanical response of the structure. Thus, if the system corroded or cracked, the structural response would deviate from the healthy response, and it would be possible to see the effect of the damage through the mechanical impedance change. Of course, the damaged impedance relationship for the system would have to be derived, and it might prove difficult to derive the mechanical impedance relationship for the healthy system over a wide frequency range for a complex structure.

That is the beauty of the impedance method; the mechanical impedance (structural response) is indirectly measured through the coupled electrical impedance of a piezoelectric material bonded to the structure. With no structural model, the response is measured and can be visualized by plotting the impedance signature. As the structure corrodes, the response changes in relation to the healthy response, and that change can be quantified in useful ways.

1.4.2 Properties of Piezoelectric Materials

Piezoelectric materials like the ones seen in Figure 1.4.4 have useful mechanical and electrical properties. In general, when piezoelectric materials are mechanically strained an

electrical field is produced. Conversely, when an electric field is applied to piezoelectric materials a mechanical strain is produced. Piezoelectric materials have unique molecular structures which allow bidirectional electromechanical coupling between electric field and strain. Because of their unique properties piezoelectric materials prove useful for self-sensing actuators, power harvesting, and SHM applications [28].

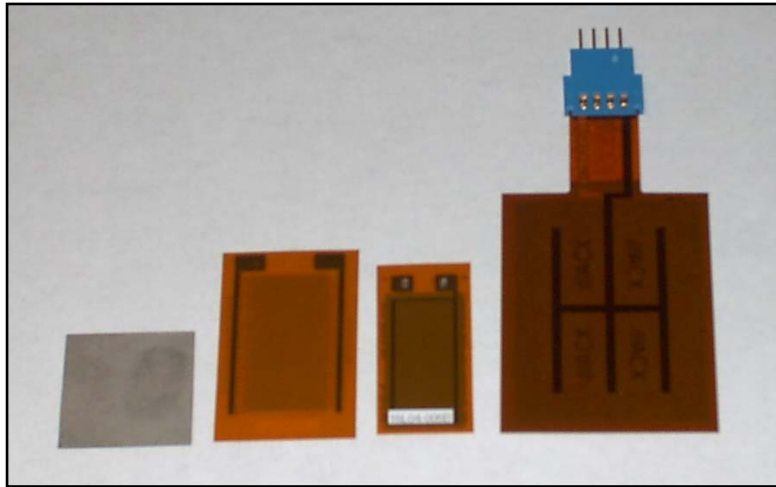


Figure 1.4.4: Pictures of several commercially available piezoelectric actuators.

When piezoelectric materials are bonded to a structure, the electromechanical coupling allows the electrical impedance of the piezoelectric to be directly related to the mechanical impedance of the structure it is bonded to [32]. As the structure is damaged the mass, stiffness, and/or damping changes cause the mechanical impedance to vary. Because the electrical impedance of the piezoelectric material is coupled with the mechanical impedance of the structure, any change in the mechanical impedance leads to changes in the measured electrical impedance of the piezoelectric material. Therefore, by monitoring the electrical impedance of the piezoelectric, damage can be detected as the impedance signatures shifts from a healthy state to a damaged state. Additionally, the self-sensing properties of the piezoelectric allow one piece of material to sense the input voltage and measure the output current. Relative to the mass of aircraft panels, the mass and size of the patch is small, so the dynamic effect on the structure is minimized. Piezoelectric materials like Lead Zirconate Titanate (PZT) are the key component in impedance based structural health monitoring [28].

1.4.3 Impedance Method

Liang et al. (1994), is credited with the initial development of the impedance method. Since then many others have further developed the impedance method for SHM. For a complete review on the development see Park et al. (2003). In general, PZT is bonded to a structure, and high frequency (30-300 kHz) low voltage (less than 1V) structural excitations are used to monitor the electrical impedance of the PZT patch. The mechanical impedance of the structure is known through the coupling with the electrical impedance the PZT patch. A diagram of the components involved in the impedance method may be seen in Figure 1.4.5. A one degree of freedom fixed-free structure is represented by a mass, spring, and damper, and is driven by a PZT patch fixed to the structure. The electromechanical interaction between the structure and piezoelectric can be understood through the electrical admittance $Y(\omega)$ equation developed by Liang et al. The electrical admittance is the inverse of the combined PZT electrical impedance $Z_a(\omega)$ and structural impedance $Z_s(\omega)$

$$Y(\omega) = \frac{I}{V} = ai\omega \left(\varepsilon^T_{33}(1 - i\delta) - \frac{Z_s(\omega)}{Z_s(\omega) + Z_a(\omega)} d_{3x}^2 Y^E_{xx} \right) \quad (1.10)$$

where a is the geometric constant of the PZT, δ is the dielectric loss of PZT, ε^T_{33} is the dielectric permittivity at constant stress, d_{3x} is the piezoelectric strain coefficient, and Y^E_{xx} is the Young's modulus of the piezoelectric at zero electric field. So long as the PZT, bond, and structural properties remain constant, equation 10 outlines how the mechanical impedance can be monitored through the PZT electrical impedance much like that of an frequency response function (FRF) [28].

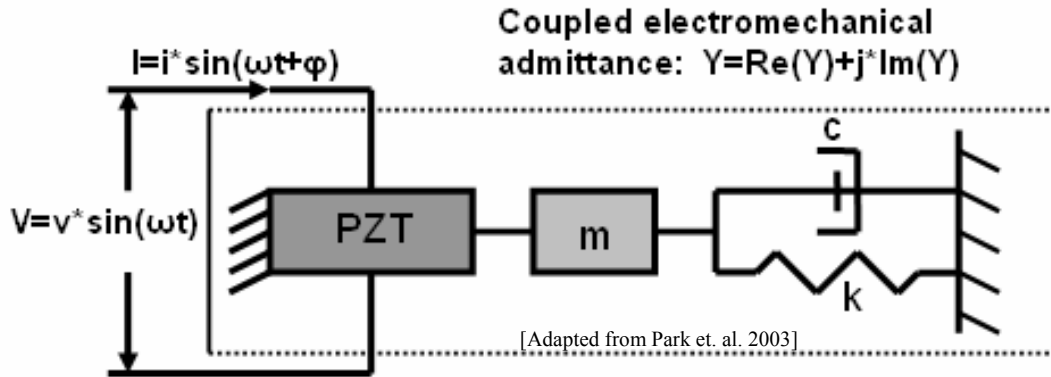


Figure 1.4.5: An electromechanical model of the admittance [28].

Most researchers have used the real part of the electrical impedance to assess the health of structures. Typically, the frequency ranges for the impedance signatures are chosen to have high peak densities that are sensitive to damage. Once multiple healthy and damage impedance signatures are obtained, damage metrics are utilized to quantify the difference between the signatures and reduce the data significantly. Details on the real part of the impedance, frequency selection, and damage metrics are discussed in Chapter 2.

1.5 Literature Review

The impedance method has been successfully used to detect various defects in the following: high temperature structures [2830], pipe line networks [33], bolted joints [32], scaled bridge sections [32], cracked aircraft panels [100], and concrete composites [32]. These are just a few of the damage detections applications for the impedance method, and a more complete overview may be found in Park et al. (2003) [28]. However, for corrosion detection, much less research has been performed using the impedance method. The following literature review will discuss some of the important results in the field of impedance-based corrosion detection. Since the purpose of this thesis is to experimentally evaluate using piezoelectric materials in conjunction with the impedance methods to detect, locate, and quantify pre-crack surface corrosion damage in beams and plates the literature review will define the current state-of-the-art in the field.

1.5.1 Impedance-Based Corrosion Detection

Lalande et al. (1996) used the impedance method to investigate complex precision parts like those found in gear sets. Gears are widely used high tolerance parts, so it was speculated that the impedance method could detect gear tooth damage through the base structure. Tooth bending fatigue and abrasive tooth wear are the most common types of damage in complex machines, and it was possible to detect both types of damage using the impedance method. Abrasive wear is similar to erosion (a type of corrosion), so this demonstrates the usefulness of the impedance method [22].

Park et al. (2000) explained the basics of impedance based structural health monitoring. A one-dimensional model of PZT and host structure are mathematically analyzed using the wave equation to show how the electrical impedance change in the bonded PZT is similar to the frequency response of the system at higher frequencies. At the time of publication, there was no correlation between the electrical impedance change within the PZT and a change in the mechanical property of the system. The spectral method was utilized to develop an analytical model for a free-free bar comprised on ten spectral elements. Damage is introduced by increasing the wavenumber, which is correlated to a change stiffness and the Young's Modulus of the structure. A damage location vector indicates levels of damage for each element and correctly identifies the damaged element. Experimental verification is made by bonding multiple PZT patches to a free-free beam, and impedance tests are conducted at 70-90 kHz. Bolts are added to the structure to change the mass and stiffness properties of the systems. The real part of the impedance signal is used for analysis because it is more sensitive to change than the imaginary part or the magnitude which are capacitive and less sensitive to change. Later, accelerometers are attached to the beam and frequency response functions are measured in the longitudinal direction. The results show good agreement between the analytical and experimental models, showing the usefulness of impedance based structural health monitoring. Additionally, Park noted the ability of the impedance method to detect minor structural changes, and described the mass loss condition associated with corrosion [29].

Sodano et al. (2003) was the first to investigate macro-fiber composites (MFC D_{31}) as self-sensing actuators for damage detection with the impedance method. MFCs have rather unique properties compared to traditional piezoelectrics. MFCs consist of many interdigitated electrodes sandwiched between layers of Kapton, so unlike monolithic PZT, MFCs are conformable, flexible and have some amount of environmental protection for the electrodes. Since MFCs still possess the electromechanical coupling like PZT, it is suitable for self-sensing and damage

detection. Sodano showed the new material was effective in self-sensing vibration control achieving vibration reduction of up to 50% when used in closed-loop positive position feedback control. Additionally, MFCs were shown to detect loose bolts in free-free bolted joint sections when using the impedance method. It was noted that MFCs seem to have a directional sensing capability not seen in PZT actuators that could prove useful in damage location. The system was not used to detect corrosion, but the directional sensing capability of MFC could be useful in corrosion location schemes using the impedance method. Plus, MFC electrodes are protected by Kapton, and would be robust sensors/actuators in corrosive environments [36].

Giurgiutiu (2003) used built-in piezoelectric wafer active sensors (PWAS) to detect and locate damage in laboratory experiments on aircraft panels. The PWAS sensors were used to generate guided Lamb waves in pulse-echo mode. After subtracting the reflections from the plate edge, PWAS was capable of detecting a 12.7 mm crack 100mm from the sensor. By sequentially triggering an array of PWAS sensors, the ultrasonic wave front was steered to locate 19 mm cracks when used in conjunction with impedance tests. The impedance method was also used to successfully detect the 12.7 and 19 mm cracks in aircraft panels. PWAS were also used for impact detection, simulated acoustic emission detection on a flat structural aircraft panel. Giurgiutiu concluded PWAS could be used to detect corrosion and cracking, but the experimental work focused only on through-crack detection. [13].

Peairs et al. (2004) developed a miniaturized, low-cost impedance measuring device to increase the accessibility and portability of the impedance method. Previously, implementing the impedance method required costly, bulky, and expensive impedance analyzers like the HP4194A. The low-cost method replaces the impedance analyzer with an FFT analyzer and a current measuring circuit. Since commercial hardware and software now allows for FFT on a single chip the whole system can be implemented on a computer chip. The low-cost impedance method was calibrated against an impedance analyzer and tested on pipeline and composite structures to show the accuracy of the low-cost method on real-world structures. Even though it was not tested on corrosion damage, this low cost alternative is a must for future impedance based autonomous SHM devices [34].

Kwun et al. (2002) used a thin-strip MsS guided wave sensor the wave direction is perpendicular to the length-wise direction of the sensor. Two 6 mm thick test plates were welded together to experimentally tested for the MsS sensor. Two sensors were used to detect a weld defect and simulated corrosion (five 6.35mm diameter 50% through thickness holes). The system could detect the corrosion damage when three or more holes were made. It proved difficult to subtract all of the unimportant reflections from the signal, and the width of the area monitored

prevented both sensors from being able to detect the damage. The system did not test for corrosion using the impedance method with the sensors, but systems like this could use guided waves and impedance methods both to detect and quantify corrosion [21].

1.6 Thesis Overview

1.6.1 Chapter 1 Summary

Chapter 1 introduces the scope of the corrosion problem in terms of economic cost and the challenges it presents for the structural health of aircraft. The corrosion problem was presented in terms of aircraft corrosion because it is a significant challenge for that industry and it has been well documented. The same corrosion challenges exist in all major industries, and it would be wise to learn from those examples. Corrosion is a major factor in the long-term health of structures because it causes stress concentrations which more quickly develop into cracks, shortening the lifespan of the structure. Therefore, corrosion should not be ignored during the structural design and development stage when simple cost effective guidelines could be followed to prevent and control corrosion on structures. Additionally, all corrosion can never be prevented, so it is very important to avoid the “neglect phase” where corrosion maintenance is ignored until the corrosion becomes apparent. By that point, corrosion has irreversibly affected the long term health of the structure and it is very expensive if not impossible to repair and maintain the structure. Thus, it would be very useful to develop corrosion detection tools like the impedance method to inspect structures on a continuous basis (to supplement routine inspections) so pre-crack surface corrosion could be detected and treated before cracking begins and permanently degrades the structure. A literature review on the topic indicates no work has been conducted on using the impedance method to detect corrosion. Thus, my research focuses on using and adapting the impedance method for SHM to detect, track, and quantify the earliest stages of pre-crack surface corrosion in beam and plate-like structures

1.6.2 Chapter 2 Summary & Contributions

Chapter 2 focuses on detecting 1.4% surface coverage of light pre-crack surface corrosion in aluminum beams. Recommendations for sensitivity testing and frequency selection for impedance-based corrosion detection are outlined. Methods for managing ambient variation

in the impedance signatures are discussed so that the corrosion damage is distinguishable from experimental noise. The most common types of corrosive chemical reactions and the resulting mechanical effect on aluminum aircraft structure are presented. Experimental methods for accelerating the corrosion process in the laboratory while still achieving the desired mechanical defects are described. The mechanical effects between the actual and simulated corrosion are nearly identical. The importance of damage metrics is explained, several damage metrics were tested for corrosion detection, and RMSD metrics were chosen to analyze the impedance data. For the first time in literature, realistic amounts of corrosion are detectable using the impedance method. The experimental results indicate multiple site damage of 1.4% surface coverage of light (less than 25 micron pits) pre-crack surface corrosion is detectable and distinguishable at distances up to 150 cm on aluminum beams. Some frequency ranges proved to be better for detecting corrosion, and the patterns conducive and non-conducive to corrosion detection are described in detail.

1.6.3 Chapter 3 Summary & Contributions

From Chapter 2 it is clear the impedance method can detect the earliest stages of pre-crack surface corrosion on beam-like structures. Since the method is very sensitive to the damage, it would be useful to not immediately repair the corrosion damage that does not pose a problem for the structure as is the common practice in the airline industry today. For such cases, it would be very useful to use the impedance method and other NDE techniques to quantify key aspects of the damage and track it until repair is required. Three of the most important corrosion damage variables to quantify are location, pit depth, and surface coverage. It is unlikely that any NDE technique including the impedance method could provide all of that data, so it is important to know which corrosion variables the impedance method best correlates with. In the future, this knowledge could tell the designers of autonomous SHM devices which variables to measure with each technique and how to correlate it with other maintenance records.

Chapter 3 involves the design of three different tests on aluminum beams to quantify how impedance damage metrics correlate with corrosion location, pit depth, and surface coverage changes. The experimental setups and procedures for each of the three tests are described. Results from the tests show the impedance method correlates best with corrosion pit depth changes, which is beneficial because pit depth is a key variable in corrosion adjusted fatigue life calculations. If used in conjunction with routine maintenance it might be possible to make corrosion pit depth prediction based on impedance data from the structure. Results from the

location and surface coverage tests are not as conclusive as the pit depth results, so used in this manner the impedance method might not be as well suited to quantify corrosion location and surface coverage. When used in conjunction with other NDE techniques like Lamb Wave Propagation (which uses the same sensor/actuators) the impedance method could help maintenance technicians quantify the corrosion process.

1.6.4 Chapter 4 Summary & Contributions

In aircraft the wing and fuselage surfaces are primarily plate-like structures, and those surfaces are some of the thinnest and least rigid structures on aircraft. Aircraft panels are required to provide lift, reduce drag, protect mechanicals, and withstand repeated internal and external pressurization and thermal cycles. Due to the large surface areas, corrosion penetration of aircraft panels can generate large forces when the damage panels deflect in the air stream and lead to fast and sometimes catastrophic failure modes. It would be beneficial if the corrosion damage to panels and plates could be monitored continuously.

The structural response of plates is more complex than the response of beams, so the differences in the impedance signatures of plates and beams are plotted. The effect the change in response difference is discussed and used to adapt sensitivity testing and frequency selection procedures for plates. The experimental setup and procedures for the plate corrosion test are described, and an array of PZT sensors is used for plate corrosion detection. Experimental results show the impedance method can detect and distinguish 1% and 0.25% surface coverage of light to moderate pre-crack surface corrosion on a 1 m² aluminum plate. The detection results are compiled by frequency range and by damage location to provide insights into the best ways to test for plate corrosion.

1.6.5 Chapter 5 Summary & Contributions

Corrosion presents some unique detection challenges for the impedance method, and Chapter 5 will address those issues. The impedance method requires healthy system data as a reference to determine when the system becomes damaged. If corrosion directly damages the piezoelectric sensor, the healthy system reference is lost, and it becomes difficult to diagnose the structure. Chapter 5 is devoted to experiments which quantify and avoid sensor degradation so that healthy system references can be maintained. First, the corrosive effect on PZT and MFC sensors is experimentally quantified to identify the effect and patterns of sensor corrosion. Second, the

corrosion detection capabilities of Kapton protected MFC D_{31} and D_{33} piezoelectrics are assessed. Finally, sensor corrosion can be avoided by locating sensors on the structure opposite the corrosion damage. MFC D_{31} , MFC D_{33} , and PZT sensor are tested for through-structure corrosion detection.

The exact pattern of PZT and MFC sensor corrosion could not be identified because some of the results are contradictory. However, the contradictory results demonstrate the importance of isolating and protecting sensors from harsh corrosive environments. Recommendations for sensor selection and protection are made. MFC D_{31} and D_{33} piezoelectrics were shown to detect light pre-crack surface corrosion at distance up to 50 cm from the sensor. Additionally, MFC D_{31} , MFC D_{33} , and PZT were shown to detect light pre-crack surface corrosion through the structure.

Chapter 2

Detecting Corrosion Damage in Beams

2.1 Introduction

In aircraft structures beams are widely used to construct floors, doorways, galleys, fuselage load structures, fasteners on the upper wing skin, trailing edges, hinge lugs, stringers, and airframe web members [20, 27]. Most of these beam-like structures in aircraft are located in areas prone to corrosion damage and require regular monitoring and repair during routine maintenance intervals to ensure aircraft safety. In order to avoid costly maintenance it is necessary to use nondestructive inspection (NDI) techniques to detect corrosion early in the development stage [20]. The goal of this chapter is to design an experiment to determine if the impedance method can detect multiple instances of pre-crack surface corrosion in beam-like structures similar to those found in aircraft.

2.2 Testing Procedure & Experimental Setup

2.2.1 Impedance Terminology and Definitions

Before discussing the testing methodology, it is important to define the meaning of terms which will be used throughout the chapter. Impedance measurement will imply all impedance data for one frequency range which will consist of 2000 samples for beam testing. For beams, an impedance sweep will refer to all impedance measurements for one data run which will consist of

12000 samples compiled from 6 impedance measurements each at a different frequency. A baseline refers to the 30 or more repeated impedance sweeps made for the undamaged structure and each level of damage to the structure.

2.2.2 Experimental Setup & Sensitivity Testing

A beam of dimensions 183 x 2.54 x 0.159 cm was selected for corrosion detection testing. A beam longer than 1 m in length was chosen because it allows for long-range corrosion detection. The beam was made from a 6063 T5 aluminum alloy, an alloy that is highly resistant to corrosion, but possesses lower ultimate and yield strength than aircraft grade (2000 and 7000 series) aluminums [27]. Specification sheets rate the material as SCC resistant; however, when the material is corroded intergranular pitting is produced. This makes 6063 T5 a good candidate for corrosion testing because it experiences the same mechanical defects when corroded that aircraft grade aluminum would experience. The main advantage 2000 and 7000 series aluminums have is ultimate and yield stresses that are twice as large as 6061 T5, so those materials are better suited for aircraft fittings, bolts, and fasteners [27]. This partially explains why aircraft (especially early generations) have so many corrosion problems, corrosion resistance was not as important as material strength during the design and material selection stages. Of course, some corrosion resistant alloys did not even exist during the 1950s and 1960s.

The centerline of a 2.54 x 2.29 x 0.0267 cm piece of PZT 5A material was bonded to the beam 7.62 cm from the edge of the beam. PZT 5A material was used because it is less sensitive to temperature changes than 5H material. A small hole was drilled into the end of the beam so it could be hung vertically during testing to simulate free-free boundary conditions. Electrodes were attached to the PZT and connected to an HP 4194A impedance analyzer. The analyzer utilized a GPIB port to interface with a laptop computer running a LabView program to control the analyzer and record system data. Sensitivity tests between 20 and 320 kHz were conducted to determine the individual frequency ranges to measure. To find frequencies sensitive to damage a broad impedance sweep was made for the healthy beam. Later, a small piece of wax was added to the structure, and another impedance sweep was made. Visual comparisons of the two baselines allow test frequencies to be chosen that are sensitive to damage and have adequate peak densities (5-10 peaks/range). Figure 2.2.1 shows the results of the sensitivity test. Impedance sweeps between 20-22 kHz, 54-56 kHz, 71-73 kHz, 96.5-98.5 kHz, 103-105 kHz, and 126-128 kHz had high peak densities and were responsive to beam corrosion damage. In Chapter 4, a

better approach to sensitivity testing will be discussed, and the approach will be modified to account for damage sensitivity and ambient variations.

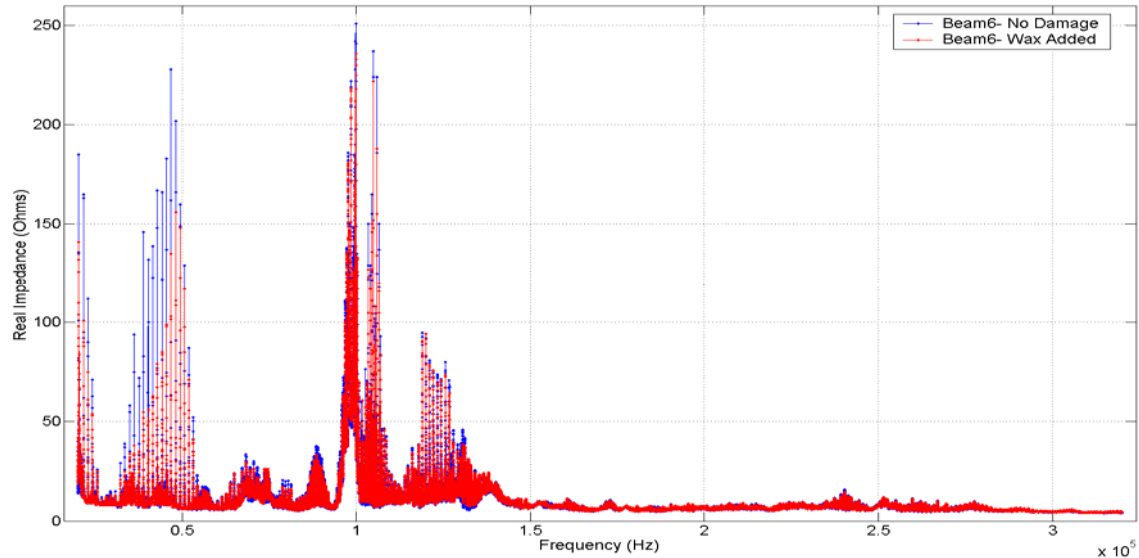


Figure 2.2.1: Sensitivity tests aid frequency selection by showing areas responsive to damage.

A frequency resolution of 1 Hz was used for each impedance measurement. Thirty-three baseline impedance measurements were made over a 5 day period to quantify the ambient noise and variation expected in the damage tests. All tests were performed in a climate controlled laboratory, so the temperature variations were limited to within a few degrees. After the healthy baseline samples were collected, 2.54 cm² (1.4% coverage) areas of the beam were chemically corroded with hydrochloric (HCl) acid at distances of 12.5, 25, 50, 100, and 150 cm from the PZT sensor. After each instance of corrosion was added, a new baseline impedance measurement of at least 30 sweeps was collected over a 1 day period. The original beam had a surface roughness of 0.799 microns, and the surface corrosion depth ranged from 4.375 microns to 12.85 microns for the five levels of damage as measured by a PDI Surfometer Series 400 profilometer. In all five instances of damage, the corrosion depth would classify the damage as light. A diagram of the beam in its final state may be seen in Figure 2.2.2.

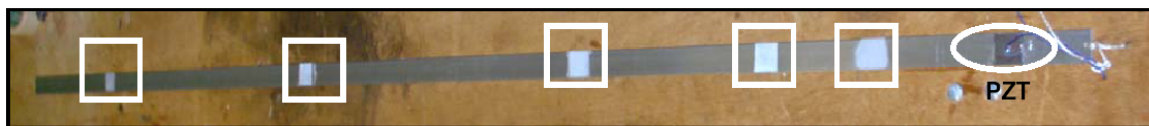


Figure 2.2.2: An aluminum beam after the corrosion detection tests with squares marking the damage and an oval marking the sensor.

2.2.3 Introducing Corrosion Damage

Hydrochloric acid (HCl) was utilized to quickly simulate the intergranular pitting corrosion damage an aircraft panel would experience over several years. There are three reasons why HCl was used to corrode the structure. First, aluminum in an industrial environment pits at an approximate rate of 0.81 microns/year, so the corrosion growth rate must be advanced [500]. Second, the two most common types of aircraft corrosion are crevice and intergranular pitting corrosion, so those types of corrosion should be simulated for the experiment [500]. HCl produces intergranular pitting corrosion on the aluminum beam, so HCl simulates the desired mechanical defect. Third, the chemical reaction of HCl acid and aluminum is similar to chemical reactions that occur when aluminum is in the presence of chlorine (Cl) and hydrogen (H₂). The chlorine reacts with the aluminum to produce AlCl₃, and the hydrogen product embrittles the aluminum leading to SCC. A table listing the common aluminum reactions may be seen in Table 2.2.1 [1]. It should be noted that similar chemical reactions may exist in the presence of cleaning, deicing, environmental, or maintenance fluids and compounds.

Table 2.2.1: Common corrosion reactions for corroding aluminum.

Environment	Reactants	Products
Air	$4Al + 3O_2 \rightarrow$	$2Al_2O_3$
Chlorine	$2Al + 3Cl_2 \rightarrow$	$2AlCl_3$
Bromine	$2Al + 3Br_2 \rightarrow$	Al_2Br_6
Iodine	$2Al + 3I_2 \rightarrow$	Al_2I_6
Hydrochloric Acid	$2Al + 6HCl \rightarrow$	$2Al^{3+} + 6Cl^- + 3H_2$
Sulphuric Acid	$2Al + 3H_2SO_4 \rightarrow$	$2Al^{3+} + 2SO_4^{2-} + 3H_2$
Sodium Hydroxide	$2Al + 2NaOH + 6H_2O \rightarrow$	$2Na^+ + [Al(OH)_4]^- + 3H_2$

2.2.4 Managing Ambient Variation Not Associated With Damage

For structural health monitoring methods based on structural response measurements, it is very important for the techniques to be able to distinguish the differences between structural changes due to damage and piezoelectric and structural changes due to ambient changes. The effect of temperature on the impedance method has been well documented by Park [30]. Ambient changes can be very problematic for corrosion detection because the changes in impedance signatures due to corrosion defects are small in comparison to those due to through cracks and loose bolts. Therefore, the corrosion damage must be distinguishable from the random ambient

changes. In this study, the following procedures were used to minimize random variation. Most of these procedures are based on knowledge of the admittance formula

$$Y(\omega) = \frac{I}{V} = ai\omega \left(\varepsilon^T_{33}(1-i\delta) - \frac{Z_s(\omega)}{Z_s(\omega) + Z_a(\omega)} d_{3x}^2 Y^E_{xx} \right) \quad (2.1)$$

where a is the geometric constant of the PZT, δ is the dielectric loss of PZT, Z_a and Z_s are the actuator and structural impedance, ε^T_{33} is the dielectric permittivity, d_{3x} is the piezoelectric strain coefficient, and Y^E_{xx} is the Young's modulus of the piezoelectric at zero electric field.

First, PZT 5A was used as a sensor material instead of PZT 5H because the capacitance changes less with respect to changes in temperature. The piezoelectric strain coefficient (d_{3x}) and dielectric permittivity (ε^T_{33}) are both temperature dependant and increase as the temperature increases [30]. The complex Young's modulus (Y^E_{xx}) of the piezoelectric at zero electric field changes slightly with respect to temperature. However, the change in the dielectric permittivity with respect to temperature affects the impedance signature the most because it modifies the capacitive admittance (the first term in Equation 2.1) which shifts the impedance signature. The dielectric constant (K) is the ratio of the permittivity of the material to the permittivity of free space, so permittivity variations affect the dielectric constant [30]. Impedance signature variance can be reduced by using PZT 5A material. Plots of the piezoelectric coefficients relationship versus temperature for 5A and 5H material may be found in Figures 2.2.3 and 2.2.4. The temperature dependant piezoelectric coefficient plots are provided courtesy of www.piezo.com.

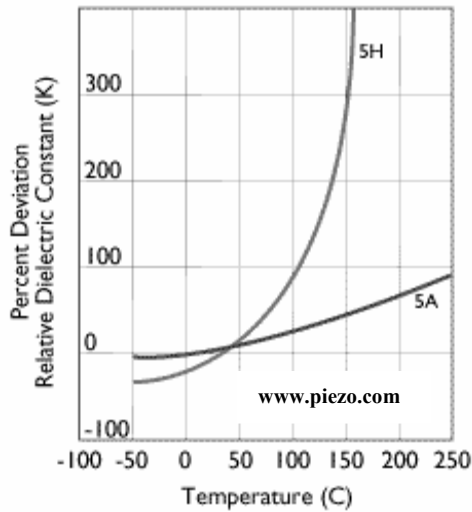


Figure 2.2.3: Dielectric constant versus temperature for piezoelectrics [2].

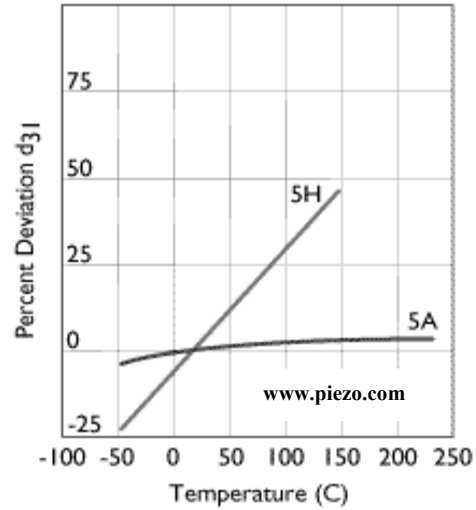


Figure 2.2.4: Coupling coefficient versus temperature for piezoelectrics [2].

Second, the real part of the impedance was used for damage detection because it is more sensitive to structural changes than the imaginary part [30]. The imaginary part of the impedance varies more with boundary condition changes (temperature, loading, and bonding) than the real part of the impedance. Third, a good compression bond between the structure and sensor is necessary to create the desired bond condition between the piezoelectric and the structure. It is preferable to vacuum bond the piezoelectric to the structure because it is thought to create a more even bond. Fourth, the piezoelectric perceives the structure as frequency dependant boundary stiffness, so the bond must be preserved and constant during the impedance measurements. In these experiments this was accomplished by using chemical corrosion (no structural impact), and limiting the handling of the structure. Finally, gloves were used to handle the structure to limit mass loading due to oils.

Experimental random variation may be minimized; however, some variation will remain in the experiment. A systematic approach was used to quantify the random variations in the experiment when they could be reduced no further. For all experiments the impedance sweeps were repeated 30 or more times to achieve a large sample size which reduces the 95% confidence interval on the sample mean. Smaller confidence intervals imply the range where the population mean may exist is reduced. In all plots, only the positive portion of the 95% interval will be shown, but the negative portion of the interval is implied. For the initial “undamaged” baseline the individual measurements were drawn out over 5 days to quantify the long term variation and repeatability of the measurements. The remainder of the damaged baselines were measured in

one day each, but the total time for all data collection was less than the data collection time of the original baseline. This procedure quantifies the random variation over a long time interval, so the random ambient variations in the measurements can be distinguished from structural corrosion damage. It should also be noted that no outlier detection has been performed, so the results could still be improved by performing outlier detection [28].

2.2.5 Converting Impedance Data to a Useable Form

When plotted, impedance signatures measured by the piezoelectric resemble frequency response function (FRF) plots. Remember, FRFs represent the ratio of the measured system output per measured system input. Thus, frequency response function plots visually depict how the output to input ratio varies with frequency. Impedance signature plots are just like FRF plots except that the output and input are more narrowly defined. For impedance signatures, the system output is the measured current in the piezoelectric and the input is the voltage applied to the piezoelectric. Since there is coupling between the piezoelectric and mechanical structure it is bonded to, the input voltage to the piezoelectric causes a force to be applied to the structure. The current output by the piezoelectric is related to the velocity response of the mechanical structure.

A baseline measurement consists of 30 or more repeated impedance signatures. Before corrosion occurs to the structure, a baseline measurement is made to characterize the impedance signatures for a healthy structure. Therefore the response of the healthy structure to a known input is quantified, and the only difference between each signature is due to random experimental error. After corrosion damage occurs on the structure, a new baseline measurement of 30 or more repeated impedance signatures is made. This characterizes the response of the damaged structure to a known input. Each impedance signatures within the new “damaged” baseline measurement will be similar to other measurements within the same baseline with only slight difference due to random error. However, when the damaged baseline is compared to the healthy baseline the differences will be significant because the healthy and damaged systems respond differently. This happens because the corrosion damage changes the mass, stiffness, and/or damping properties of the structure which in turn causes the shape of the impedance signature to change. Figure 4 represents a visual example of this how the impedance signatures change/shift as the condition of the structure changes. In Figure 4, each shift was caused by the addition of 0.05g of wax to the aluminum beam. Visual observation of the impedance signature shifts between baselines is not sufficient to quantify or characterize damage detection.

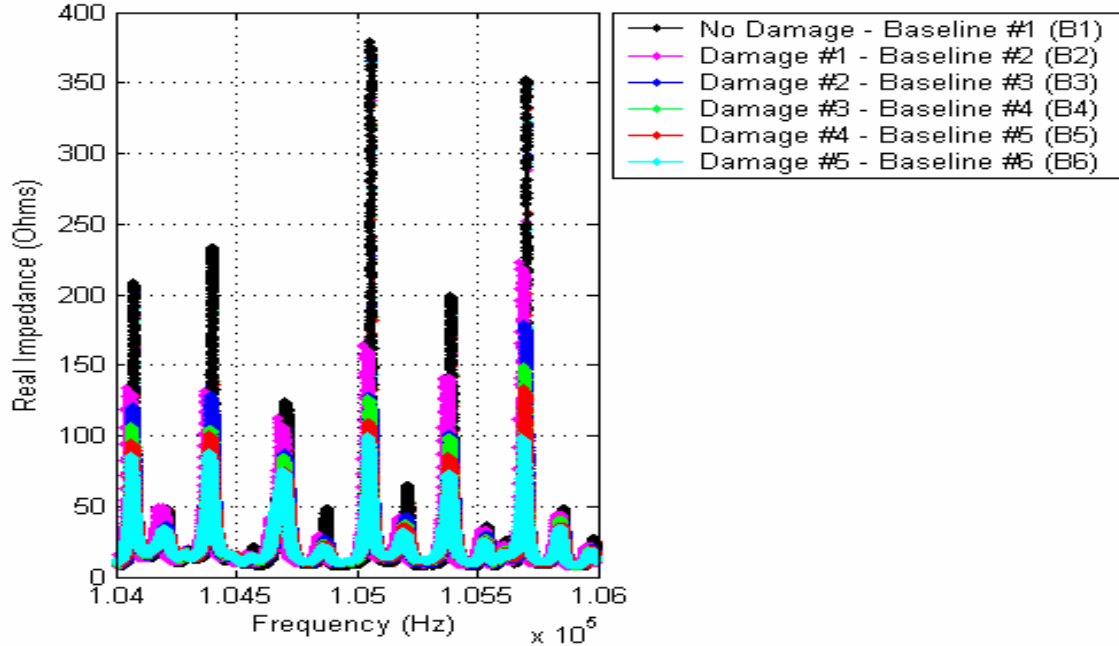


Figure 2.2.5: The baseline measurements show changes in the impedance signatures due to damage in beams.

Damage metrics are utilized to mathematically quantify the damage while reducing the data to a single scalar value. Previous studies have shown the advantages and disadvantages of various damage metrics [28]. For this study only the RMSD metric was used because it is a good metric to detect damage. The RMSD metric is defined as

$$RMSD = \sum_{i=1}^N \left[\frac{(\text{Re}(Y_{i,1}) - \text{Re}(Y_{i,2}))^2}{\text{Re}(Y_{i,1})^2} \right]^{\frac{1}{2}} \quad (2.2)$$

where the real impedance of the first measurement is $\text{Re}(Y_{i,1})$, the real impedance of the second measurement $\text{Re}(Y_{i,2})$, and N is the number of samples in the impedance sweep. The result is a single scalar number which quantifies the variation between the two impedance signatures. Damage metrics can be calculated between impedance signatures within the same baseline or they can be calculated between impedance signatures from two different baselines. Ideally, the damage metric between measurements within a single baseline will be zero, and damage metrics between measurements within different baselines will be large. If the damage metric between two impedance signatures is large enough and the random error is small enough damage can be

detected and distinguished. For this study, detection will imply the sample means of the RMSD damage metrics shows that damage has occurred. Distinguishable damage will have a 95% confidence interval for the population mean that does not overlap the confidence intervals of other baselines. Other methods to detect and distinguish damage are discussed in Chapter 1. For this method there is no need to set threshold levels to distinguish between the damaged and healthy cases.

The damage metrics were calculated in two ways to determine the corrosion damage detection capabilities of the system based on the frequency range used for the calculations. First the damage metrics were calculated using entire impedance sweep (12000 points for the beam). All 30 or more sweeps within the baseline were used to calculate N-1 damage metrics. Calculating damage metrics for the baselines cause the loss of one degree of freedom. The sample mean and standard deviation of those N-1 damage metrics was found. The damage is quantified as the sample mean, and the number of samples and standard deviation are used to establish 95% confidence intervals which represent the range the population mean may fall into. Second, the damage metrics were calculated using the impedance measurements (2000 points for the beam). Each method has advantages and disadvantages which will be discussed in the following sections.

Additionally, there are two more ways to calculate the damage metric, and they are based on the reference frame for the damage. First, all damage can be measured relative to the initial healthy baseline. Thus, for one healthy baseline (B1) and five different damaged baselines (B2, B3, B4, B5, and B6) all levels of damage will be measured relative to the initial healthy baseline. For this example, the following damage metrics would be calculated D12, D13, D14, D15, and D16. The nomenclature is described in more detail in Table 2.2.2. Second, all damage can be measure relative to the previous level of damage. Thus, for one healthy baseline (B1) and five different damaged baselines (B2, B3, B4, B5, and B6) all levels of damage will be measured relative to the previous baseline. For this example, the following damage metrics would be D12, D23, D34, D45, and D56. Once again this nomenclature is described in Table 2.2.2.

Table 2.2.2: Nomenclature definitions for the experimental system.

Symbol	General Meaning	Structure Specific Meaning
B1	Baseline #1 – No Damage Metric compares B1 to B1	No Damage - Healthy Beam Initial surface roughness 0.799 micron
B2	Baseline #2 – Damage #1 Metric compares B2 to B2	Corrosion at 12.5 cm, 1.4% coverage, 4.375 micron depth
B3	Baseline #3 – Damage #2 Metric compares B3 to B3	Corrosion at 25.0 cm, 1.4% coverage, 10.98 micron depth
B4	Baseline #4 – Damage #3 Metric compares B4 to B4	Corrosion at 50.0 cm, 1.4% coverage, 10.98 micron depth
B5	Baseline #5 – Damage #4 Metric compares B5 to B5	Corrosion at 100.0 cm, 1.4% coverage, 12.85 micron depth
B6	Baseline #6 – Damage #5 Metric compares B6 to B6	Corrosion at 150.0 cm, 1.4% coverage, 10.41 micron depth
D12	Metric compares B1 to B2 1 Level of Damage, MSD & SSD	Compares the corrosion at 12.5 cm to the No Damage case
D13	Metric compares B1 to B3 2 Levels of Damage, MSD	Compares the corrosion at 25.0 cm to the No Damage case
D14	Metric compares B1 to B4 3 Levels of Damage, MSD	Compares the corrosion at 50.0 cm to the No Damage case
D15	Metric compares B1 to B5 4 Levels of Damage, MSD	Compares the corrosion at 100.0 cm to the No Damage case
D16	Metric compares B1 to B6 5 Levels of Damage, MSD	Compares the corrosion at 150.0 cm to the No Damage case
D23	Metric compares B2 to B3 1 Level of Damage, SSD	Compares the corrosion at 25.0 cm to the corrosion at 12.5 cm
D34	Metric compares B3 to B4 1 Level of Damage, SSD	Compares the corrosion at 50.0 cm to the corrosion at 25.0 cm
D45	Metric compares B4 to B5 1 Level of Damage, SSD	Compares the corrosion at 100.0 cm to the corrosion at 50.0 cm
D56	Metric compares B5 to B6 1 Level of Damage, SSD	Compares the corrosion at 150 cm to the corrosion at 100 cm

There is an important distinction between calculating the damage metric relative to the healthy baseline and calculating the baseline relative to previous levels of damage. When more than one damaged baseline is present calculating the damage metric relative to the healthy baseline has the effect of monitoring multiple site damage (MSD). This is desirable, but it makes detecting and distinguishing corrosion damage more difficult. When the metrics are plotted as bar charts, each bar representing a damaged case must have confidence intervals which do not overlap the confidence intervals of associated baselines and previous levels of damage. On the other hand, damage metrics calculated relative to previous levels of damage only requires the confidence intervals (CI) of the damage not to overlap the CI of the associated baselines to be

distinguishable. This may seem subtle, but the effect will be made obvious in the results sections. Later in plate experiments, this concept will be very important.

2.3 Beam Corrosion Detection Results for All Frequencies

2.3.1 Corrosion Detection Relative To Baseline #1 For All Frequencies

Recall that the damage metrics were calculated in two ways. The first method yields a single damage metric for all six frequencies tested for each baseline comparison. A plot of the corrosion detection results for the beam may be seen in Figure 2.3.1. The first six bars B1-B6 represent the sample means of the individual baselines. The magnitudes of bars B1-B6 are small because the damage metrics were calculated from impedance sweeps from the same baseline. The confidence intervals represent the range the population mean should fall within. Since the metrics are calculated relative to the healthy baseline, the plot actually depicts damage accumulation in the structure (MSD). Based on the sample means, the impedance method can detect the light, MSD, pre-crack surface corrosion, so damage is being detected and monitored before crack formation begins.

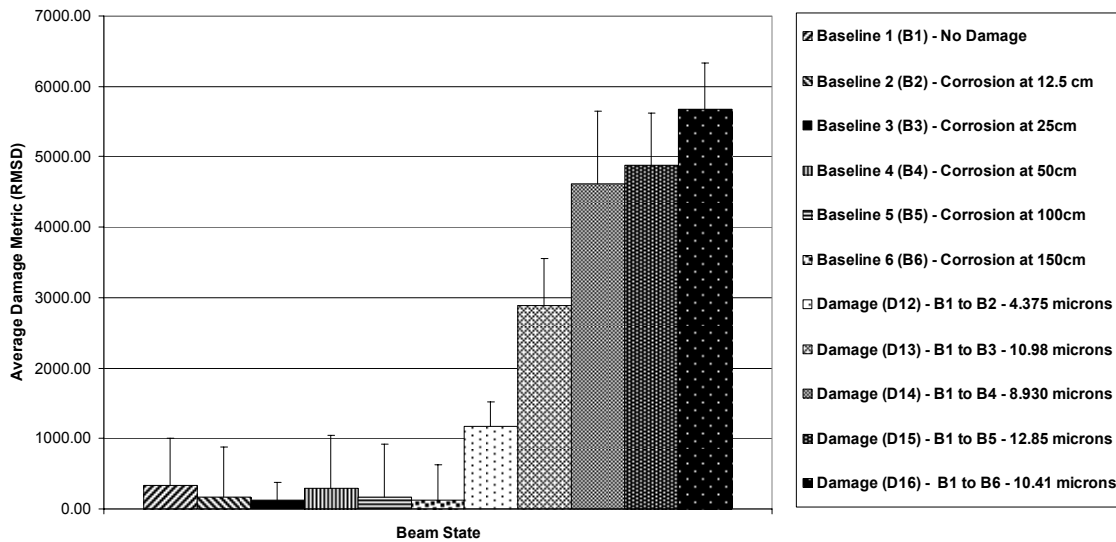


Figure 2.3.1: Beam corrosion detection results for the beam for all tested frequencies measured relative to the baseline #1.

From Figure 2.3.1, bar D12 represents the damage metric calculated between the undamaged baseline 1 and the baseline 2 (1.4% coverage of 4.375 micron deep pits at 12.5 cm). There is a detectable increase in the sample mean of the damage metric; however, the error bars of D12 overlap B1, so the population means of D12 and B1 are not distinguishable. Thus, based on our 95% confidence interval detection is uncertain. Bar D13 compares the baseline B1 to B3 (1.4% coverage of 10.98 micron deep pits at 25cm), and it is distinguishable from the error of B1, B3, & D12, so it is detectable and distinguishable. Like D13, D14 is distinguishable from the baselines and previous damage cases, so it is detectable and distinguishable. As the damage moves to 100 and 150cm the damage becomes indistinguishable again because the CI intervals overlap CIs of previous levels of damage. Measuring the damage based on a global metric composed of all six frequencies and measuring the damage relative to the healthy baseline allows all five damage cases to be detected but only two are distinguishable using the impedance method.

This method may not be the best detection method because the damage is not always distinguishable from the baselines or previous instances of damage. This happens because all the frequencies influence the damage metric, and some have large variability which reduces the ability to detect and distinguish corrosion. Also, the metrics for each frequency are scaled differently, so some frequencies dominate the metric. This does not mean this method will not work or is void of any potential benefit. If the detection frequencies were carefully chosen, the damage pit depth was increased (closer to 25 microns), or the confidence interval reduced the method could work well. If detection over all six frequencies is successful only a single metric for each level of damage would be required versus six damage metrics when damage is quantified at each frequency range. For remote SHM devices, this would mean there would be less data to transmit (the most energy intensive process for remote devices).

Modified versions of this approach could prove even more useful. Before the metrics of all six frequencies ranges are summed to become one metric, the individual metrics could be normalized to make each range participate equally in the single global metric. An even better approach might be to base the normalization on the known confidence intervals associated with the individual frequency range. If the confidence intervals are large, one could weight that frequency range to participate less in the global metric. If the confidence intervals are small, one could weight the frequency range to participate more in the global metric. The ultimate approach would be to normalize each peak in the impedance signatures based on its contribution to error. Each suggestion requires more processing, but onboard processing for remote devices is less energy intensive. Most of those sub-calculations are made in the damage metric calculation process anyway. Of course, if the system is trained properly during sensitivity testing and

sensitive frequencies with low error are chosen, weighting based on the quality of the data could be avoided altogether.

2.3.2 Corrosion Detection Relative to Previous Baselines

In an effort to improve upon the previous method, the damage metrics were calculated relative to previous baselines instead of baseline #1. Viewing the damage in this way eliminates the ability to see damage accumulation in the system because the damage is not quantified from the initial baseline. However, it removes the requirement for the confidence intervals of the damage cases to not overlap to be considered distinguishable damage. From Figure 2.2.2, all of the damaged sample means are larger than the first six baselines, so all five instances of damage are detectable. Once again, bar D12 is not distinguishable from B1 & B2 because of confidence interval overlap. The other four damage cases D23, D34, D45, and D56 are all distinguishable from their associated baselines based on no confidence interval overlap. All five light, pre-crack, 1.4% surface coverage corrosion damages are detectable, and 4 of the 5 are distinguishable using the impedance method. Therefore, trading the ability to detect MSD aids the ability to distinguish damage using single site damage (SSD) methods.

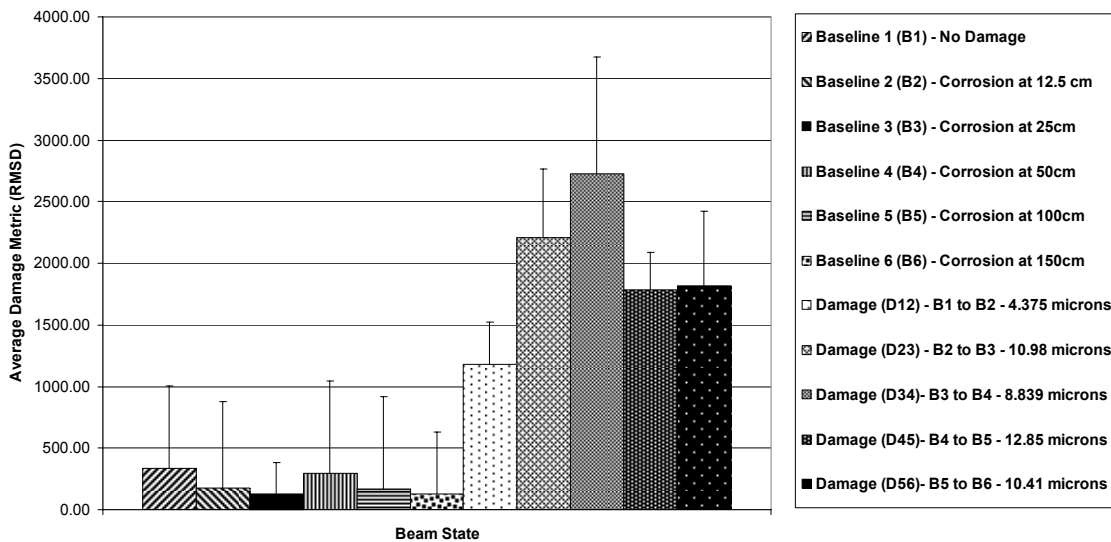


Figure 2.3.2: Beam corrosion results measured relative to previous instances of damage.

Even though damage D12 was closest to the sensor it still could not be distinguished. Part of the explanation for this is the pit depth is only 4.375 microns deep, and the healthy beam has an average pit depth of 0.799 microns. Hence, the change in surface roughness due to

corrosion is so small the damage is not distinguishable. Chemical corrosion is hard to control and the intent was for all damage case to be around 10 microns, the depth that was simulated during the sensitivity testing. The other four damage cases are closer to 10 microns, still well within the 25.4 micron light classification. Even though each of the last four damages is further from the PZT sensor, they are all distinguishable because they have greater pit depths.

2.4 Improved Beam Detection Results

2.4.1 Improved Corrosion Detection Relative to Baseline #1

The second method calculates one damage metric for each level of damage within the six frequency ranges. This method greatly aids corrosion detection because frequencies with large confidence intervals may be ignored, and detection can be based on frequency ranges with favorable confidence intervals. An example of this may be seen in Figure 2.4.1. From 20-22 kHz the damage can be detected and distinguished at every level out to 150 cm on the beam. Since the 95% confidence intervals do not overlap, there is a 95% certainty that the population means will not overlap. That implies each instance of corrosion is detectable and distinguishable using the impedance method in the beam tested. This is a very important result because the estimated mass loss for each instance of corrosion is approximately 0.05g, and the impedance method can detect and distinguish that damage. Since all five levels of damage are distinguishable it can be said that light, pre-crack, 1.4% surface coverage, multiple site damage (MSD) corrosion is detectable out to 150 cm using the impedance method. So long as the damage does not occur simultaneously, MSD corrosion detection is possible using the impedance method.

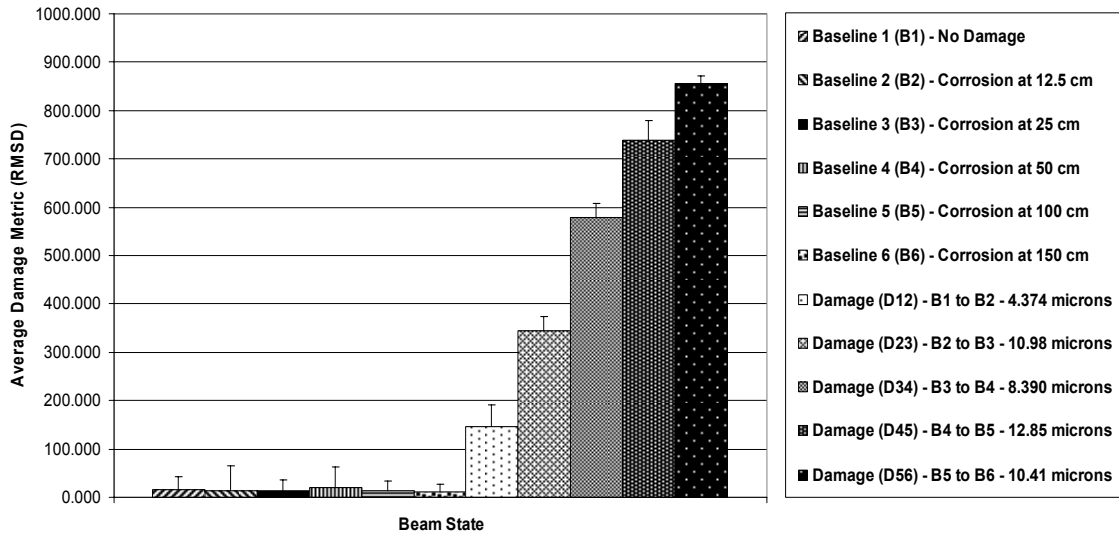


Figure 2.4.1: Beam corrosion damage detection for impedances sweeps from 20-22 kHz.

All testing frequencies do not perform equally well detecting corrosion using the impedance method. Figure 2.4.2 is the best result of the six frequencies, and Figure 2.4.3 shows the worst corrosion detection results for an individual frequency range. At 103-105 kHz, the confidence intervals are large relative to the change in the sample mean of the damage metric, so the population mean of the damage levels are indistinguishable. At 71-73 kHz the damage confidence intervals are small, but the accumulation trend is not correct. Of the six frequencies tested, the lower frequencies 20-22 kHz (5 of 5 distinguishable) and 54-56 kHz (4 of 5 distinguishable) provide the best results. The 71-73 kHz range can distinguish 3 of 5 damages, and 126-128 kHz can distinguish 1 of 5 damages. The 95.5-97.5 kHz and 103-105 kHz frequencies cannot distinguish any of the damages due to confidence interval overlap. It should be noted that the damage trends are correct, and if less confidence is required, or more damage tolerance is acceptable, these frequencies could be used for damage detection. Also, no outlier detection has been performed on the data, so eliminating outliers would reduce variability and increase damage detection [28].

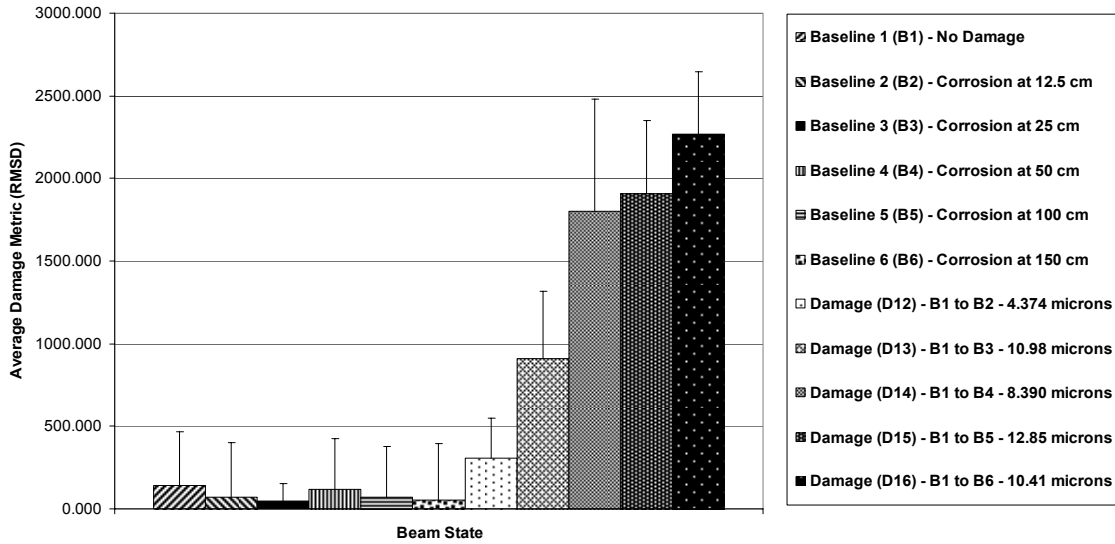


Figure 2.4.2: Corrosion detection results for beam impedance testing between 103-105 kHz.

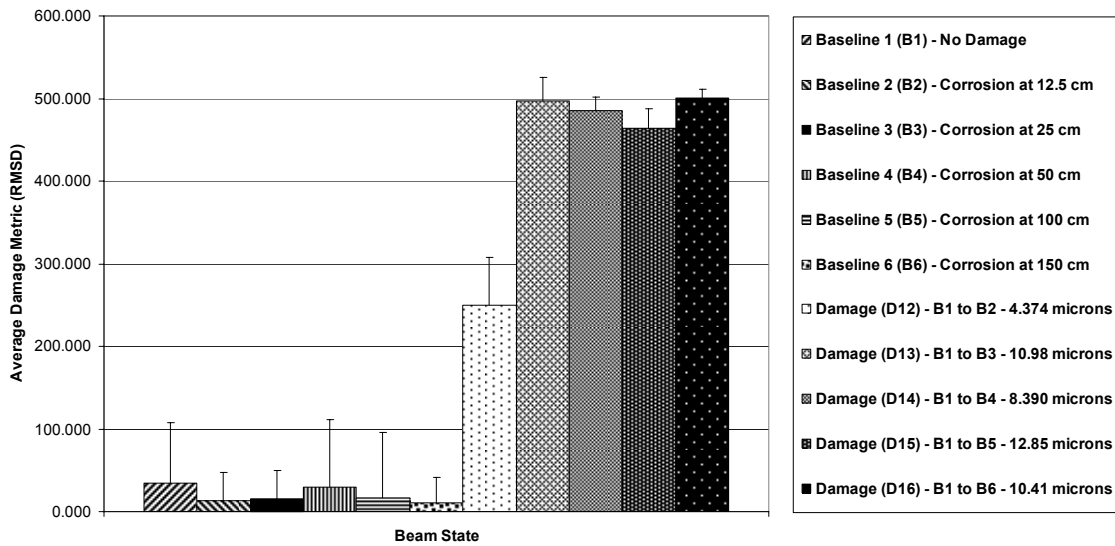


Figure 2.4.3: Corrosion detection results for beam impedance testing between 71-73 kHz.

2.4.2 Improved Corrosion Detection Relative to Previous Baselines

Once again the ability to track accumulated MSD damage can be traded to increase the ability to distinguish corrosion by calculating damage metrics relative to previous baselines. Doing this substantially increases the ability to distinguish damage. Figure 2.4.4 shows the damage metrics plotted for the 71-73 kHz range which fared poorly using the previous damage calculation

method. Now, all five levels of damage are distinguishable from their associated baselines, so all five damages are distinguishable. The frequencies of 20-22, 54-56, and 71-73 kHz distinguish 5 of 5 damages. At 95.5-97.5 kHz, three of the five damages are distinguishable. The frequencies of 103-105 kHz and 126-128 kHz cannot distinguish any of the 5 damages. Table 2.4.1 summarizes all of the beam detection results. Appendix A contains all the impedance signature, average damage metric plots, MSD, and SSD plots.

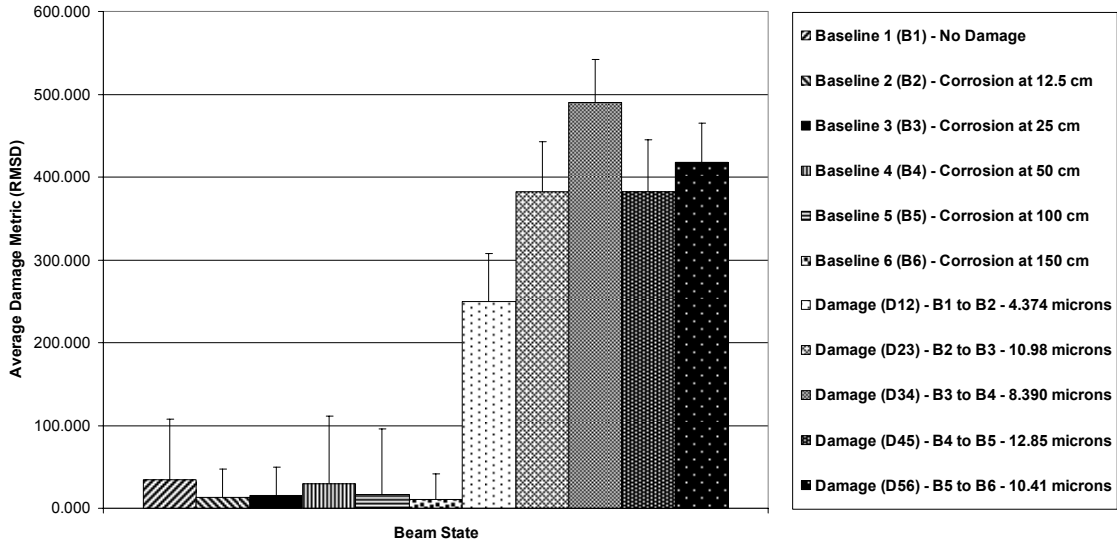


Figure 2.4.4: All five levels of corrosion damage are distinguishable for 71-73 kHz.

Table 2.4.1: Impedance based corrosion detection results for an aluminum beam.

Frequency (KHz)	Detection MSD	Distinguish MSD	Detection SSD	Distinguish SSD
20-22	5 of 5	5 of 5	5 of 5	5 of 5
54-56	5 of 5	4 of 5	5 of 5	5 of 5
71-73	3 of 5	3 of 5	5 of 5	5 of 5
95.5-97.5	4 of 5	0 of 5	5 of 5	3 of 5
103-105	5 of 5	0 of 5	5 of 5	0 of 5
126-128	4 of 5	1 of 5	5 of 5	0 of 5
All Six	5 of 5	2 of 5	5 of 5	4 of 5

2.5 Corrosion Detection Patterns

2.5.1 Patterns Conducive to Corrosion Detection

The impedance method can clearly identify corrosion in beams, but the ability to detect the damage depends on the damage surface coverage, location, pit depth, and test conditions. Structural health monitoring relies heavily upon pattern identification, so it is useful to identify patterns in the impedance signatures that are conducive to corrosion detection. For remote structural health monitoring devices, this information may not be available to the end user, but all of these calculations will be made onboard the device and could be used to identify damage. The 20-22 kHz frequency range proved to be good for distinguishing corrosion damage because the frequency was sensitive to damage without producing too much error. The impedance baselines for 20.25-21 kHz are plotted in Figure 2.5.1, and each colored line is actually 30 or more individual impedance signatures. The three groups of smaller peaks in Figure 2.5.1 show the same pattern, but the larger peak does not.

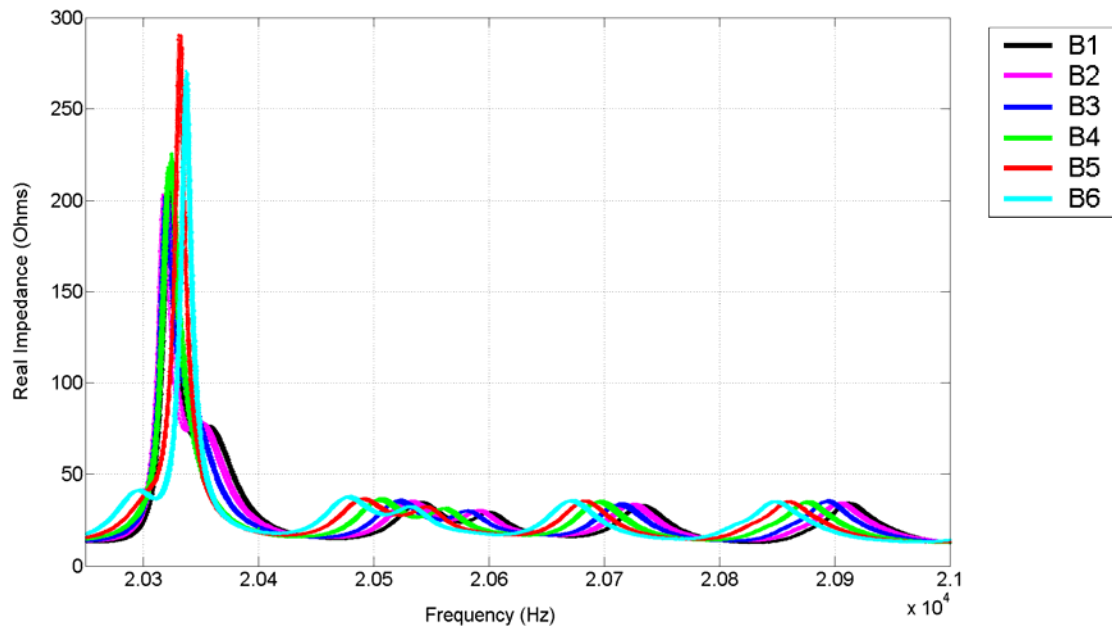


Figure 2.5.1: Impedance signatures from 20.25-21.00 kHz.

To show how the peak patterns affect the damage metric the metrics at each frequency have been average and plotted in Figure 2.5.2. The damage pattern desired is for $D12 < D13 < D14 <$

D15 < D16 in the presence of impedance peaks. The smaller peaks follow the pattern, but the largest peak does not, so it will contribute to error that makes the damage more difficult to distinguish. For the best corrosion damage detection, it is necessary to choose frequencies sensitive to damage that do not produce too much variation. During sensitivity testing it should be possible to focus the detection on frequencies most conducive to detecting damage. Ultimately new damage metrics should be developed and better statistical and digital processing tools should be developed and introduced to impedance based damage detection.

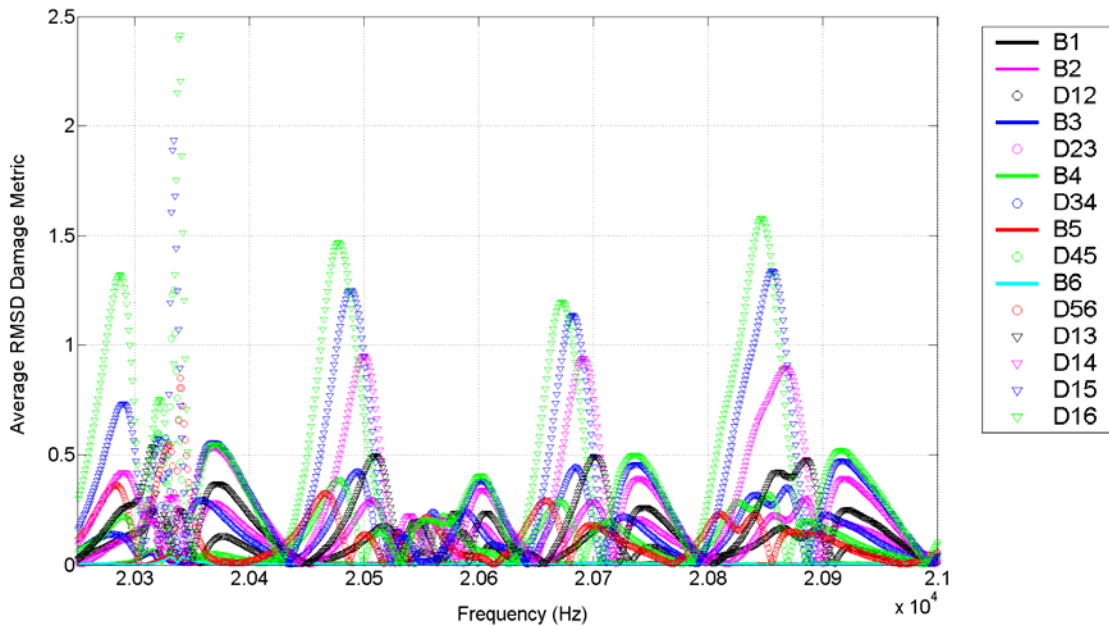


Figure 2.5.2: Average damage metrics versus frequency plot identifies which individual impedance peaks are sensitive to damage.

2.5.2 Patterns Not Conducive to Corrosion Detection

The 71-73 kHz frequency range did not fare as well during corrosion detection as the two lower frequencies did. In fact, careful analysis of the impedance signatures shows that it is too sensitive for the peak density at that frequency. The impedance signature plot in Figure 2.5.3 shows that the corrosion damage shifts the peaks so much that they move under previous peaks. This actually caused the damage metric to correlated better when the damage is actually getting worse. Thus, the damage metric (a correlation) does not consistently get larger because the shifts align peaks with other peaks as the damage occurs. The average damage metrics in Figure 2.5.4 shows that the peaks do not follow a pattern that is conducive to damage identification. In this case, the detection fails, but the metric is sensitive to damage.

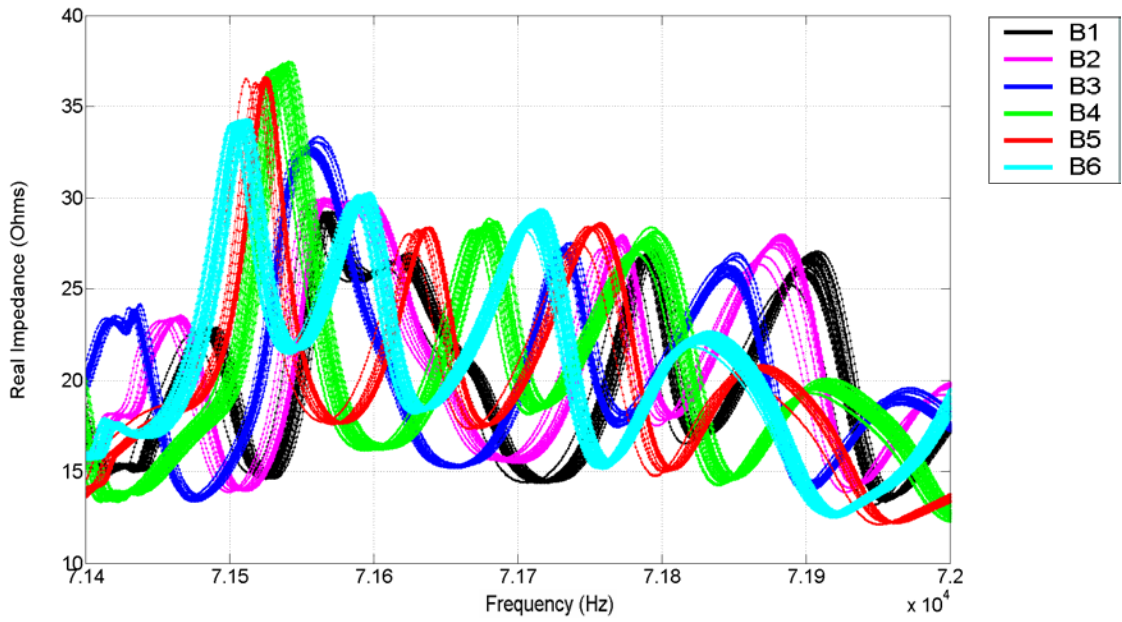


Figure 2.5.3: Impedance signatures from 71.4-72 kHz.

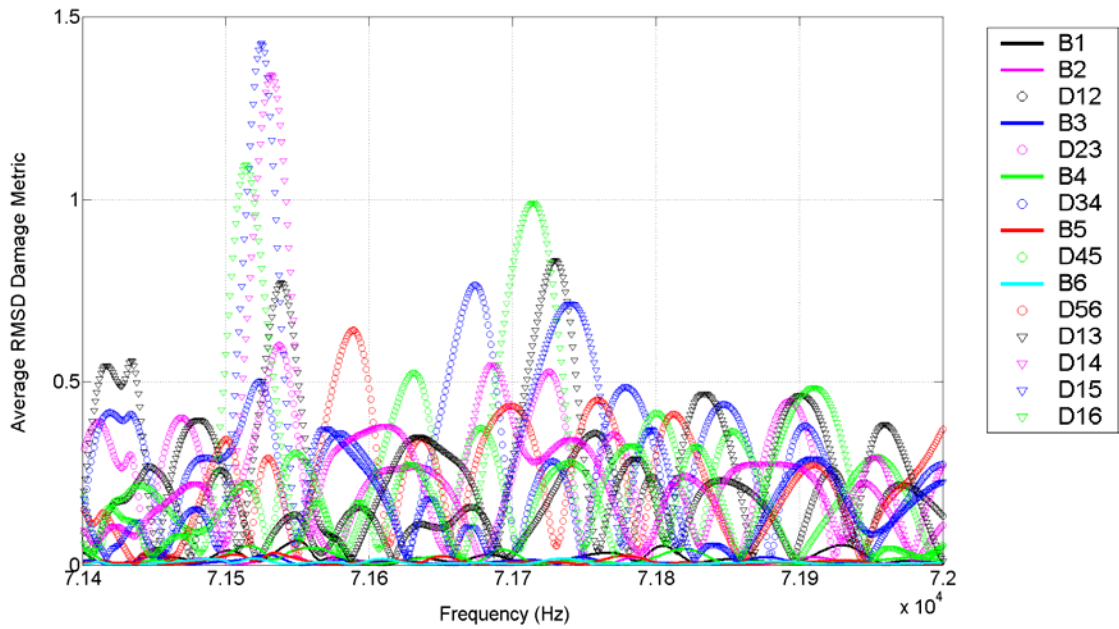


Figure 2.5.4: Average damage metrics versus frequency plot identifies which individual impedance peaks are sensitive to damage but can't distinguish damage.

Chapter 3

Quantifying Beam Corrosion Damage

3.1 Introduction

The impedance method can detect the earliest stages of pre-crack surface corrosion on beam-like structures. Since the method is very sensitive to corrosion damage, it would be useful to not immediately repair corrosion damage that does not pose a mechanical problem for the structure as is the common practice in the airline industry today. For such cases, the impedance method and other NDE techniques to quantify key aspects of the corrosion damage and track it until repair is required. Three of the most important corrosion damage variables to quantify are location, pit depth, and surface coverage. It is unlikely that any single NDE technique, including the impedance method, could determine all three key corrosion variables, so it is important to know which corrosion variables the impedance method best correlates with. The goal of Chapter 3 is to determine how well impedance-based damage metrics can be correlated to changes in corrosion location, pit depth, and surface coverage. In the future, this knowledge could tell the designers of remote SHM systems which corrosion variables to measure with each damage detection technique and how to correlate it with other maintenance records.

3.2 Testing Procedure & Experimental Setup

3.2.1 Pit Depth Testing Experimental Procedure

For the pit depth detection test a smaller beam was chosen, so that the mass loss could be accurately recorded with a balance. A PZT 5H4 patch 2.54 x 2.28 x 0.0254 cm patch was bonded to a 62.9 x 2.54 x 0.159 cm 6063 T5 alloy aluminum beam which was hung vertically to simulate free-free boundary conditions. The centerline of the PZT was 7.62 cm from the edge of the beam, and all of the damage was added in a 2.54 cm² area 25 cm from the PZT patch. The beam was baselined for 5 days before damage was added. The impedance measurements were made 20-22 kHz, 44-46 kHz, 54-56 kHz, 72-74 kHz, 97-99 kHz, and 104-106 kHz. To damage the beam, hydrochloric acid was placed on the beam for predetermined time intervals. The surface roughness and mass of the beam were measured before and after each addition of damage. The goal of the experiment was to determine if the damage metric could be correlated to a change in pit depth or material mass loss. This correlation could prove very useful for fatigue life adjustments based on known amounts of corrosion found during routine inspections. The results show the impedance method and damage metric can be correlated to material loss. Figure 3.2.1 shows the beam after five levels of corrosion.



Figure 3.2.1: The beam used for pit depth detection after 5 levels of corrosion damage.

3.2.2 Location Testing Experimental Procedure

For the location tests, a PZT 5A patch 2.54 x 2.29 x 0.0254 cm was bonded to a 183 x 2.54 x 0.159 cm 6065 T5 aluminum beam which was hung vertically in a free-free boundary condition. Due to the inability to accurately control material loss and pit depth with chemical corrosion, another test method was devised. From experimental tests a pit depth of 6.325 microns over a 2.54 cm² area on the beam corresponds to a mass loss of 0.0500 g. Hence, 0.0500g of wax was

placed 12.5, 25, 50, 100, and 150 cm from the sensor centerline on the beam to simulate the movement of a known amount corrosion (2.54 cm² surface coverage at a 6.325 micron pit depth). An attempt was made to press the wax out over the same area to ensure a similar bonding area between the wax and the structure. This is not a mass loss like that associated with corrosion pitting, but it was the best available method to simulate corrosion without damaging the PZT or its bond with the structure. Over a 5 day period, 56 baseline measurements were made on the structure. The impedance measurements were made at 20-22 kHz, 54-56 kHz, 71-73 kHz, 96.5-98.5 kHz, 103-105 kHz, and 126-128 kHz. Then the 0.0500g of wax was moved to each position and at least 30 measurements of each new baseline were made. There was only one patch of wax added to the beam at any time. Between baselines the wax was removed and the structure was wiped clean before the wax was move to the next location on the structure.

3.2.3 Surface Coverage Tracking Experimental Procedure

The goal of this experiment is to show the impedance method can track the surface expansion of corrosion. A 2.54 x 2.29 x 0.0254 cm PZT 5A patch was mounted to a 173 x 2.54 x 0.159 cm aluminum beam which was hung vertically simulating free-free boundary conditions. More than 30 baseline impedance measurements were made over a 5 day period to determine the healthy state of the beam. The impedance measurements were made at 20-22 kHz, 46-48 kHz, 57-59 kHz, 72-74 kHz, 104-106 kHz, and 130-132 kHz. Again, wax was added to the structure to simulate corrosion since chemical corrosion does not allow pit depth and mass loss to be precisely controlled. The first damage state was simulated by attaching the 0.0500g of wax to the beam 25 cm from the edge of the PZT sensor. To simulate a second 2.54cm² expansion of the previous corrosion coverage, 0.0250 g of wax was placed 1.91 cm on each side of the first ball of wax. Figure 3.2.2 shows the beam in its final damaged state. The expansion of corrosion was simulated for five levels of damage, and the 30 or more baseline sweeps were recorded for each instance of damage.



Figure 3.2.2: The aluminum beam used in the corrosion coverage test in its final damage state.

3.3 Corrosion Quantification Results

3.3.1 Corrosion Pit Depth/Mass Loss Tracking

The mass loss due to corrosion can be assessed in multiple ways as was the case for the corrosion detection test in Chapter 2. The corrosion pit depth changes (mass loss) can be detected and distinguished using MSD (every baseline compared to the original) and SSD (each baseline compared to the previous baseline) methods. Also, the metrics calculated from MSD and SSD methods can be determined for all frequencies or for each of the six test frequencies. Table 3.3.1 shows the results of the corrosion pit depth tracking test.

Table 3.3.1: Results of the corrosion pit depth tracking test.

Frequency (KHz)	Detection MSD	Distinguish MSD	Detection SSD	Distinguish SSD
20-22	5 of 5	5 of 5	5 of 5	5 of 5
44-46	4 of 5	4 of 5	5 of 5	5 of 5
54-56	5 of 5	4 of 5	5 of 5	5 of 5
72-74	4 of 5	4 of 5	5 of 5	5 of 5
97-99	5 of 5	3 of 5	5 of 5	3 of 5
104-106	5 of 5	4 of 5	5 of 5	4 of 5
All Six Combined	5 of 5	5 of 5	5 of 5	5 of 5
MSD Totals	33 of 35	29 of 35		
SSD Totals			35 of 35	32 of 35

There are multiple levels of damage, but all occur at the same location, so surface coverage and damage location are held constant. The total mass loss for each of the five instances of damage ranges from 0.0353 to 0.1003 g. Remember that 0.0500 g of mass loss corresponds to a 6.32 micron pit depth. The results show these changes in pit depth (mass loss) are detectable in 68 of the 70 cases, and distinguishable in 61 of the 70 cases. Multiple site corrosion pit depth changes in the light corrosion range are detectable and distinguishable using the impedance method. The results are clear enough that the single damage metric summed for all six frequency ranges can detectable and distinguish all instances of corrosion as seen in Figure 3.3.1. It was mentioned in Chapter 2 that detection across all six frequencies is possible, these findings illustrate that point. There are some disadvantages to this approach (mentioned in Chapter 2); however, this implies the entire data set for all healthy and damaged cases could be

reduced to just 11 numbers. The individual frequency analysis requires six times that many numbers to characterize the system.

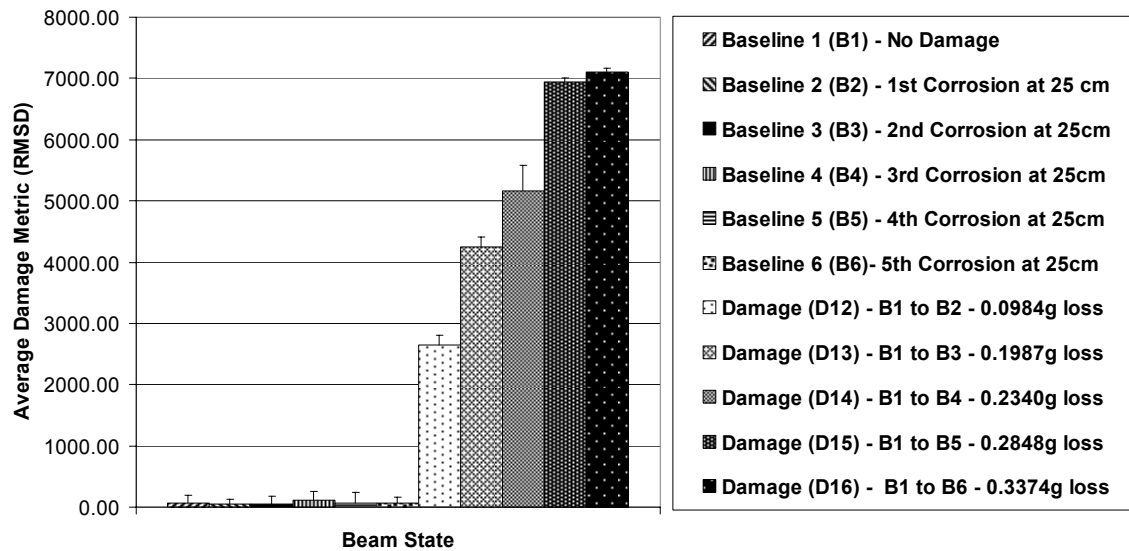


Figure 3.3.1: For 22-106 kHz, corrosion pit depth changes are detectable and distinguishable.

When the corrosion pit depth changes are analyzed using RMSD metrics calculated for each of the six frequencies the structural changes are distinguishable for all five levels of damage in 1 of the 6 frequencies ranges tested. Four of the six frequencies can distinguish 4 levels of damage, and one frequency range can only distinguish 3 levels of damage. The results for 20-22 kHz range can be seen in Figure 3.3.2. Once again, multiple site damage of light pre-crack surface corrosion is distinguishable. All damage metric plots can be seen in Figures B.1-B.60 shown in Appendix B.

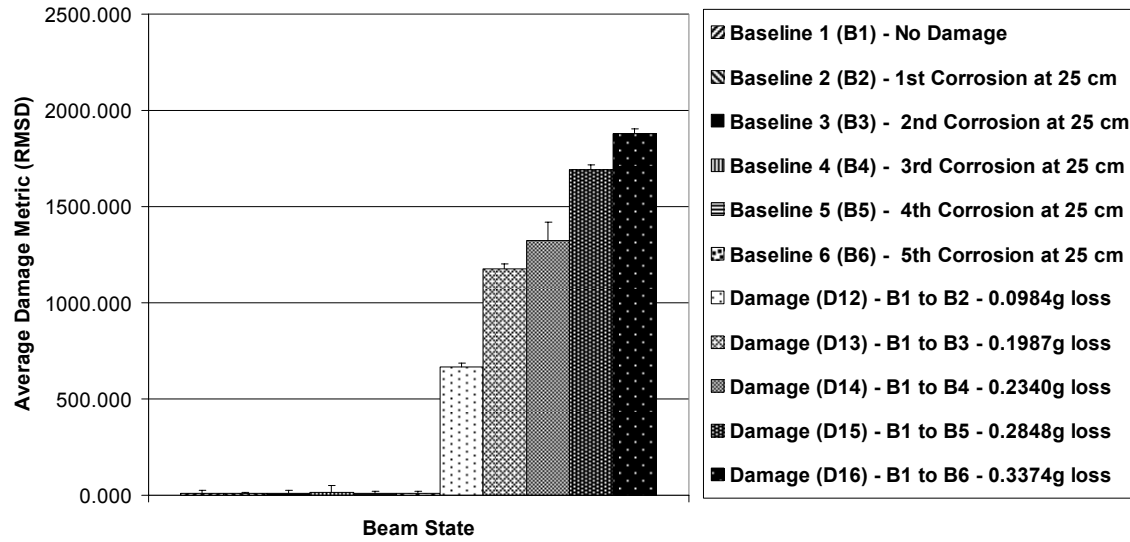


Figure 3.3.2: For 20-22 kHz, corrosion pit depth changes are detectable and distinguishable.

The impedance method can track corrosion pit depth changes in aluminum beams. The correlation between the damage metric and the pit depth changes is both frequency and structure dependant, but if used in conjunction with maintenance records it might be possible to establish a trend and make some qualitative predictions about pit depth growth. Figure 3.3.3 demonstrates this concept. In Figure 3.3.3, the damage metrics increase as mass loss due to corrosion accumulates on the structure. For the 20-22 kHz frequency range, the relationship is linear with an R^2 -value of 0.994, and the 95% confidence interval for each point is small. At different frequencies the relationship is not so linear, but there is a relationship which could be fused with other data or records to predict corrosion pit depth growth.

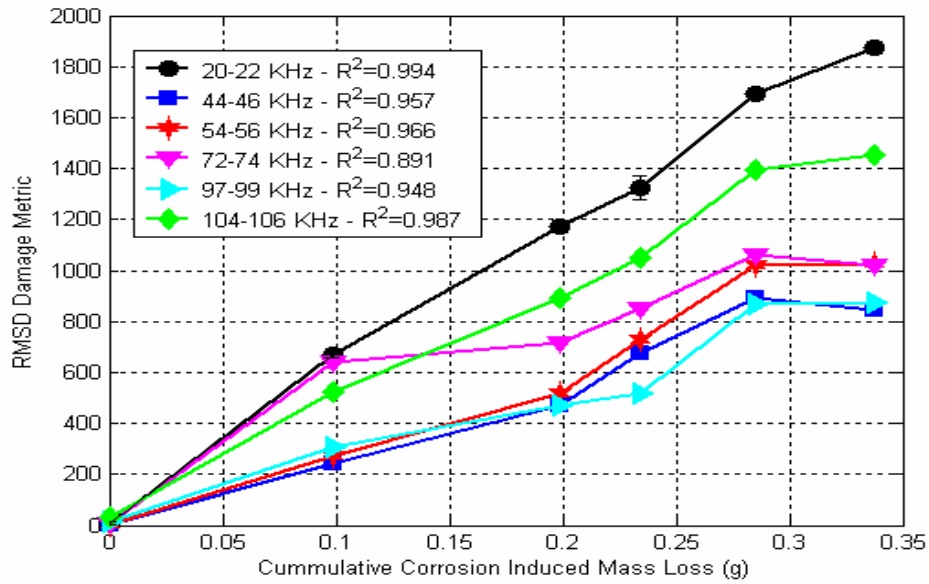


Figure 3.3.3: The relationship between damage metrics and cumulative corrosion mass loss.

The correlation between damage metrics and mass loss can be also be viewed in a non-cumulative sense as seen in Figure 3.3.4. Here the damage metrics are plotted against the individual instances of corrosion pitting. For each frequency a relationship between the two exists and in some cases the relationship is very linear. In the 72-74 kHz range, the R^2 -value is 0.994.

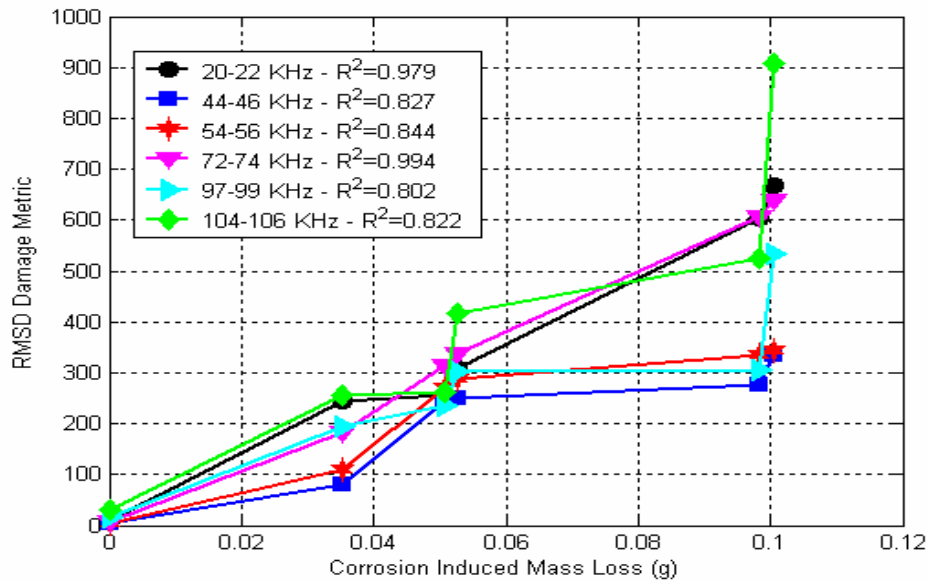


Figure 3.3.4: Relationship between damage metrics versus corrosion induced mass loss.

3.3.2 Corrosion Location Tracking Results

The corrosion location testing was not as conclusive as the corrosion pit depth testing. Also, there is no cumulative damage for this experiment because the mass simulating the corrosion damage is simply moved along the beam. The single site damage can be measured relative to the initial healthy baseline or relative to previous baseline measurements to arrive at a damage metric; however, there is no cumulative (MSD) damage accounted for in this test. The detection results for the corrosion location can be seen in Table 3.3.2.

Table 3.3.2: Corrosion location results for a beam-like structure.

Frequency (KHz)	Detection Relative Initial Baseline (RIB)	Distinguish Relative Initial Baseline (RIB)	Detection Relative Previous Baseline (RPB)	Distinguish Relative Previous Baseline (RPB)
20-22	5 of 5	1 of 5	5 of 5	3 of 5
54-58	5 of 5	0 of 5	5 of 5	0 of 5
71-73	5 of 5	1 of 5	5 of 5	3 of 5
96.5-98.5	5 of 5	0 of 5	5 of 5	0 of 5
103-105	5 of 5	0 of 5	5 of 5	0 of 5
126-128	5 of 5	0 of 5	5 of 5	0 of 5
All Six Combined	5 of 5	0 of 5	5 of 5	0 of 5
RIB Totals	35 of 35	2 of 35		
RPB Totals			35 of 35	6 of 35

There is no expected trend in the response as the corrosion damage (0.0500g of added wax) is moved along the beam. The response depends on the mode shapes at very high frequencies, so it is difficult to predict how the changing mass location affects the response. This implies that damage metric values (D12, D13, D14, D15, D16, D23, D34, D45, and D56) only have to be detectable and distinguishable from the associated baselines (B1, B2, B3, B4, B5, and B6). During sensitivity testing it appeared that moving 0.0500 g (corresponding to 6.32 micron pitting of 1.4% of the surface) of wax along the beam would be detectable and distinguishable, but the testing variation was not accounted for during sensitivity testing. Thus, the variation in the impedance signatures to ambient condition changes tended to make the simulated damage indistinguishable in most cases.

In all cases the impedance method can detect (based on the sample means) simulated light 1.4% pre-crack surface corrosion at distances up to 150 cm. However, the impedance method cannot distinguish the addition and movement of simulated light corrosion along the

beam as seen in Figure 3.3.5. The large error bars and small magnitude changes in the damage metrics indicate the impedance method is not as sensitive to changes in the simulated corrosion location. Narrowing the test frequency range and measuring relative to previous baselines does not make the damage distinguishable in all cases. Even for the best result seen in Figure 3.3.6, only three of the five instances of damage are distinguishable. All damage metric plots can be seen in Figures B.1-B.60 of Appendix B.

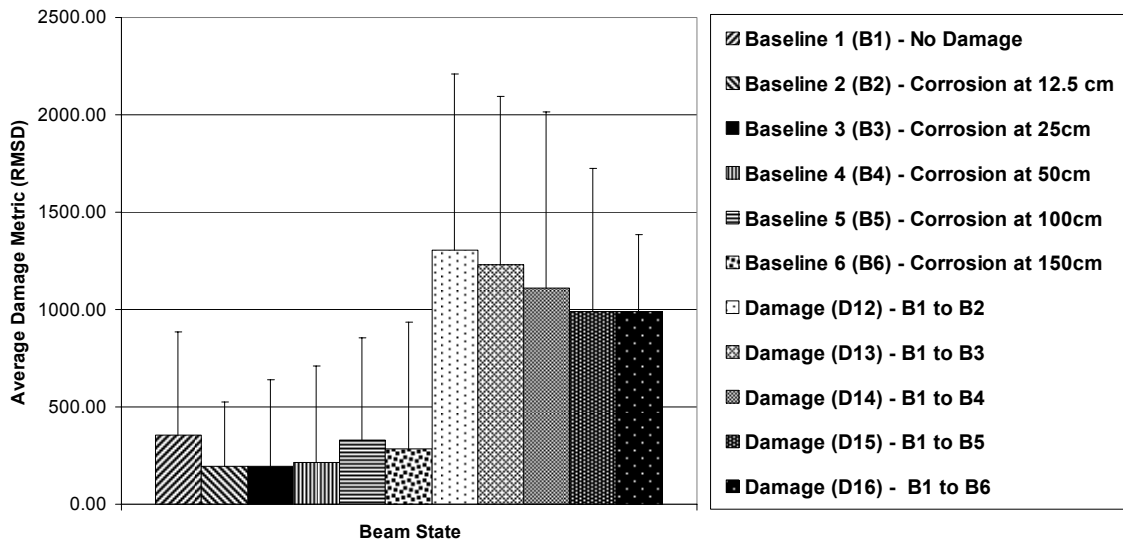


Figure 3.3.5: For damage metrics calculated across all six frequencies the damage is detectable.

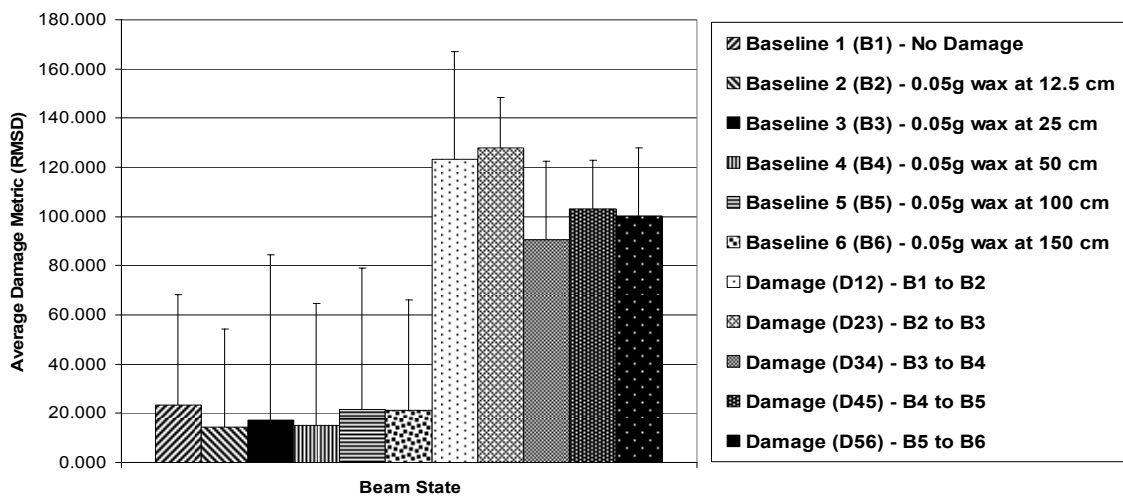


Figure 3.3.6: From 20-22 kHz, three levels of damage are distinguishable.

The main purpose of the location testing was to see if there is a relationship between the damage metrics and corrosion location. From the testing this relationship was established for each of the test frequencies, and Figure 3.3.7 shows the results. The plot shows that the damage metric seems to decrease as the corrosion location moves away from the sensor; however, the error in each measurement makes this assumption somewhat inconclusive. There is clearly a pattern, but the experimental error reduces. For simulated 1.4% coverage of light 6.32 micron corrosion, impedance-based corrosion location detection may not be the optimal technique. If the tolerance for damage was greater, the test frequencies were raised, or a more damage sensitive structure were utilized the method may be better able to establish a pattern that could be used in a predictive manner. The impedance method and damage metric could be used to locate damage on a structure; however, the impedance method may be better suited to other quantification tasks.

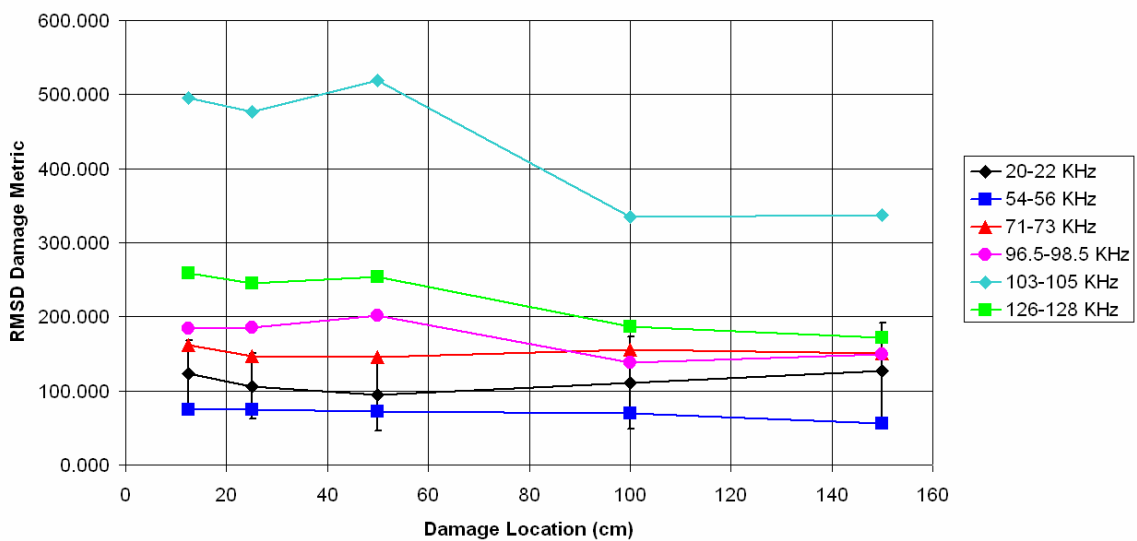


Figure 3.3.7: Damage metric values versus corrosion damage location in beams.

3.3.3 Corrosion Surface Coverage Tracking Results

Like the previous corrosion location results the corrosion surface coverage testing did not yield conclusive results for all levels of corrosion damage for any of the six test frequencies. The corrosion detection results were more conclusive for some frequencies, and the correct detection trends do exist as seen in Table 3.3.3. Additionally, there is a general trend between the damage

metric and the surface coverage for each frequency tested. However, in most cases the trends were not distinguishable beyond the ambient noise of the experiment.

Table 3.3.3: Corrosion surface coverage detection results.

Frequency (KHz)	Detection MSD	Distinguish MSD	Detection SSD	Distinguish SSD
20-22	4 of 5	2 of 5	5 of 5	1 of 5
54-56	4 of 5	2 of 5	5 of 5	3 of 5
71-73	5 of 5	2 of 5	5 of 5	1 of 5
96.5-98.5	4 of 5	2 of 5	5 of 5	4 of 5
103-105	4 of 5	0 of 5	5 of 5	0 of 5
126-128	4 of 5	0 of 5	5 of 5	1 of 5
All Six Combined	4 of 5	1 of 5	5 of 5	1 of 5
MSD Totals	29 of 35	9 of 35		
SSD Totals			35 of 35	11 of 35

Figure 3.3.8 shows the findings of the corrosion coverage results for a single damage metric calculated for all six test frequencies measured relative to the initial baseline. For each change in corrosion surface coverage (simulated by a 0.0500g mass change) the damage should increase as the level of damage on the structure increases. For this global test, only the first instance of damage (D12) does not follow the expected detection trend. The other four surface coverage changes increase the damage in a detectable manner that follows the expected trend. Only the first instance of damage is distinguishable based on the 95% confidence interval. As the simulated surface coverage increases the last four levels of damage are not distinguishable because of the large relative error caused by ambient changes.

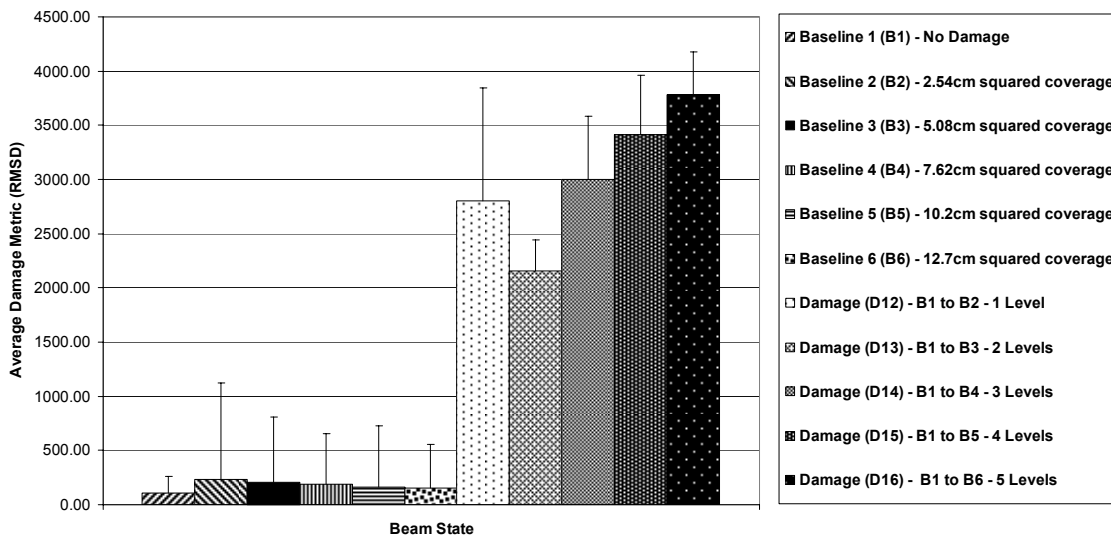


Figure 3.3.8: The results of the surface coverage test for all of the test frequencies combined.

Surface coverage tracking can be improved by narrowing the test frequencies to ranges sensitive to the damage but insensitive to ambient changes. In four of the six frequencies tested, only two of the levels of damage are distinguishable, and the other two frequencies cannot distinguish any levels of damage. An example of the individual testing results may be found in the Figure 3.3.9. Thus, the surface coverage tracking results are not conclusive for distinguishing changes in surface corrosion coverage. The cause of the over prediction of the first instance of damage is unknown, but it occurs for 5 of the 6 frequency ranges tested. All of the surface coverage damage metric plots and related impedance signature plots can be found in Figures B.1-B.60 in Appendix B.

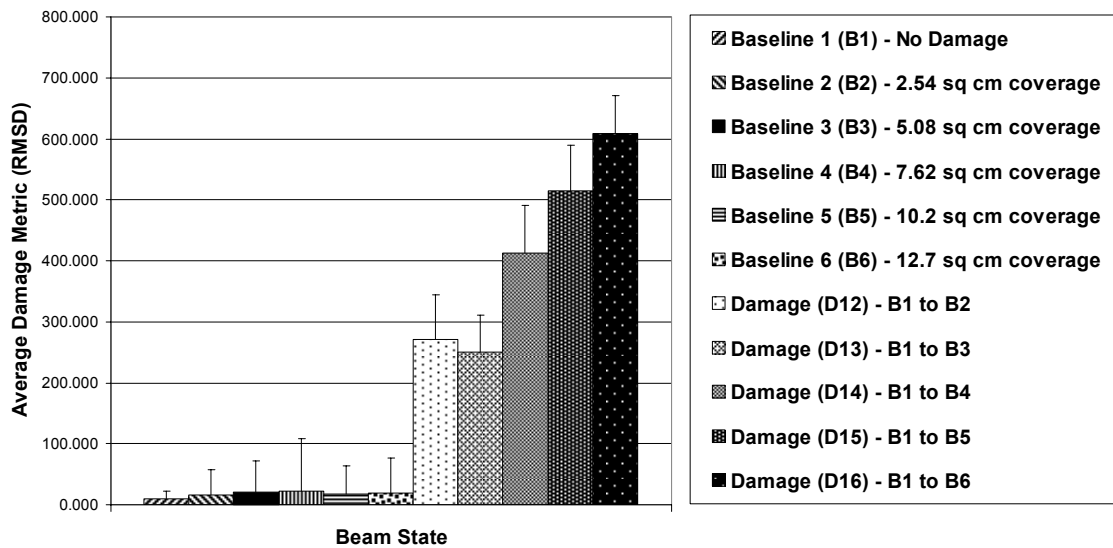


Figure 3.3.9: The results of the surface coverage for all for 20-22 kHz shows all are detectable.

For this surface coverage experiment, each level of damage was simulated by adding 0.0500 g of wax to the structure to simulate a 1.4% surface coverage increase of 6.32 micron pit depth. If the simulated pit depth were closer (by tripling the mass loading) to the upper limit of light corrosion of 25.4 microns, the levels of damage would have been more distinguishable and the test more conclusive. The ambient error would remain nearly the same, but the damage metrics would have increased. Even before the testing was complete, it was known that the tests were going to be inconclusive, but the simulated damage could not be increased without altering a second variable which decreases the statistical power of the experiment.

One of the main purposes of the surface coverage test was to determine if there was any correlation between the changes in corrosion surface coverage and the damage metric. If a

relationship between the two exists then the data could be fused with maintenance records to track and even predict the spread of surface corrosion with respect to time. Figure 3.3.10 shows a plot of the RMSD damage metric versus the cumulative change in the corrosion surface coverage for each of the six test frequencies. To prevent visual obstruction of the plot, the error bars are only displayed for 20-22 kHz because they are representative of the error for other frequencies. At all of the frequencies there is an increase in the damage metric as a function of surface coverage, but it is debatable whether or not the relationship is linear. However, since there is a relationship between the two it could be possible (when used in conjunction with other maintenance data) to define the relationship in order to use it in a tracking or predictive fashion.

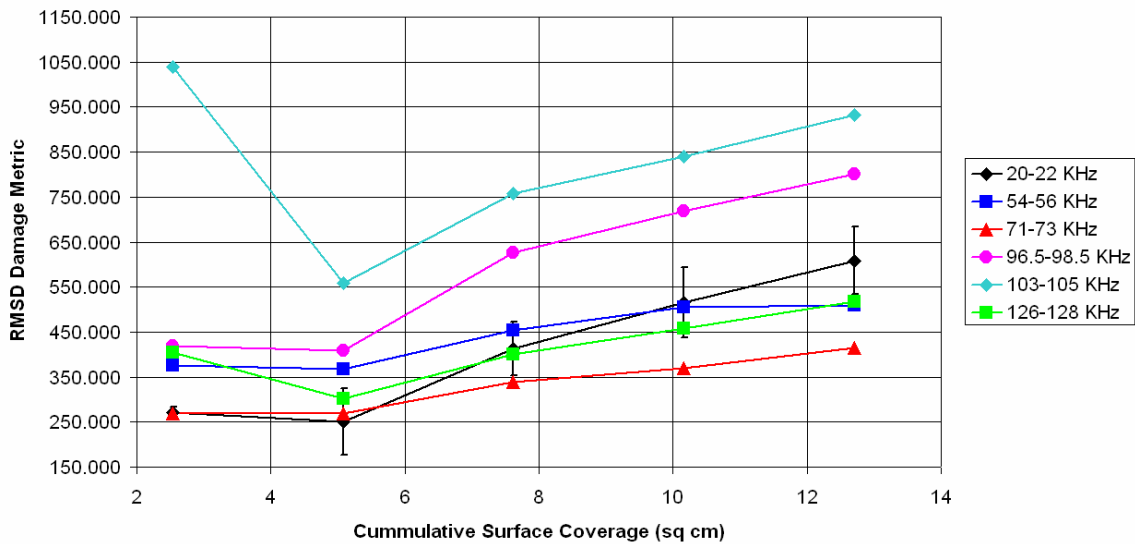


Figure 3.3.10: Plots of the damage metric versus surface coverage correlation for each frequency.

3.4 Corrosion Quantification Conclusions

For single site corrosion damage there are three key variables (damage depth, damage locate, and damage size) that must all be known to enable fatigue life and mean time till crack formation predictions. It would be very useful to maintenance personnel and engineers if autonomous structural health monitoring devices could use a variety of techniques to identify those key corrosion variables. To know all of the key variables may require the combining of several NDE methods because it is unlikely that any single method can accomplish all three goals. Additionally, combining impedance testing with modeling could help in the identification of key damage variables.

Here it has been shown that there is a relationship between damage metric changes and corrosion location, pit depth and surface coverage changes. For pit depth detection the relationship is well defined and the ambient error is small enough to make correlation useful. For corrosion location and surface coverage tests there is a correlation, but for the tested damage size, ambient error, and associated nonlinearity prevents the relationship from being useful. However, the location and surface coverages tests correlations would be better defined if damage tolerance increased, ambient noise reduced, or the structural response was more sensitive to the corrosion damage.

The relationship between changes in the damage metric and mass loss/pit depth seem to be strongest, so the impedance method may be best suited for corrosion detection, and pit depth tracking. This is a good result because pit depth is the key random variable in probabilistic fatigue life calculations for corrosion defects. Other NDE methods such as Lamb Waves or Acoustic Emission may be required to locate damage and determine corrosion surface coverage.

Chapter 4

Corrosion Detection in Plates

4.1 Introduction

In aircraft the wing and fuselage surfaces are primarily plate-like structures, and those surfaces are some of the thinnest and least rigid structures on aircraft. Aircraft panels are required to provide lift, reduce drag, protect mechanicals, and withstand repeated internal and external pressurization and thermal cycles. Due to the large surface areas, corrosion penetration of aircraft panels can generate large forces when the damage panels deflect in the air stream and lead to fast and sometimes catastrophic failure modes. The goal of Chapter 4 is to determine if the impedance method can detect and quantify pre-crack surface corrosion on plates, like those which comprise wing and fuselage structures on aircraft.

4.2 Testing Procedure & Experimental Setup

4.2.1 Beam and Plate Differences

Throughout the vibration community it is well known that the structural response of beams is very different from the structural response of plates. Since impedance based corrosion detection depends heavily on the structural response, it is worthwhile to explore the subtle differences between the high frequency responses of beams and plates because the damage metric calculations are affected by the response. Figure 4.2.1 contains an impedance signature for a typical beam, and Figure 4.2.2 contains a single impedance signature for a plate. Both signatures

extend from 20-250 kHz, the test range considered for most structures. In general, the impedance peak density for a beam is much lower than the impedance peak density in plates. Also, the real impedance magnitude in beams varies much more than those in a plate. Remember from chapter 2 it was noted that some of the best corrosion detection occurred for well-spaced impedance peaks with small magnitudes in beams. In plates, the impedance peak density is so high, finding well-spaced peaks is difficult especially for peak with small magnitudes. These general observations play a role in the amount of error incurred when calculating damage metrics.

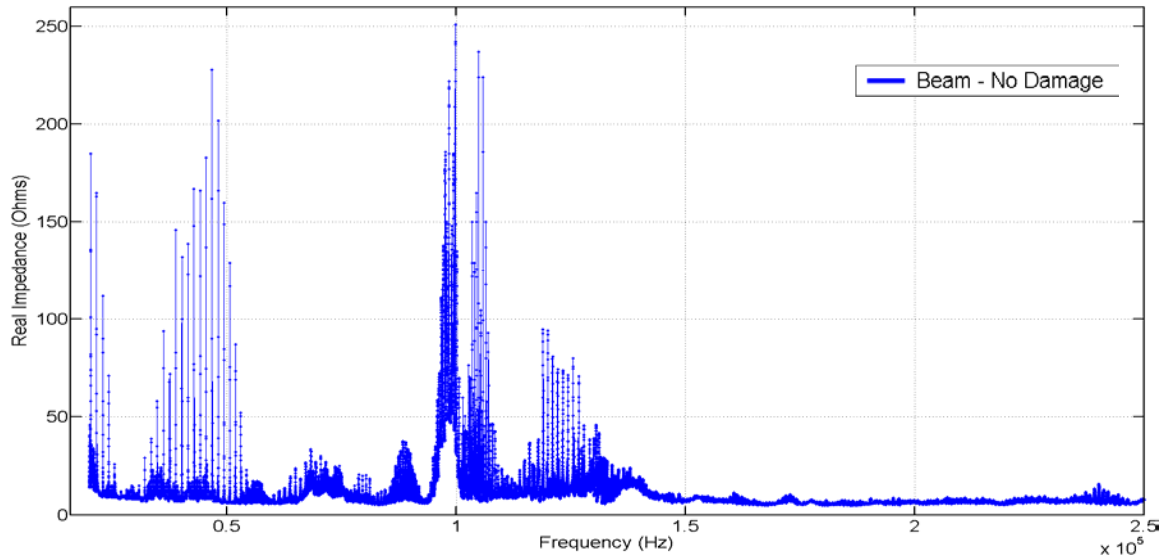


Figure 4.2.1: The peak density for beam-like structures is low relative to plate-like structures.

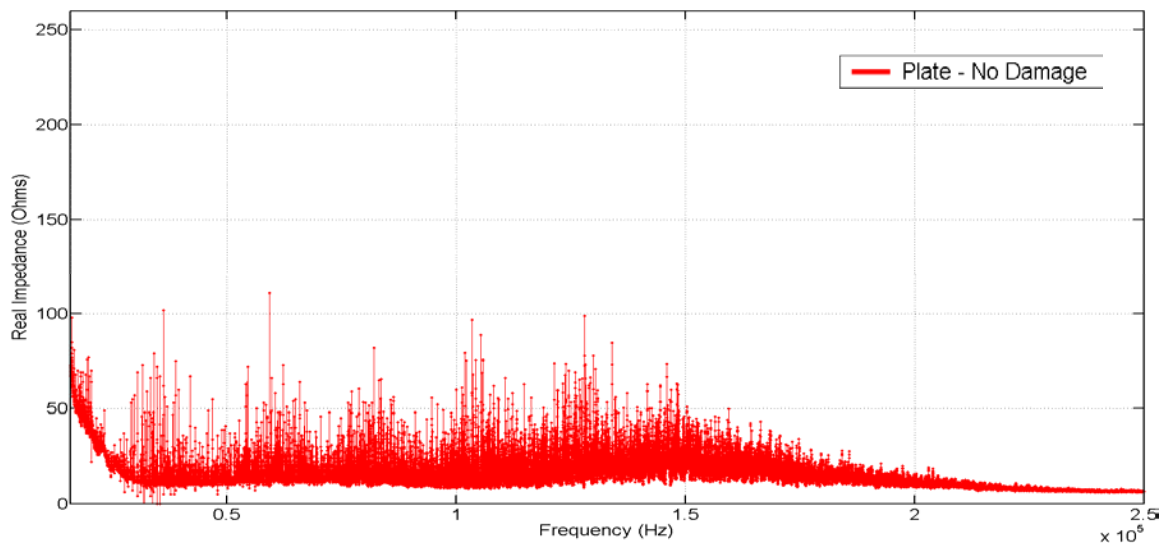


Figure 4.2.2: The peak density and real magnitudes for plate-like structures is large.

A closer look at the impedance responses over a smaller frequency range yields more valuable observations. Figures 4.2.3 and 4.3.4 show the impedance signatures for beams and plates from 40-80 kHz. It should be noted that this data was recorded for sensitivity testing at a frequency resolution of 1 point per 5 Hz, which causes the peaks to appear jagged. For the actual impedance testing, the frequency resolution was always set to 1 point per 1 Hz, which tends to smooth out all but the steepest and narrowest peaks. In the beam plot, many of the smaller peaks (less than 50 Ohms) appear to be short and fat like a well damped peak in a traditional FRF. For the plate plot, most of the peaks appear tall and narrow relative to most beam peaks. The tall narrow peaks cause variations in the damage metrics to increase in the presence of ambient noise like temperature induced variation. Think of the damage metric as the inverse of the correlation between the same impedance peak recorded at different times. For tall narrow impedance peaks in the healthy impedance sweep, ambient lateral shifts (may be temperature induced) for the corresponding impedance peak in the damaged impedance sweep causes the RMSD damage metric to rapidly increase (the correlation rapidly decreases). Thus, tall narrow peaks in plates are more sensitive to impedance changes than short wide peaks in beams. For damaged induced impedance shifts the added sensitivity is advantageous, but the drawback is that ambient induced impedance shifts are greater. The two tend to offset one another, and make distinguishing damage induced changes from ambient induced changes more difficult in plates than beams. It may seem subtle, but this fact makes detecting and distinguishing corrosion in plates more challenging than for beams.

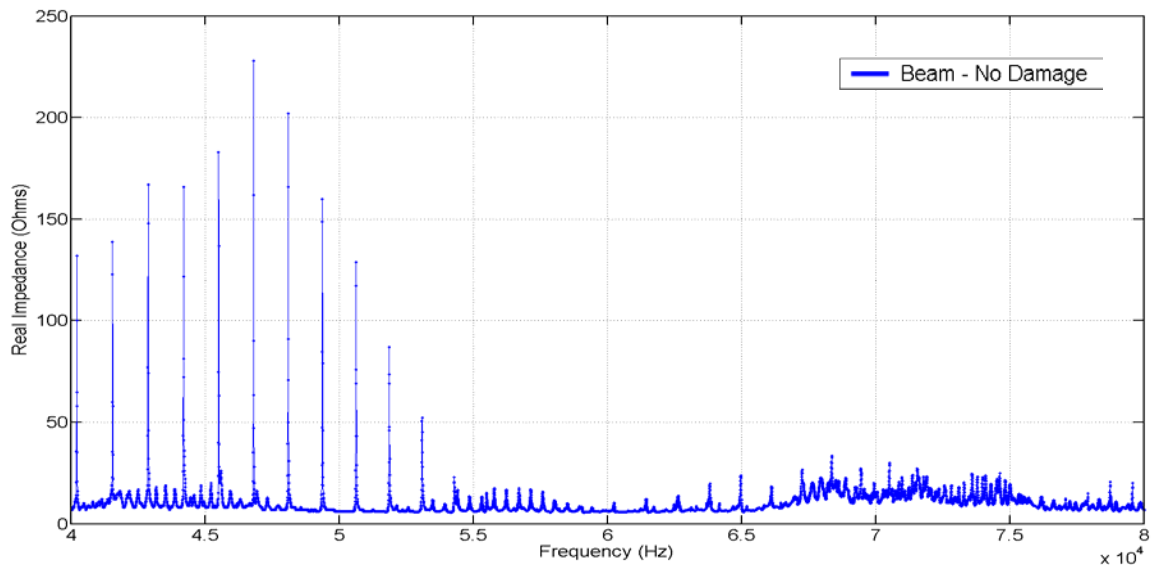


Figure 4.2.3: The peak magnitudes are lower and appear to be more damped in beams.

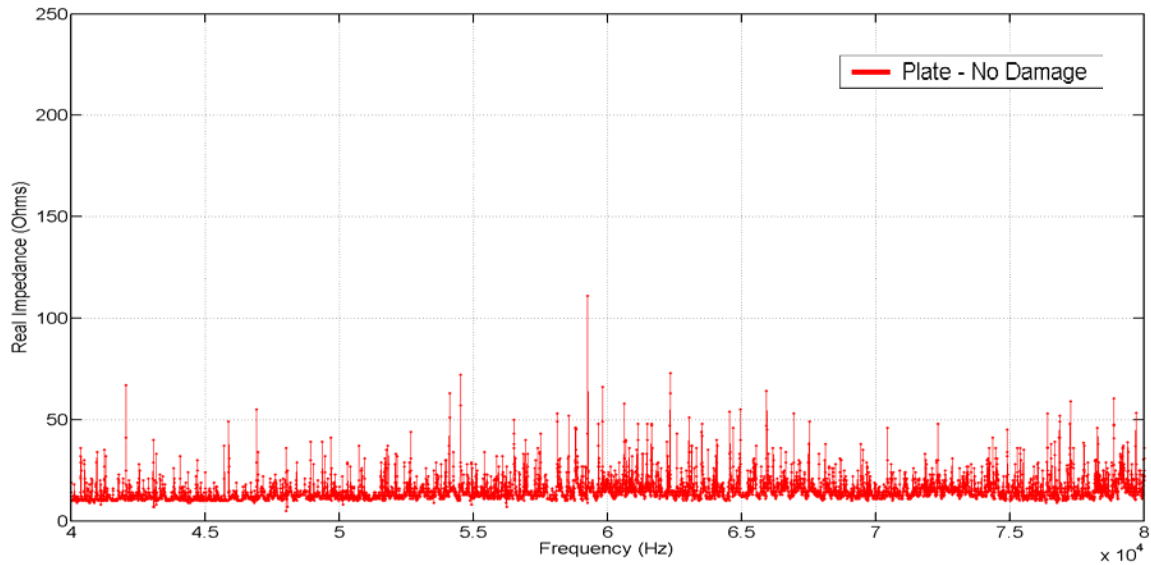


Figure 4.2.4: The peak magnitudes are larger and the less damped in plates.

4.2.2 Sensitivity Testing and Frequency Selection in Plates

Since it is more difficult to detect and distinguish plate corrosion, sensitivity testing and frequency selection become more important. For beams the test frequencies were selected by measuring a healthy impedance signature then measuring a damaged signature simulated by adding a small amount of wax to the structure. The two baselines were plotted, and based on the visual differences between the signatures test frequencies were selected. For plates, the same process was repeated with one additional step. For each frequency, the difference between the two impedance signatures was computed and then overlaid on the two impedance signatures to visually depict frequencies sensitive to damage. Figure 4.2.5 shows an example of the sensitivity test for one of the plate sensors.

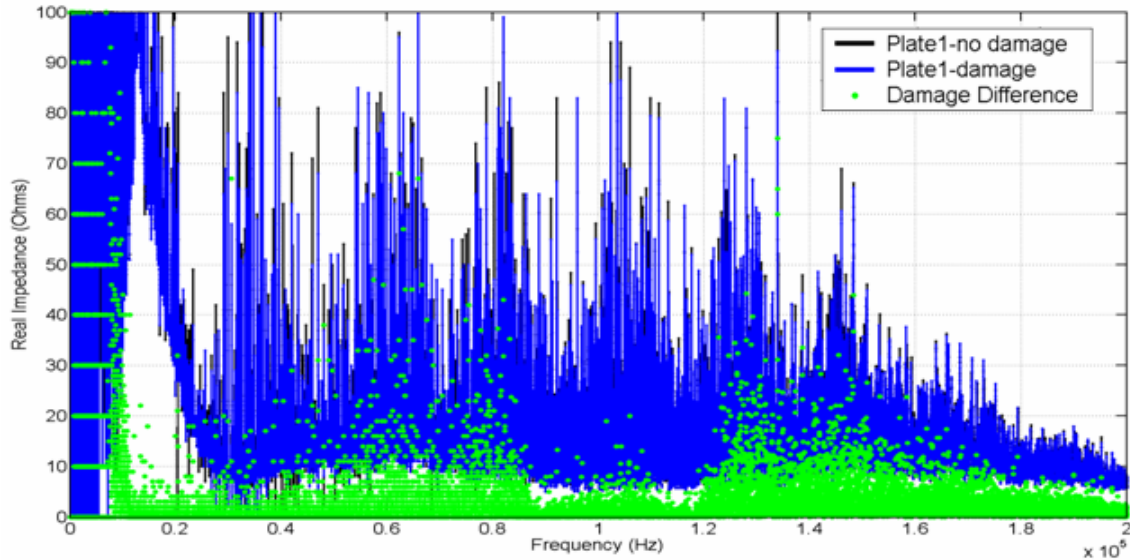


Figure 4.2.5: A sensitivity test on a plate with the damage metric difference overlaid.

By zooming in on different areas of the plot it is easy to recognize test frequencies sensitive to changes in the structure. Based on these results, twelve test frequencies were chosen for the plate. However, there is one weakness with this frequency selection method. Although the frequencies sensitive to damage are easy to identify, this selection method does not account for the error associated with each metric. Think of this as a signal to noise ratio (SNR) with the damage metric divided by the confidence interval. Ideal test frequencies will have large damage metrics insensitive to ambient error (large SNR); however, this selection method does not account for the error associated with each metric. Therefore, this frequency selection method is not the most favorable. Another frequency selection method is discussed in the section 4.3.3.

4.2.3 Plate Corrosion Testing Procedure

For the plate testing, a 122 x 122 x 0.098 cm sheet of aluminum 3105-H12 was cut from sheet stock. A 1 x 1 m square grid was laid out in the center of the aluminum sheet and 4 pieces of 1.905 x 1.905 x 0.0267 cm PZT 5A material were bonded to the four corners of the grid. The 1 m² area was subdivided into sixteen 25 x 25 cm squares with the intersections of the grid serving as possible corrosion damage locations. A picture of the plate may be seen in Figure 4.2.6. Leads were attached to the piezoelectrics, and then entire plate was hung vertically from two ropes to simulate free-free boundary conditions. The leads from the piezoelectrics were attached to an HP 4194A impedance analyzer which was controlled with LabView GPIB interface. Initially, sensitivity tests were conducted from 0.100-500.1 kHz to determine useful

testing frequencies. Twelve frequency ranges between 7.5 and 231.2 kHz were chosen for plate impedance testing based on adequate peak density and damage sensitivity. For each of the twelve frequency ranges the impedance was measured over a 1200 Hz range at 1 Hz resolution for each of the four piezoelectric sensors.



Figure 4.2.6: Ovals mark the PZT locations and squares mark the corrosion damage locations.

While the plate was in pristine condition, at least 30 samples of impedance data (baseline) were collected from each piezoelectric for the frequency range. The baseline measurement was made over a 7 day period to capture the ambient variability of the system. Once the initial baseline measurement was complete, the plate was corroded with hydrochloric acid. To reduce boundary condition changes, damage to sensors, and non-corrosion damage to the plate, all corrosion damage was added to the plate while it was hanging. The damage was “slight to moderate” corrosion with a 1% (depth 58.7 microns) and 0.25% (depth 66.0 microns) surface coverage. Slight to moderate corrosion damage was chosen for testing because that type of damage is of the magnitude found in aircraft entering the aging maturity phase [22]. A new baseline impedance measurement was made, and the process was repeated for each damage case. Damage locations were chosen such that the distance from each sensor ranges from 25, 75, 103, and 125 cm. This is important because with the plate and piezoelectric configuration used in this study, the greatest distance damage can occur from a sensor is 70.7 cm. Thus, the setup allows for the 3 sensors to detect the damage at distances greater than 70.7 cm.

For plate corrosion detection, a 122 x 122 x 0.098 cm sheet made from 3105-H12 aluminum was used. Aluminum 3105-H12 is more corrosion resistant than the T6063 T5 aluminum used in beam testing. The beam experienced intergranular pitting corrosion (imagine a sugar and sand

mixture exposed to water). The 3105-H12 aluminum does corrode when exposed to HCl, but the damage tends to be transgranular corrosion (imagine flat flakes that slowly dissolve). This indicates this plate would be less susceptible to SCC because the surface roughness does not change as much during corrosion, although the associated mass loss with transgranular corrosion will be greater. The plate was exposed to two corrosions of the following specifications: 1% surface coverage of “light to moderate corrosion” and 0.25% surface coverage of light to moderate corrosion. Each instance of corrosion was monitored with four sensors at 25, 75, 103, and 125 cm from the sensors (see Figure 4.2.6 for details). During the first damage application, PZT #1 was damaged, so only three sensors could be used for the damage baselines. Actually, the damage to PZT #1 has provided some very useful insights about the corrosive effect on PZT sensors which will be discussed in Chapter 5.

4.3 Plate Corrosion Detection Results

4.3.1 Corrosion Detection Results for Damage #1

For each undamaged sensor, impedance tests were conducted across 12 frequencies ranges from 7.5 to 231.2 kHz, and distances of 25 to 125 cm from the corrosion damage. Therefore, the corrosion damage could possibly be detected and distinguished up to 12 times for each of the undamaged sensor locations. For damage #1 to be detectable the sample mean of the damage metric (D_{12}) between baseline #1 (B_1) and baseline #2 (B_2) must be greater than the damage metrics for B_1 and B_2 . For damage #1 to be considered distinguishable, the sample mean D_{12} minus its 95% confidence interval ($D_{12} - CI_{D_{12}}$) must be greater than sample means of baseline #1 and #2 plus their confidence intervals ($B_1 + CI_{B_1}$ and $B_2 + CI_{B_2}$). Based on these criteria, Table 4.3.1 has been constructed to show the impedance based detection results for damage #1 on an aluminum plate. All plate plots of impedance signatures and damage states maybe found in Appendix C.

Table 4.3.1: Impedance based corrosion detection results for damage #1.

Damage to Sensor Distance (cm)	SSD	
	Damage #1	
	1% coverage, 58.7 μm deep	
	Detected	Distinguished
25	N/A	N/A
75	12/12	5/12
103	12/12	7/12
125	12/12	3/12
Total	36/36	15/36

All three undamaged sensors could detect and distinguish damage #1 (1% coverage with a 58.7 micron depth) for at least 3 of the 12 frequencies tested; however, no sensor could distinguish the damage for more than 7 of the 12 frequencies tested. For all sensors at all test frequencies, the sample mean of the damage baseline (D12) is detectable from the undamaged baseline (B1), but the confidence intervals used to predict the range of the population mean prevents damage #1 from being distinguishable based on the population means for some frequencies. PZT #2 was 75cm from the damage, and could detect and distinguish the damage for 5 of the 12 frequency ranges tested. PZT #3 was 103 cm from the damage, and could detect and distinguish the damage for 7 of the 12 frequency ranges tested. PZT #4 was 125 cm from the damage, and the damage could only be detected and distinguished for 3 of the 12 frequency ranges.

One percent coverage of light to moderate corrosion is detectable and distinguishable at distances up to 125 cm from the damage location. Since the greatest distance damage can occur from any sensor on this plate is approximately 71 cm (when all sensors are operable), it is implied that this type of damage could be identified anywhere on the plate. Figure 4.3.1 shows the results of damage #1 measured from sensor #2. Sensor #2 is 75 cm from the damage, and since sensor #1 was damaged and unavailable sensor #2 was closest to the damage. From 52-53.3 kHz, damage #1 is detectable and distinguishable from sensor #2, so it should be distinguishable anywhere on the plate.

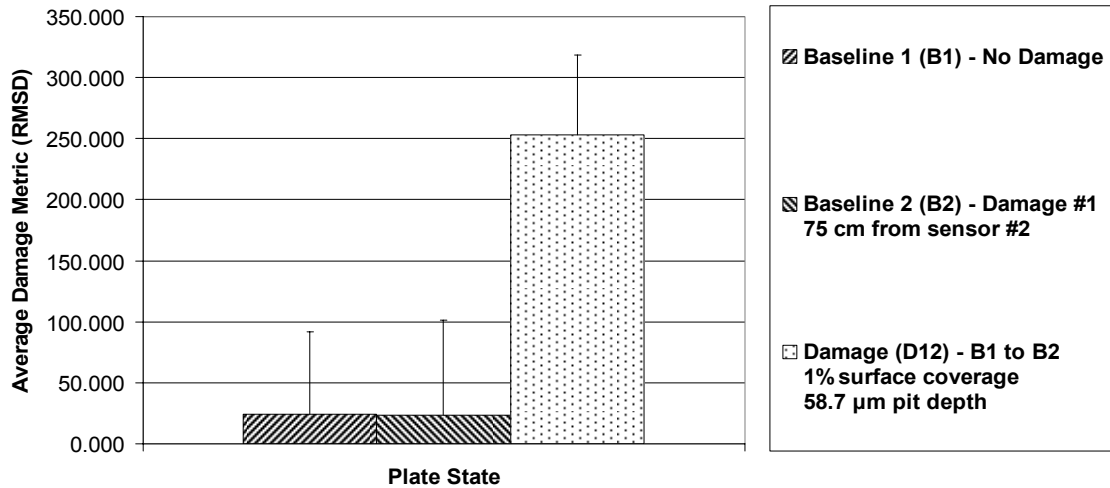


Figure 4.3.1: Corrosion detection results from PZT #2 at 52-53.2 kHz.

Figure 4.3.2 shows that sensor #2 can also distinguish damage #1 at high frequencies like those from 230-231.2 kHz. Sensor #4 is 125 cm from the location of damage #1; however, damage can still be distinguished. Figure 4.4.3 shows the damage plot for sensor #4 from 7.5-8.7 kHz. Based on these results we can assume that 1% coverage of light to moderate corrosion is detectable anywhere on the surface of the plate.

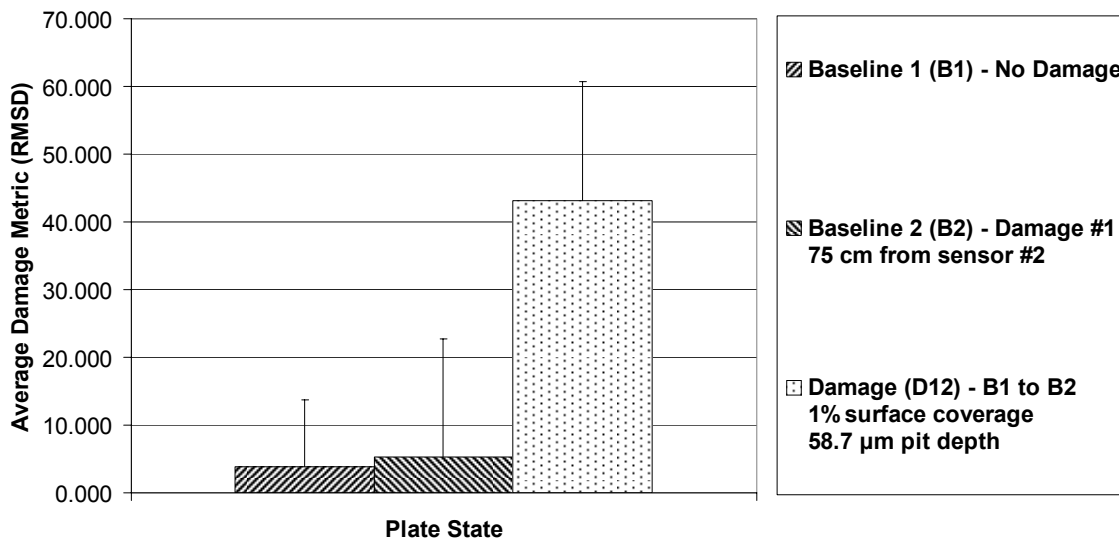


Figure 4.3.2: Corrosion detection results from PZT #2 at 230-231.2 kHz.

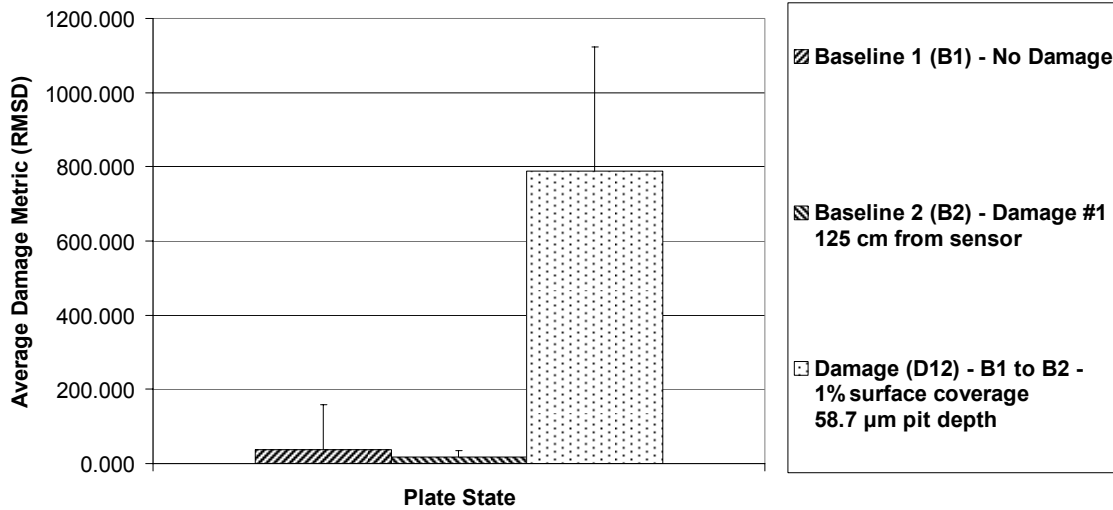


Figure 4.3.3: Corrosion detection results from PZT #4 at 7.5-8.7 kHz.

4.3.2 Corrosion Detection Results for Damage #2

For impedance based detection of damage on plates the corrosion damage can be categorized in two ways. The damage can be viewed as multiple site damage (MSD) measured relative to the healthy baseline or single site damage (SSD) measured relative to previous baselines. The following Excel based formulas in Table 4.3.2 layout the algorithms for damage detection. The MSD algorithms require damage #2 to be detectable and distinguishable from damage #1. Thus, distinguishing damage by MSD methods is more challenging, and in most cases only SSD results will be described because MSD methods are not very effective for plate-like structures. Table 4.3.3 contains the detection results for detecting damage #2. All plate plots of impedance signatures and damage states may be found in Appendix C.

Table 4.3.2: Damage algorithms used for damage #2.

Detection Type	Damage Algorithm
MSD Detection	$If \left(Or \left(D_{13} > \max(B_1, B_3, D_{12}), \right. \right. \\ \left. \left. And(D_{13} < D_{12}, D_{13} > \max(B_1, B_2)) \right) \right)$
SSD Detection	$If(D_{23} > \max(B_2, B_3))$
MSD Distinguishable	$If \left(Or \left((D_{13} - D_{13E}) > \max(B_1 + B_{1E}, B_3 + B_{3E}, D_{12} + D_{12E}), \right. \right. \\ \left. \left. And \left((D_{13} + D_{13E}) < (D_{12} - D_{12E}), \right. \right. \right. \\ \left. \left. \left. (D_{13} - D_{13E}) > \max(B_1 + B_{1E}, B_3 + B_{3E}) \right) \right) \right)$

MSD Distinguishable	$If((D_{23} - D_{23E}) > \max(B_2 + B_{2E}, B_3 + B_{3E}))$
------------------------	---

Table 4.3.3: Corrosion detection results for damage #2.

Damage to Sensor Distance (cm)	MSD		SSD	
	Damage #2		Damage #2	
	1% coverage, 58.7 μm deep		1% coverage, 58.7 μm deep	
	Detected	Distinguished	Detected	Distinguished
25	12/12	1/12	12/12	1/12
75	12/12	1/12	12/12	8/12
103	N/A	N/A	N/A	N/A
125	12/12	0/12	12/12	6/12
Total	36/36	2/12	36/36	15/36

The second instance of corrosion damage (0.25% surface coverage of light to moderate) can be distinguished from the baselines and damage #1 (MSD) by only two of three undamaged sensors. Figure 4.3.4 show one of the two cases were damage #1 and damage #2 can both be distinguished using an MSD algorithm. In this case the impedance method can distinguish MSD corrosion damage, but if required to distinguish more than two instances of damage this method would likely not fail. In plates, the magnitude of error relative to the damage metrics is large making it difficult to distinguish MSD corrosion damage.

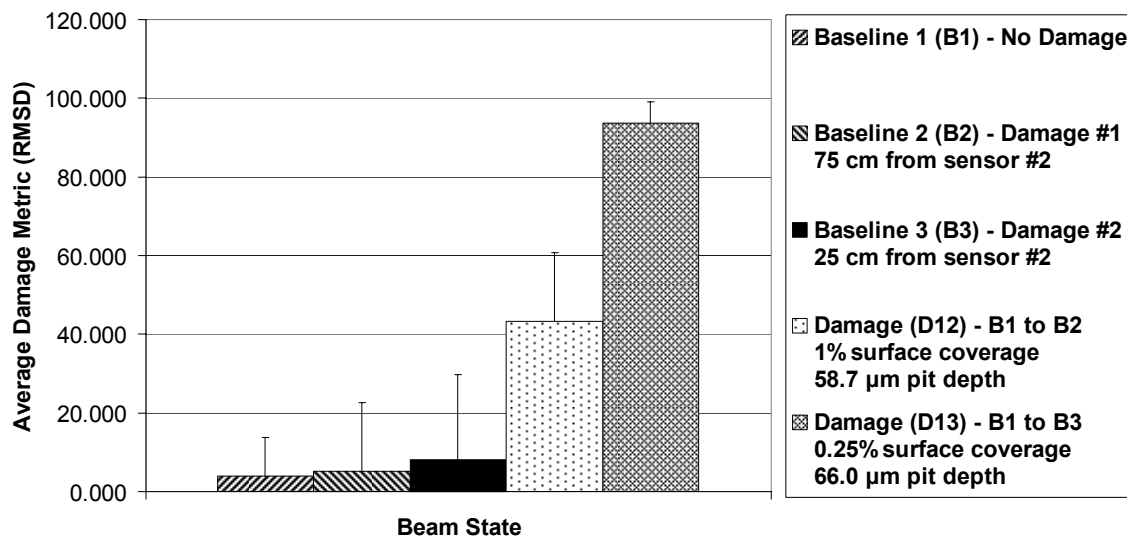


Figure 4.3.4: At 230-231.2 kHz the corrosion damage #2 is distinguishable from PZT#2.

When the damage metric is calculated relative to previous baselines to avoid having to distinguish the damage #2 from damage #1 (SSD), damage #2 can be distinguished for 22 of the

36 cases. For the six test 1200 Hz frequencies intervals between 7.5-91.2 kHz, damage #2 is distinguishable in 2 of 18 cases. The six 1200 Hz frequency intervals from 120-231.2 kHz, damage #2 can be distinguished in 13 of the 18 possible cases, so the higher frequencies perform better for distinguishing damage. The possible cause for this result will be discussed later.

PZT #4 is 75 cm from damage #2, and PZT #4 can distinguish the damage in 8 of the 12 cases, two in the lower and six in the upper frequency intervals. Figure 4.3.5 show the low frequency detection of damage #2 from PZT #4, and Figure 4.3.6 show the high frequency detection capability. It should be noted that the greatest distance damage can exist from any sensor in this sensor array is 71 cm. The fact that PZT #4 can distinguish 0.25% surface coverage of light to moderate corrosion at 75 cm is an indicator that this type of damage should be distinguishable anywhere on the plate. To further support this claim damage #2 could be distinguished in six of 12 cases for PZT #3 which is 125 cm from the damage.

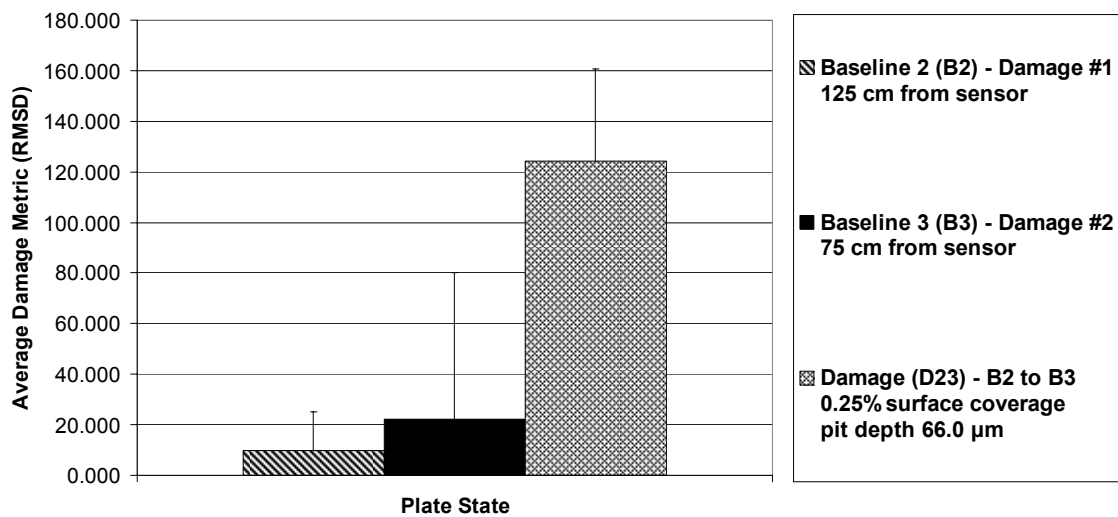


Figure 4.3.5: Damage #2 is distinguishable from PZT #4 at 52-53.1 kHz.

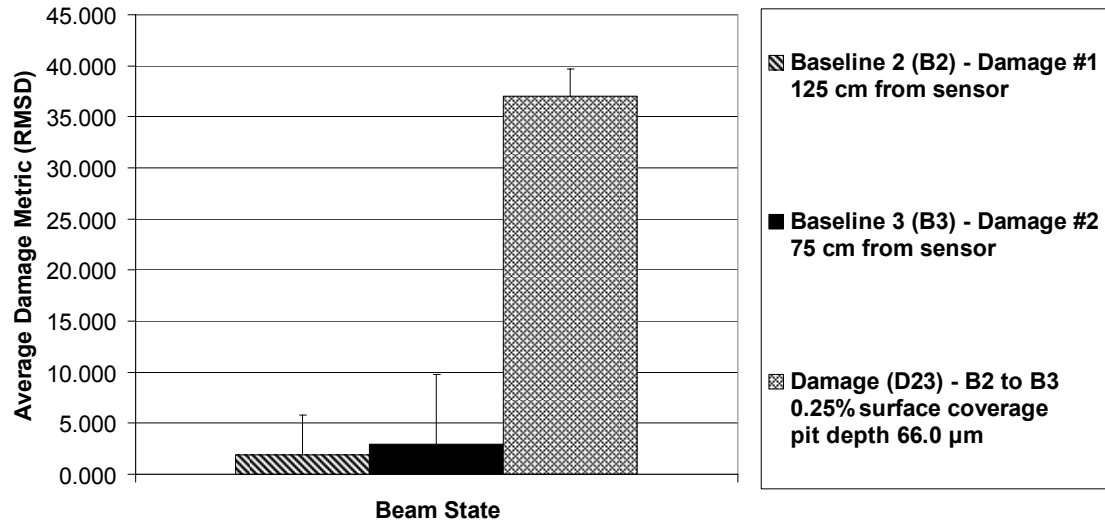


Figure 4.3.6: Damage #2 is distinguishable from PZT #4 at 230-231.2 kHz.

4.3.3 Corrosion Detection Patterns in Plates

For structural health monitoring purposes it is useful to identify the general and specific patterns of damage detection. After studying the plate data seen in Table 4.4.4 and impedance signatures in Appendix C, some general corrosion detection patterns can be identified. First, the damage is detectable, so the correct detection trend exists but the damage cannot always be distinguished because of ambient error. Thus, more research needs to be performed to select frequencies that are sensitive to damage but insensitive to ambient noise. Second, higher frequencies tend to be better able to distinguish damage. From the impedance signature plots in Appendix C, high frequencies tend to have smaller real impedance magnitudes, and the base of the peak is spread over larger frequencies intervals (short and wide) which produces less error due to change in ambient condition. Third, although lower frequencies have tall, narrow impedance peaks, at some frequencies the associated error is small enough to allow the corrosion damage to be distinguishable. Fourth, there does not seem to be a correlation for the distance between the damage and sensor and the ability to distinguish damage. To locate corrosion damage, other SHM techniques, like Lamb waves, may be required. Fifth, the impedance method is sensitive to 1% or less surface coverage of light to moderate surface corrosion meaning the damage can be identified in structures before cracks form.

Table 4.3.4: Plate corrosion results compiled by sensing location and frequency.

PZT #2									
SSD					SSD				
Test Frequency	Damage #1 Detection	Damage #1 Distinguished	Damage #2 Detection	Damage #2 Distinguished	Test Frequency	Damage #1 Detection	Damage #1 Distinguished	Damage #2 Detection	Damage #2 Distinguished
7.5-8.7 KHz	1	1	1	0	130-131.2 KHz	1	0	1	0
32-32.2 KHz	1	0	1	0	150-151.2 KHz	1	0	1	0
53-53.2 KHz	1	1	1	0	170-171.2 KHz	1	0	1	0
62-63.2 KHz	1	0	1	0	190-191.2 KHz	1	1	1	0
74-75.2 KHz	1	0	1	0	210-211.2 KHz	1	1	1	0
90-91.2 KHz	1	0	1	0	230-231.2 KHz	1	1	1	1
Distance	75	75	25	25	Distance	75	75	25	25
PZT #3									
SSD					SSD				
Test Frequency	Damage #1 Detection	Damage #1 Distinguished	Damage #2 Detection	Damage #2 Distinguished	Test Frequency	Damage #1 Detection	Damage #1 Distinguished	Damage #2 Detection	Damage #2 Distinguished
7.5-8.7 KHz	1	0	1	0	130-131.2 KHz	1	1	1	1
32-32.2 KHz	1	0	1	0	150-151.2 KHz	1	1	1	1
53-53.2 KHz	1	1	1	0	170-171.2 KHz	1	1	1	1
62-63.2 KHz	1	0	1	0	190-191.2 KHz	1	1	1	1
74-75.2 KHz	1	0	1	0	210-211.2 KHz	1	1	1	1
90-91.2 KHz	1	0	1	0	230-231.2 KHz	1	1	1	1
Distance	103	103	125	125	Distance	103	103	125	125
PZT #4									
SSD					SSD				
Test Frequency	Damage #1 Detection	Damage #1 Distinguished	Damage #2 Detection	Damage #2 Distinguished	Test Frequency	Damage #1 Detection	Damage #1 Distinguished	Damage #2 Detection	Damage #2 Distinguished
7.5-8.7 KHz	1	1	1	0	130-131.2 KHz	1	0	1	1
32-32.2 KHz	1	0	1	0	150-151.2 KHz	1	0	1	1
53-53.2 KHz	1	0	1	1	170-171.2 KHz	1	0	1	1
62-63.2 KHz	1	0	1	1	190-191.2 KHz	1	0	1	1
74-75.2 KHz	1	1	1	0	210-211.2 KHz	1	0	1	1
90-91.2 KHz	1	1	1	0	230-231.2 KHz	1	0	1	1
Distance	125	125	75	75	Distance	125	125	75	75

To better quantify specific patterns in plate corrosion detection an extra test was performed in an attempt to study frequencies not tested and to perhaps find a better way to conduct sensitivity testing and frequency selection. For PZT #3 and PZT #2, five long impedance sweeps from 0.100-300 kHz at 1 Hz resolution was collected. A third corrosion (1% coverage of light to moderate) was added to the plate 25 cm above and to the right of PZT #3. Then, five damaged impedance sweeps were collected for PZT #3 and PZT #2. The long impedance sweeps allow damage metrics minus the 95% confidence intervals to be calculated over any size interval of interest and laid over the impedance data. Figures 4.2.7 and 4.3.8 show damage metrics calculated over 1000 Hz intervals with the 95% confidence interval was subtracted from the metrics such that positive values indicate frequency intervals good for detecting and distinguishing damage. For PZT #3 (35 cm from the damage), the damage tends to be most distinguishable from 20-80 kHz and 230-290 kHz. However, the frequencies from 80-230 kHz tend to have errors so large that the damage would not be distinguishable. For PZT #2 (106 cm from the damage), the damage was most distinguishable between 90-140 kHz. This implies it is very difficult to find specific patterns for corrosion detection on plates. The detection trend for one sensor at one location does not hold for all sensors. Although, it may be useful to perform such a test in the sensitivity testing phase because it may aid the frequency selection process. For plates, it is very easy to select frequency ranges for impedance testing not optimal for corrosion

detection. More research is still required in this area so that autonomous SHM devices can conduct sensitivity tests without the aid highly-trained technicians.

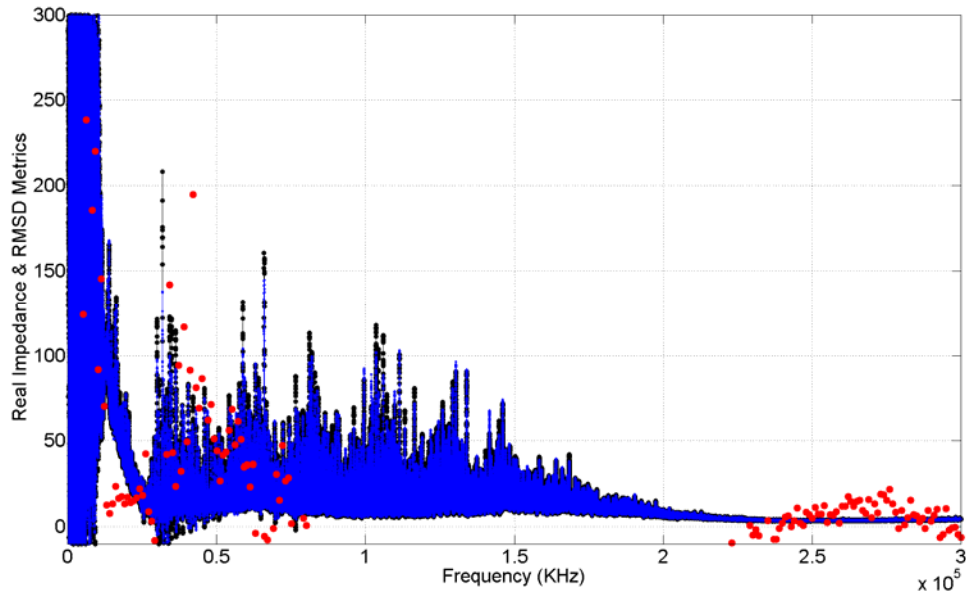


Figure 4.2.7: Impedance signatures with distinguishable damage overlaid for PZT #3.

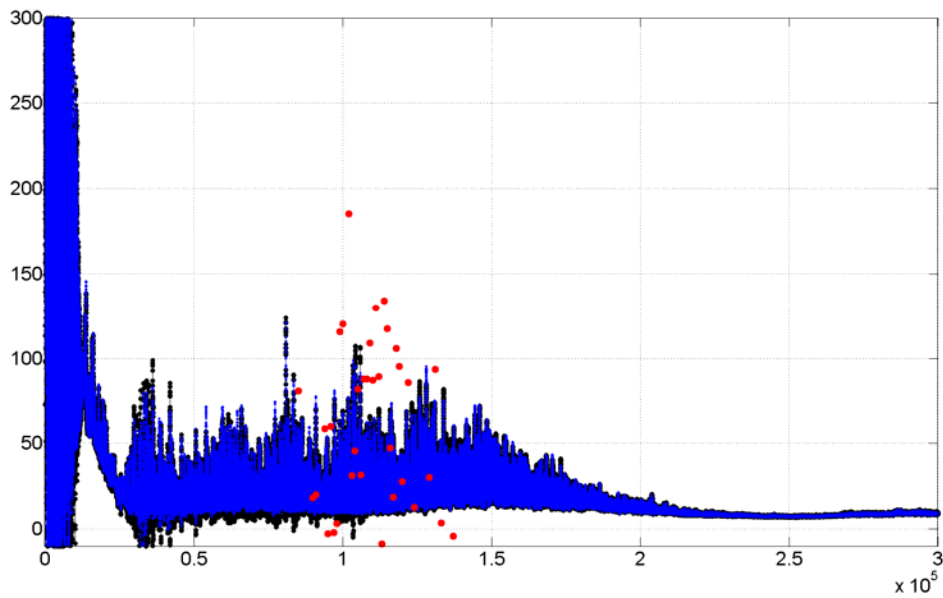


Figure 4.2.8: Impedance signatures with distinguishable damage overlaid for PZT #2.

Chapter 5

Impedance Sensor Corrosion

5.1 Introduction

Corrosion presents some unique detection challenges for the impedance method, and Chapter 5 will address those concerns. The impedance method requires healthy system data as a reference to determine when the system becomes damaged. If corrosion directly damages the piezoelectric sensor or bond condition, the healthy system reference is lost, and it becomes difficult to diagnose the structure. This section is devoted to three experiments which quantify the corrosive effect on impedance sensors, and develop ways to avoid sensor corrosion issues. The first experiment will quantify the corrosive effect on unprotected PZT sensors used in impedance testing. Second, an experiment will be conducted on Kapton protected MFC D_{31} and D_{33} piezoelectrics for corrosion detection. The experiment will determine if those sensors can detect corrosion, and if they are resistant to corrosive environments. The third experiment, will determine if PZT, MFC D_{31} , and MFC D_{33} piezoelectrics can detect damage when the sensor is mounted opposite the corrosion damage. Understanding the sensor corrosion challenge yields valuable insights into ways to directly measure the corrosion rate based on direct corrosion of the piezoelectric sensors.

5.2 How Corrosion Affects PZT & MFC Sensors

During the plate corrosion testing described in Chapter 4, one of the piezoelectric sensors (PZT #1) was damaged during the application of corrosion damage #1. The testing protocol and data provided some evidence that the sensor changes were likely caused by corrosion; however,

the exact cause is not known. The data from the damaged sensor was post processed in an attempt to better understand the effect corrosion has on sensors. Later, a separate experiment was designed to determine the corrosive effect on PZT and MFC piezoelectric self-sensing actuators. The experimental setup and results are discussed in this section.

5.2.1 Initial Observations on PZT Sensor Corrosion

As was mentioned in Chapter 4, PZT#1 was damaged during the application of corrosion to the plate. During the corrosion process the PZT sensors are covered with plastic and sealed with tape. The area to be corroded is taped off to control the coverage of the chemical etching. When the tape was being removed, PZT#1 had to be uncovered due to tape overlap, and it is thought that corrosion products were exposed to sensor #1. From the time of possible exposure until measurement began 80 minutes past, and then 4 hours of data (approximately 1 sample per 7 minutes) was collected from PZT#1. Figure 5.2.1 and 5.2.2 shows a plot of the initial undamaged baseline in black (43 plus measurements over 7 days), and the first damage baseline (30 plus measurements over 4 hours) is plotted with a blue to green color-map. There is a definite trend in the first damage baseline, and most importantly, the same trend was seen in all six test frequencies. As time increases the impedances shift upward and slightly to the left. There seems to be a rate associated with the impedance shift as it is increasing at a decreasing rate. From a corrosion prospective, this makes sense because the chemical reaction should slow in a logarithmic fashion as the reactants are converted to products and the reaction approaches equilibrium.

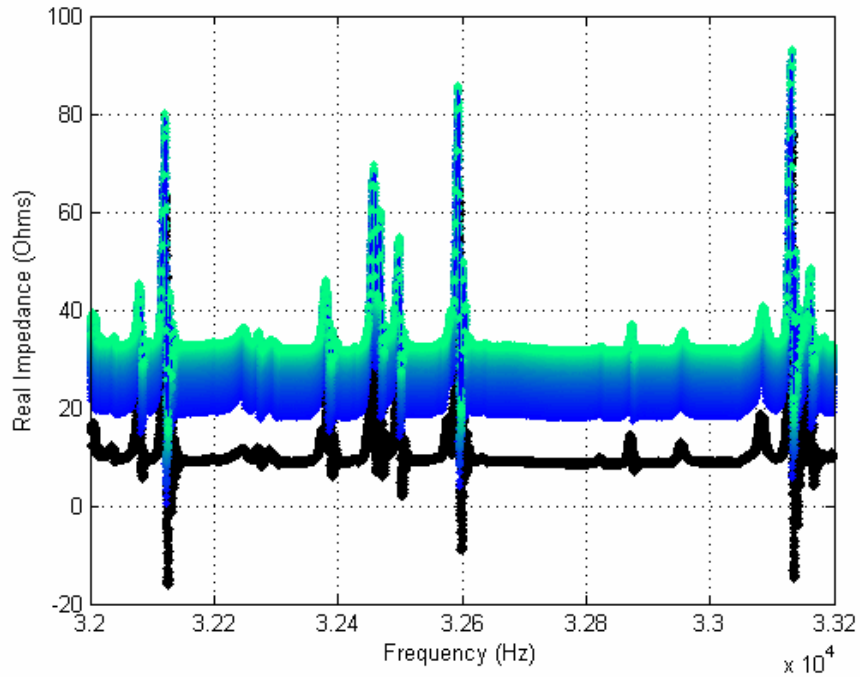


Figure 5.2.1: The impedance change in PZT #1, where black is 43 undamaged signatures and the blue to green colormap is the 33 signatures for damage #1 measured with a corrosion damaged sensor.

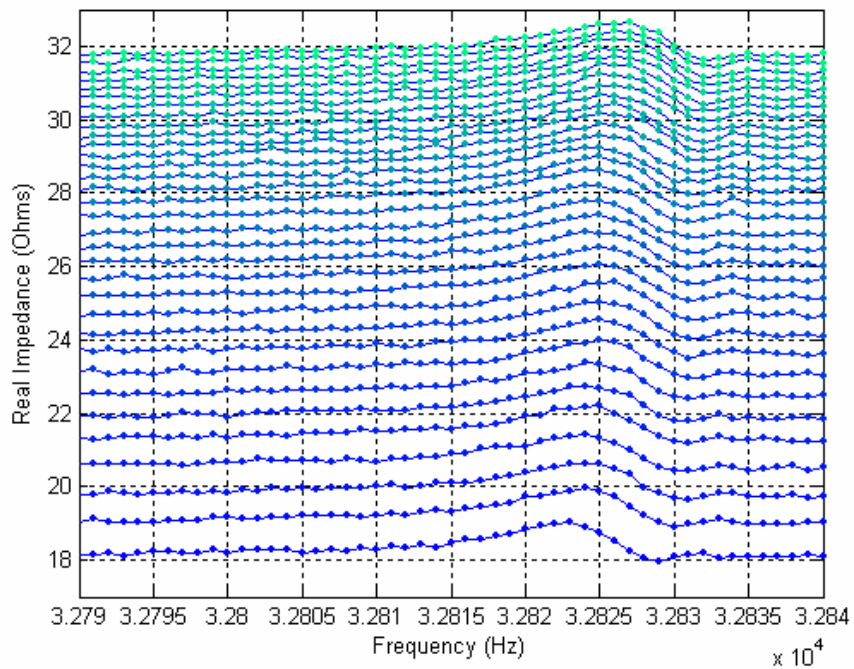


Figure 5.2.2: Over a narrow frequency band, it is easy to see the time dependant shift in the impedance signature caused by the corrosion damaged sensor.

To confirm there is a time-dependant trend in the impedance and capacitance of the PZT as it corrodes, impedance and capacitance versus time plots were created for all six test frequencies. Figure 5.2.3 shows the real impedance versus time plot for all frequencies, and each shift is fitted with exponential trend lines to confirm the trend. The 6 trend lines yield curve fits with R-squared values ranging from 0.9885 to 0.9999. Figure 5.2.4 show how the capacitance of the PZT exponentially decreases with respect to time for all 6 of the test frequencies. Trend lines fitted to the capacitance data yields R-squared values ranging from 0.9913 to 0.9998. Thus, there is significant evidence to indicate time dependant shifts in the impedance and capacitance of the PZT sensor, and the cause of the change is thought to be sensor degradation due to corrosion. The exact cause of the damage in PZT#1 is not precisely known. The cause of the damage could be bond changes, a cracked piezoelectric, or corrosion of the electrode. However, since there is a definite logarithmic increase in the impedance and an exponential decrease in the capacitance, the author believes the changes are results of sensor corrosion. Changes in the sensor bond conditions or a cracked sensor would likely not lead to the same time-dependant trends.

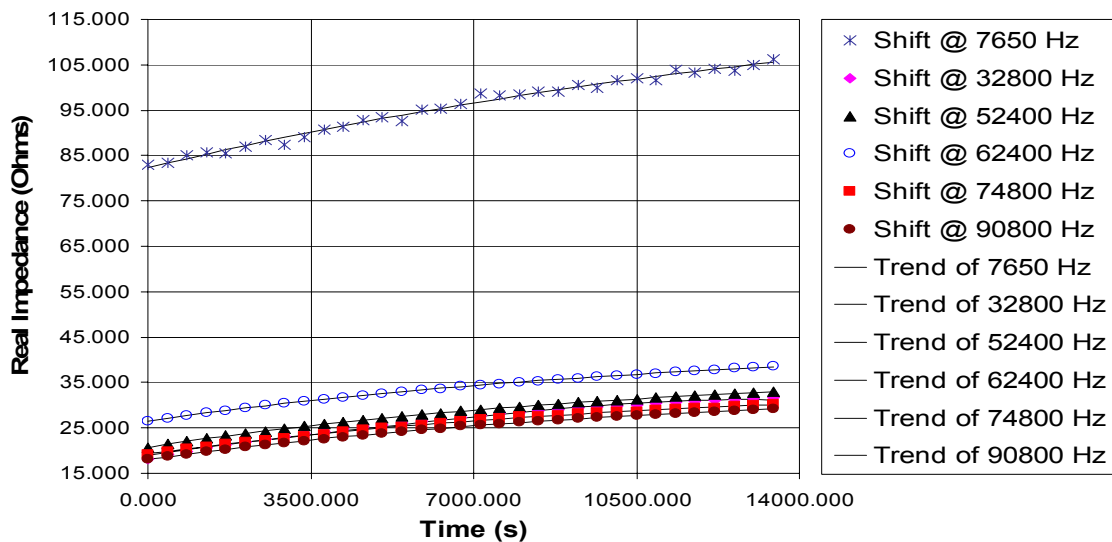


Figure 5.2.3: Impedance versus time plot for a damage PZT sensor show definite trends.

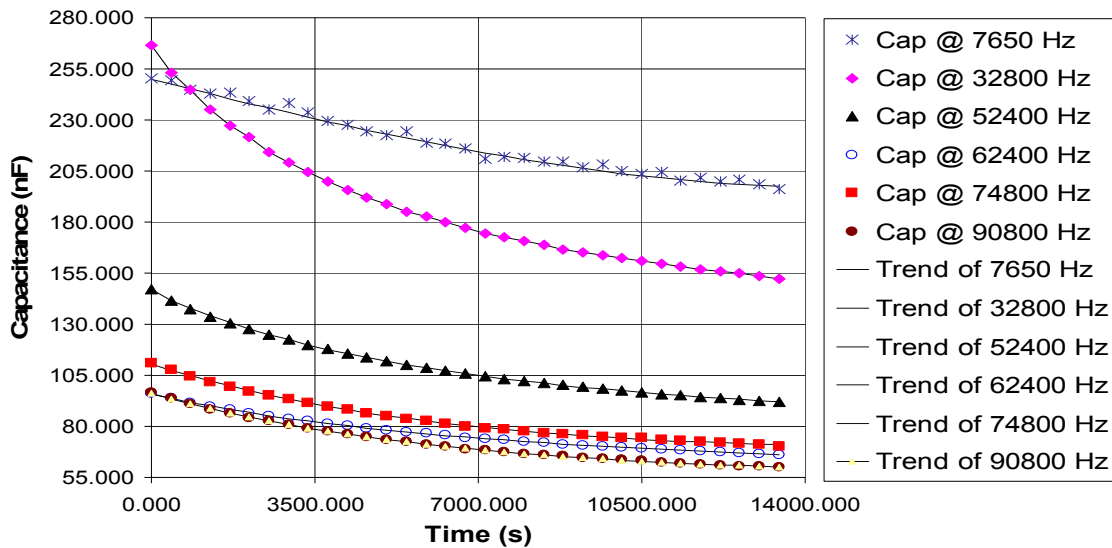


Figure 5.2.4: Capacitance versus time plot for a damage PZT sensor show definite trends.

To further strengthen the hypothesis that this effect is corrosion related other possible logarithmic and exponential causes were ruled out. Based on the experimental log, the corroded area was cleaned with room temp DI water, and later cleaned with room temperature isopropyl alcohol. The evaporative cooling effect of the water and alcohol could have reduced the plate temperature slightly such that the plate temperature would have risen during data collection, and this could shift the impedance data. Temperature changes may also have caused the exponential trends in the data, but this was ruled out because the trend moves in the wrong direction. As the temperature rises, the impedance magnitude should decrease, and in this case it increases with time [31]. Thus, temperature effects were ruled out as a cause of this fact lending more weight to the corroded sensor hypothesis. Also, some quick informal and not statistically supportable tests on PZT bonded to aluminum yielded similar shifts. The PZT manufacture of the PZT claims the PZT electrodes are made of pure nickel with traces of vanadium which should make the material relatively corrosion resistant.

5.2.2 Experimental Setup for Sensor Corrosion Testing

An experiment was designed to verify the suspected corrosion trend in PZT, and to verify that Kapton protected MFC piezoelectrics could avoid sensor corrosion. A 122 x 5.08 x 0.318 cm aluminum beam seen in Figure 5.2.5 served as the test structure. On side #1 of the beam, two pieces of 2.54 x 2.54 x 0.0254 cm PZT A4 material were bonded to the structure. On side #2, an

M-2814-P2 MFC D_{31} and M-2814-P1 MFC D_{33} were bonded to the structure. For each piezoelectric, 35 or more impedance sweeps of 400 Hz from 20-72 kHz were made to establish a healthy baseline #1. A solution of 5 mol HCL was prepared as a corrosive solution. The corrosive solution was brushed onto the top surface of each piezoelectric, and left for 3 minutes. After 3 minutes the excess HCl solution was wiped from the piezoelectrics to eliminate mass loading, and the system was allowed to dry for 3 more minutes. Then, an impedance sweep of the corroded sensor was conducted. Each impedance sweep of all six frequencies required 300 seconds, so each baseline (30 or more sweeps) required at least 2.5 hours to acquire.

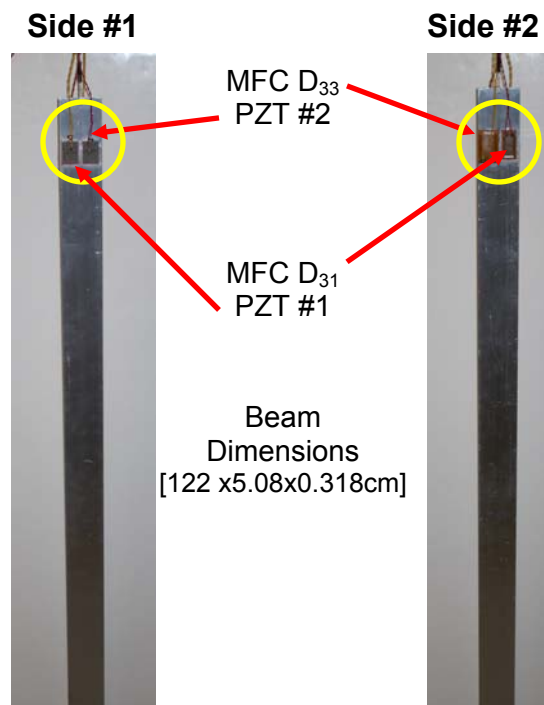


Figure 5.2.5: The test structure for sensor corrosion testing.

5.2.3 Experimental Results of Sensor Corrosion Testing

The sensor corrosion testing refutes the earlier finding of sensor degradation in the presence of corrosive solutions. The impedance signatures showed very little variation between the healthy impedance measurements and the corroded measurement. A statistical analysis of the damage metrics confirmed that the variations between the corroded and healthy sensors (both MFC and PZT) were detectable but not distinguishable beyond the 95% confidence intervals. At the start of the test it was expected that the MFC would not show appreciable sensor corrosion damage, but the PZT sensors were expected to be degraded. However, the PZT sensors did not

show statistically significant degradation during this test. This result does not agree with the earlier finding that PZT sensors were damaged by corrosion products.

There are several possible causes for these conflicting results. First, the exposure time to the corrosive solution may have been too short to significantly damage the sensor. Second, for this test no corrosive solution was allowed to contact the bond layer (Cyanoacrylate), so maybe it was the bond layer that degraded in the previous test. The second conclusion is supported by the fact that pure nickel is relatively corrosion resistant, but the corrosive effects on the cyanoacrylate bond layer are not known. Regardless of the sensor corrosion testing outcome, several major recommendations are made. For the impedance method to properly identify damage, it is necessary for the piezoelectric sensors and structural bond to remain nearly constant. Corrosive compounds may or may not change the sensor or bond, but it is necessary to take some precautions. If possible piezoelectrics and bond layers used for impedance-based corrosion detection should be protected from harsh environments to prevent sensor degradation. Before unprotected piezoelectrics are used in corrosive environments more testing needs to be conducted to confirm that the sensor will not degrade.

5.3 Macro-Fiber Composites Used for Corrosion Detection

The electrodes of Macro-Fiber Composites (MFC) are protected by a layer of Kapton, and the interdigitated electrodes allow these self-sensing actuators to be flexible. Since Kapton is relatively corrosion resistant, MFCs would be useful as sensors in impedance-based corrosion detection schemes so long as they can detect pre-crack surface corrosion. This section discusses an experiment to confirm MFC D_{31} and D_{33} piezoelectrics can detect pre-crack surface corrosion damage using the impedance method.

5.3.1 MFC and PZT Corrosion Detection Setup

The experimental setup described below is designed to accomplish two goals. First, MFC D_{31} and D_{33} self-sensing actuators will be used for corrosion detection using the impedance method, and the results will be compared to impedance-based corrosion detection using PZT sensors. Second, the impedance method will be tested with MFC D_{31} , MFC D_{33} , and PZT sensors to detect corrosion which occurs on the side of the structure opposite the sensor. One experiment was designed to accomplish both goals.

A 110 x 2.54 x 0.159 cm, 6063 T5 aluminum alloy aluminum beam was chosen as a test structure. The centerline of both sides of the beam serves as the corrosion damage site. On side #1 of the beam, a Smart Materials M-2814-P2 MFC D_{31} is bonded 50 cm from the damage site, and a 1.9 x 2.8 x 0.254 cm (the same size as the MFC D_{31} electrode) piece of PZT A4E material is bonded 50 cm from the other side of the damage location. A picture of side #1 of the structure may be seen in Figure 5.3.1. On side #2 of the beam, a Smart Materials M-2814-P1 MFC D_{33} was bonded 50 from the damage centerline, and a 1.9 x 2.8 x 0.254 cm (the same size as the MFC D_{33} electrode) piece of PZT A4E material is bonded 50 cm from the other side of the damage location. A picture of side #2 of the structure may be seen in Figure 5.3.1. The aluminum beam was hung vertically to simulate free-free boundary conditions. Assuming no sensors are damaged during testing, this experimental setup will allow both experimental goals to be accomplished.

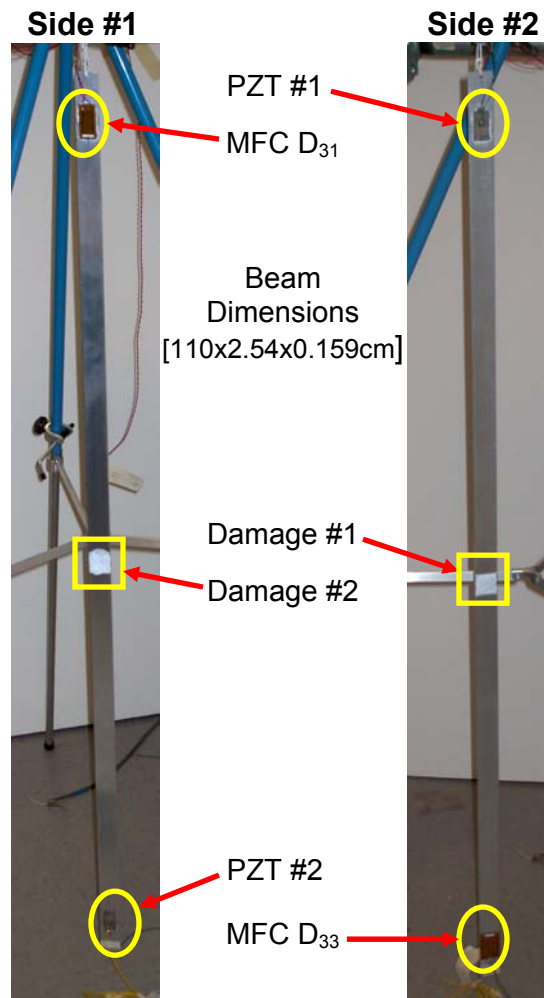


Figure 5.3.1: Both sides of the test structure with all sensors and levels of damage shown.

The next step involved sensitivity testing and frequency selection. For each sensor, a 5 Hz – 300 kHz impedance sweep was made for each sensor in a healthy condition. Then, a 0.100 g piece of wax is placed on the damage location to simulate a corrosion induced change in the system. A new impedance sweep was made for each sensor, and then the data is compared to quantify which frequencies are sensitive to damage. Based on the sensitivity testing, 12 frequencies between 3 and 208 kHz were selected. The impedance response for the three sensor materials is different, so care was taken to select frequencies that should be sensitive to the damage. Figure 5.3.2 shows how the impedance responses differ over one of the selected frequency test ranges.

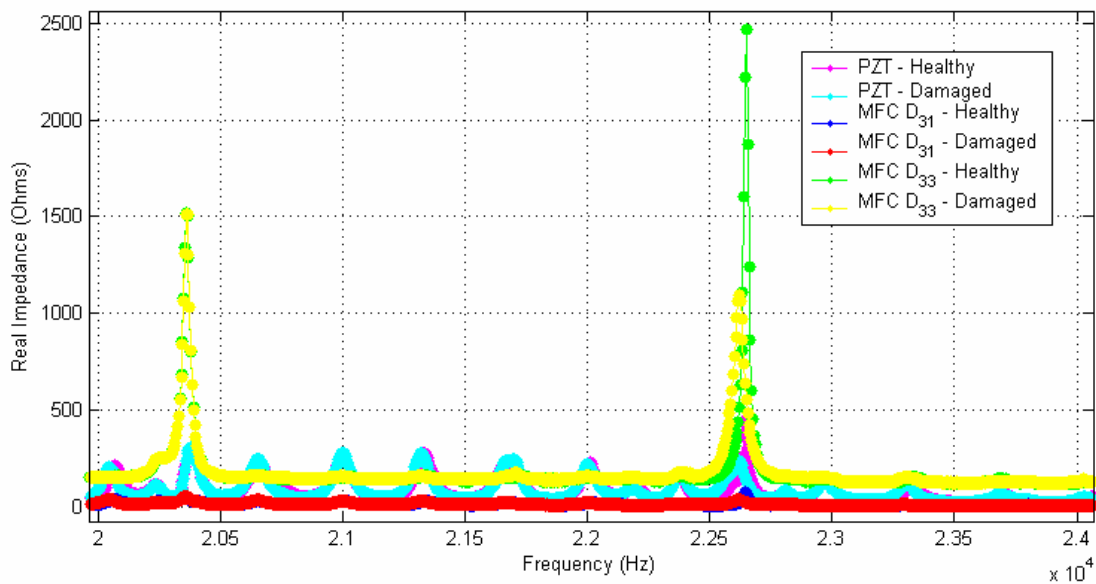


Figure 5.3.2: Sensitivity test results show the impedance response differences between PZT, MFC D₃₁, and MFC D₃₃.

Once the test frequencies were selected, impedance testing began. For each frequency range, 2000 Hz samples of 1 Hz resolution were recorded, and each impedance sweep was repeated 30 or more times. For the initial healthy baseline of the structure the data was collected over a 7 day period to quantify the ambient changes in the system. HCl acid was used to accelerate the pitting of the beam for damage #1 & #2. Damage #1 was at the midpoint between the sensors covering a surface area of 2.3% of the beam and pitted to 10.7 microns to simulate light corrosion. Damage #2 consisted of 2.3% surface coverage of 17.9 micron pitting as measured with a surface profilometer. Each instance of damage was measured with all of the operable piezoelectric sensors.

During testing, the fragile copper electrodes on both PZT sensors were torn by the weight of the sensor wires, and this caused a shift in the impedance measurement that prevented the sensor from being used to detect damage #1 and/or #2. In order to prove PZT can indeed detect corrosion damage opposite the sensor, the test procedure was modified slightly. The experiment was modified by corroding the opposite side of the beam used for pit depth testing seen in Chapter 3. The same experimental procedure was used with one minor change. For opposite side corrosion detection using PZT, the corrosion damage was placed 25 cm from the sensor to accommodate the smaller test structure. Also, the high frequency (100-208 kHz) detection results for damage #1 were not productive enough to justify high frequency detection attempts of damage #2, so there are no high frequency results for damage #2. The high frequency results will be discussed more in a later section.

5.3.2 Experimental Results MFC and PZT Same-Side Corrosion Detection

The single experiment described above was designed to prove the same-side and through-structure corrosion detection abilities of PZT A4, MFC D₃₁, and MFC D₃₃. Damage #1 (2.3% surface coverage of 17.9 μm pit depth corrosion) was placed on side #2 of the structure. The MFC D₃₃ and PZT #2 were on the mounted on the same side as the corrosion damage #1 and MFC D₃₁ and PZT #1 were located opposite corrosion damage. Damage #2 (2.3% surface coverage of 10.7 μm pit depth corrosion) was placed on side #1 of the structure. MFC D₃₃ and PZT #2 are located on the same side as damage #2, and MFC D₃₁ and PZT #1 are opposite damage #2.

For the purposes of the results discussion, same-side and through-structure corrosion detection will be broken down into tables for each of the three sensor types. For each sensor the multiple site damage (MSD) and single site damage (SSD) result are presented. MSD calculates all damage metrics relative to the healthy baseline #1, and the SSD method calculates damage metrics relative to previous baselines. Since MSD represents the highest corrosion detection standard by showing damage accumulation, only those results will be discussed. All damage metric plots depicting the damage will show same-side and through-structure detection results on a single plot.

MFC D₃₁, MFC D₃₃, and PZT A4 material were all successfully used to detect and distinguish light pre-crack surface corrosion at distances up to 50 cm from the sensor and on the same surface as the sensor. The MFC D₃₃ results in Table 5.3.1 show the low (3-72.5 kHz) and high (100-208 kHz) frequency detection results for 2.3% surface coverage of 17.9 μm corrosion

of damage #1. For the low frequency range the MFC D₃₃ self-sensing actuator can detect and distinguish the corrosion damage for 6 of the 6 test frequencies, but at higher frequencies the damage cannot be distinguished for any of the six test frequencies. PZT #1 could detect and distinguish damage #1 for all six low and high frequency tests as seen in Table 5.3.2. MFC D₃₁ could detect damage #2 (2.3% surface coverage of 10.7 μm surface corrosion) for 5 of the six low frequencies, and no data was taken for high frequency same-side corrosion detection for this sensor. The MFC D₃₁ results may be seen in Table 5.3.3. Figures 5.3.3, 5.3.4, and 5.3.5 show the damage metric plots for the three sensors at select frequencies. All impedance signatures and damage metric plots for the three sensors may be seen in Appendix D.

Table 5.3.1: Same side corrosion detection results for an MFC D₃₃.

MFC D ₃₃				
Frequency Ranges	MSD		SSD	
	Damage #1 – Same Side 2.3% coverage, 17.9 μm deep		Damage #1 – Same Side 2.3% coverage, 17.9 μm deep	
	Detected	Distinguished	Detected	Distinguished
Low Totals	6/6	6/6	6/6	6/6
High Totals	6/6	0/6	6/6	0/6
Total	12/12	6/12	12/12	6/12

Table 5.3.2: Same side corrosion detection results for PZT #1.

PZT #1				
Frequency Ranges	MSD		SSD	
	Damage #1 – Same Side 2.3% coverage, 17.9 μm deep		Damage #1 – Same Side 2.3% coverage, 17.9 μm deep	
	Detected	Distinguished	Detected	Distinguished
Low Totals	6/6	6/6	6/6	6/6
High Totals	6/6	6/6	6/6	6/6
Total	12/12	12/12	12/12	12/12

Table 5.3.3: Same side corrosion detection results for an MFC D₃₁.

MFC D ₃₁				
Frequency Ranges	MSD		SSD	
	Damage #2 – Same Side 2.3% coverage, 10.7 μm deep		Damage #2 – Same Side 2.3% coverage, 10.7 μm deep	
	Detected	Distinguished	Detected	Distinguished
Low Totals	6/6	5/6	6/6	6/6
High Totals	Not Tested	Not Tested	Not Tested	Not Tested
Total	6/6	5/6	6/6	6/6

5.3.3 Through-Structure Corrosion Detection Results for MFCs and PZT

All three self-sensing actuators were tested for through-structure corrosion detection, and all three could successfully detect and distinguish light pre-crack surface corrosion. Using MSD detection standards, MFC D₃₁ could distinguish corrosion damage #1 through the structure for 5 of the six low frequencies tested and for 1 of the 6 higher frequencies. The MFC D₃₁ results may be seen in Table 5.3.4. Through the structure, MFC D₃₃ could detect damage #2 for 4 of the 6 test frequencies, and the damage was distinguishable for 2 of the 6 low test frequencies. The MFC D₃₃ results may be found in Table 5.3.5. Due to the electrode damage of PZT #1 & #2, the through-corrosion detection test was performed on another beam. For PZT, through-structure detection of 2.3% surface coverage 14.5 μm pit depth corrosion 25 cm from the sensor was possible. For 6 of the 6 low frequencies test PZT could detect and distinguish corrosion through the structure as seen in Table 5.3.6. All of the detection results are presented using the MSD standard, and the results improve if the SSD standard is used. Figures 5.3.3, 5.3.4, and 5.3.6 show the damage metric plots for the three sensors at select frequencies. All impedance signatures and damage metric plots for the three sensors may be seen in Appendix D.

Table 5.3.4: Opposite side corrosion detection results for an MFC D₃₁.

MFC D ₃₁				
Frequency Ranges	MSD		SSD	
	Damage #1 – Opposite Side 2.3% coverage, 17.9 μm deep		Damage #1 – Opposite Side 2.3% coverage, 17.9 μm deep	
	Detected	Distinguished	Detected	Distinguished
Low Totals	6/6	5/6	6/6	6/6
High Totals	6/6	1/6	6/6	1/6
Total	12/12	6/12	12/12	7/12

Table 5.3.5: Opposite side corrosion detection results for an MFC D₃₃.

MFC D ₃₃				
Frequency Ranges	MSD		SSD	
	Damage #2 – Opposite Side 2.3% coverage, 10.7 μm deep		Damage #2 – Opposite Side 2.3% coverage, 10.7 μm deep	
	Detected	Distinguished	Detected	Distinguished
Low Totals	4/6	2/6	6/6	6/6
High Totals	Not Tested	Not Tested	Not Tested	Not Tested
Total	4/6	2/6	6/6	6/6

Table 5.3.6: Opposite side corrosion detection results for PZT.

PZT				
Frequency Ranges	MSD		SSD	
	Damage #1 – Opposite Side 2.3% coverage, 14.5 μm deep		Damage #1 – Opposite Side 2.3% coverage, 14.5 μm deep	
	Detected	Distinguished	Detected	Distinguished
Low Totals	6/6	6/6	6/6	6/6
High Totals	Not Tested	Not Tested	Not Tested	Not Tested
Total	6/6	6/6	6/6	6/6

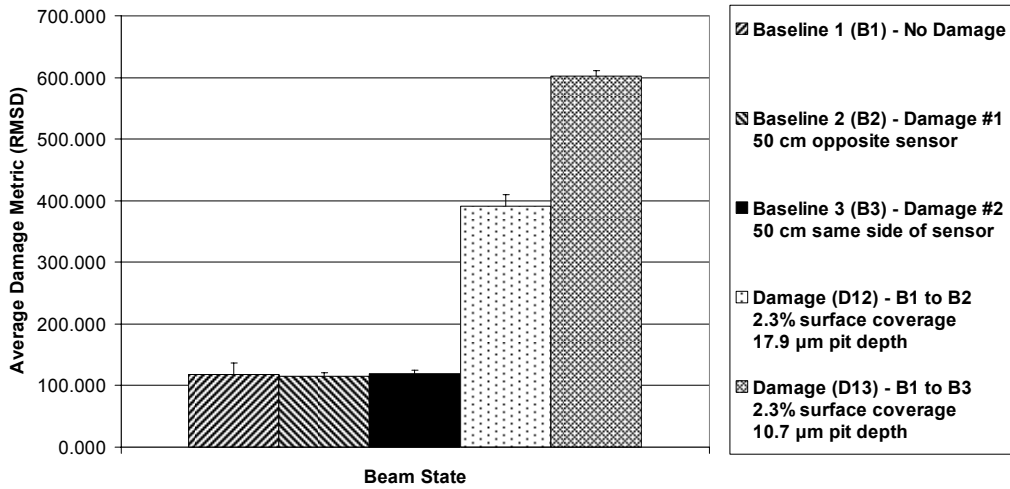


Figure 5.3.3: MFC D₃₁ can detect and distinguish both levels of damage at 3-5 kHz.

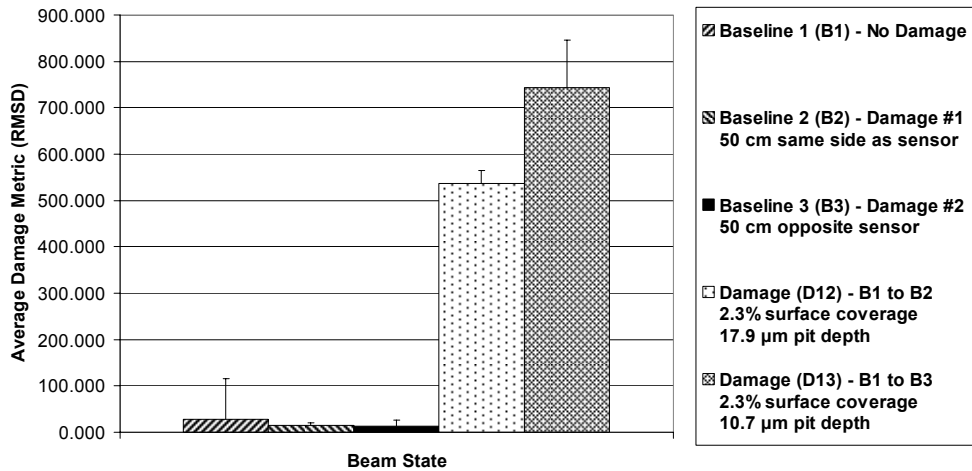


Figure 5.3.4: MFC D₃₃ can detect and distinguish both levels of damage at 33-35 kHz.

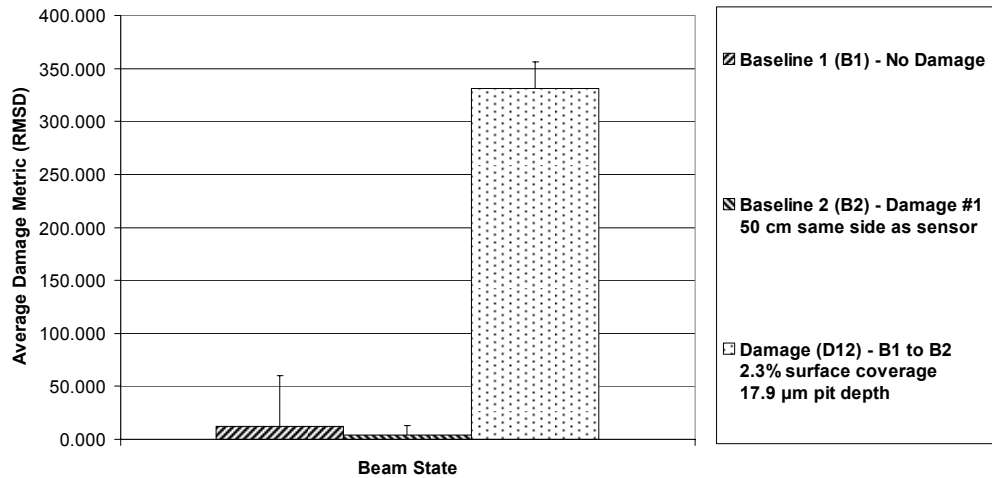


Figure 5.3.5: PZT #1 can detect and distinguish same-side corrosion damage at 70.5-72.5 kHz.

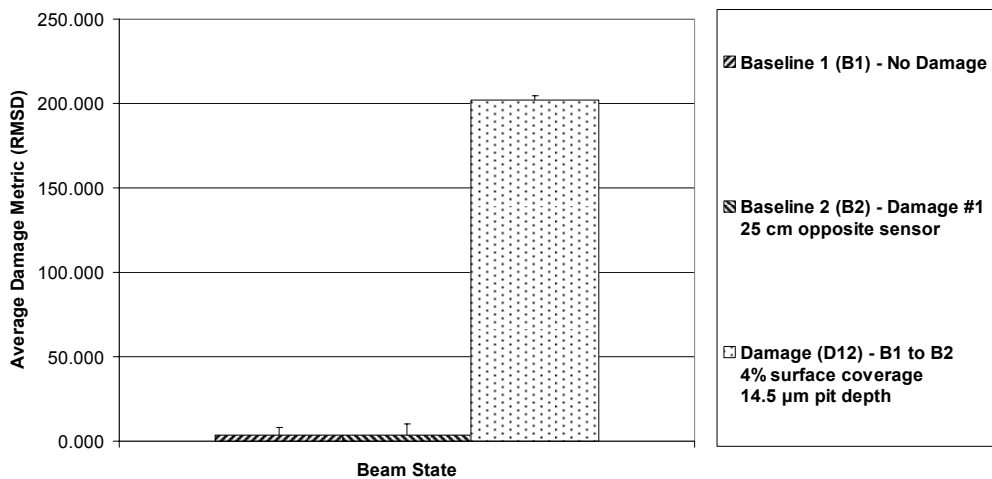


Figure 5.3.6: PZT can detect and distinguish through-structure corrosion damage at 50-52 kHz.

5.3.4 High Frequency Detection Results

As noted earlier, the high frequency tests were not continued after damage #1 because of the MFCs inability to detect the corrosion at high frequencies. On the other hand, the same-side PZT test (using PZT #1 before the copper electrode was torn) indicated corrosion detection for all six high frequencies between 100-208 kHz. Reviewing the high frequency impedance signatures helps to explain this result. Figure 5.3.7 show the healthy and damaged impedance signatures for PZT #1. Figure 5.3.8 and 5.3.9 show the 206-208 kHz impedance measurements for the two MFCs. The difference in the high frequency detection results can be seen in the healthy baseline shown in blue. The initial baseline data collected over 7 days shows some ambient variation for

the PZT, but the variation is not nearly as great as the initial baselines for the MFCs. The variance in the healthy baseline increases the error and makes it more difficult to distinguish the damage. The exact cause of the high frequency variation is not known, but could be related to the bond condition. However, it can be assumed that the cause must be frequency dependant because it is not seen in the lower frequency impedance signature. All impedance signatures may be seen with corresponding damage metric plots in Appendix D.

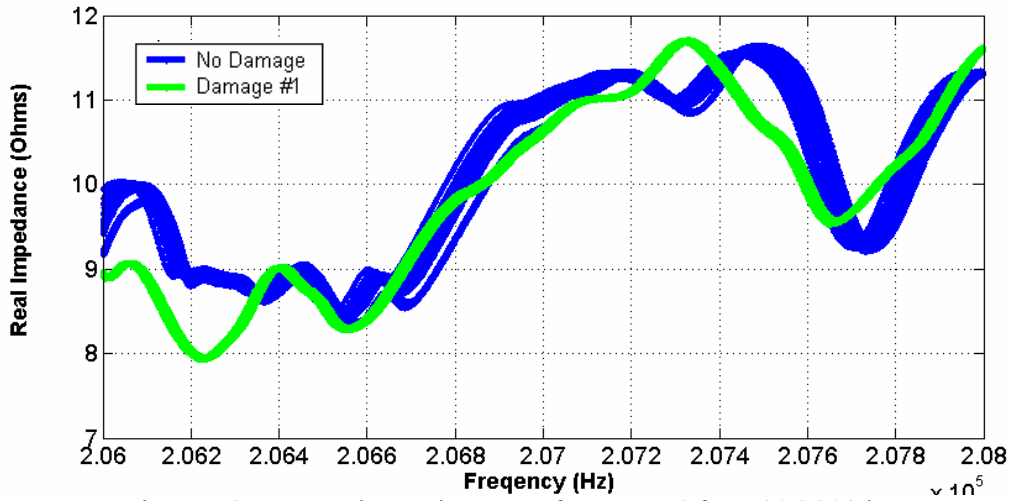


Figure 5.3.7: Impedance signatures for PZT A4 from 206-208 kHz.

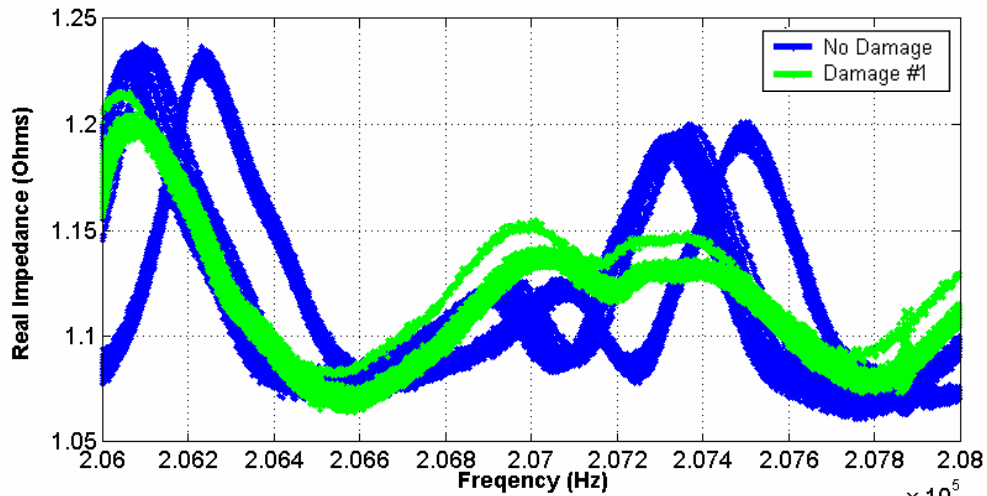


Figure 5.3.8: Impedance signatures for MFC D₃₁ from 206-208 kHz.

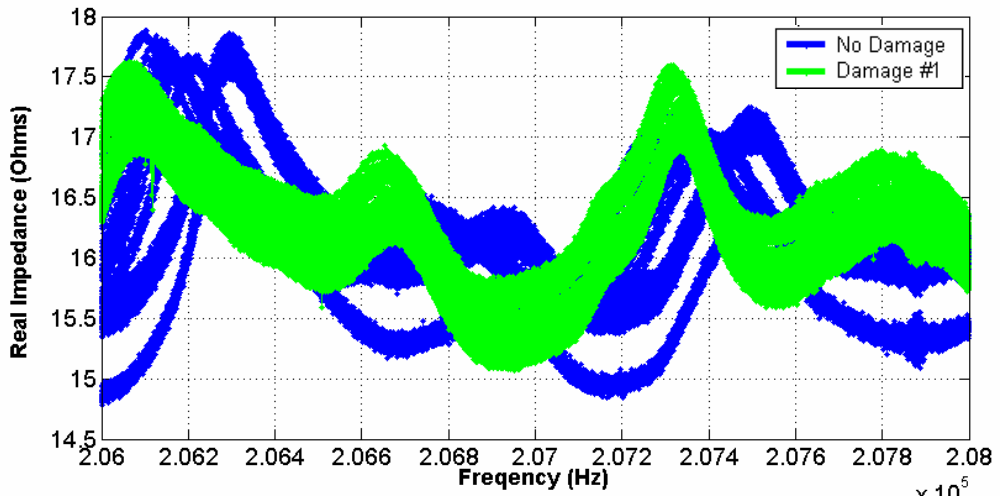


Figure 5.3.9: Impedance signatures for MFC D₃₃ from 206-208 kHz.

Chapter 6

Conclusions

This thesis has investigated the use of the impedance method for structural health monitoring to detect pre-crack surface corrosion. The impedance method uses the electromagnetic coupling of piezoelectric self-sensing actuators such as PZT and MFCs to measure high frequency structural responses in order to detect, locate, and quantify damage. In the past, the impedance method has been successfully used to detect structural damage such as cracks, loose bolts, and gear wear, but the concept has not been extended to structural corrosion which tends to reduce fatigue life and accelerate the mean time till crack formation. The scope of this work was to experimentally determine how well the impedance method can detect and quantify corrosion on structures. This chapter will provide a brief overview of the experimental results and discuss the contributions made. Finally, this chapter will end with a discussion of the future work to be conducted in this field.

6.1 Brief Summary of Thesis

The first portion of this thesis was devoted to understanding the scope of the problem corrosion presents to structures in terms of business cost and structural challenges. The commercial and military airline industries were used as examples to show the need and purpose for developing better corrosion detection techniques. The major types of corrosion were identified, and the effect each has on structures was outlined. Some routine and between-service corrosion detection methods already exist, so the advantages and disadvantages of those methods were presented. Smart materials like PZT and MFCs experience electromagnetic coupling when

bonded to structures, and the impedance method utilizes the coupling to measure the mechanical impedance of the structure. As the structure becomes damaged, the mechanical impedance of the system shifts, and damage metrics allow the change in the structural response to be quantified. Key findings from past impedance method research were presented to show the benefits of this damage detection method, and to show how the method could be useful for corrosion detection.

The second portion of this thesis was devoted to using the impedance method to detect “light” pre-crack surface corrosion on beam-like structures. Since corrosion is a small surface defect, it is necessary to manage the variability in the system so structural corrosion damage can be distinguished from ambient noise. Methods for managing variability, sensitivity testing, and frequency selection as each pertains to impedance-based corrosion detection were outlined. An aluminum beam was instrumented and corroded with 1.4% surface coverage of light pre-crack corrosion at 5 locations extending to 150 cm from the PZT sensor. All five levels of corrosion damage could be detected and distinguished within 95% confidence intervals using the impedance method.

Next, since the impedance method can detect corrosion, it is necessary to determine how well the method can locate corrosion, track corrosion pit depths, and monitor corrosion surface coverage changes. Three tests were conducted to measure how well the impedance method could perform each of those tasks. Experimentally it was found that the impedance method tracks corrosion pit depth changes best. This implies the impedance method could be correlated with maintenance records to track corrosion pit depth changes and perhaps even be used in a predictive fashion. The impedance method did not perform as well in the corrosion location and surface coverage tests, so it may be necessary to combine the method with other NDE techniques like Lamb wave detection to locate and quantify the surface corrosion surface coverage.

Many structural surfaces are constructed from plates instead of beams, so it is useful to extend the impedance-based corrosion detection results to plate-like structures. The structural response of plates is more complex than that of beams, and this affects how well damage metrics can quantify corrosion damage on plates. Experimentally it was shown that 1% and 0.25% surface coverage of “light to moderate” corrosion damage could be identified at distances up to 125 cm from PZT sensors using the impedance method. Multiple sensors were used in an array to detect corrosion damage on the aluminum plate. Improved sensitivity tests and frequency selection methods were also presented in this section.

Finally, corrosion detection using the impedance method relies heavily on the piezoelectric sensors bonded to the structure. The exact pattern of PZT and MFC sensor

corrosion could not be identified because some of the results are contradictory. However, the contradictory results demonstrate the importance of isolating and protecting sensors from harsh corrosive environments. Recommendations for sensor selection and protection were made. MFC D_{31} and D_{33} actuators were experimentally shown to detect light pre-crack surface corrosion at distances up to 50 cm from the sensor in beam-like structures. Another way of avoiding direct sensor corrosion is to locate the impedance sensors on a side of the structure not exposed to corrosion. Through-structure detection limits the sensor exposure to the corrosive environment, but it requires the sensor to detect the corrosion through the structure. Since the impedance method detects damage based on the structural response it should be possible to detect corrosion through the structure. PZT, MFC D_{31} , and MFC D_{33} sensors were all shown to detect “light” pre-crack corrosion through the structure thus avoiding direct sensor corrosion.

6.2 Contributions

A need for new corrosion detection tools and methods exists because corrosion can significantly degrade the fatigue life of structures and is difficult to detect. When corrosion is combined with static and dynamic stresses, corrosion pits serve as nucleation sites for surface and through-cracks. Presently, most corrosion detection techniques can only detect damage at routine service intervals, and the process is expensive and time consuming. There is a need for corrosion detection methods which can be autonomously and remotely implemented between scheduled service intervals to alert operators of immediate structural problems and to speed detection at routine service intervals. Piezoelectric materials are useful between-service damage detection tools because they can be used actively or passively as actuators, sensors, or self-sensing actuators. A single piezoelectric sensor can be configured to remotely serve as an accelerometer, strain gage, load monitor, impact detector, acoustic emission sensor, Lamb wave creation and detection, and structural response measurement through the impedance method. Since piezoelectric sensors are so versatile it would be useful to prove they can successfully detect structural corrosion.

The impedance method has been utilized to detect a wide range of structural defects; however, the impedance method has never been shown to detect corrosion. Some researchers have speculated impedance-based corrosion detection was possible, but the research was not extended to prove the concept. The impedance method is well suited to for corrosion detection because the method is very sensitive to structural changes, has a localized sensing area, and is insensitive to loading, boundary conditions, and operational vibrations. For the first time, the impedance

method was shown to detect the earliest and lightest forms of surface corrosion on aluminum beams and plates for sensing areas up to 150 cm. This is a very important result because corrosion pitting leads to cracking, so detecting corrosion on structures can serve as an early warning sign of impending cracks and crack propagation.

Additionally, the impedance method was shown to quantify corrosion pit depth, location, and surface coverage changes. The impedance method performed very well in tracking corrosion pit depth changes in structures. Since corrosion pit depth is a key random variable in determining the mean time till crack formation, this is an important result. If corrosion detection and pit depth tracking information were combined with routine maintenance records it would be possible in some instances to predict when the corrosion pitting would become a problem for the structure. This would eliminate unnecessary corrosion repairs which are performed under current “find and fix” maintenance approaches. Impedance-based structural health monitoring to detect corrosion increases our understanding of how corrosion forms and progresses giving engineers and maintenance personnel better ways of predicting and controlling corrosion on structures.

One problem with corrosion detection is the fact that corrosion can directly attack SHM sensors used to monitor the corrosion. The direct corrosion of sensors or structural is problematic because it becomes necessary to troubleshoot sensors to determine the health of the sensor in order to eliminate false positives. Unlike some passive sensors, impedance based sensors have the ability to perform self-diagnostics to determine sensor health. However, the patterns of sensor corrosion must be understood well enough to facilitate self-diagnosis. PZT and MFC sensors were shown to be insensitive to 5 mol HCl so long as the corrosive fluid was applied to the electrode surface. However, other evidence was presented showing time dependant impedance shifts in corrosion measurements when PZT was exposed to corrosion products. These mixed results demonstrate a need to protect sensor and the structural bond layer for impedance-based corrosion detection. Kapton protected MFC D_{33} and D_{31} actuators are more robust to sensor corrosion, and were shown to detect light pre-crack surface corrosion in beams. In an effort to avoid corrosion detection altogether through-structure corrosion detection was proven for PZT, MFC D_{33} , and MFC D_{31} actuators. Through-structure detection is advantageous because it avoids sensor corrosion, and other NDE techniques like Lamb waves are not capable of through-structure detection.

6.3 Future Work

The impedance method has been proven for the detection and quantification of pre-crack surface corrosion, but there is still much to be accomplished in this field. To be truly useful the impedance method must be integrated into stand-alone damage detection units which can be placed in remote parts of real-world structures and communicate with other remote devices to collect and process structural data to make real-time damage prognosis possible. Much work has already been accomplished on these types of devices, but most of the algorithms are configured to detect cracks and loose bolts. Hence, it is necessary to integrate corrosion specific detection and monitoring algorithms into these devices, and train the devices to detect patterns of corrosion sensor degradation. Once the devices are commercially available, they need to be tested on real-world structures to show their value and robustness in between-service damage detection.

Secondly, no single corrosion detection tool can detect and quantify all key corrosion variables equally well. The stand-alone detection devices need to be set up to use multiple detection tools and methods to quantify corrosion damage. For example, the impedance method excels at corrosion detection and pit depth tracking, but it not as useful for corrosion location and surface coverage tracking. Lamb waves have been shown to locate corrosion and could likely quantify surface coverage, so the impedance method should be used in conjunction with Lamb wave corrosion detection methods. When impedance, Lamb wave, PH, ion concentration, and humidity sensor between-service data is fused with routine maintenance data it will be possible to understand and predict the effect corrosion has on structures. In the future, utilizing many of the tools and techniques described in this thesis structural corrosion damage should be more easily understood and predicted.

Bibliography

[1] www.corrosion-doctors.org

[2] www.piezo.com

[3] “Agilent Technologies Impedance Measurement”, December 2003

[4] Bellinger, N.C., Komorowski, J.P., Gould, R.W., 1998. “Damage Tolerance Implications of Corrosion Pillowing on Fuselage Lap Joints,” *Journal of Aircraft*, Vol. 35, No. 3, May-June 1998.

[5] Bellinger, N.C. et.al., 2002. “Preliminary Study into the Effect of Exfoliation Corrosion on Aircraft Structural Integrity,” 6th Joint FAA/DoD/NASA Aging Aircraft Conference, 2002.

[6] Beom, J., Chang, F.K., 2002. “Smart Patches for Monitoring Crack Growth in Aircraft Structures,” American Institute of Aeronautics and Astronautics, AIAA-2003-1544.

[7] Chandrasekaran, V., Taylor, A., Yoon, Y., Hoepfner, D., “Quantification and Correlation of Pit Parameters to “Small” Fatigue Cracks,”

[8] Cottis, R.A., 1982. “Stress Corrosion Cracking,” Corrosion and Protection Centre, UMIST under contract from NPL for the Department of Trade and Industry.

[9] Cottis, R.A., Al-Awadhi, M.A.A., Al-Mazeedi, H., Turgoose, S., 2001. “Measures for the Detection of Localized Corrosion with Electrochemical Noise,” *Electrochimica Acta* 46, 2001, pp. 3665-3674.

- [10] Elliot, W.R., et. al., 1995. "Maintaining Air Force Structures in Service," American Institute of Aeronautics and Astronautics, AIAA-21995-1544-CP.
- [11] Ford, T. 1999. "Corrosion Detection and Control," Aircraft Engineering and Aerospace Technology, Vol. 71, Number 3, 1999, pp. 249-254.
- [12] Fildes, J.M., Chen, P., Zhan, X., "Application of Electrochemical Impedance Spectroscopy, Color Visible Imaging, and Infrared Imaging for Non-Destructive Evaluation of Anti-Corrosion Coatings."
- [13] Giurgiutiu, V. 2003. "Multifunctional Vehicle Structural Health Monitoring Opportunities With Piezoelectric Wafer Active Sensors," American Institute of Aeronautics and Astronautics, AIAA-2003-1568.
- [14] Groner, D.J. 1997. "US Air Force Aging Aircraft Corrosion," American Institute of Aeronautics and Astronautics, AIAA-1997-1364.
- [15] Hansen, J., 2004. "The Eddy Current Inspection Method," Insight, Vol. 46, No 5, pp. 279-281, May 2004.
- [16] Hixson, E.L., 2002. "Chapter 10 – Mechanical Impedance" Harris' Shock and Vibration Handbook, 5th Addition.
- [17] Hoepfner, D.W., et al., 1995. "Corrosion and Fretting as Critical Aviation Safety Issues: Case Studies, Facts, and Figures from US Aircraft Accidents and Incidents," International Conference on Aeronautical Fatigue, May, 1995.
- [18] Kesslerand, S.S., Spearing, M. S., 2002. "In-Situ Sensor-Based Damage Detection of Composite Materials for Structural Health Monitoring," American Institute of Aeronautics and Astronautics, AIAA-2002-1545.
- [19] Kinzie, R., 2001. "USAF Cost of Corrosion Maintenance," UASF Corrosion Prevention & Control Office.

- [20] Koch, G.H., 2001. "Corrosion Cost and Preventative Strategies in the United States – Appendix P – Aircraft," Federal Highway Administration, FHWA-RD-01-156.
- [21] Kwun, H., Light, G.M., Kim, S., Peterson, R.H., Spinks, R.L., 2002. "Permanently Installable, Active Guided-Wave Sensor for Structural Health Monitoring," First European Workshop on Structural Health Monitoring, SHM 2002-063.
- [22] Lalande, F., Childs, B., Chaudhry, Z., Rogers, C.A., 1996. "High Frequency Impedance Analysis for NDE of Complex Precision Parts," Conference on Smart Structures and Materials, Feb 26-29, San Diego, CA, SPIE Publishing, Bellingham, AA, Proceedings of SPIE, Vol. 2717, 237-245.
- [23] Lindgren, E., et. al., "Enhanced Nondestructive Evaluation Techniques for the C-130 Center Wing"
- [24] Macdonald, D.D., Engelhardt, G., 2003. "Deterministic Prediction of Localized Corrosion Damage – A Reflective Review of Critical Issues," The Journal of Corrosion Science and Engineering, Vol. 6, Paper C066 ????
- [25] Marceau, J.A., Mohaghegh, M., 1992. "Design for Corrosion Prevention," American Institute of Aeronautics and Astronautics, AIAA-92-1127.
- [26] Marsh, J., 1999. "Using Electrical Impedance Spectroscopy (EIS) to Support Conventional Artificial Perspiration Testing," The Journal of Corrosion Science and Engineering, Vol. 2, Paper 25.
- [27] Mohaghegh, M., 2004. "Evolution of Structures Design Philosophy and Criteria," American Institute of Aeronautics and Astronautics, AIAA 2004-1785.
- [28] Park, G., Sohn, H., Farrar, C., Inman, D., 2003. "Overview of Piezoelectric Impedance-Based Health Monitoring and Path Forward," Shock and Vibration Digest, Vol. 35, No. 6, November 2003, pp. 451-463.

- [29] Park, G., Cudney, H., Inman, D.J., 2000. "An Integrated Health Monitoring Technique Using Structural Impedance Sensors," *Journal of Intelligent Material Systems and Structures*, Vol. 11-June 2000, pp. 448-455.
- [30] Park, G., Kabeya, K., Cudney, H., Inman, D., 1999. "Impedance-Based Structural Health Monitoring for Temperature Varying Applications," *JSME, Series A*, Vol. 42, No. 2, 1999.
- [31] Park, G., Kabeya, K., Cudney, H., Inman, D., 1998. "Removing Effects of Temperature Changes from Piezoelectric Impedance-Based Qualitative Health Monitoring," *SPIE*, v.3330, pp. 103-114, March 1998, San Diego, CA.
- [32] Park, G., Cudney, H., Inman, D., 1999. "Impedance-based Health Monitoring for Civil Structures," 2nd International Workshop on Structural Health Monitoring, pp. 523-532, 1999, Stanford, CA.
- [33] Park, G., Cudney, H., Inman, D.J., 2001. "Feasibility of Using Impedance-Based Damage Assessment for Pipeline Systems," *Earthquake Engineering and Structural Dynamics Journal* , Vol. 30, No. 10, 1463-1474.
- [34] Pearis, D.M., Park, G., Inman, D.J. 2004. "Improving the Accessibility of the Impedance-based Structural Health Monitoring Method," *Journal of Intelligent Material Systems and Structures*, Vol. 15-February 2004, pp.129-139.
- [35] Smith, H., Perez, R., Sankaran, K.K., 2001. "The Effects of Corrosion on Fatigue Life – A Non-deterministic Approach," *American Institute of Aeronautics and Astronautics*, AIAA-2001-1376
- [36] Sodano, H.A., Park, G., Inman, D. J., 2003. "An investigation into the performance of macro-fiber composites for sensing and structural vibration applications," *Mechanical Systems and Signal Processing*, Vol. 18, pp. 683-697, 2004.
- [37] "Technical Bulletin – Corrosion Prevention and Detection" Department of the Navy, 2001.

[38] Trego, A., Smith, D. 2002. "Battery Operated Health Monitoring System," Fifth Joint DoD/FAA/NASA Conference on Aging Aircraft Proceedings, San Francisco, CA. September 2002.

[39] Tuegel, E.J. "Correlation of Holistic Structural Assessment Methods With Corrosion-Fatigue Experiments," Air Force Research Laboratory.

[40] Virmani, Y., 2001. "Corrosion Cost and Preventative Strategies in the United States," Federal Highway Administration, FHWA-RD-01-156.

[41] Wang, X.D., Huang, G.L., 2004. "Study of Elastic Wave Propagation Induced by Piezoelectric Actuators for Crack Detection," International Journal of Fracture, Vol. 126, 2004, pp. 287-306.

[42] Wei, P.W., Harlow, D.G., 1994. "Probability Approach for Prediction of Corrosion and Corrosion Fatigue Life," American Institute of Aeronautics and Astronautics, AIAA, Vol. 32, No. 10, October 1994.

[43] Wei, P.W., Harlow, D.G., 2002. "Corrosion Enhanced Fatigue and MSD," American Institute of Aeronautics and Astronautics, AIAA-2002-1398.

[44] Whaley, P.W. "Corrosion Damage Tolerance Methodology For C/KC-135 Fuselage Structure," ARINC Incorporated, Oklahoma City, OK, USA.

[45] Whaley, P.W., 1998. "A Probabilistic Framework for the Analysis of Corrosion Damage in Aging Aircraft," American Institute of Aeronautics and Astronautics, AIAA-1998-1936, pp. 1908-1918.

[46] Zagrai, A.N., Giurgiutiu, V., 2002. "Electro-Mechanical Impedance Method for Crack Detection in Thin Plates," Journal of Intelligent Material Systems and Structures, Vol. 12-October 2002, pp. 709-718.

[47] Zekri, L., Zerki, N., Clerc, J.P., 2004. "Modeling of Impedance Spectroscopy of Composites by Electrical Networks," Journal of Physics D: Applied Physics, Vol. 37, 2004, pp. 535-539.

Appendix A

Beam Corrosion Detection Plots and Figures

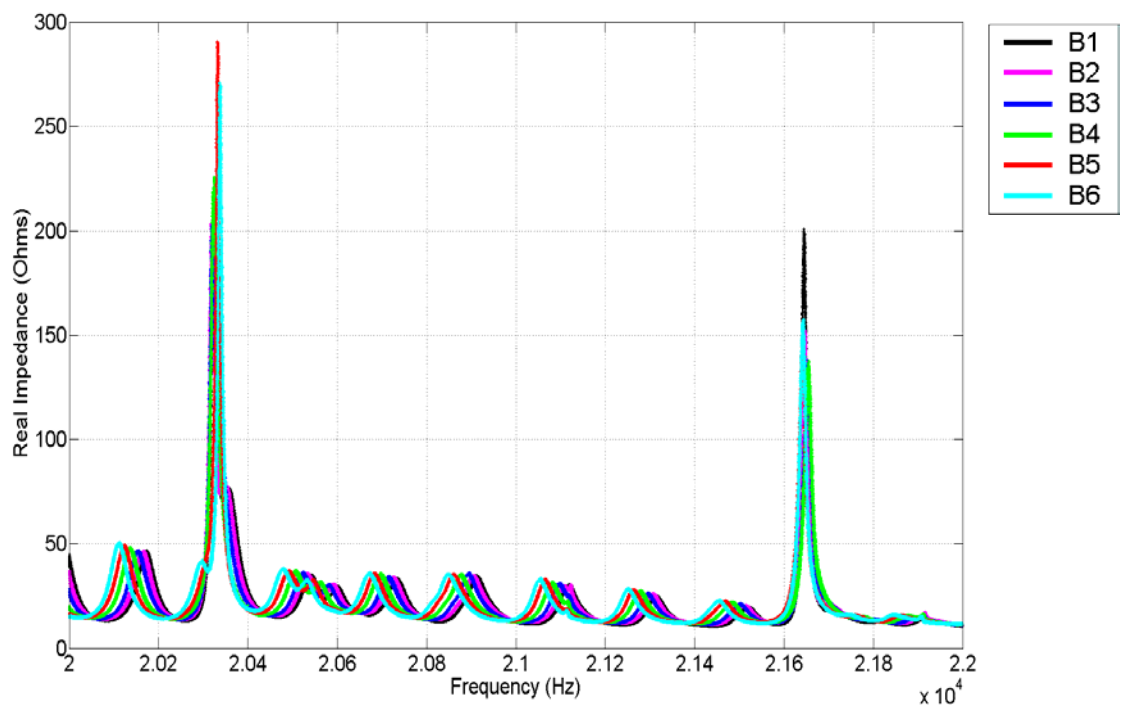


Figure A.1: Impedance signatures for beam corrosion damage from 20-20 kHz.

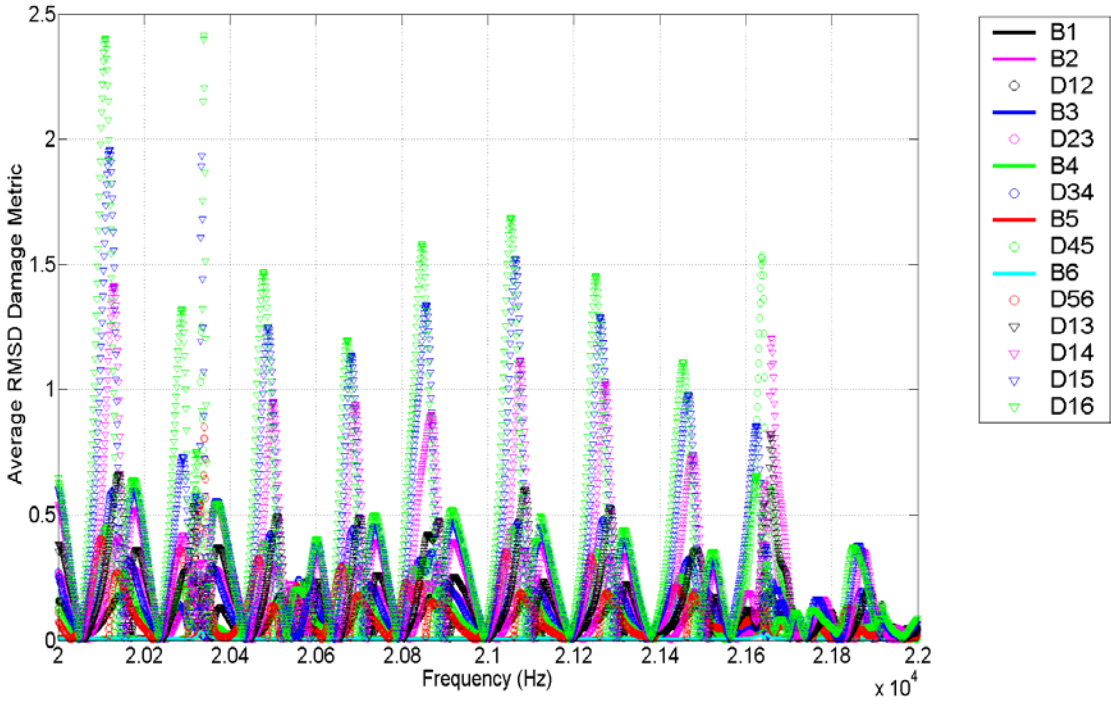


Figure A.2: Average damage metrics for beam corrosion damage from 20-20 kHz.

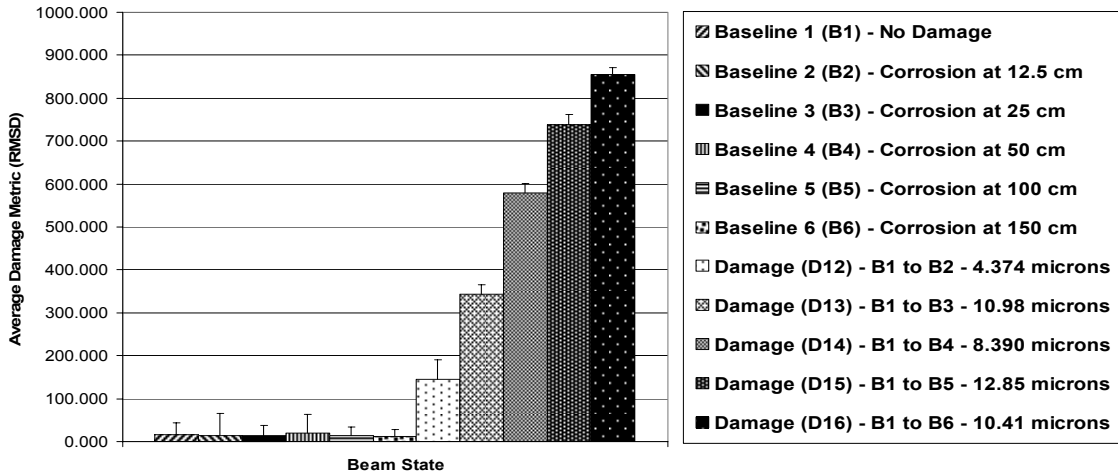


Figure A.3: Corrosion damage plots relative to baseline #1 from 20-20 kHz.

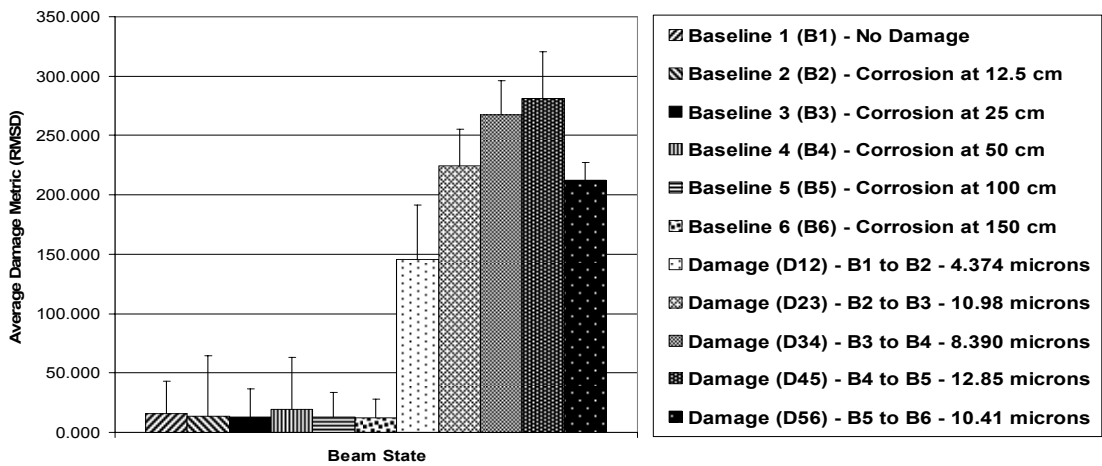


Figure A.4: Corrosion damage plots relative to previous baselines from 20-20 kHz.

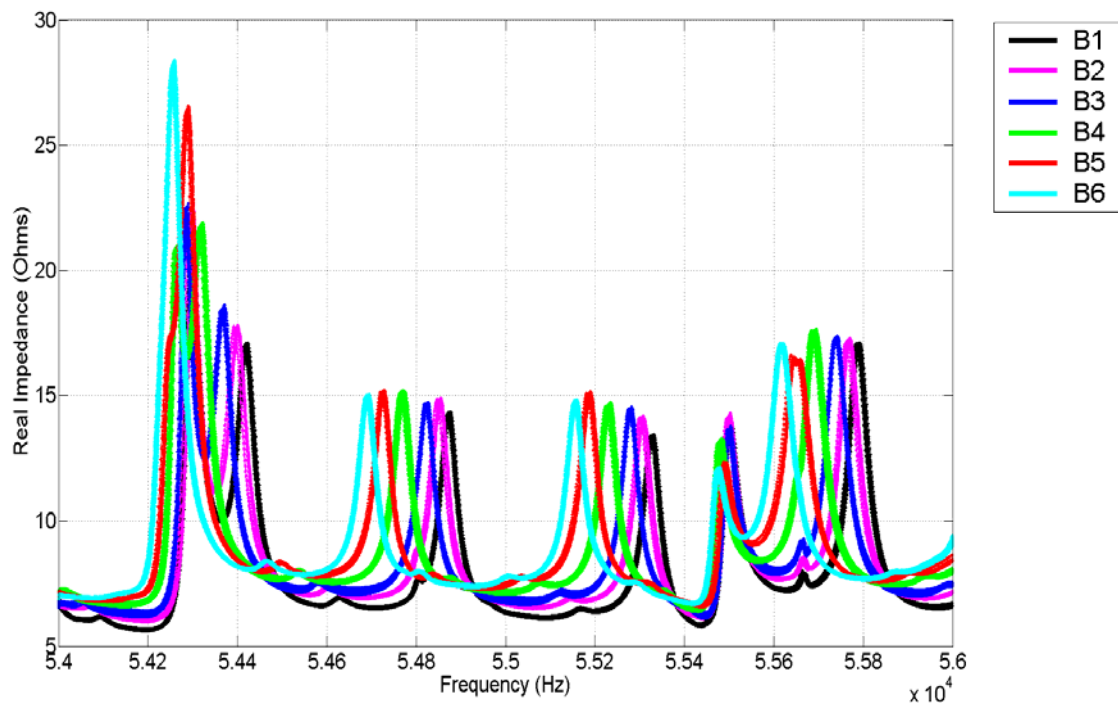


Figure A.5: Impedance signatures for beam corrosion damage from 54-56 kHz.

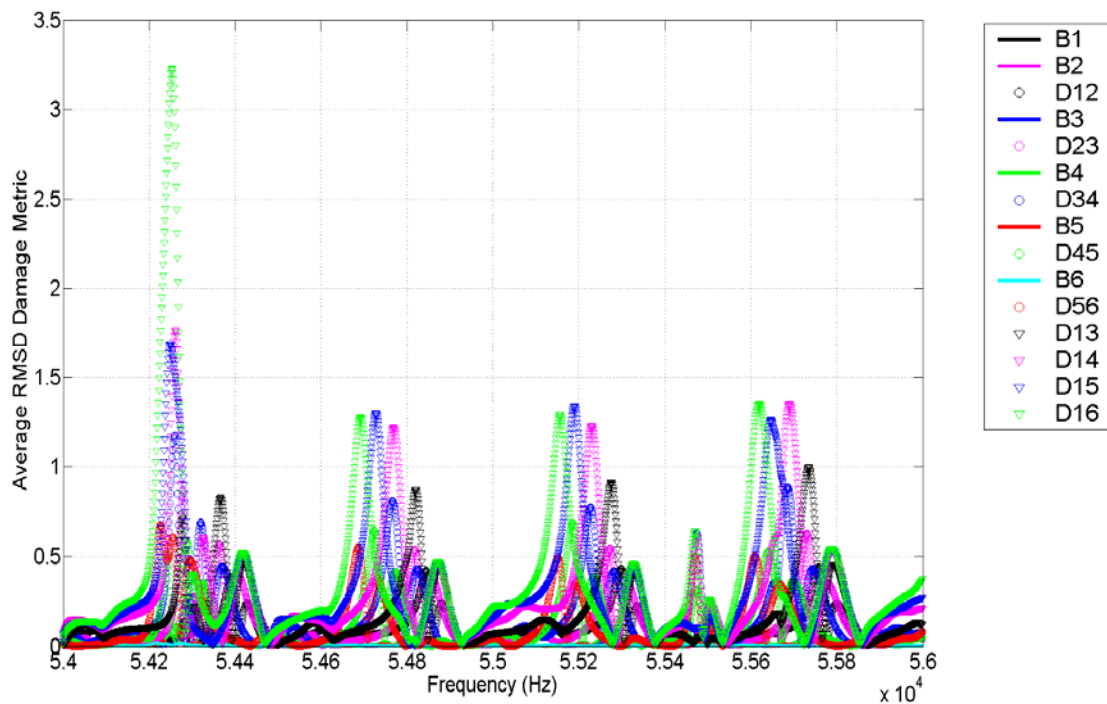


Figure A.6: Average damage metrics for beam corrosion damage from 54-56 kHz.

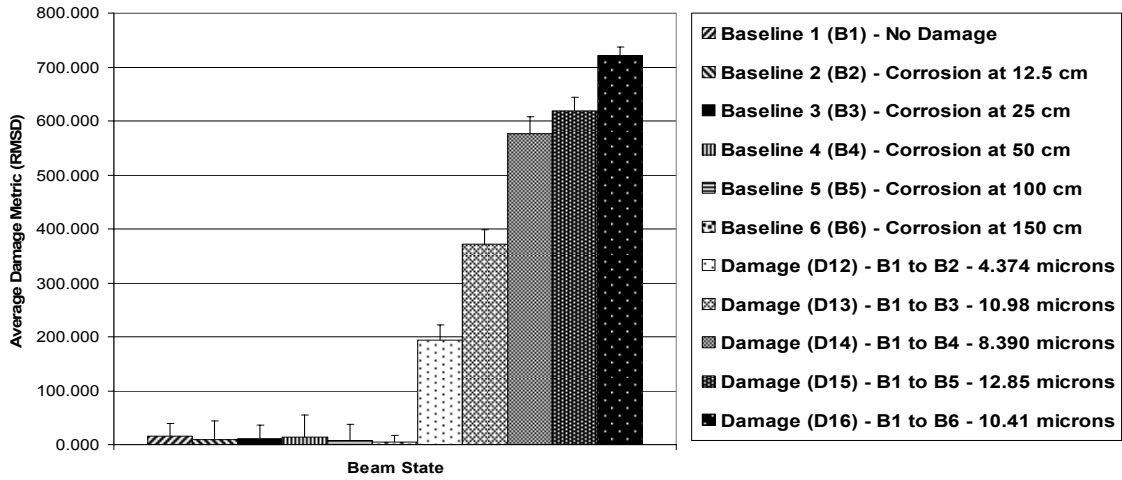


Figure A.7: Corrosion damage plots relative to baseline #1 from 54-56 kHz.

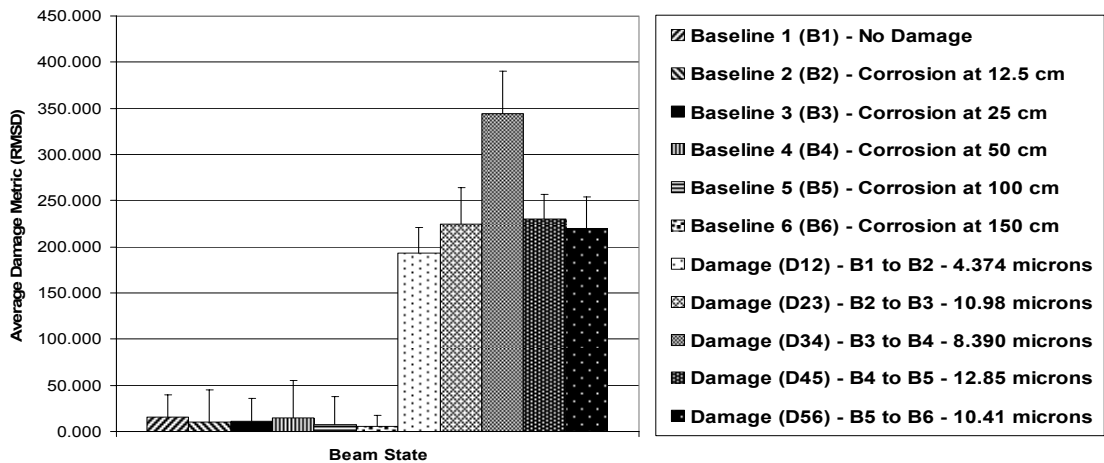


Figure A.8: Corrosion damage plots relative to previous baselines from 54-56 kHz.

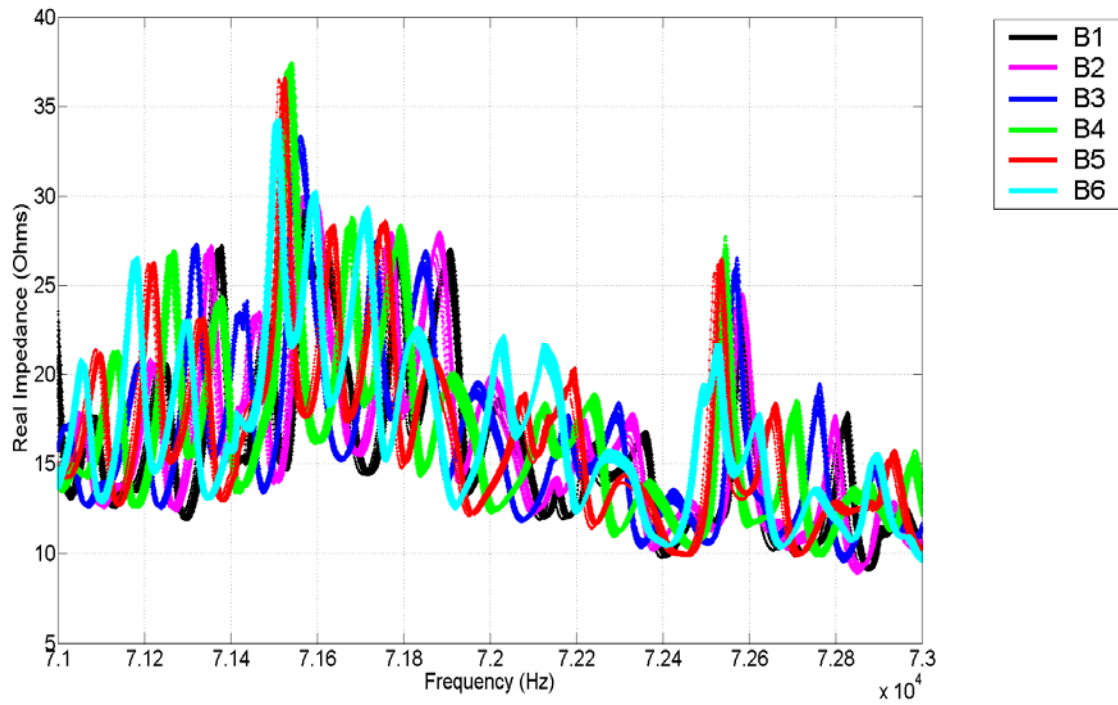


Figure A.9: Impedance signatures for beam corrosion damage from 71-73 kHz.

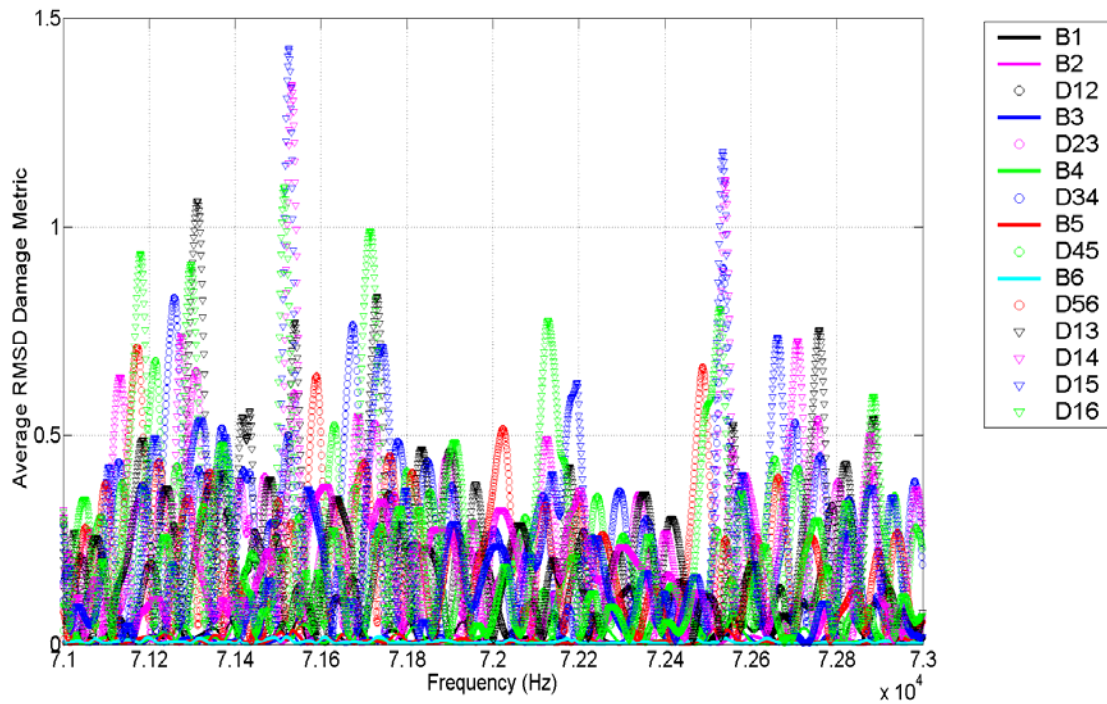


Figure A.10: Average damage metrics for beam corrosion damage from 71-73 kHz.

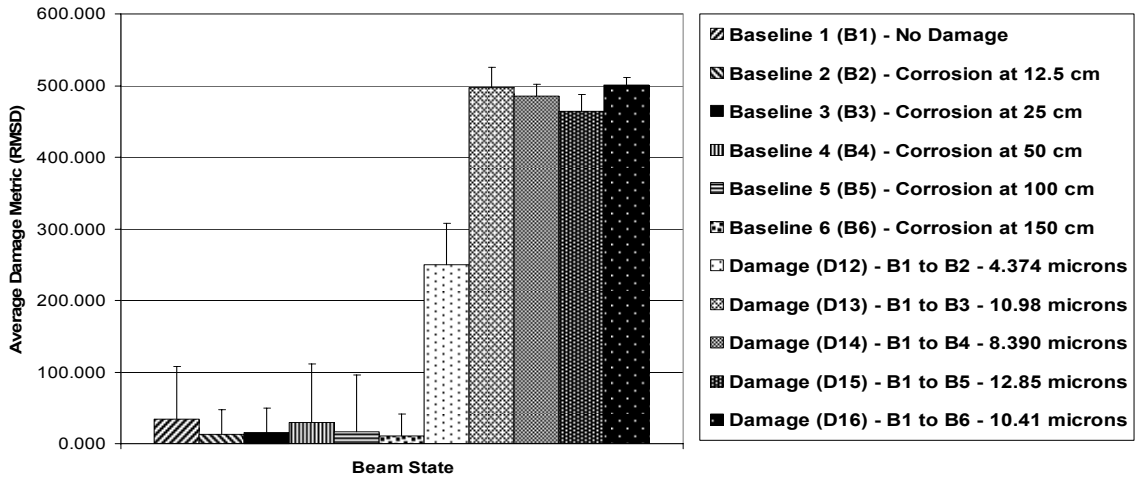


Figure A.11: Corrosion damage plots relative to baseline #1 from 71-73 kHz.

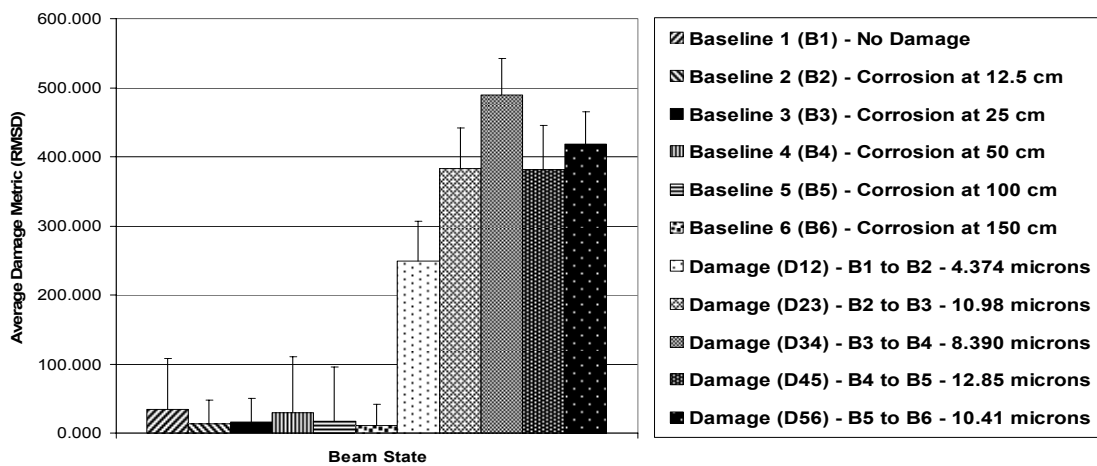


Figure A.12: Corrosion damage plots relative to previous baselines from 71-73 kHz.

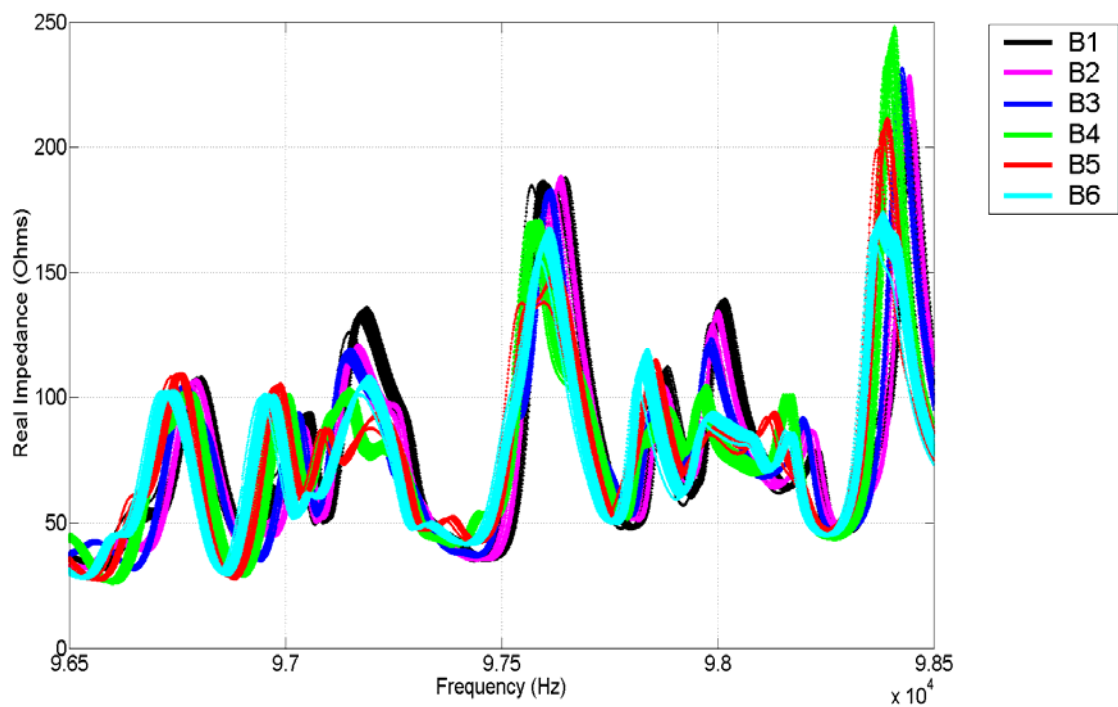


Figure A.13: Impedance signatures for beam corrosion damage from 96.5-98.5 kHz.

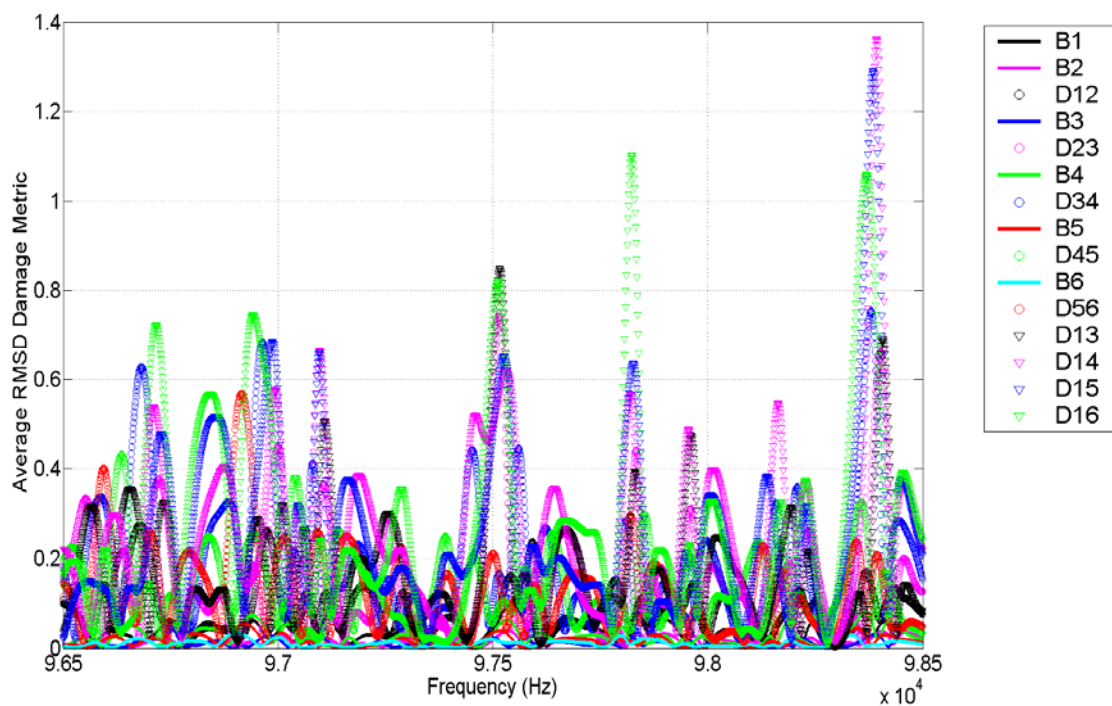


Figure A.14: Average damage metrics for beam corrosion damage from 96.5-98.5 kHz.

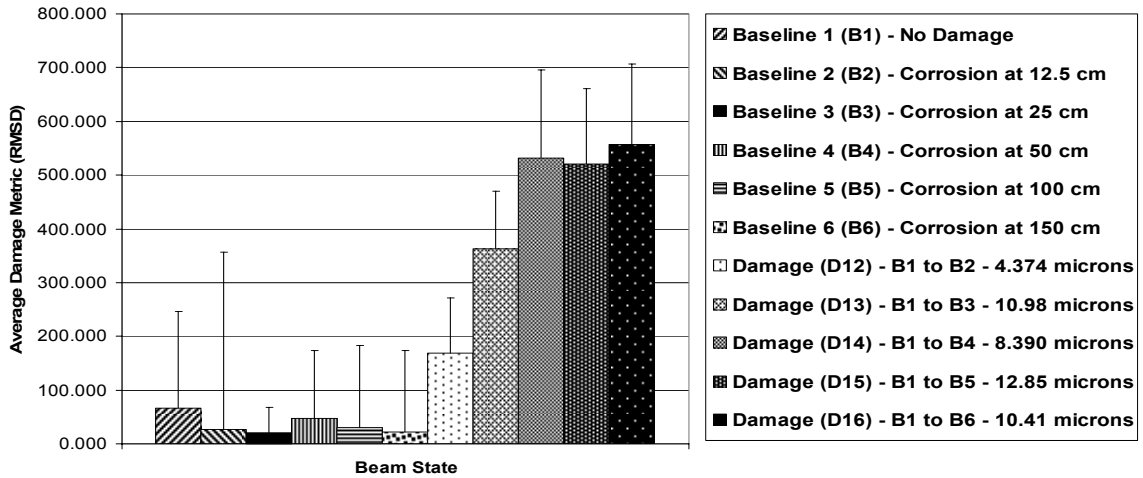


Figure A.15: Corrosion damage plots relative to baseline #1 from 96.5-98.5 kHz.

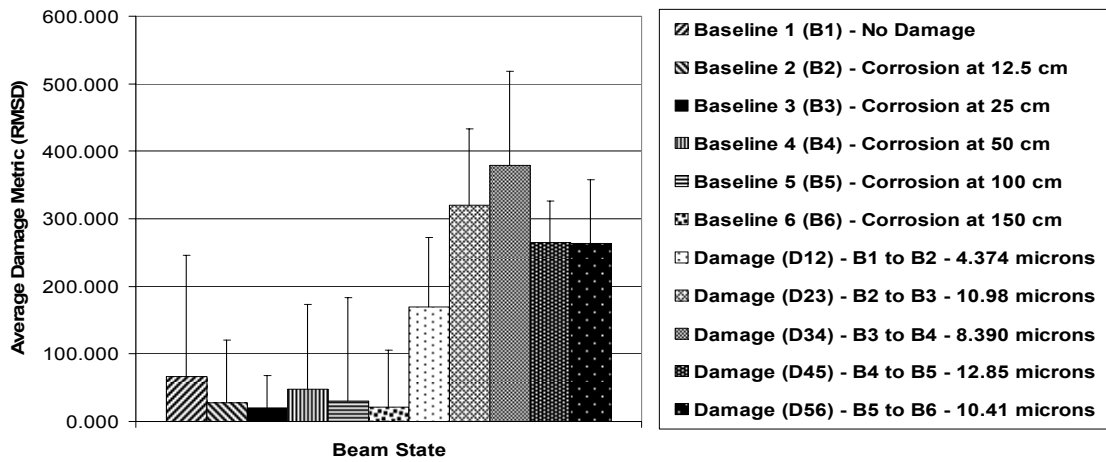


Figure A.16: Corrosion damage plots relative to previous baselines from 96.5-98.5 kHz.

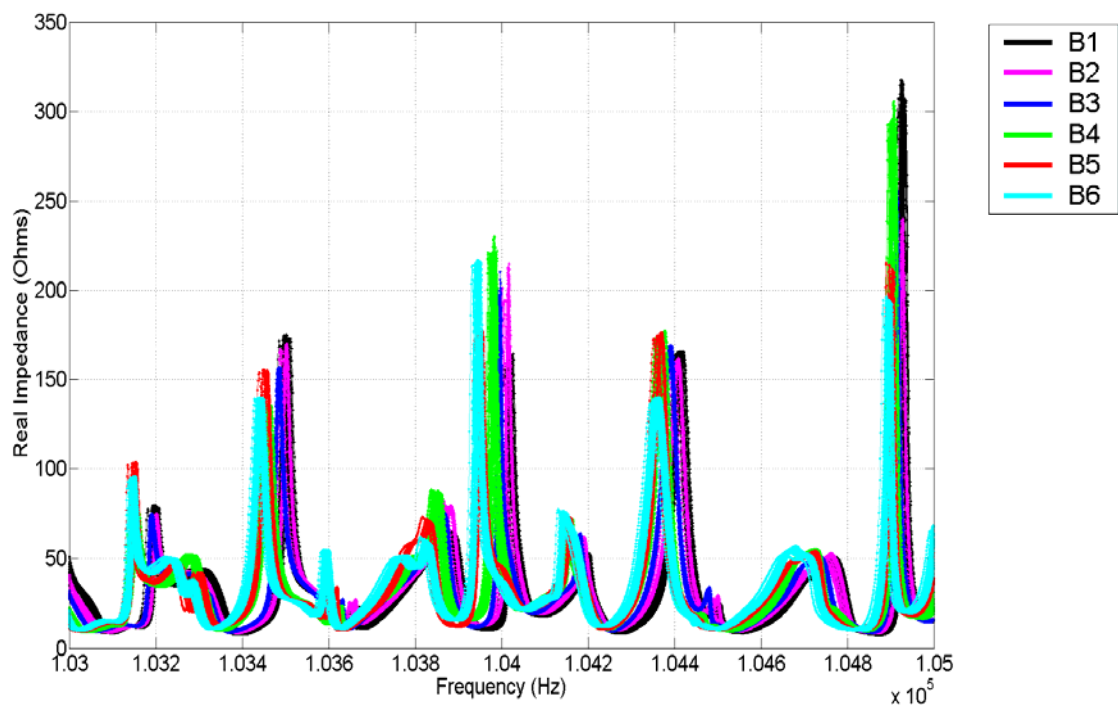


Figure A.17: Impedance signatures for beam corrosion damage from 103-105 kHz.

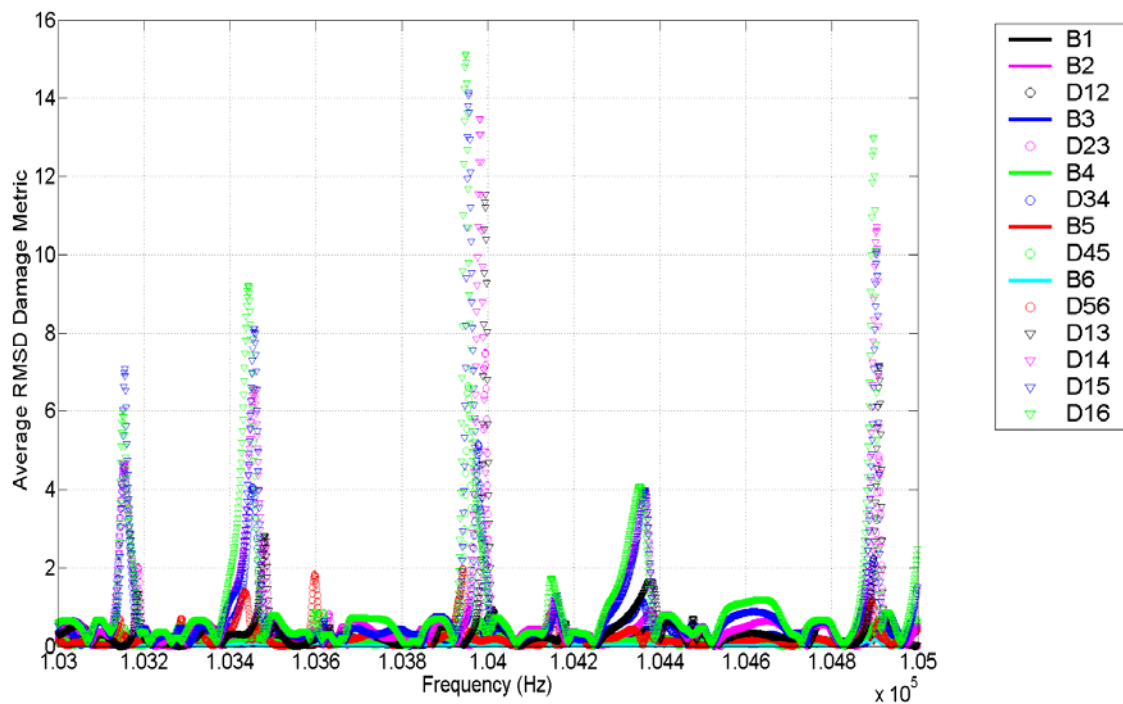


Figure A.18: Average damage metrics for beam corrosion damage from 103-105 kHz.

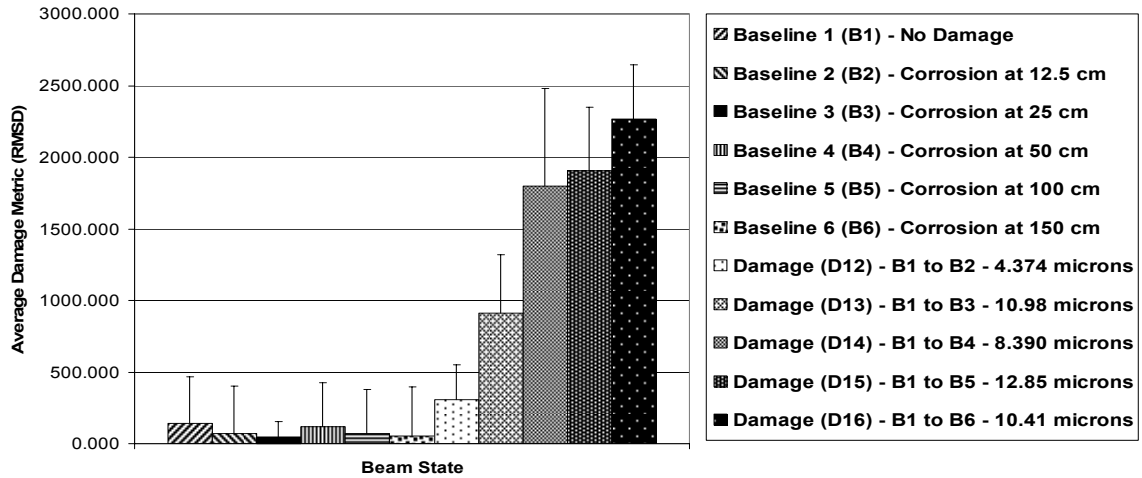


Figure A.19: Corrosion damage plots relative to baseline #1 from 103-105 kHz.

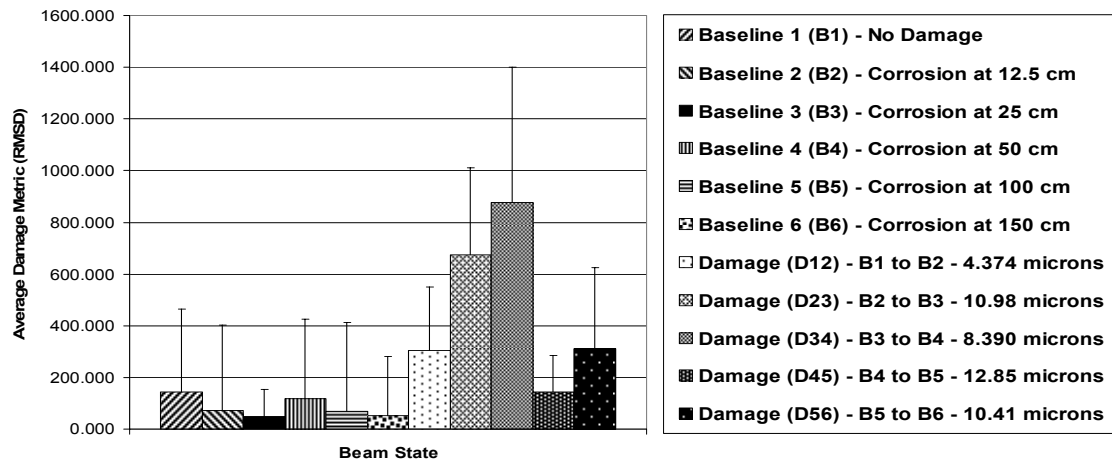


Figure A.20: Corrosion damage plots relative to previous baselines from 103-105 kHz.

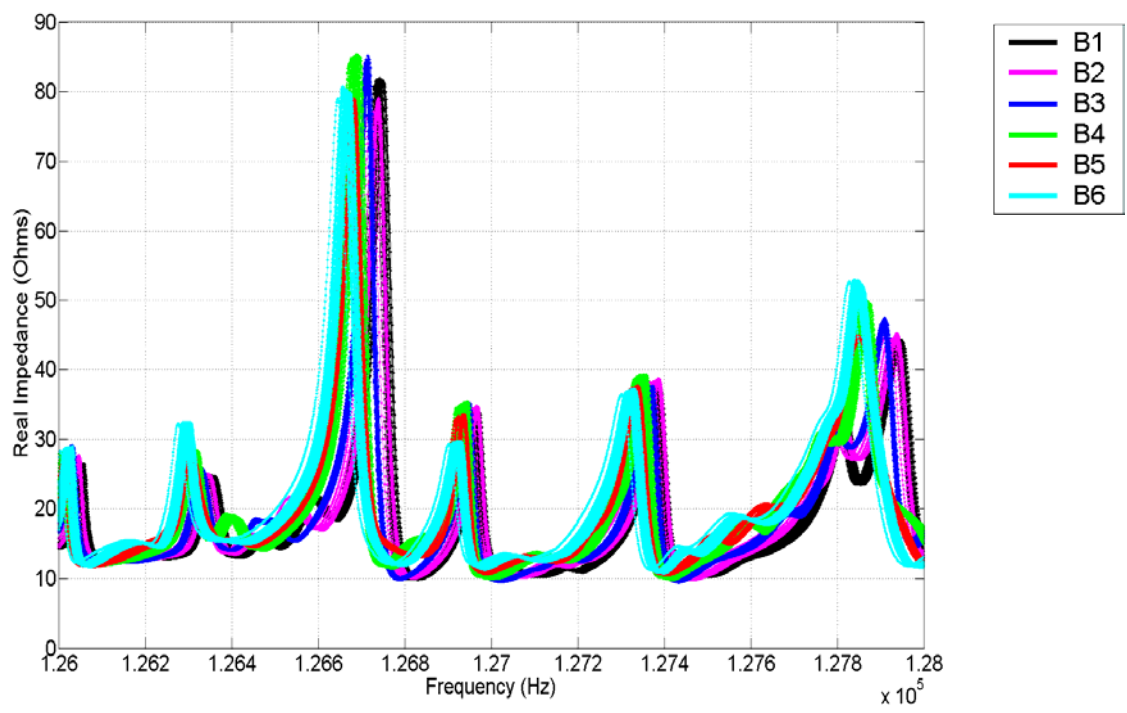


Figure A.21: Impedance signatures for beam corrosion damage from 126-128 kHz.

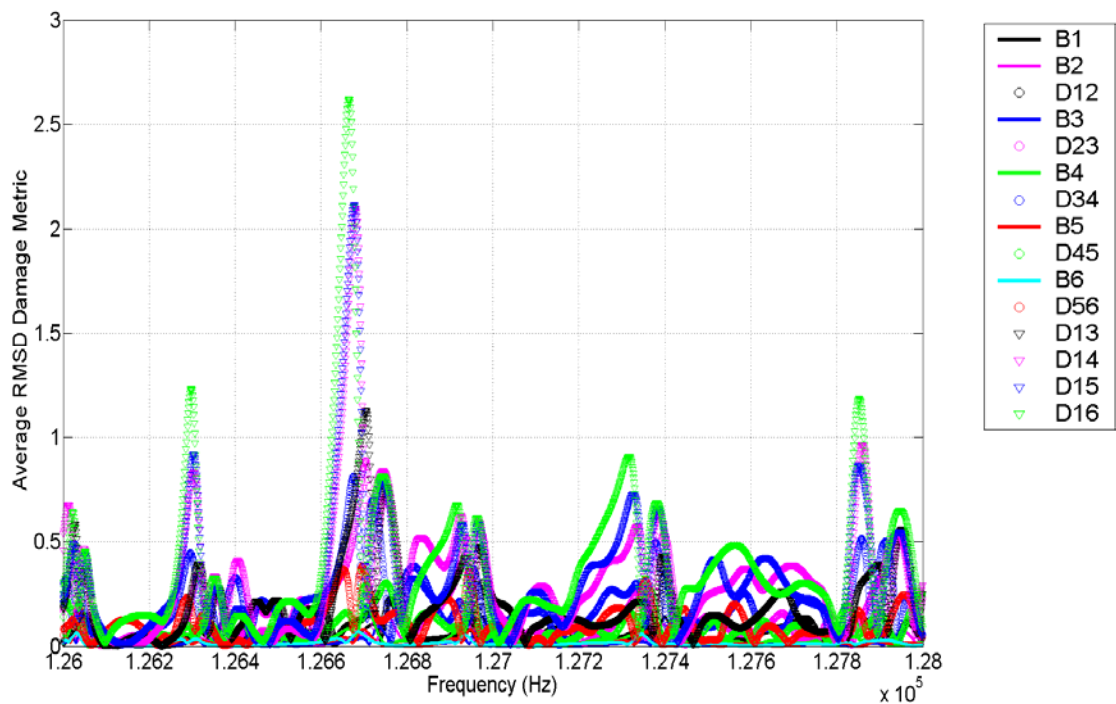


Figure A.22: Average damage metrics for beam corrosion damage from 126-128 kHz.

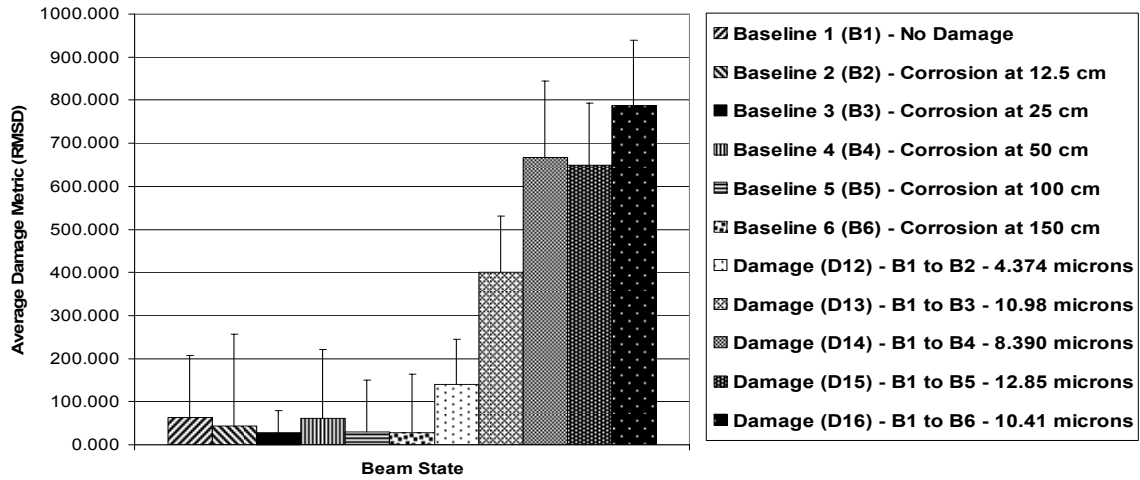


Figure A.23: Corrosion damage plots relative to baseline #1 from 126-128 kHz.

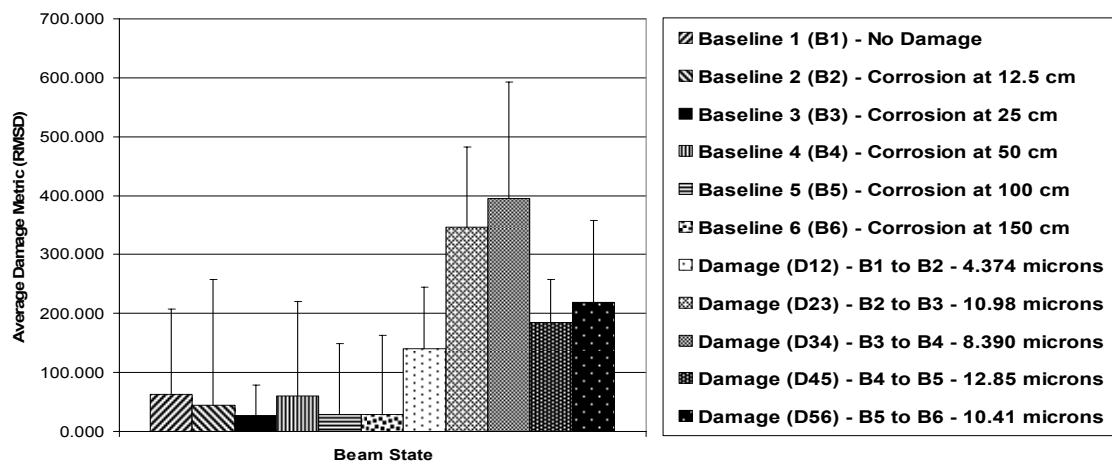


Figure A.24: Corrosion damage plots relative to previous baselines from 126-128 kHz.

Appendix B

Pit Depth, Location, and Surface Coverage Plots and Figures

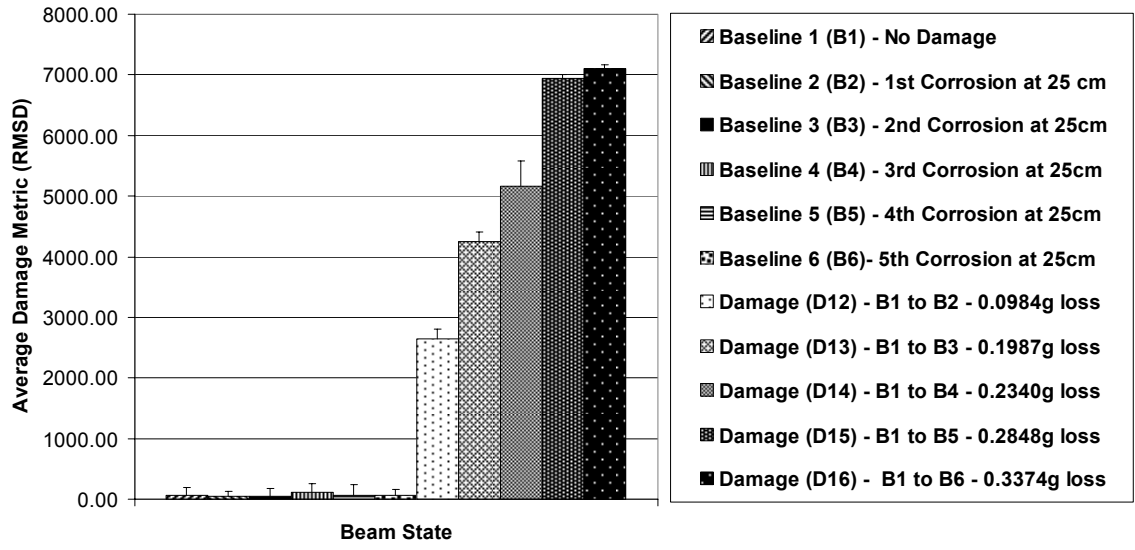


Figure B.1: Pit depth damage metric plot relative to initial baseline for all frequencies.

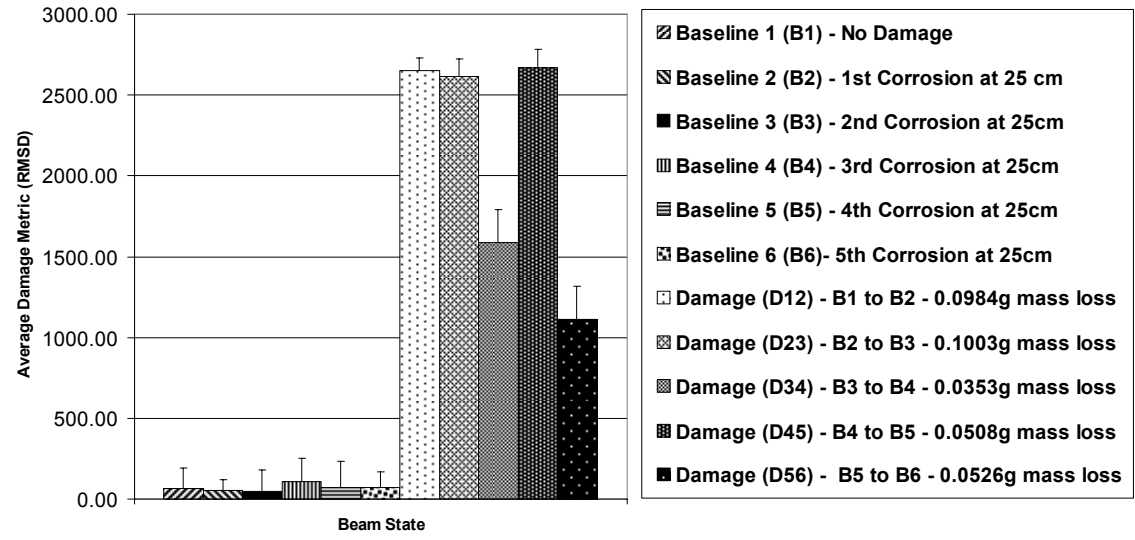


Figure B.2: Pit depth damage metric plot relative to previous baseline for all frequencies.

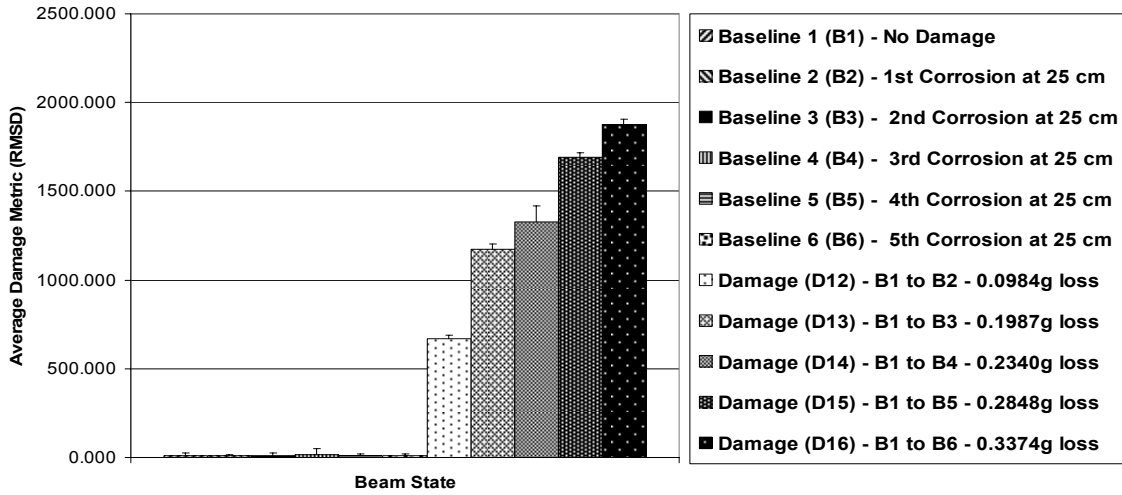


Figure B.3: Pit depth damage metric plot relative to initial baseline from 20-22 kHz.

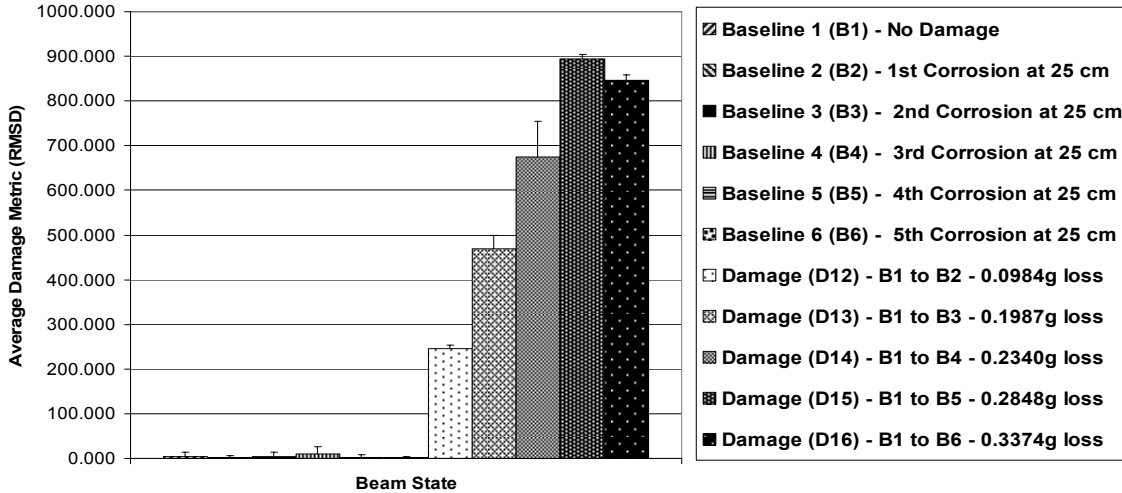


Figure B.4: Pit depth damage metric plot relative to initial baseline from 44-46 kHz.

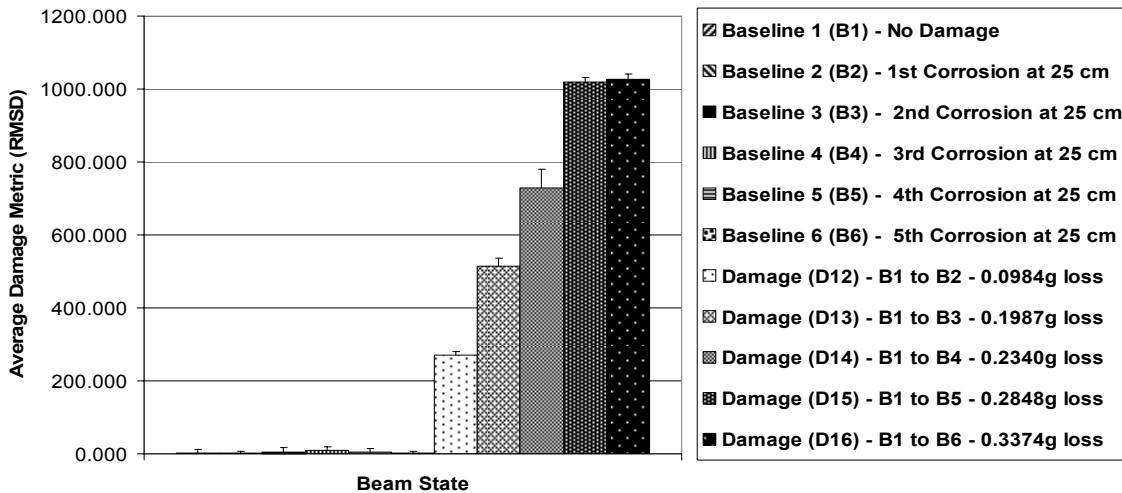


Figure B.5: Pit depth damage metric plot relative to initial baseline from 54-56 kHz.

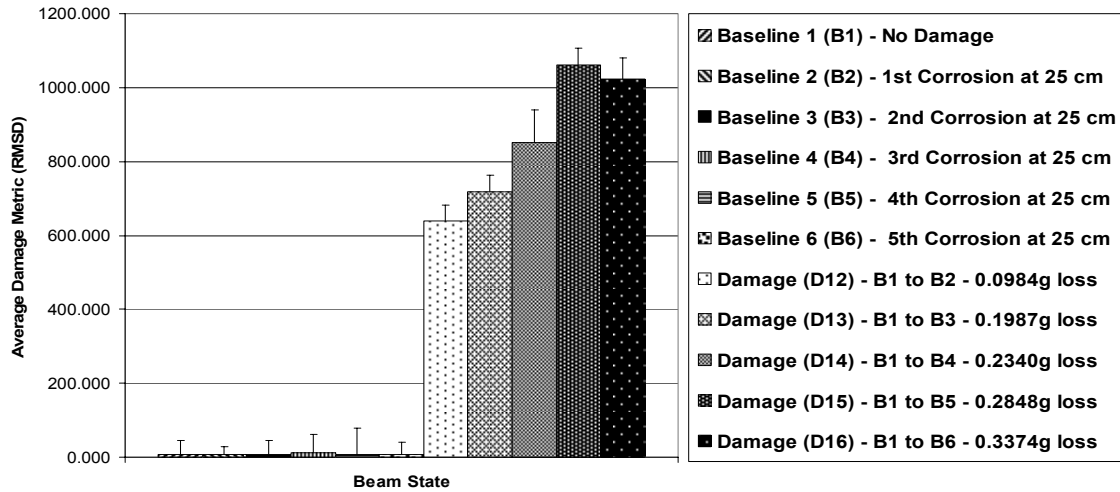


Figure B.6: Pit depth damage metric plot relative to initial baseline from 72-74 kHz.

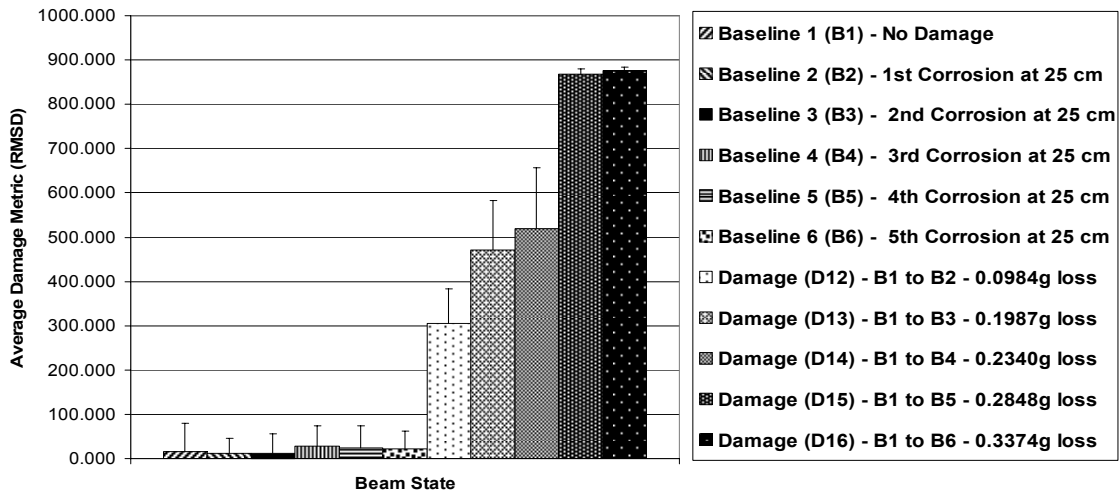


Figure B.7: Pit depth damage metric plot relative to initial baseline from 97-99 kHz.

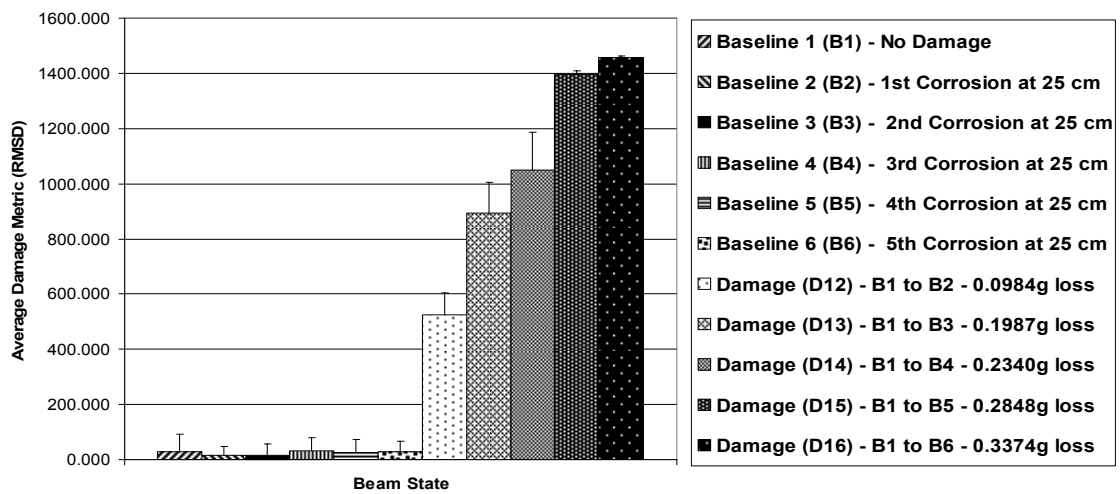


Figure B.8: Pit depth damage metric plot relative to initial baseline from 104-106 kHz.

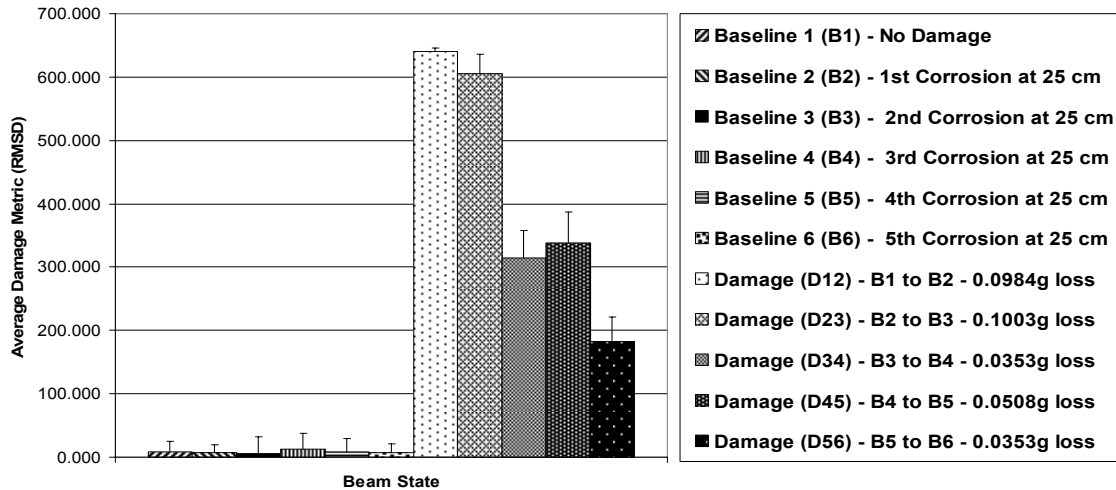


Figure B.9: Pit depth damage metric plot relative to previous baseline from 20-22 kHz.

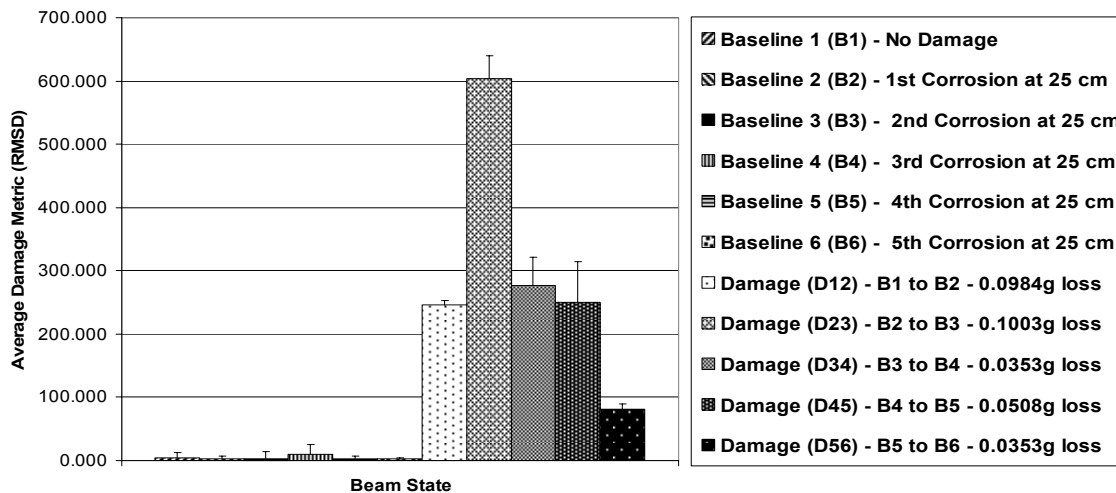


Figure B.10: Pit depth damage metric plot relative to previous baseline from 44-46 kHz.

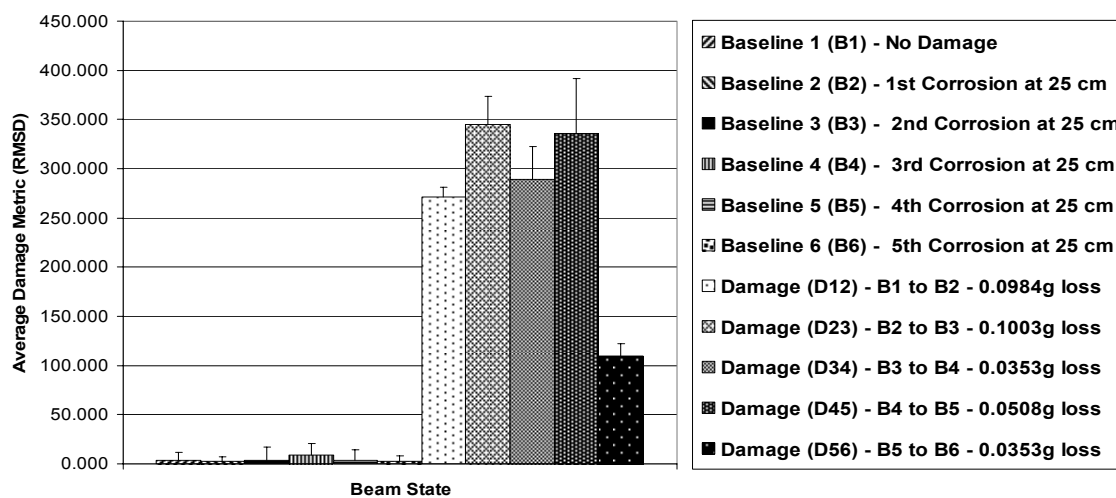


Figure B.11: Pit depth damage metric plot relative to previous baseline from 54-56 kHz.

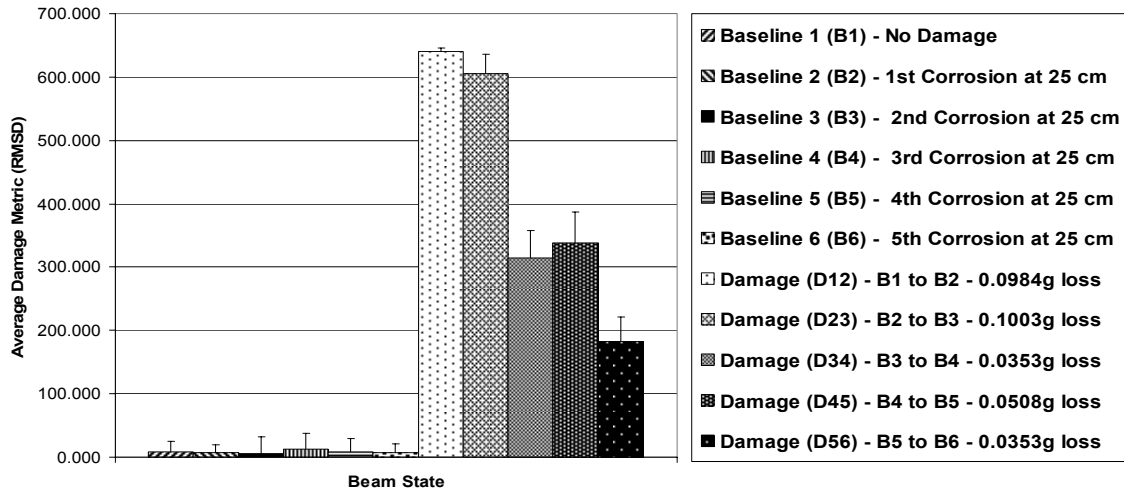


Figure B.12: Pit depth damage metric plot relative to previous baseline from 72-74 kHz.

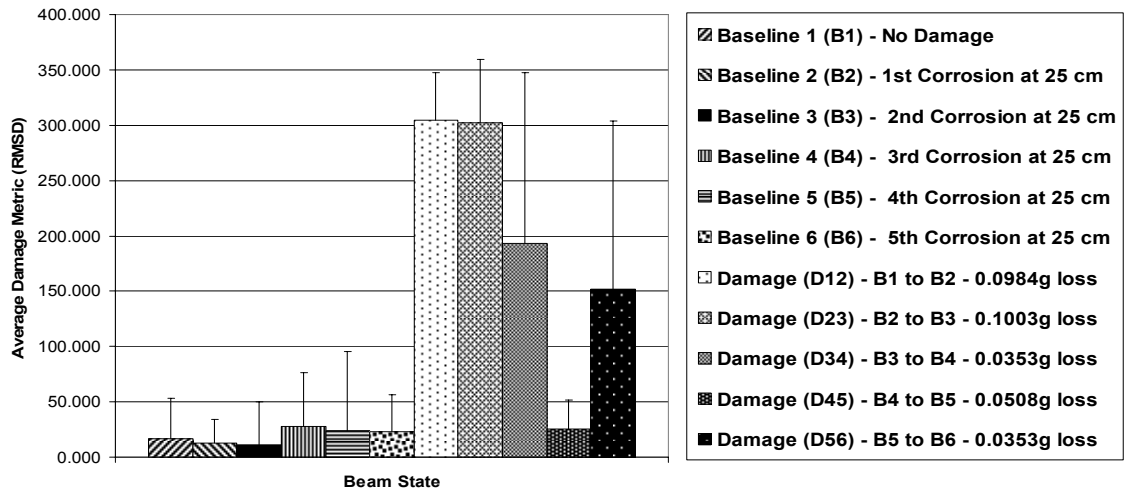


Figure B.13: Pit depth damage metric plot relative to previous baseline from 97-99 kHz.

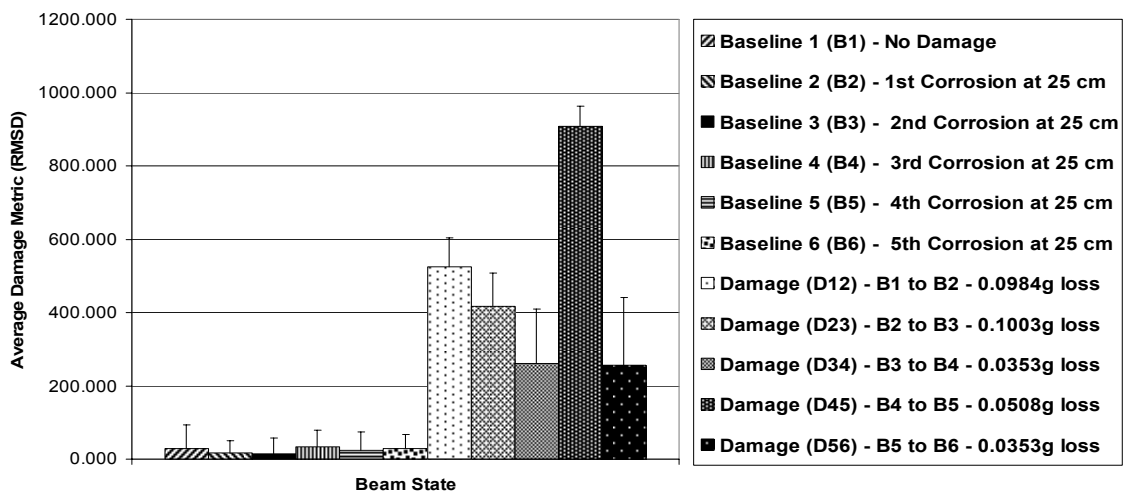


Figure B.14: Pit depth damage metric plot relative to previous baseline from 104-106 kHz.

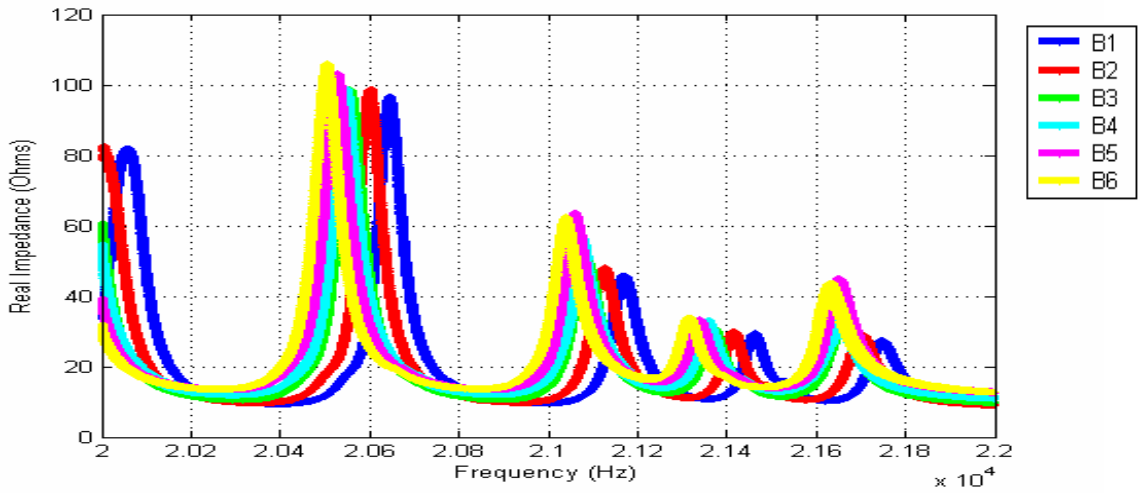


Figure B.15: Pit depth impedance signatures from 20-22 kHz.

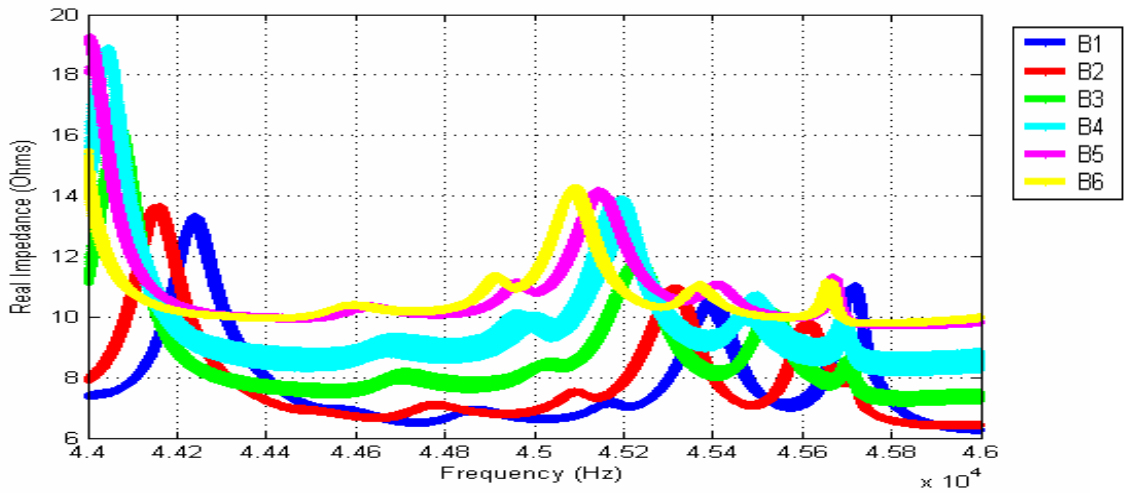


Figure B.16: Pit depth impedance signatures from 44-46 kHz.

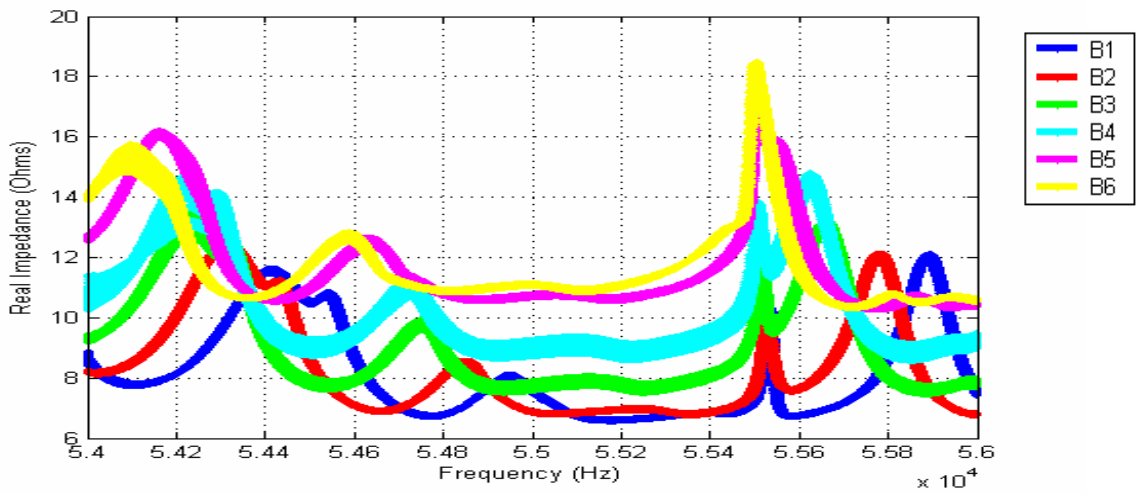


Figure B.17: Pit depth impedance signatures from 54-56 kHz.

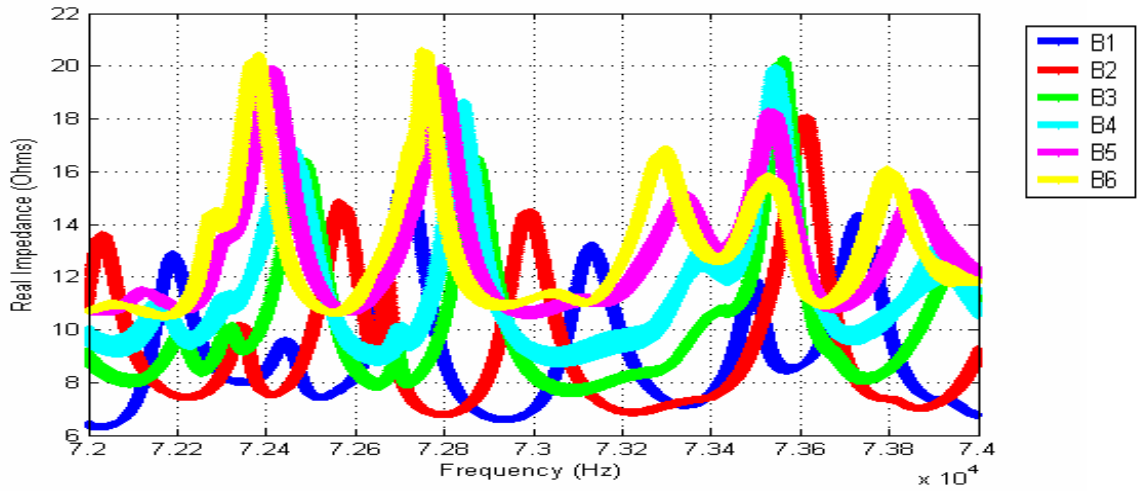


Figure B.18: Pit depth impedance signatures from 72-74 kHz.

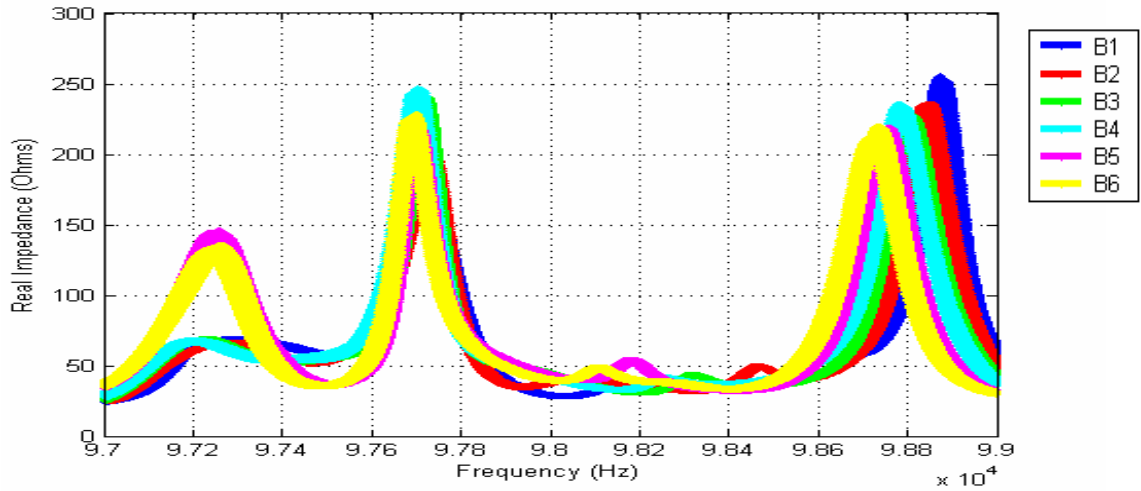


Figure B.19: Pit depth impedance signatures from 97-99 kHz.

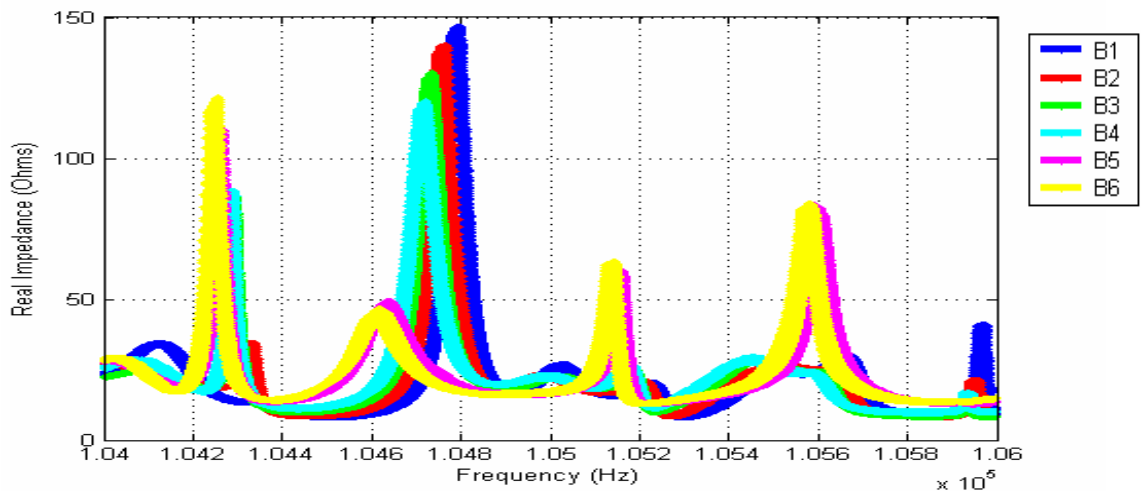


Figure B.20: Pit depth impedance signatures from 104-106 kHz.

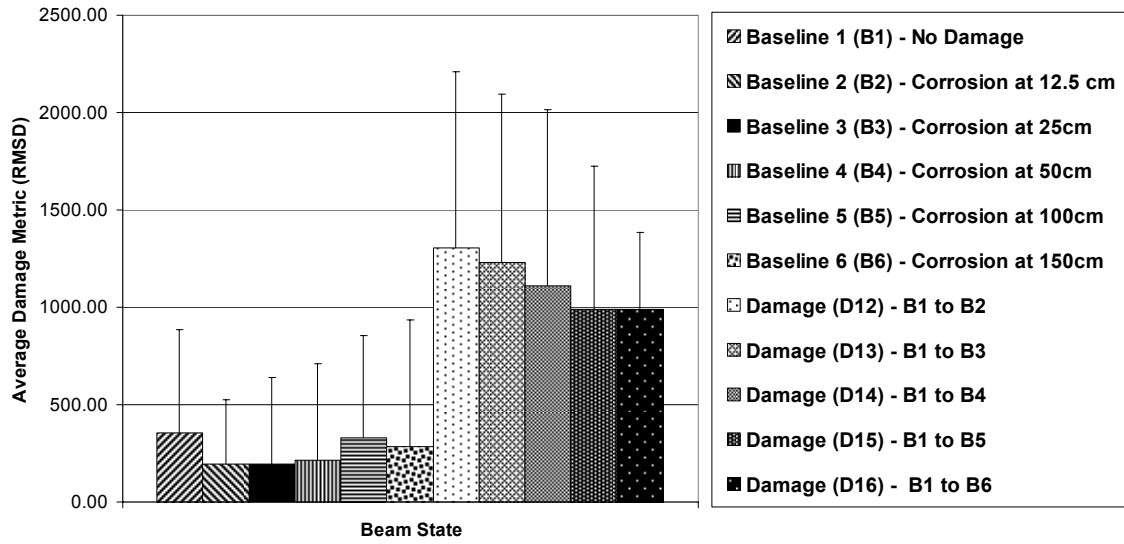


Figure B.21: Location test damage metric plot relative to initial baseline for all frequencies.

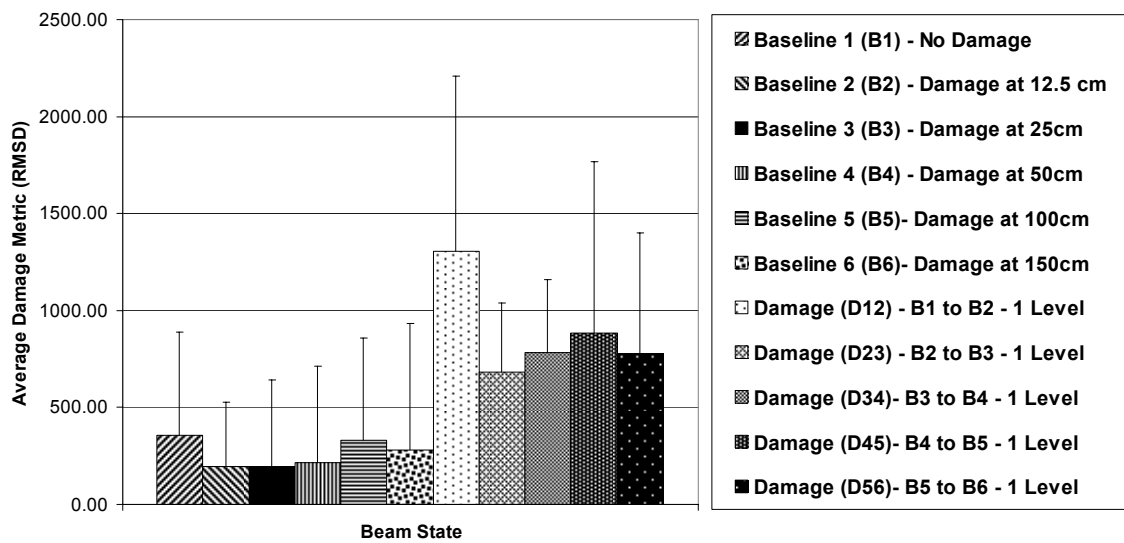


Figure B.22: Location test damage metric plot relative to previous baseline for all frequencies.

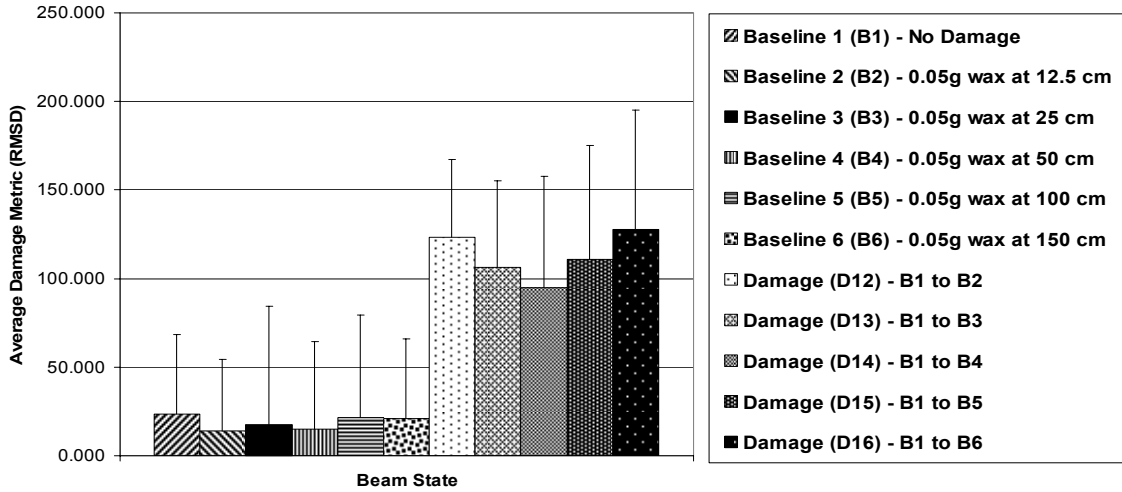


Figure B.23: Location test damage metric plot relative to baseline 1 from 20-22 kHz.

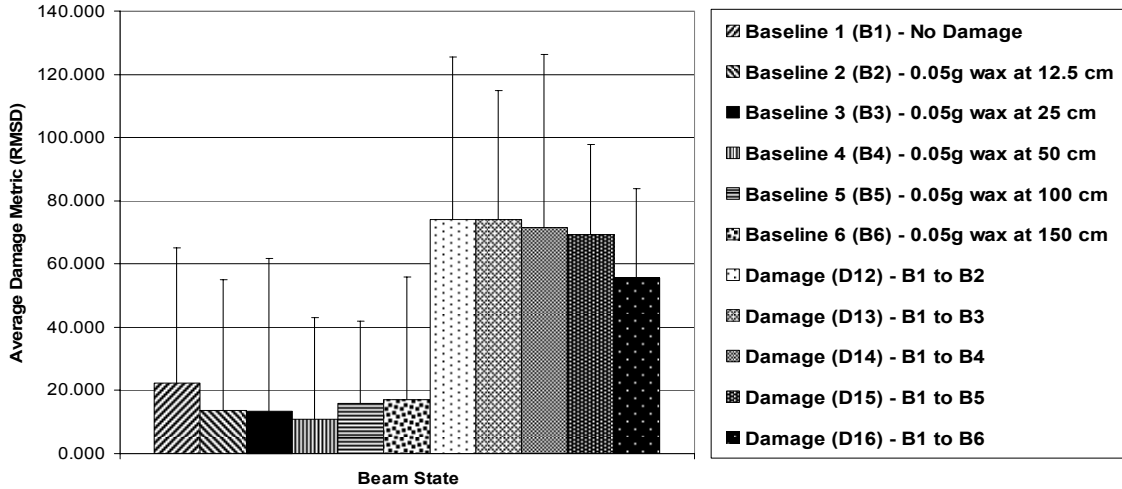


Figure B.24: Location test damage metric plot relative to baseline 1 from 54-56 kHz.

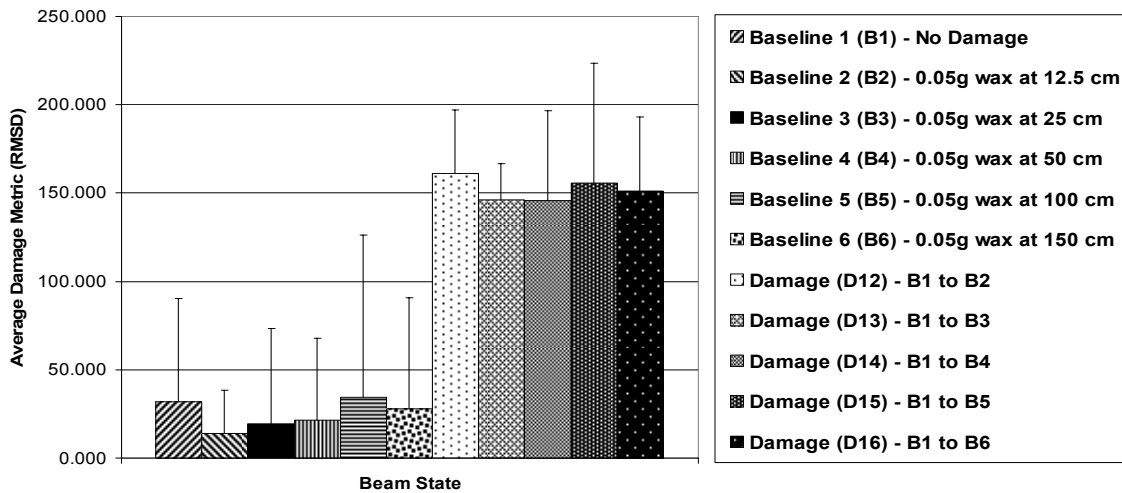


Figure B.25: Location test damage metric plot relative to baseline 1 from 71-73 kHz.

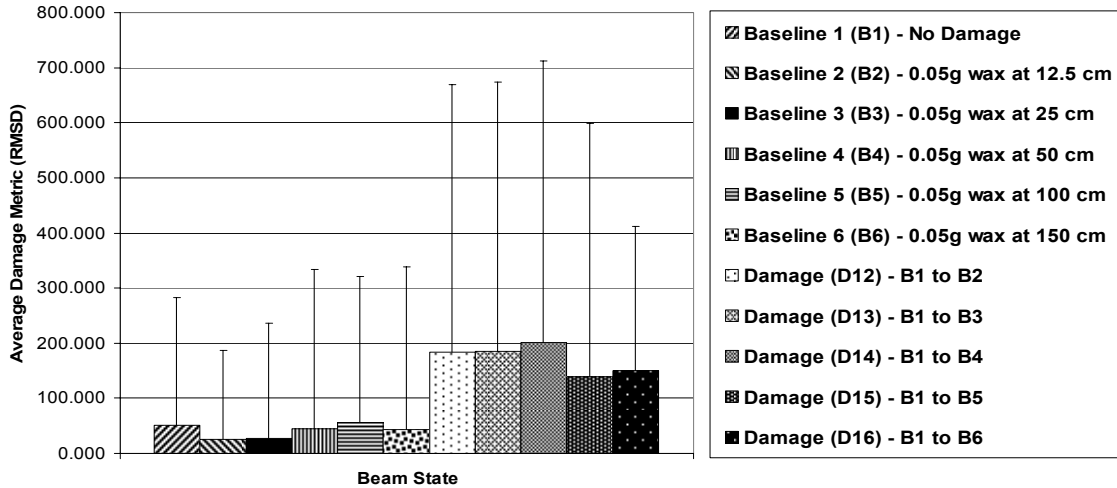


Figure B.26: Location test damage metric plot relative to baseline 1 from 96.5-98.5 kHz.

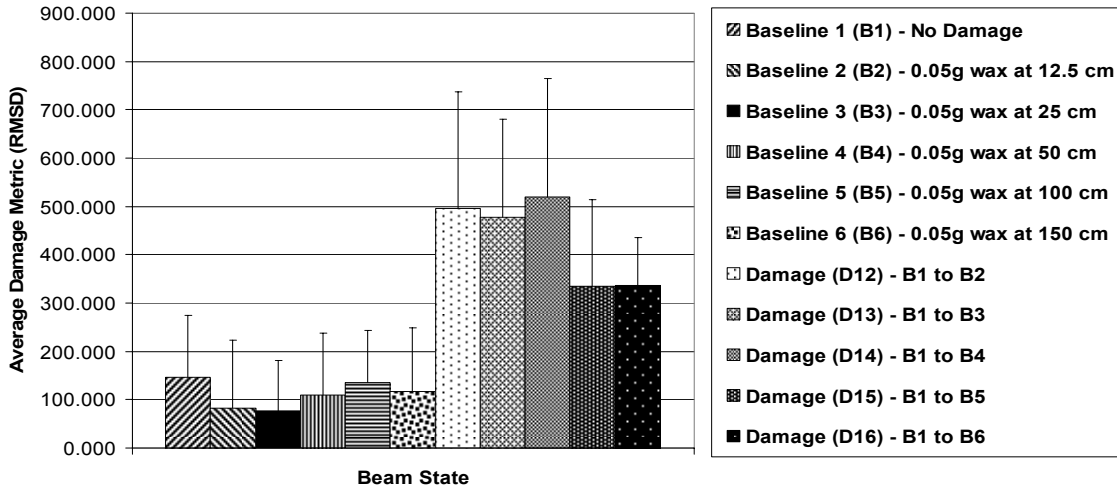


Figure B.27: Location test damage metric plot relative to baseline 1 from 103-105 kHz.

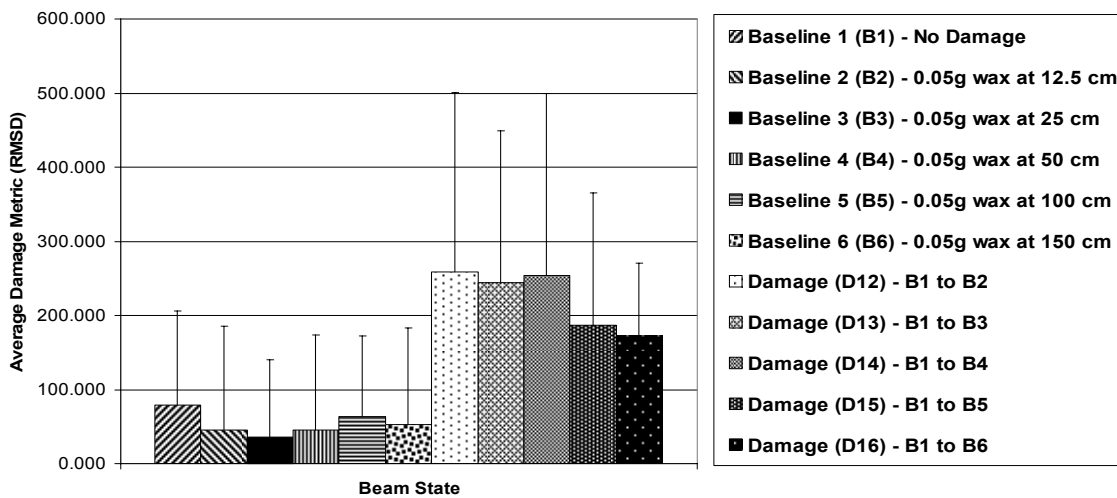


Figure B.28: Location test damage metric plot relative to baseline 1 from 126-128 kHz.

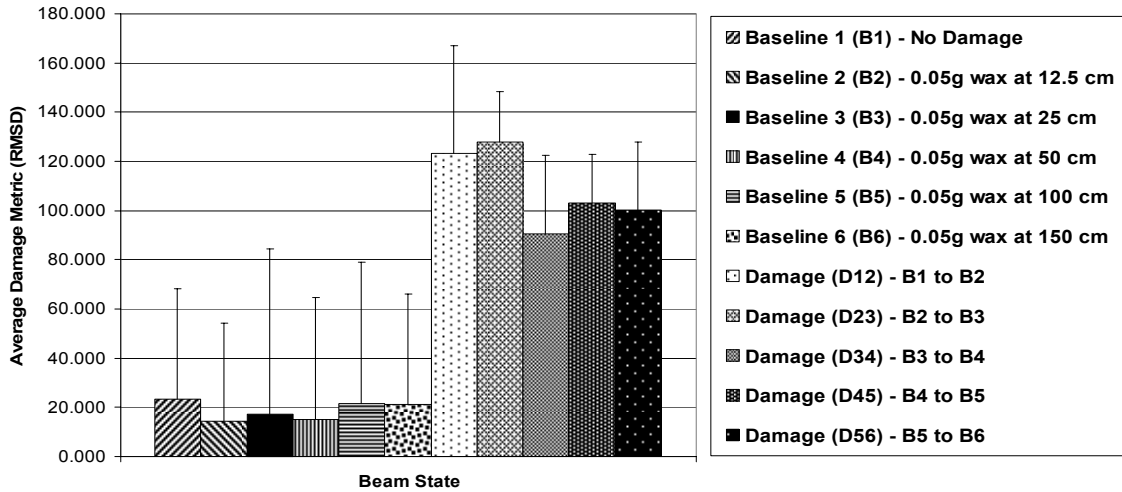


Figure B.29: Location test damage metric plot relative to previous baseline from 20-22 kHz.

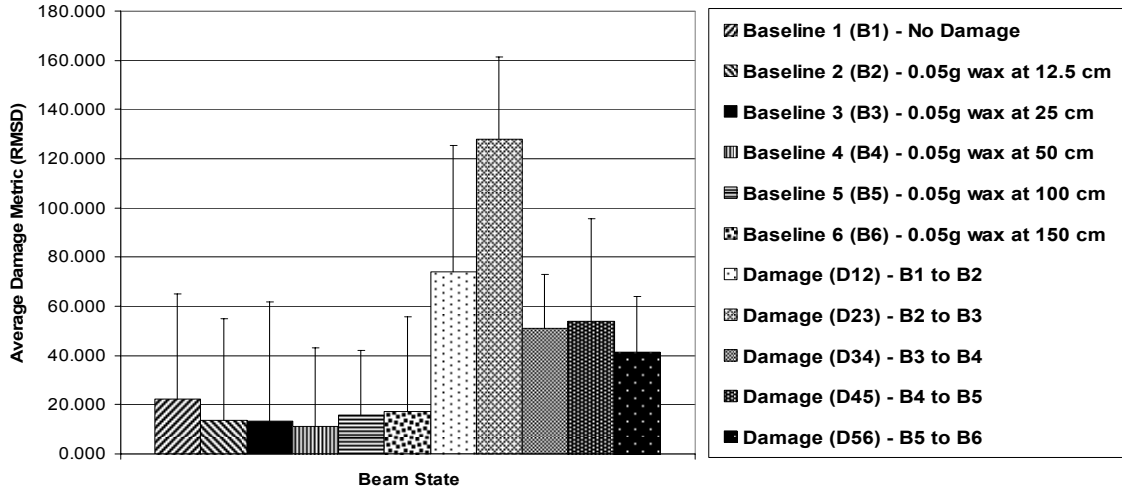


Figure B.30: Location test damage metric plot relative to previous baseline from 54-56 kHz.

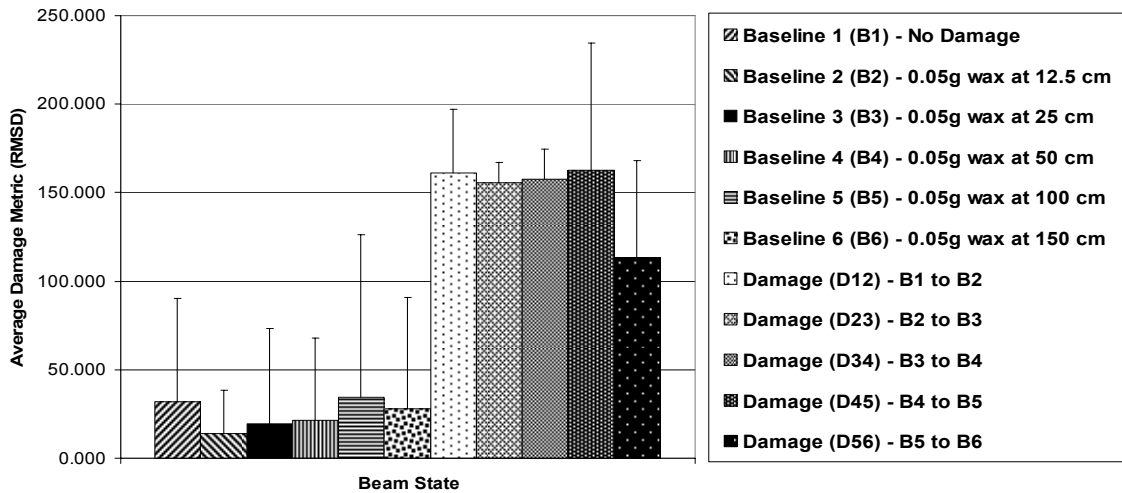


Figure B.31: Location test damage metric plot relative to previous baseline from 71-73 kHz.

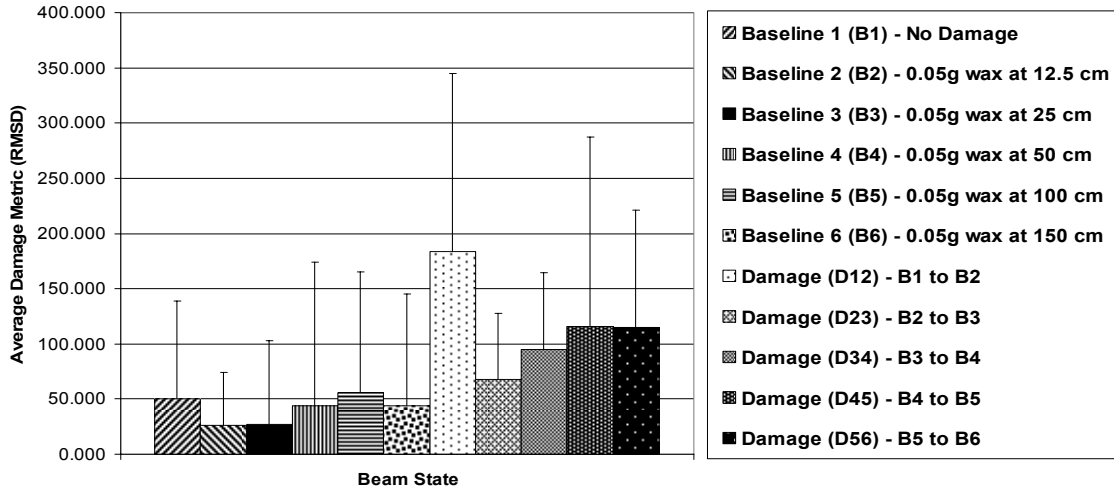


Figure B.32: Location test damage metric plot relative to previous baseline from 96.5-98.5 kHz.

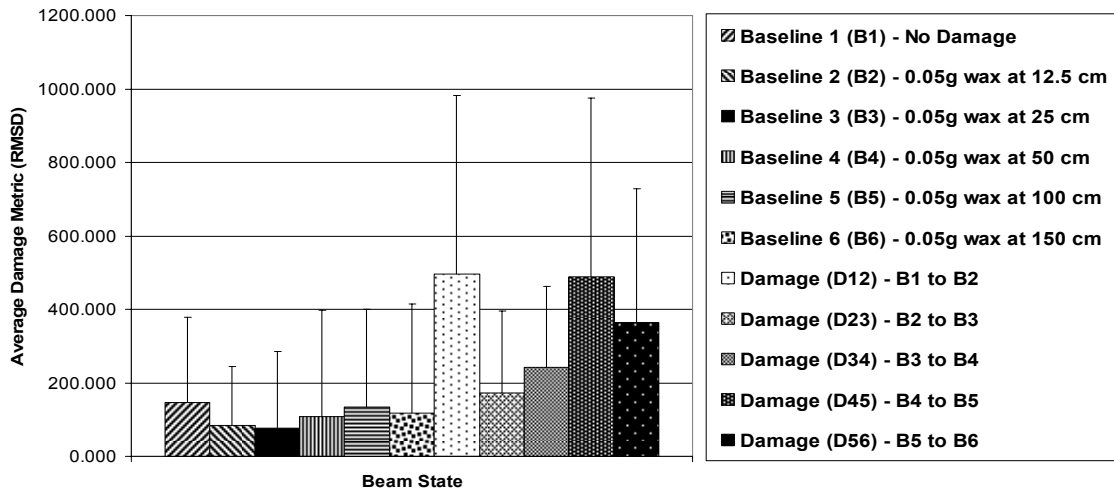


Figure B.33: Location test damage metric plot relative to previous baseline from 103-105 kHz.

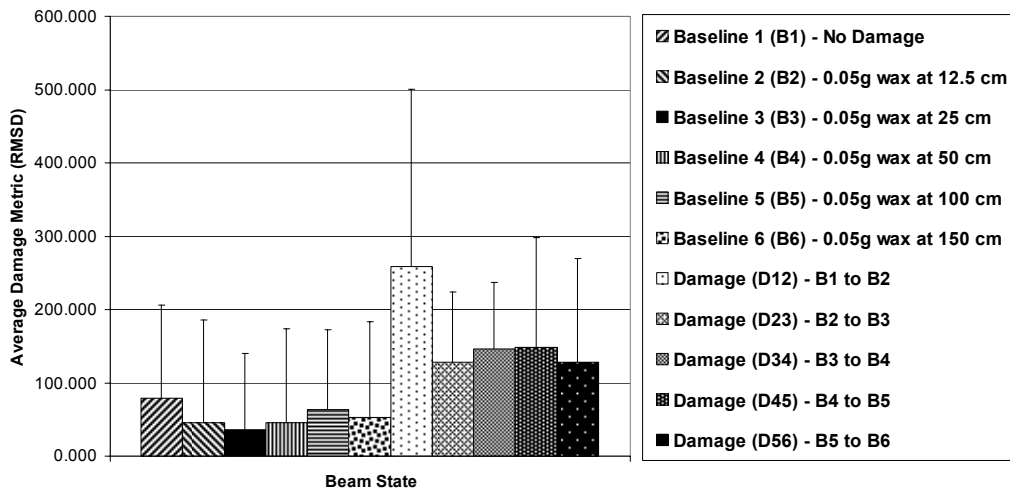


Figure B.34: Location test damage metric plot relative to previous baseline from 126-128 kHz.

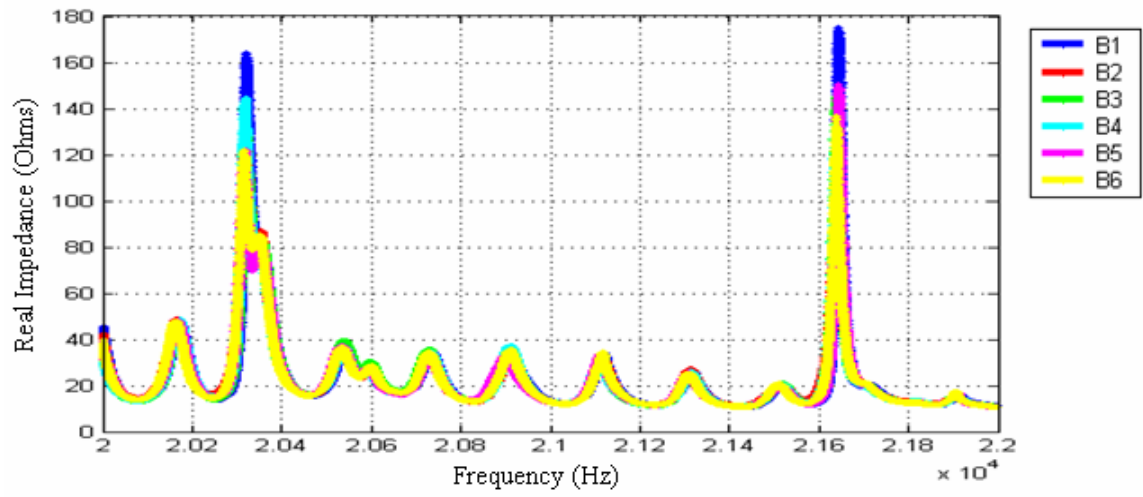


Figure B.35: Location impedance signatures from 20-22 kHz.

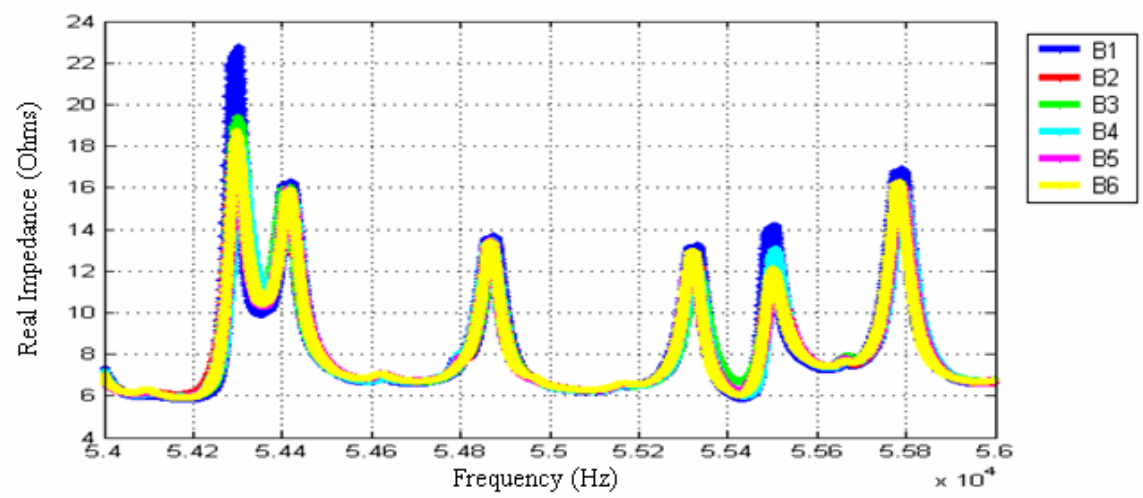


Figure B.36: Location impedance signatures from 54-56 kHz.

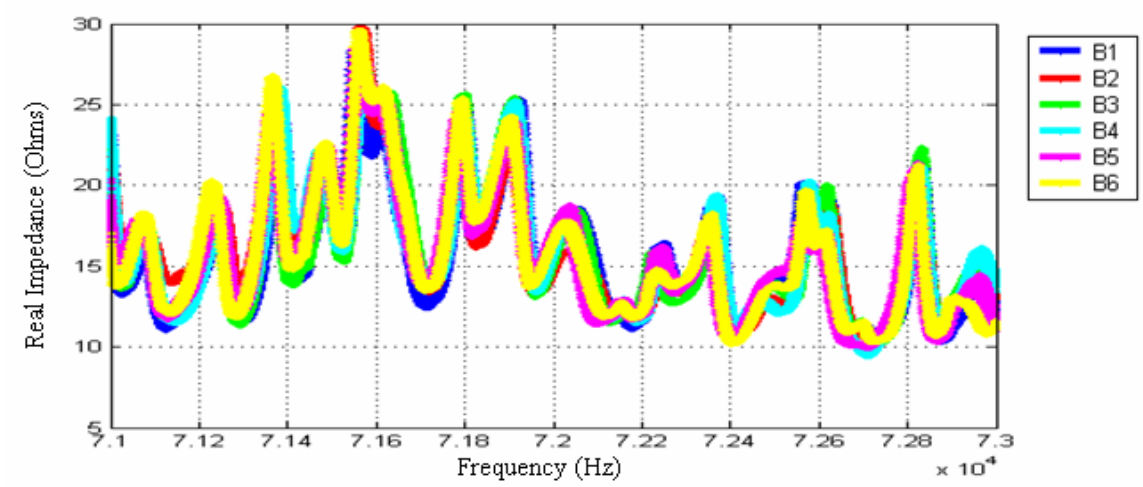


Figure B.37: Location impedance signatures from 71-73 kHz.

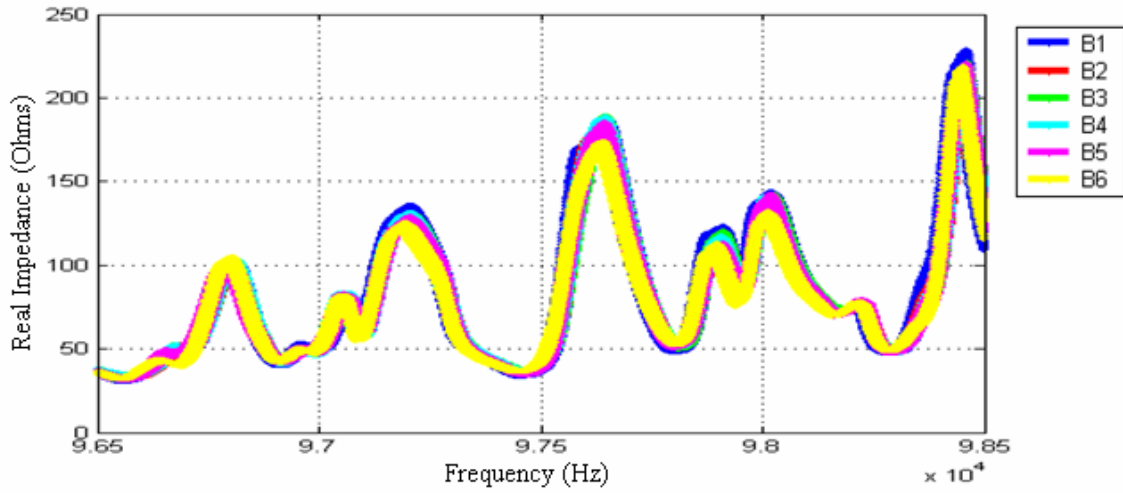


Figure B.38: Location impedance signatures from 96.5-98.5 kHz.

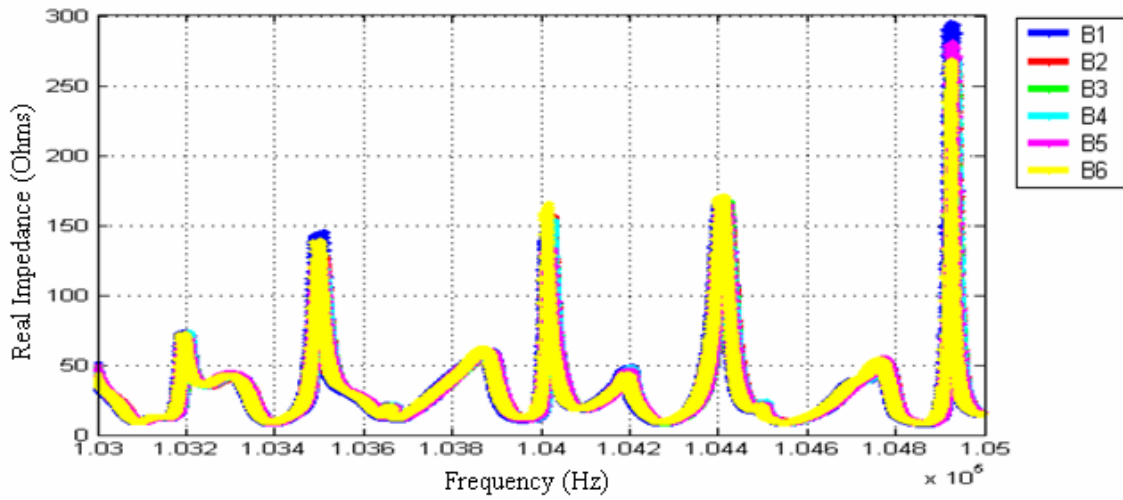


Figure B.39: Location impedance signatures from 103-105 kHz.

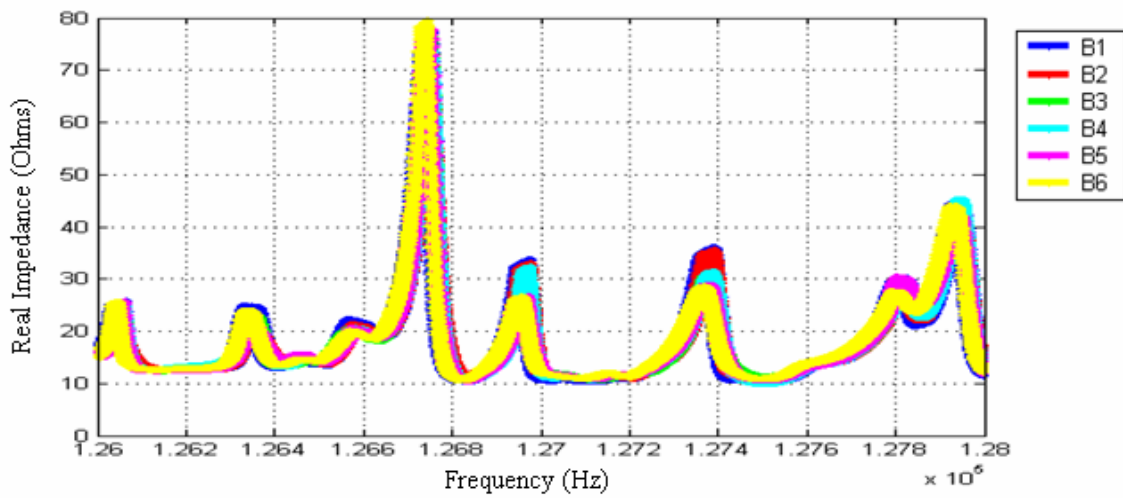


Figure B.40: Location impedance signatures from 126-128 kHz.

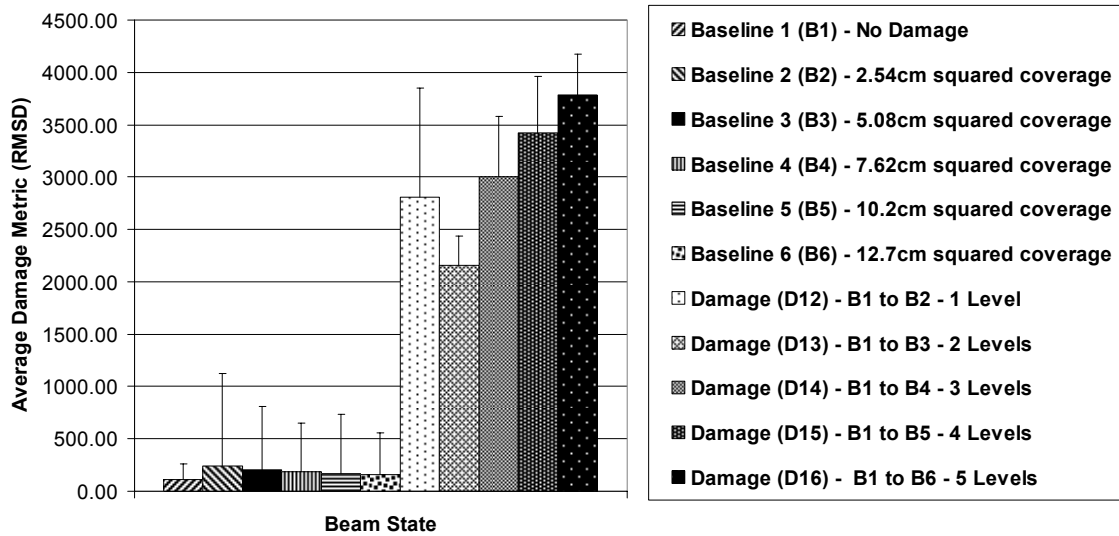


Figure B.41: Coverage damage metric plot relative to initial baseline for all frequencies.

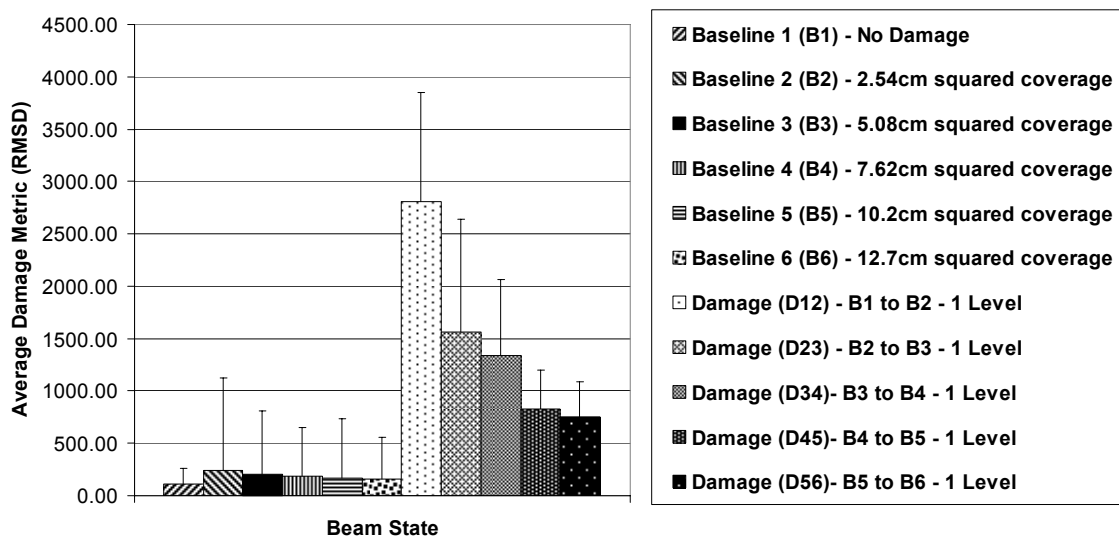


Figure B.42: Coverage damage metric plot relative to previous baseline for all frequencies.

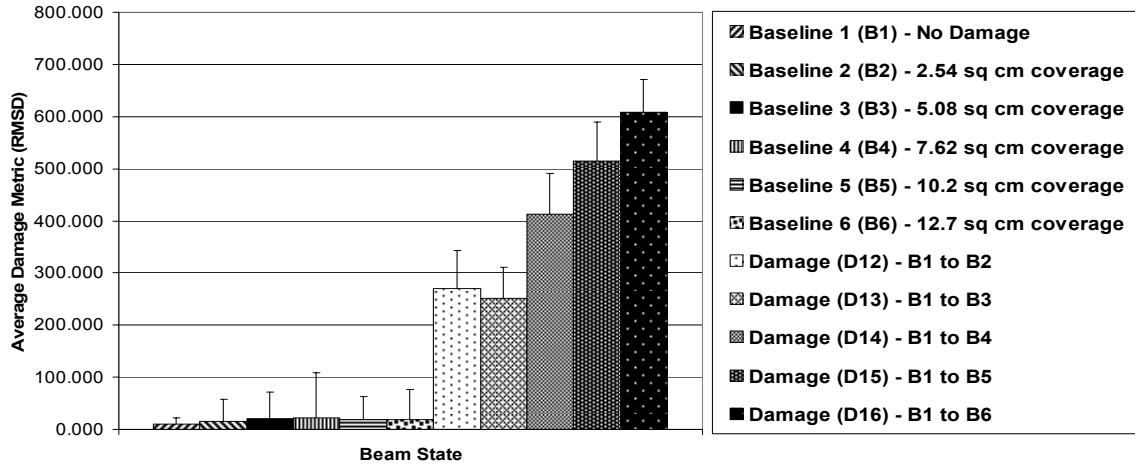


Figure B.43: Coverage damage metric plot relative to initial baseline from 20-22 kHz.

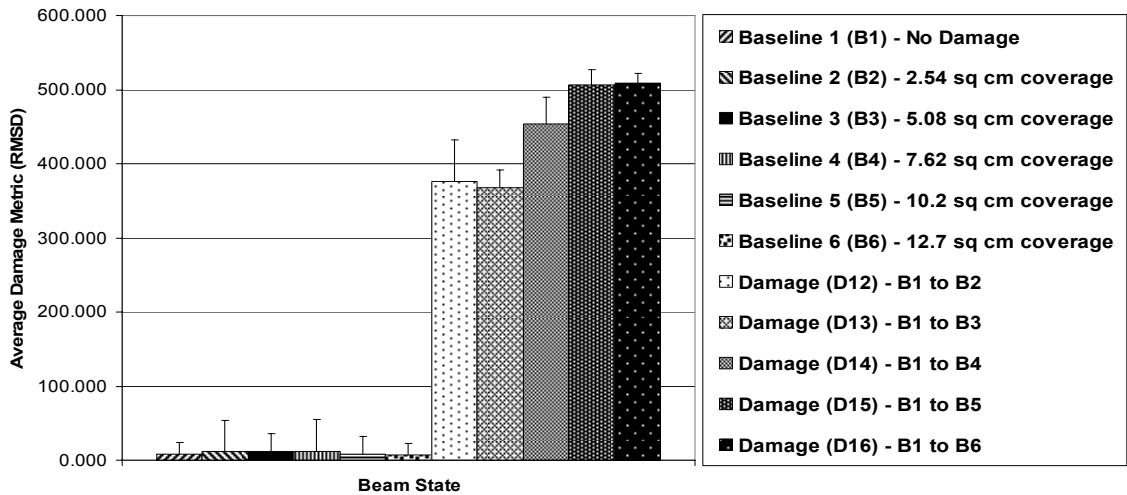


Figure B.44: Coverage damage metric plot relative to initial baseline from 54-66 kHz.

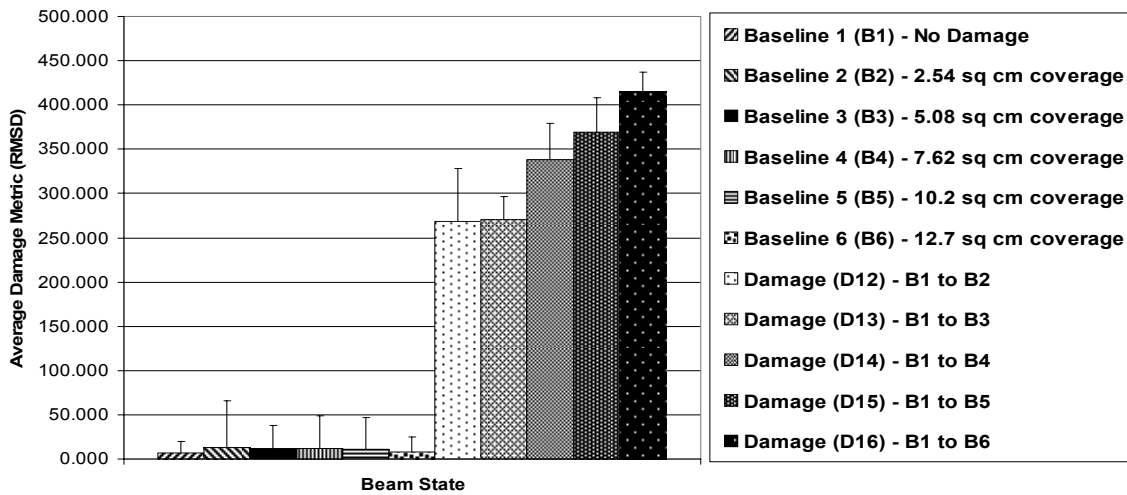


Figure B.45: Coverage damage metric plot relative to initial baseline from 71-73 kHz.

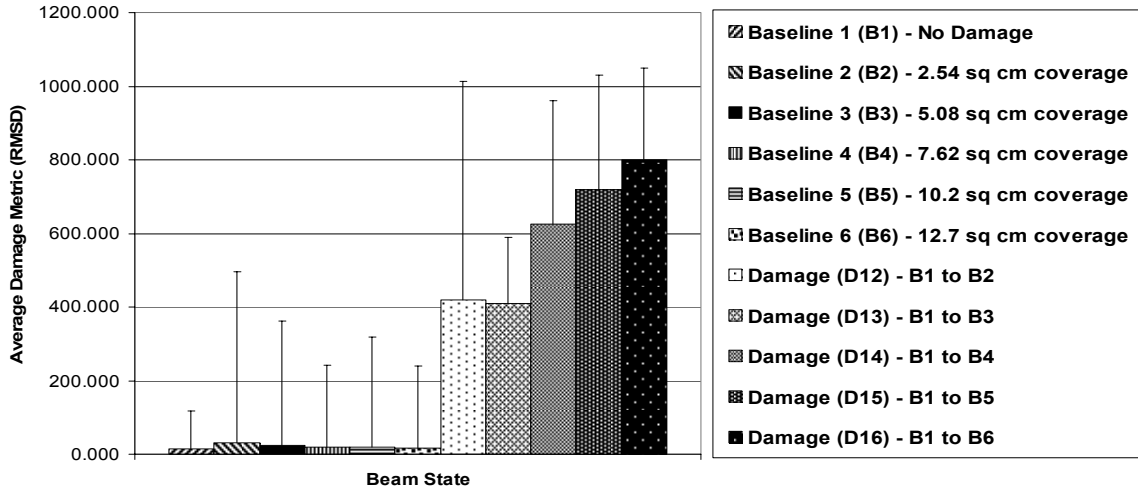


Figure B.46: Coverage damage metric plot relative to initial baseline from 96.5-98.5 kHz.

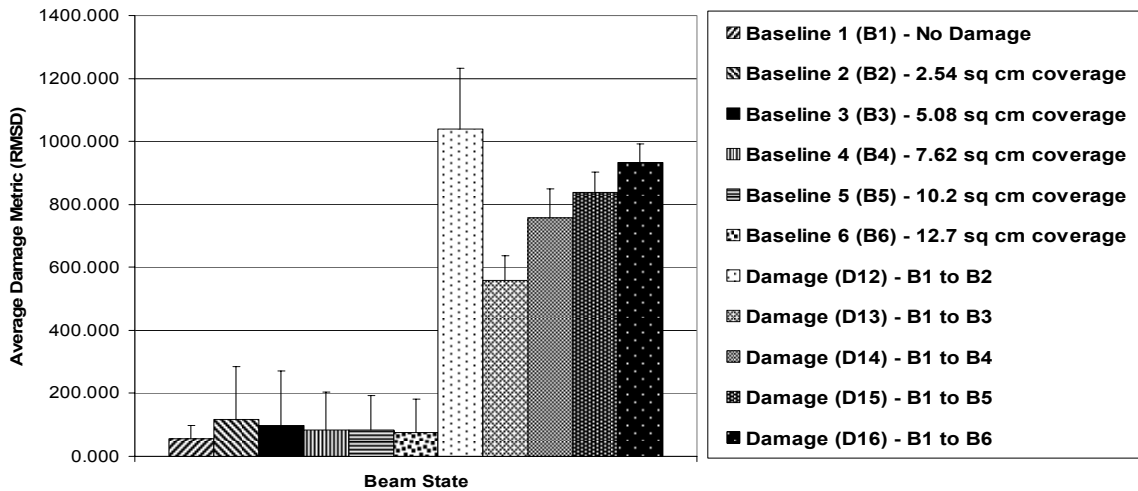


Figure B.47: Coverage damage metric plot relative to initial baseline from 103-105 kHz.

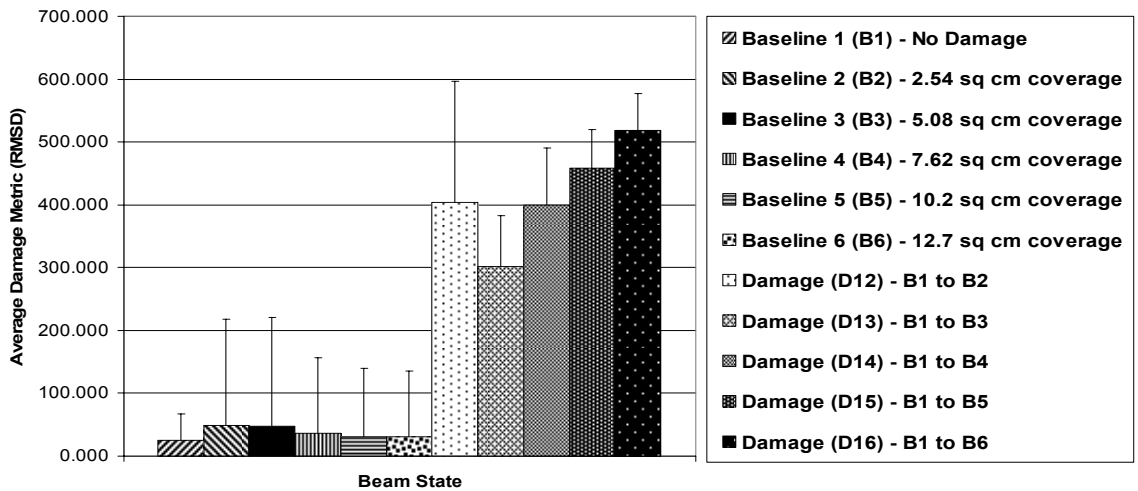


Figure B.48: Coverage damage metric plot relative to initial baseline from 126-128 kHz.

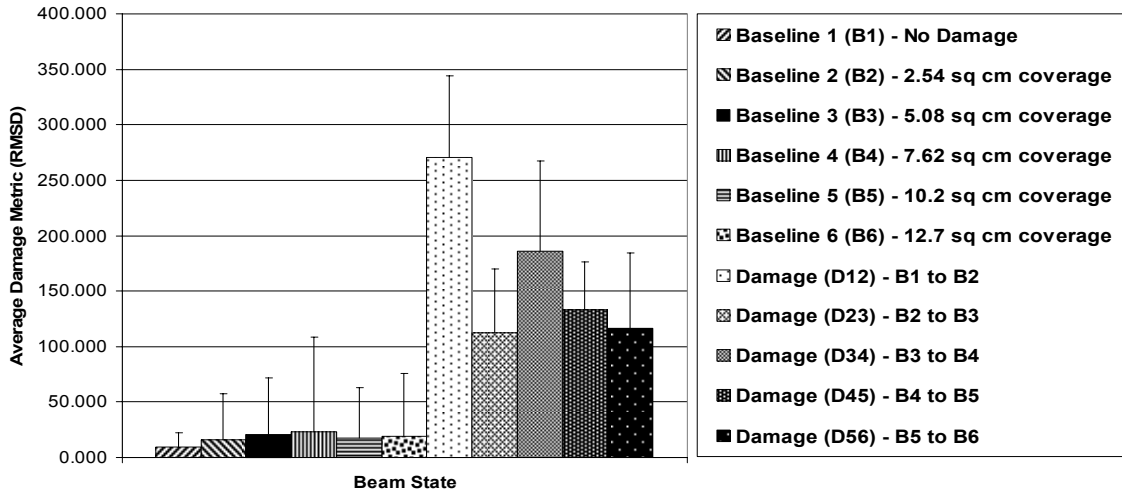


Figure B.49: Coverage damage metric plot relative to previous baseline from 20-22 kHz.

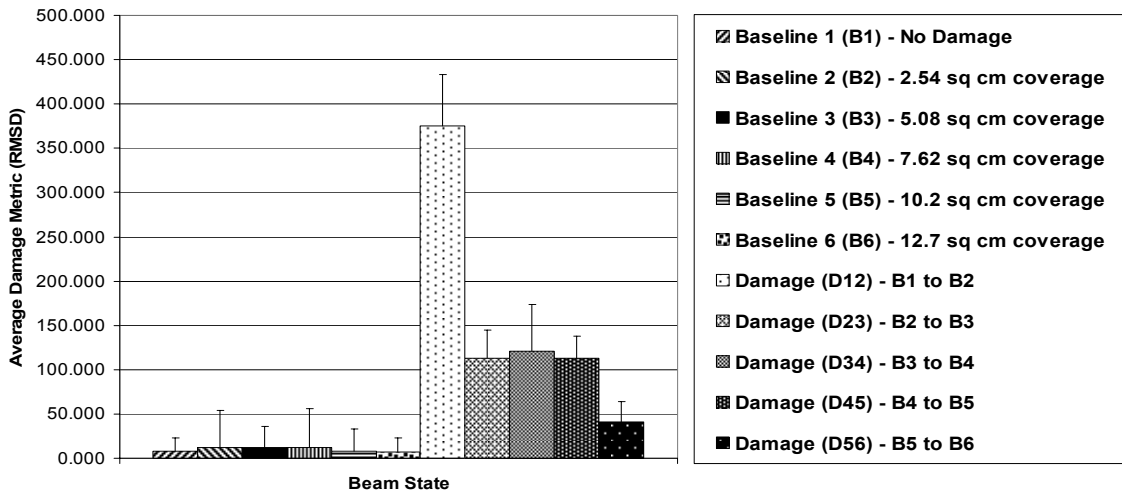


Figure B.50: Coverage damage metric plot relative to previous baseline from 54-66 kHz.

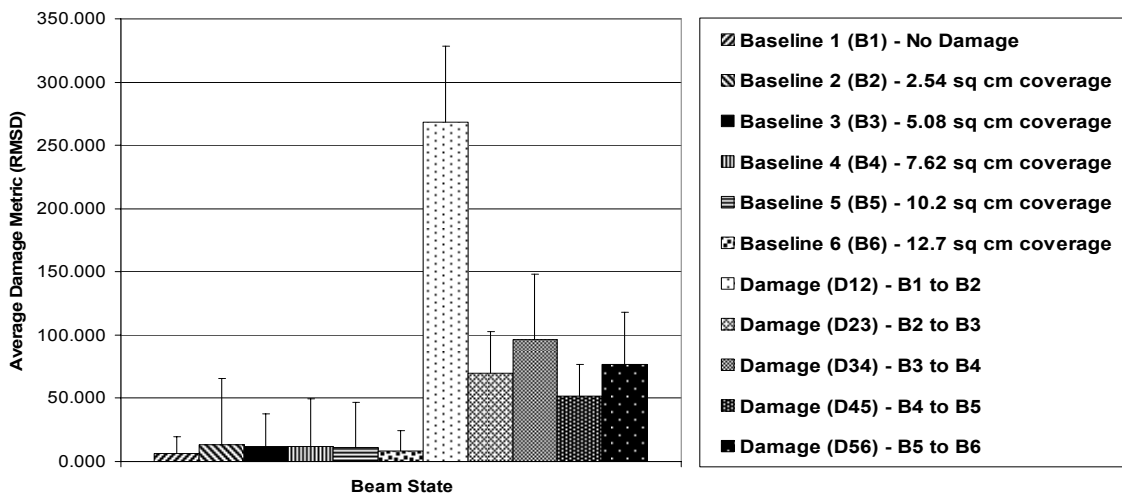


Figure B.51: Coverage damage metric plot relative to previous baseline from 71-73 kHz.

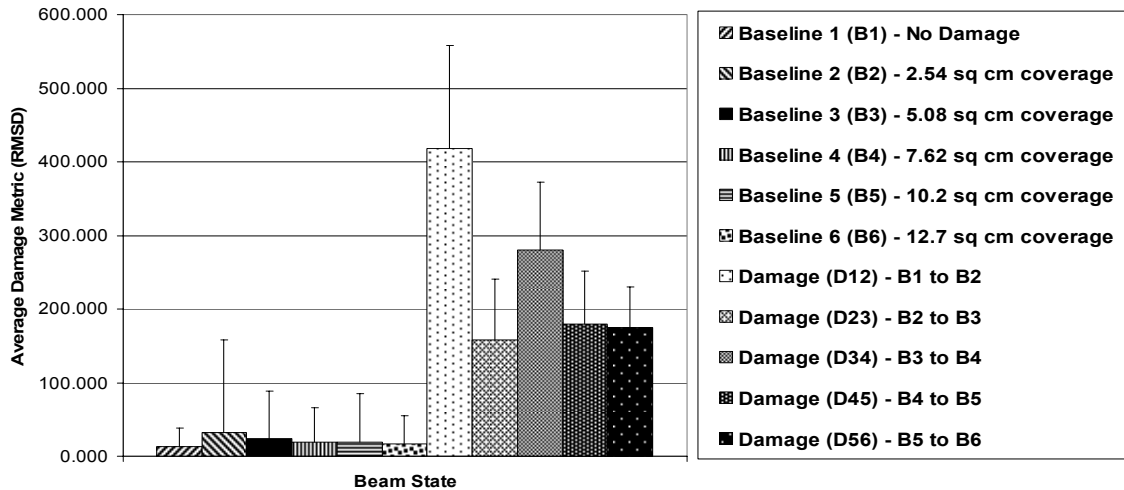


Figure B.52: Coverage damage metric plot relative to previous baseline from 96.5-98.5 kHz.

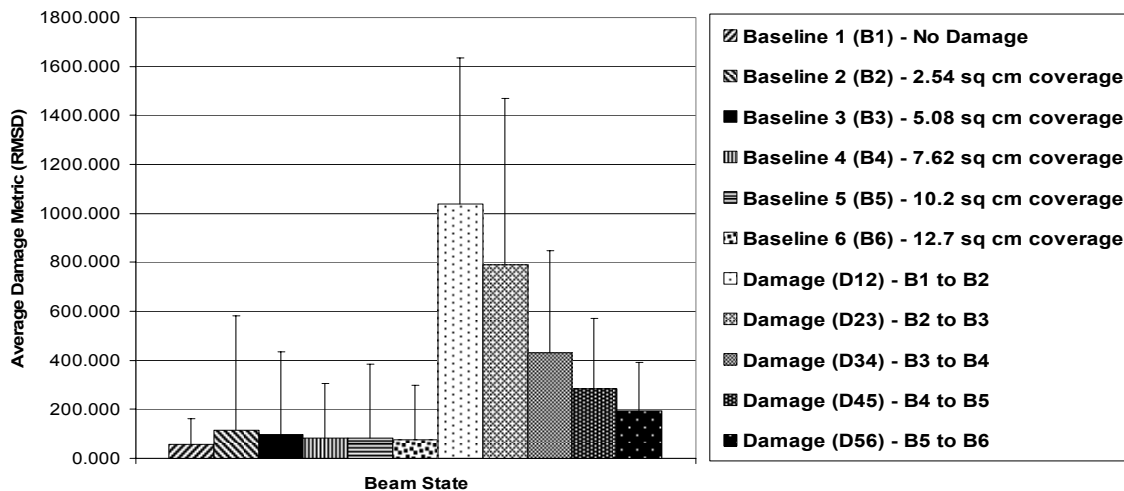


Figure B.53: Coverage damage metric plot relative to previous baseline from 103-105 kHz.

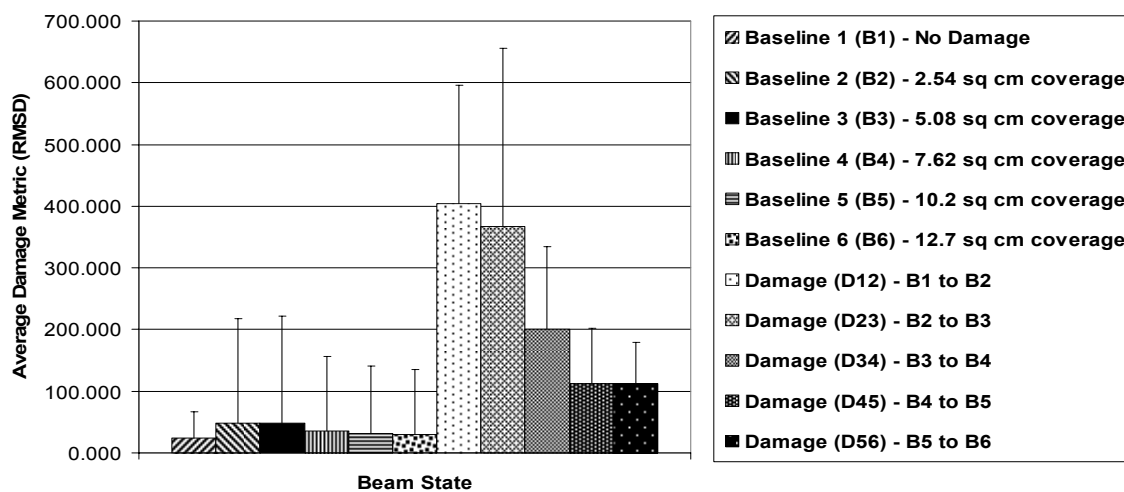


Figure B.54: Coverage damage metric plot relative to previous baseline from 126-128 kHz.

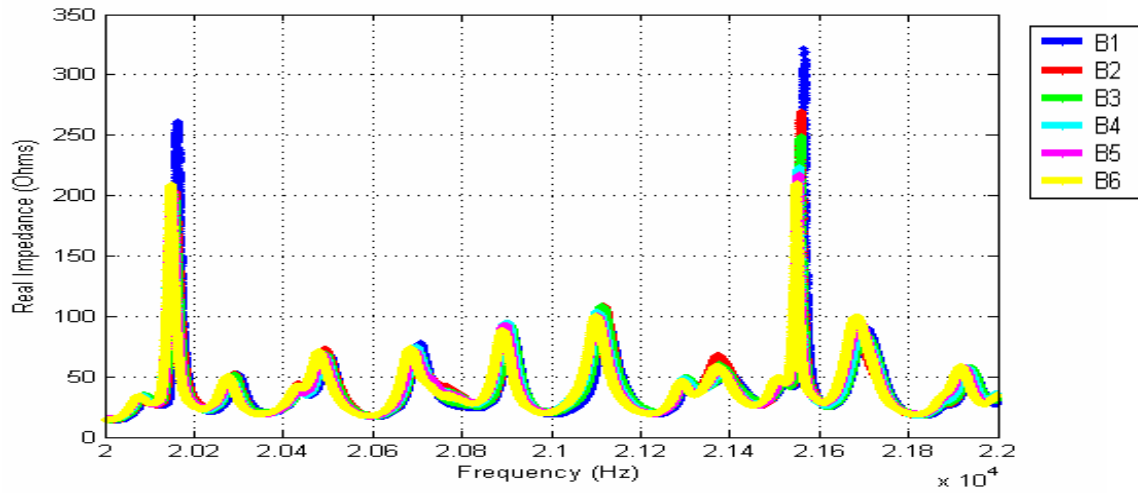


Figure B.55: Corrosion surface coverage impedance signatures from 20-22 kHz.

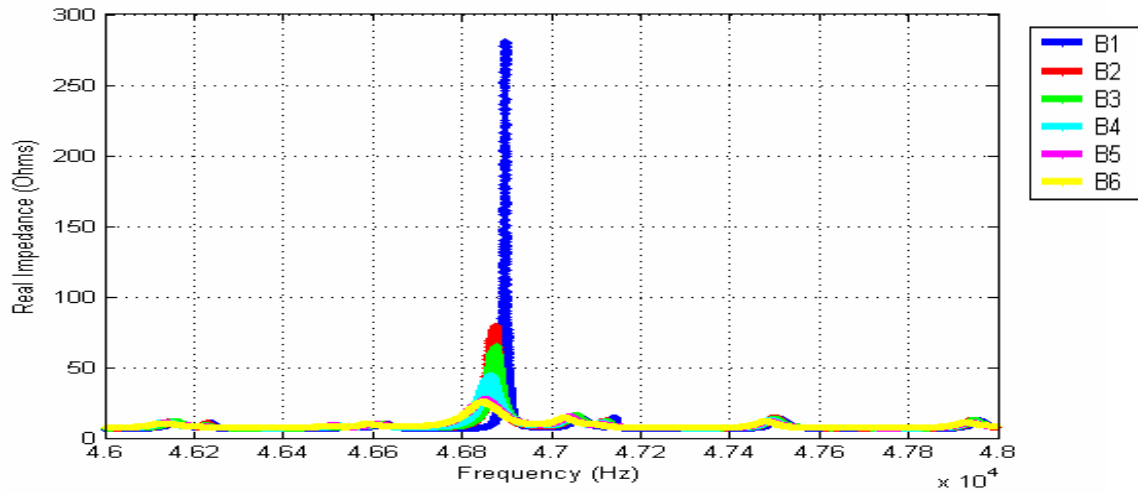


Figure B.56: Corrosion surface coverage impedance signatures from 46-48 kHz.

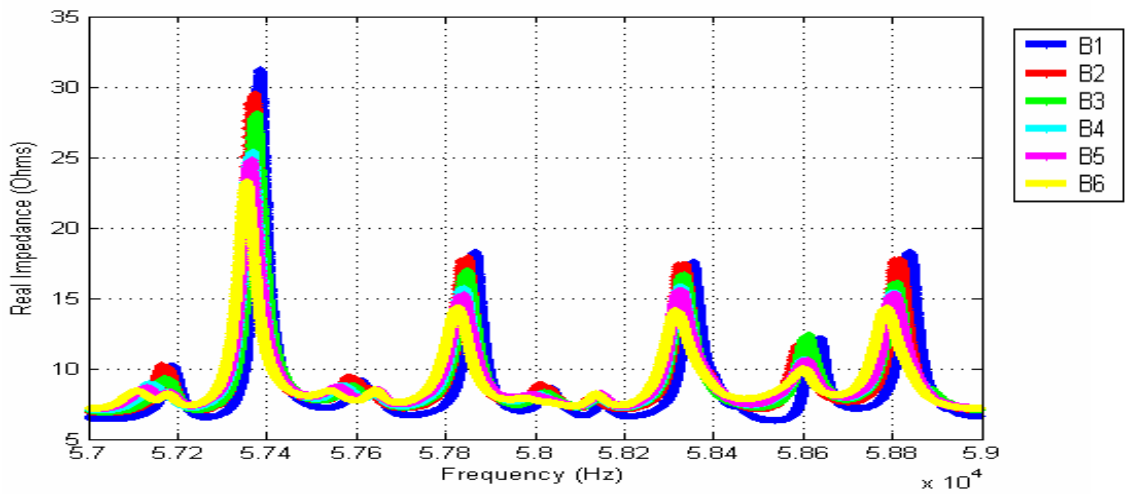


Figure B.57: Corrosion surface coverage impedance signatures from 57-59 kHz.

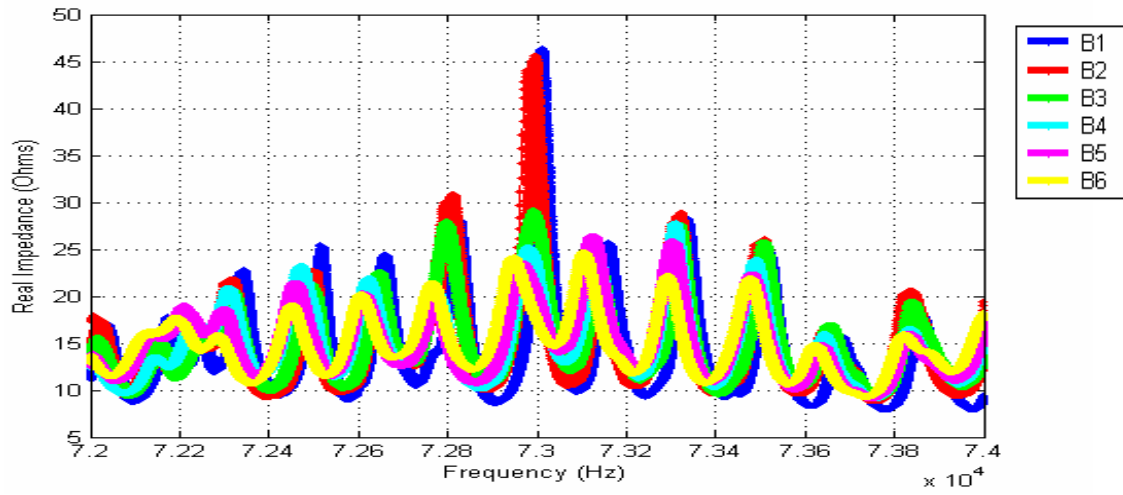


Figure B.58: Corrosion surface coverage impedance signatures from 72-74 kHz.

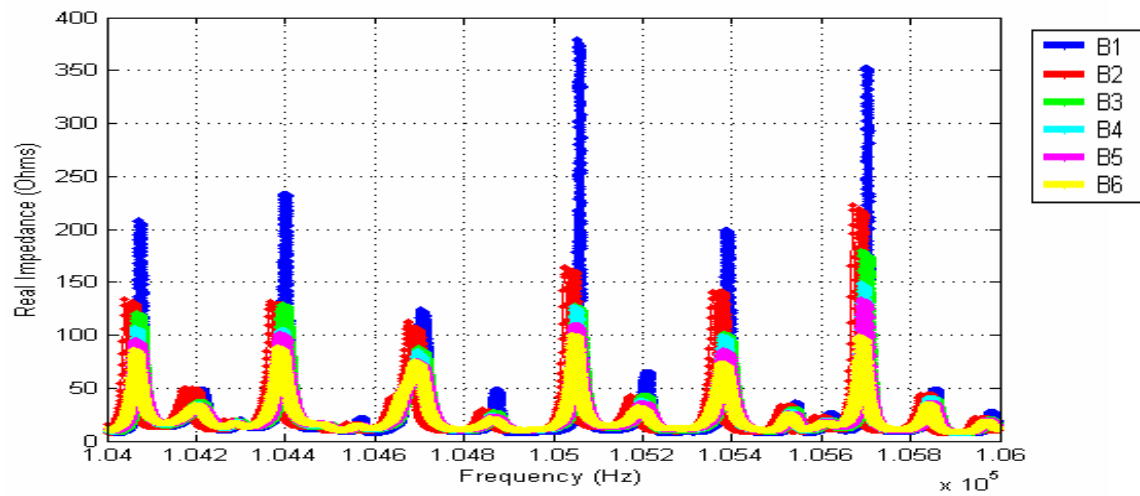


Figure B.59: Corrosion surface coverage impedance signatures from 104-106 kHz.

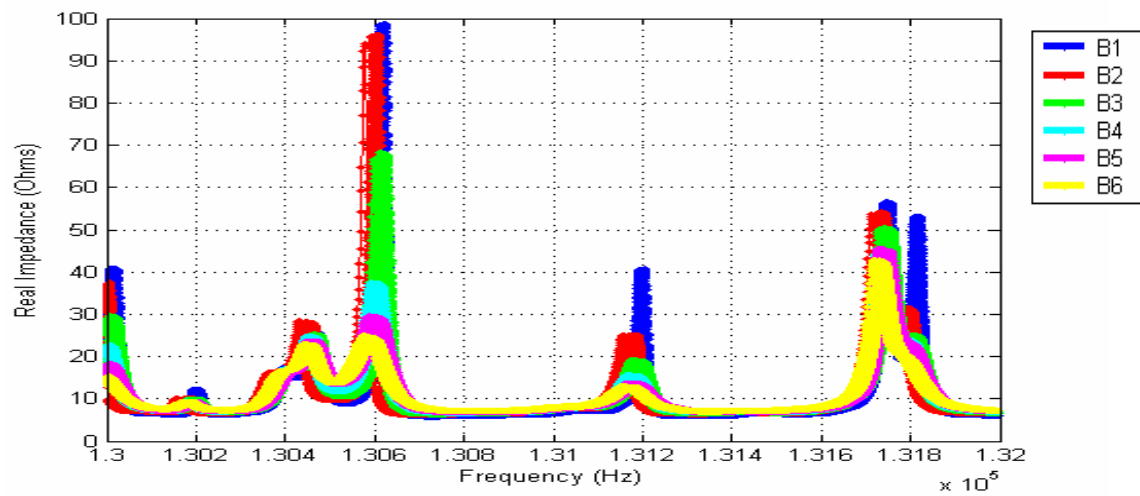


Figure B.60: Corrosion surface coverage impedance signatures from 130-132 kHz

Appendix C

Plate Corrosion Impedance and Damage Metric Plots

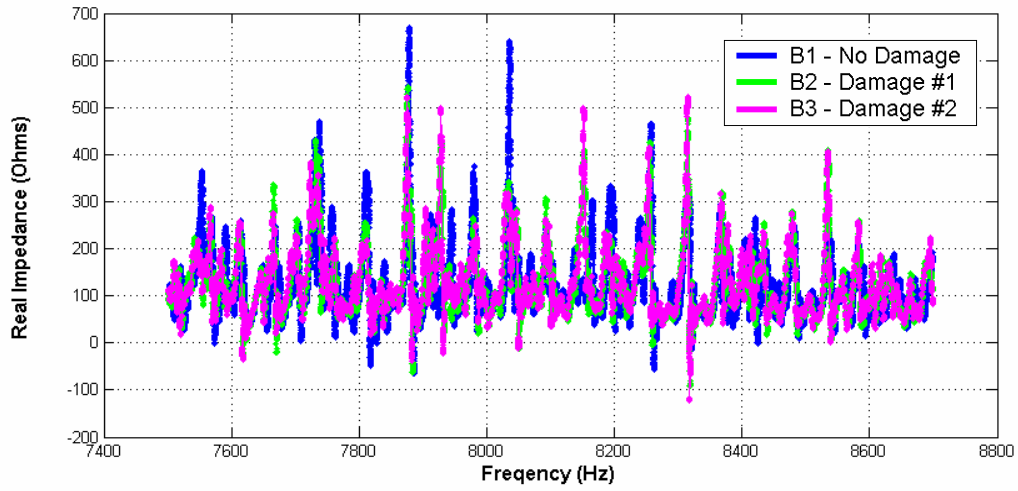


Figure C.1: Plate impedance signatures measured with PZT #2.

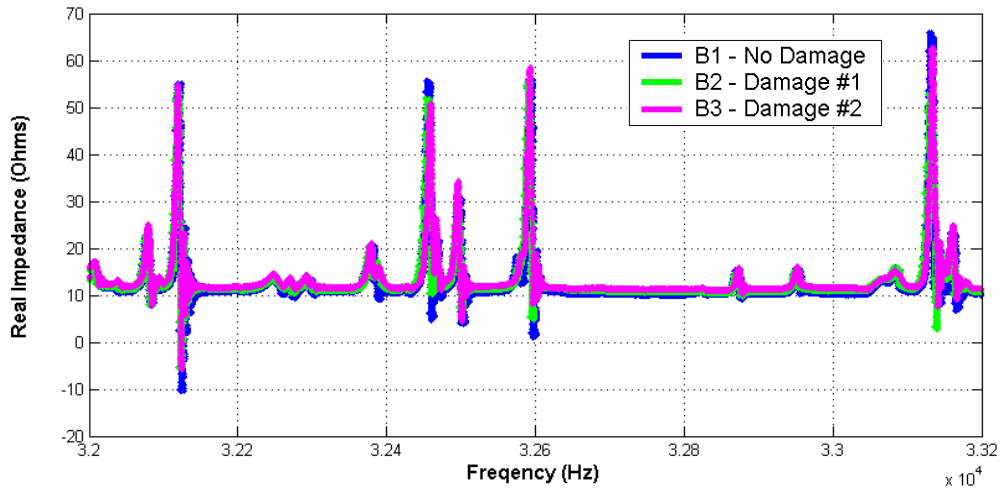


Figure C.2: Plate impedance signatures measured with PZT #2.

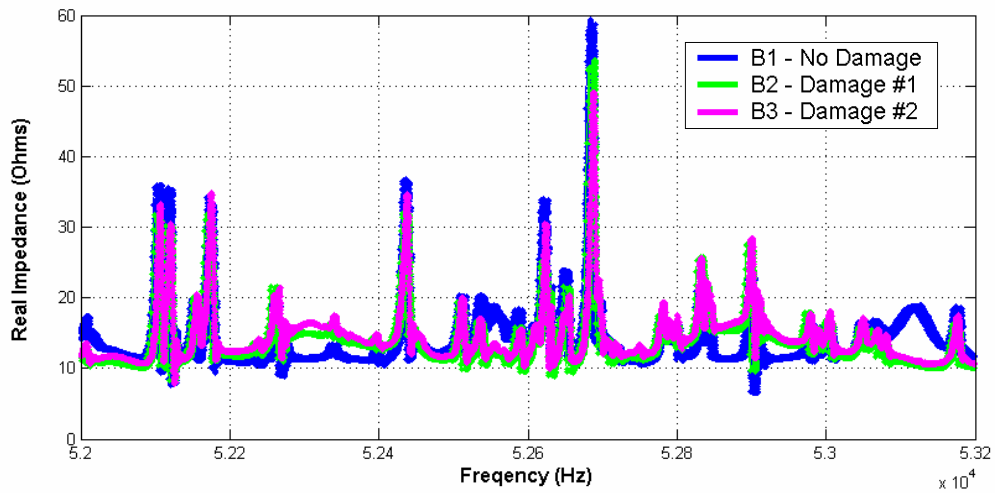


Figure C.3: Plate impedance signatures measured with PZT #2.

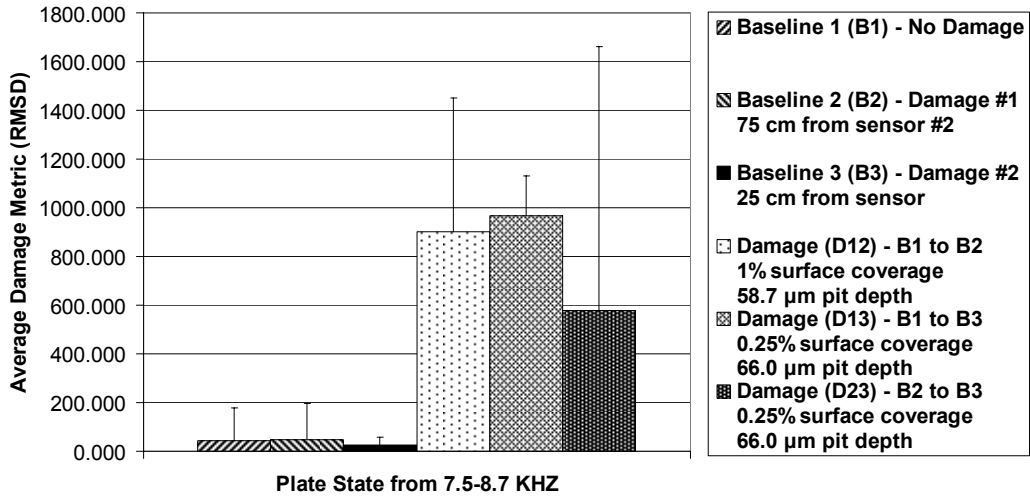


Figure C.4: Plate damage plots for PZT #2.

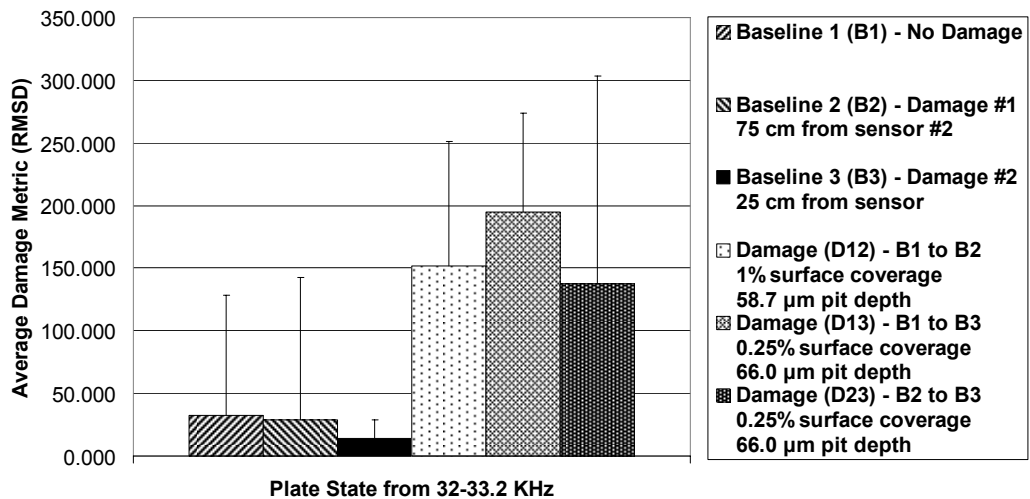


Figure C.5: Plate damage plots for PZT #2.

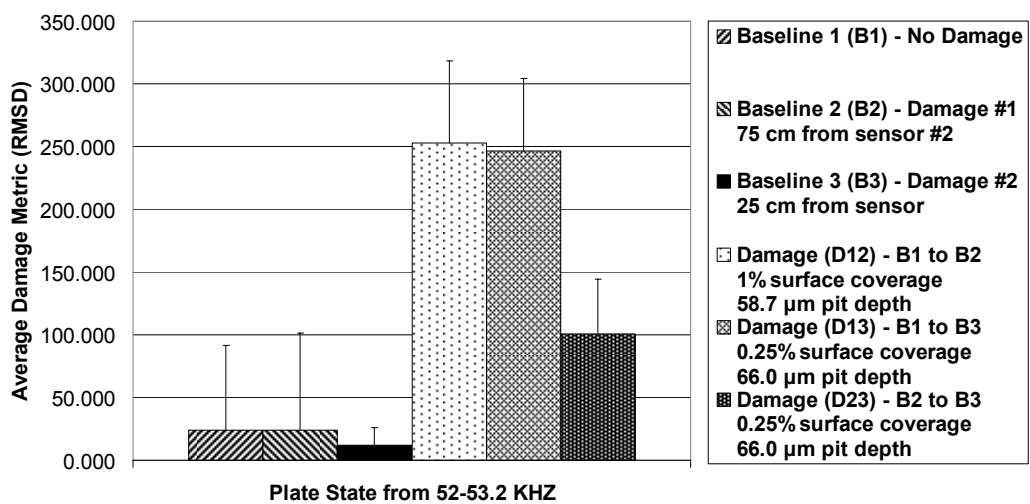


Figure C.6: Plate damage plots for PZT #2.

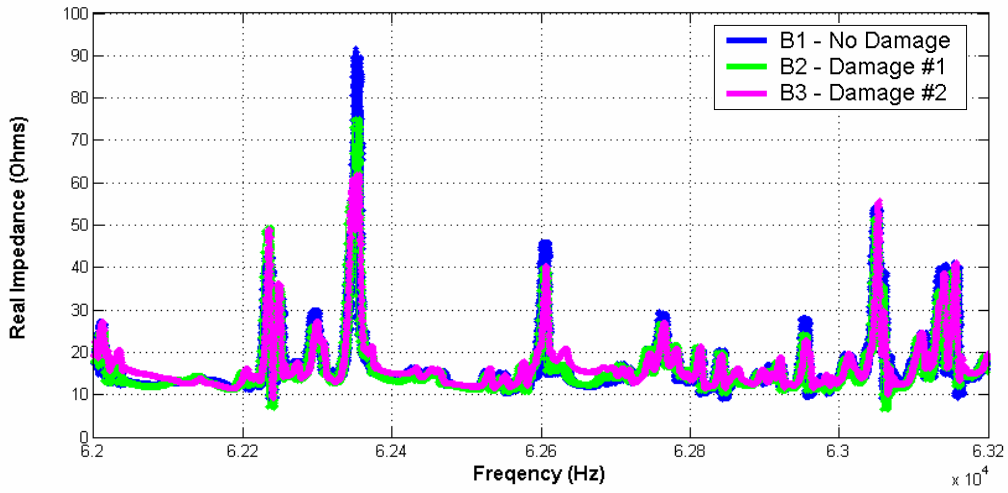


Figure C.7: Plate impedance signatures measured with PZT #2.

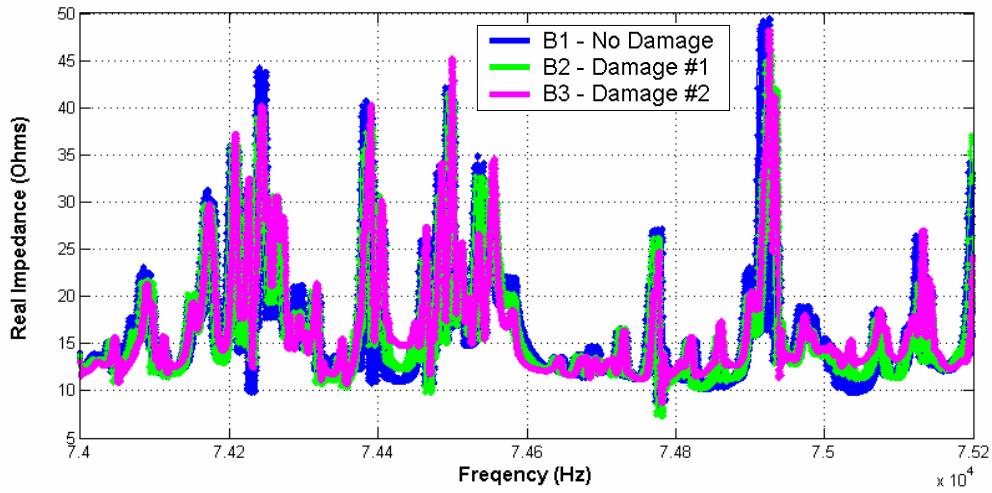


Figure C.8: Plate impedance signatures measured with PZT #2.

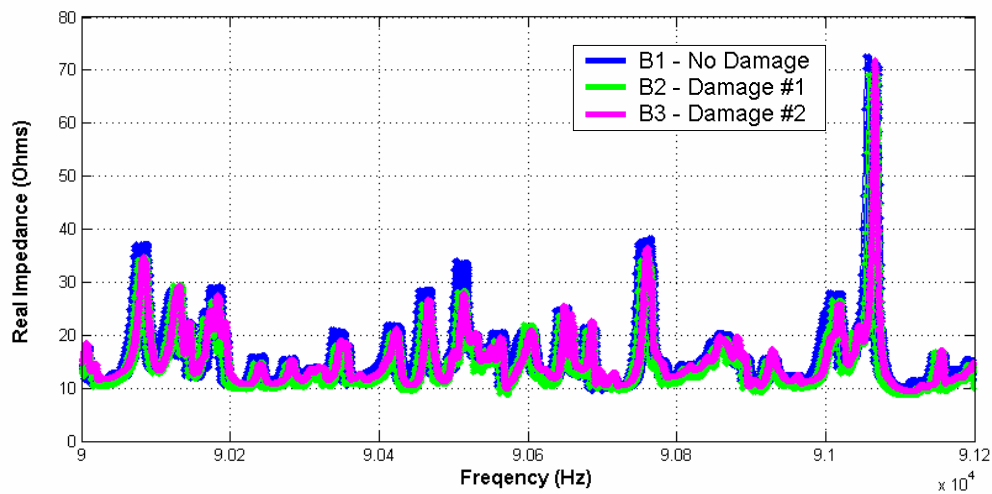


Figure C.9: Plate impedance signatures measured with PZT #2.

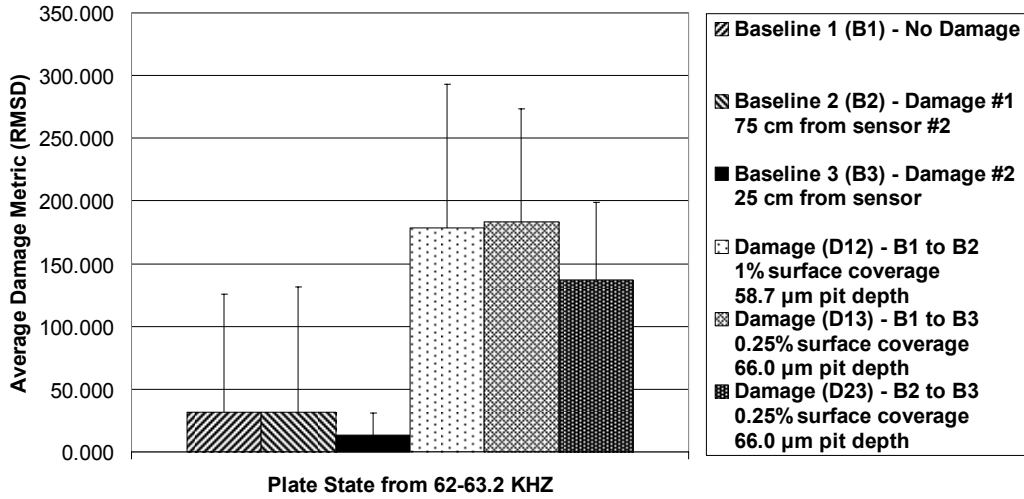


Figure C.10: Plate damage plots for PZT #2.

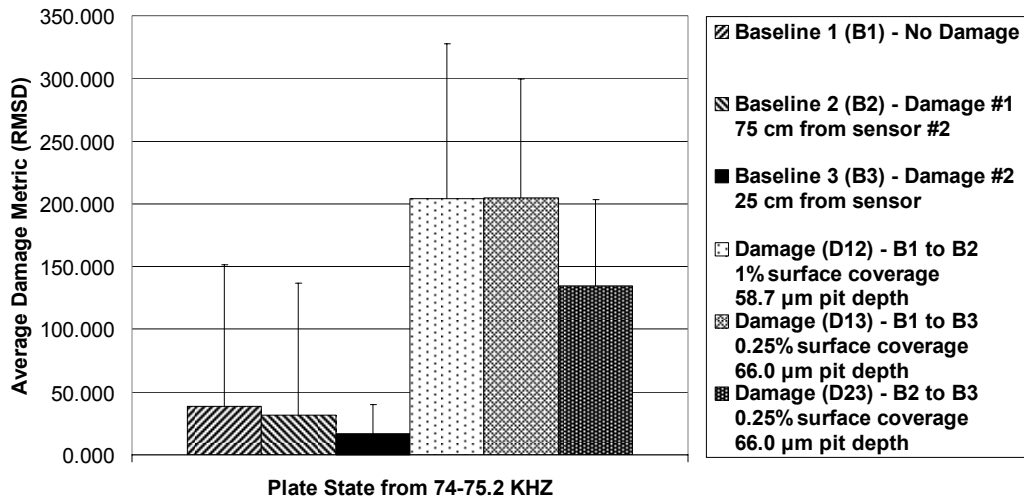


Figure C.11: Plate damage plots for PZT #2.

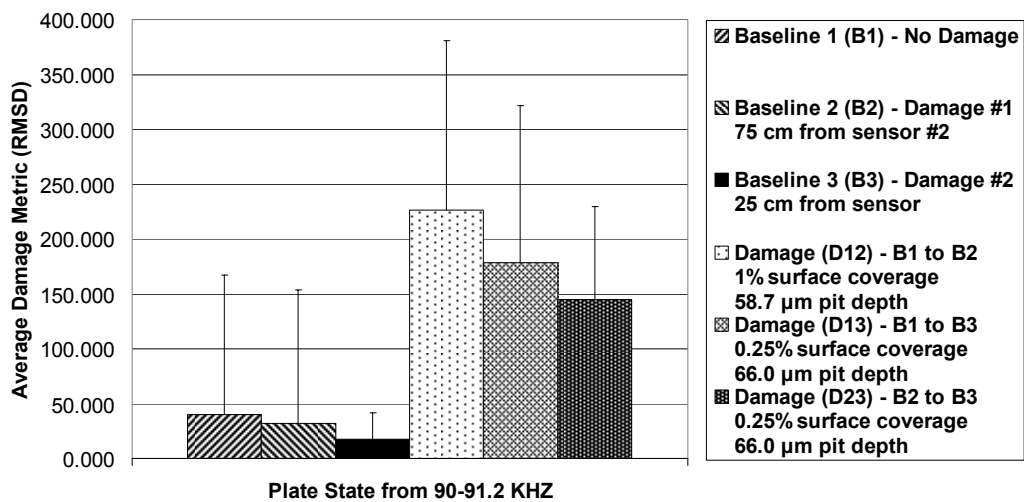


Figure C.12: Plate damage plots for PZT #2.

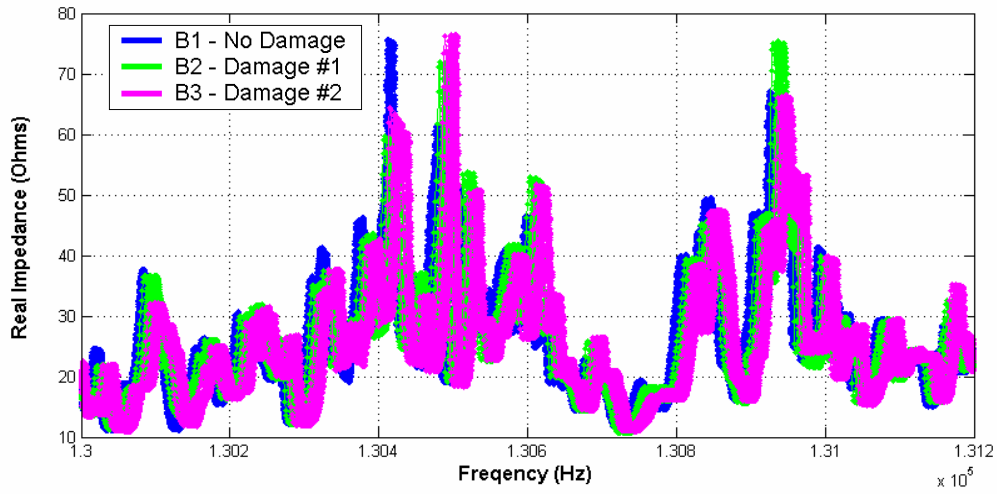


Figure C.13: Plate impedance signatures measured with PZT #2.

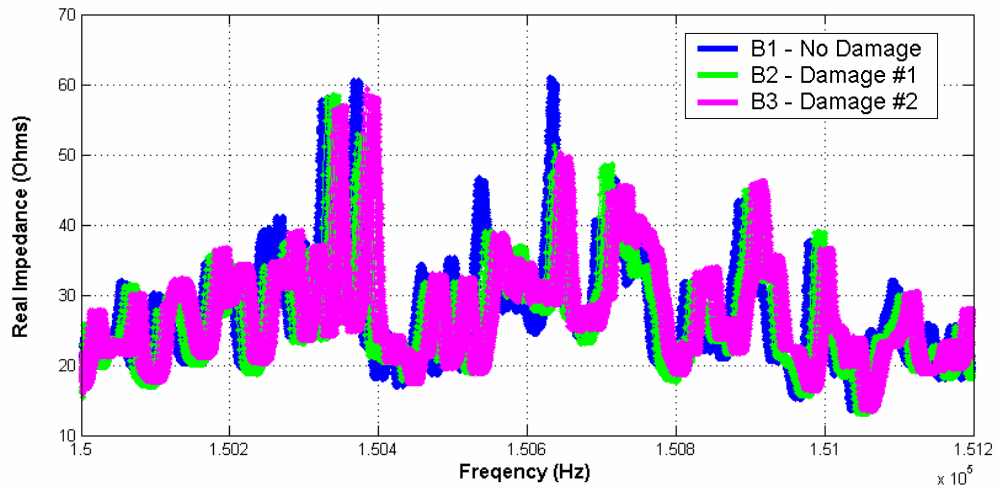


Figure C.14: Plate impedance signatures measured with PZT #2.

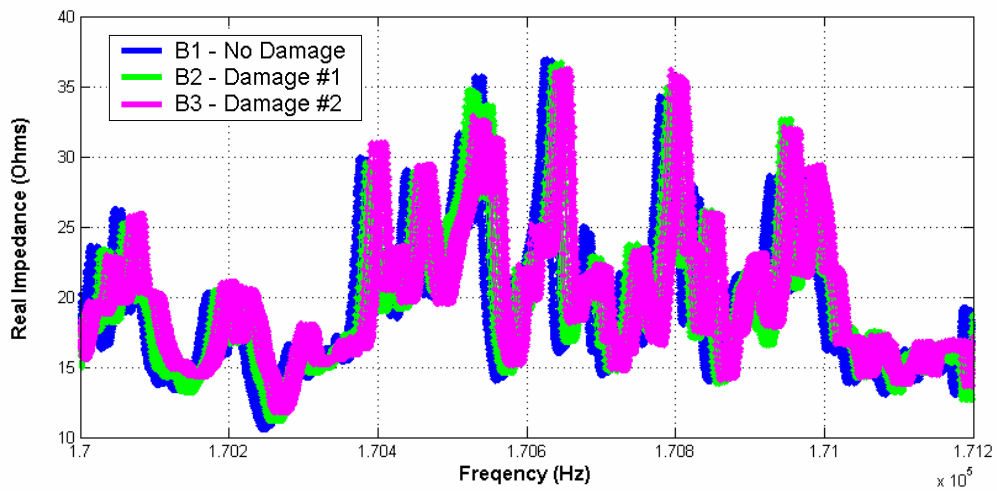


Figure C.15: Plate impedance signatures measured with PZT #2.

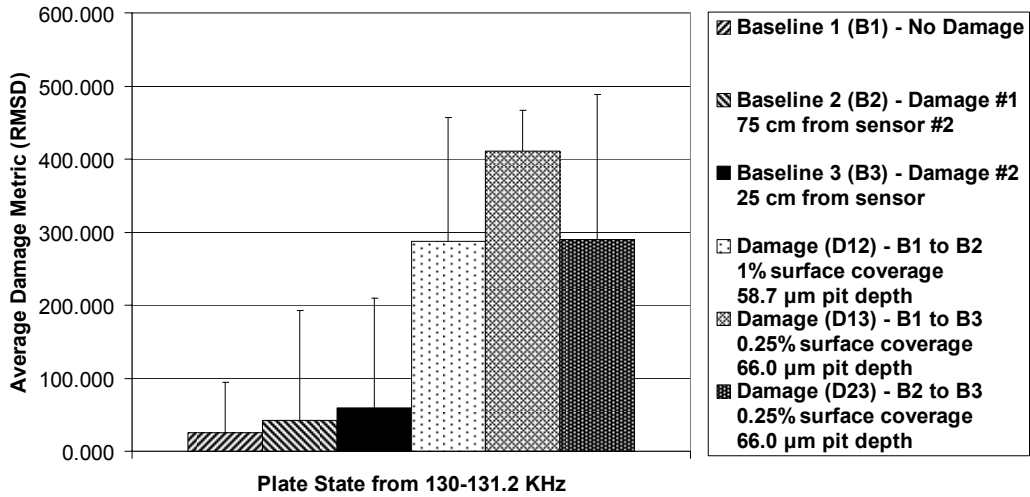


Figure C.16: Plate damage plots for PZT #2.

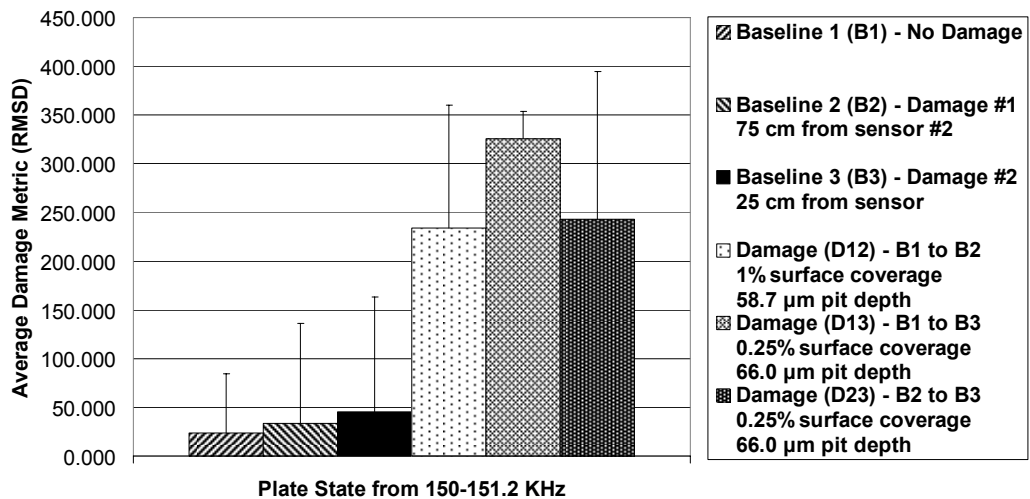


Figure C.17: Plate damage plots for PZT #2.

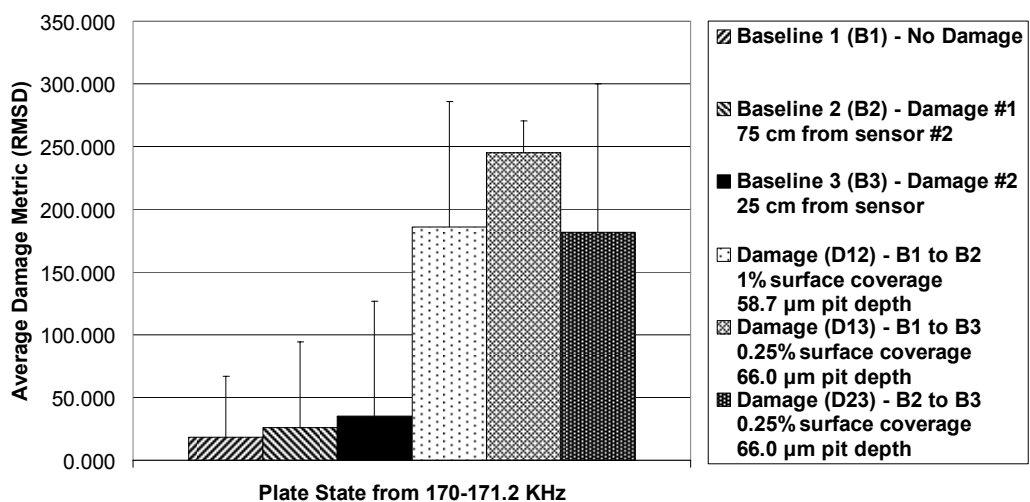


Figure C.18: Plate damage plots for PZT #2.

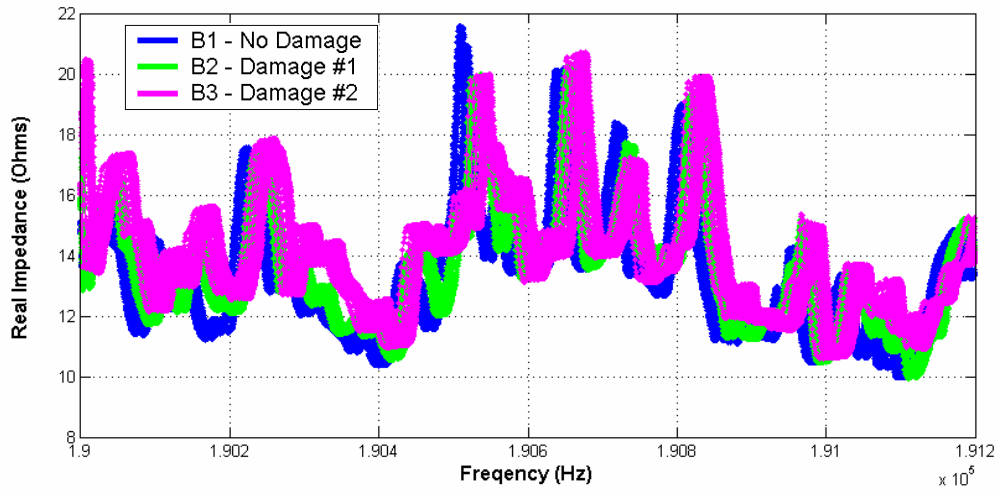


Figure C.19: Plate impedance signatures measured with PZT #2.

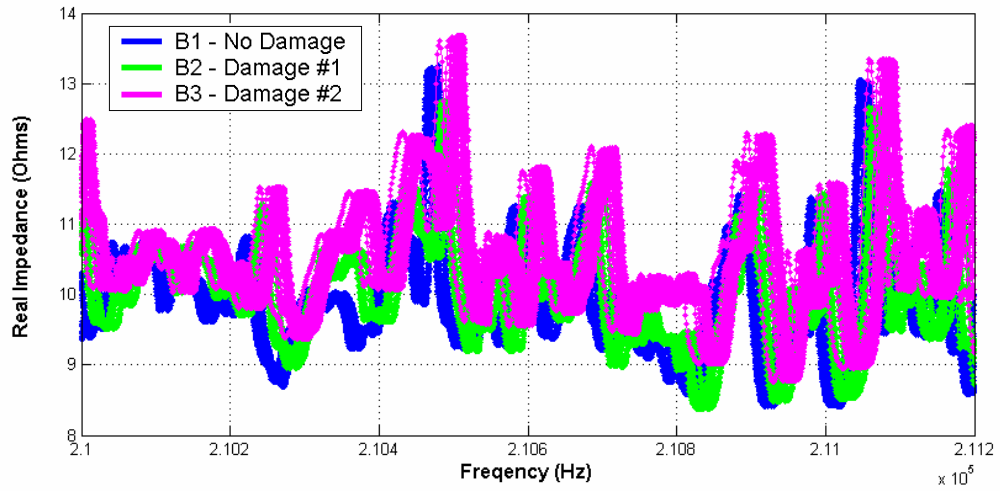


Figure C.20: Plate impedance signatures measured with PZT #2.

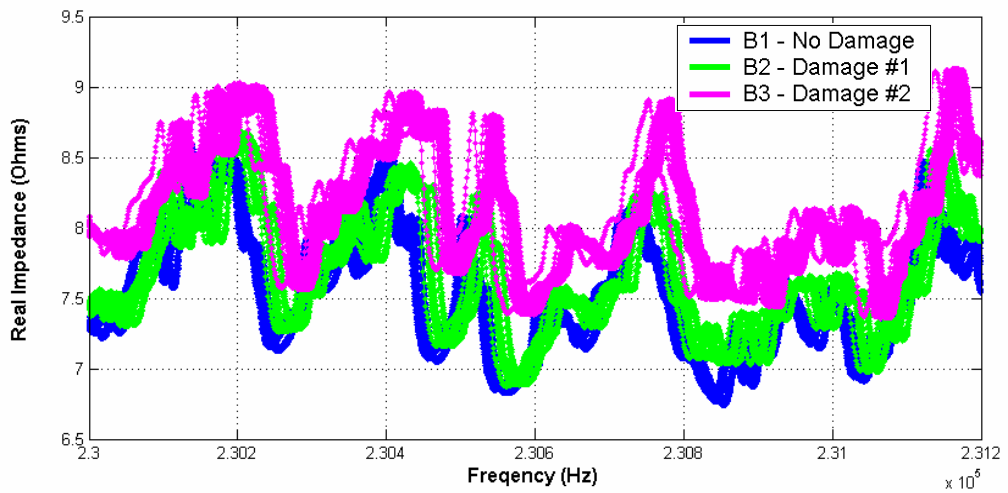


Figure C.21: Plate impedance signatures measured with PZT #2.

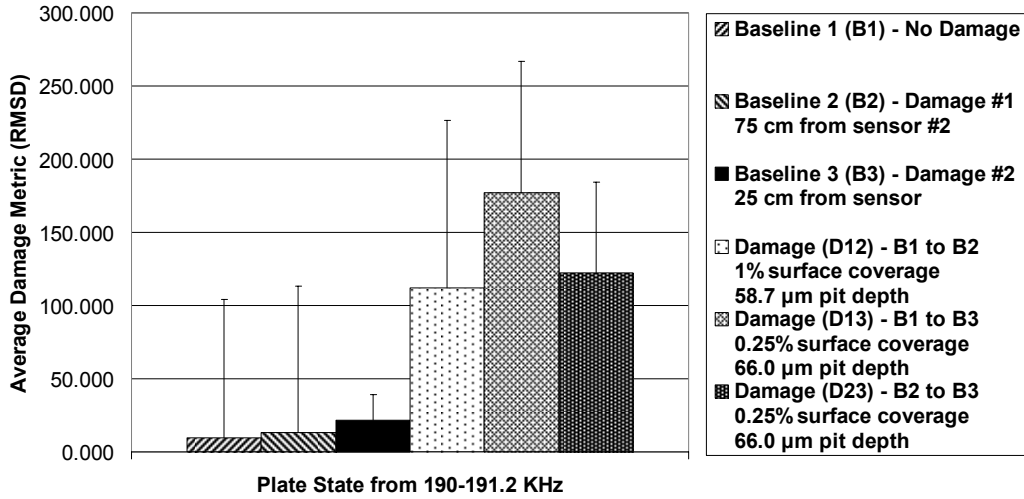


Figure C.22: Plate damage plots for PZT #2.

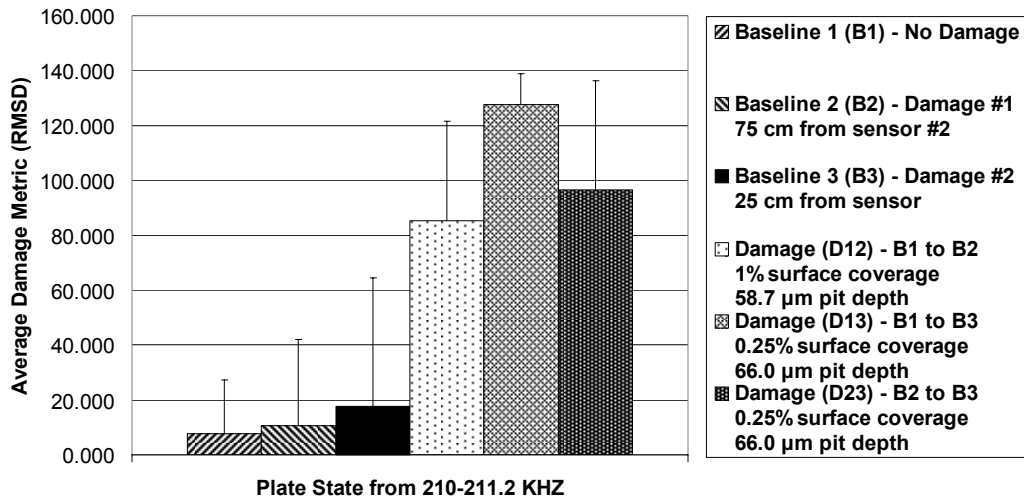


Figure C.23: Plate damage plots for PZT #2.

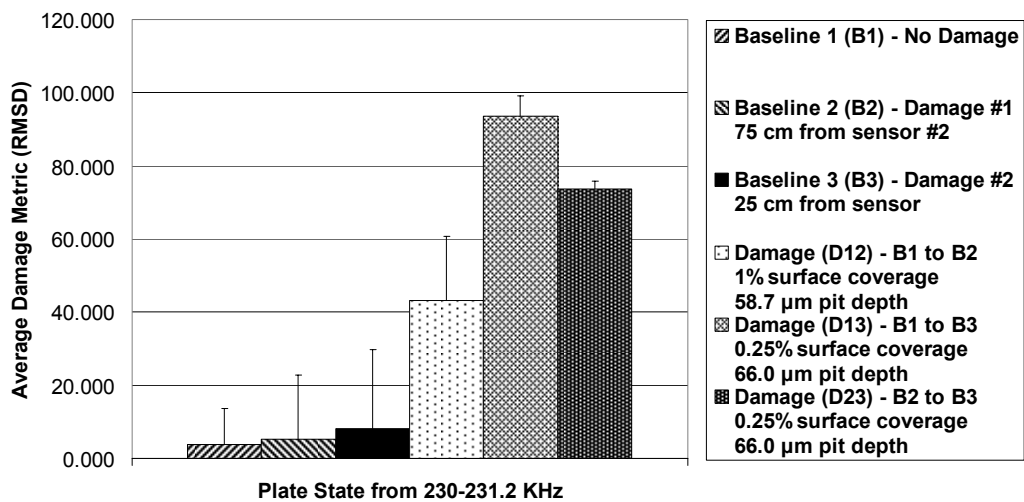


Figure C.24: Plate damage plots for PZT #2.

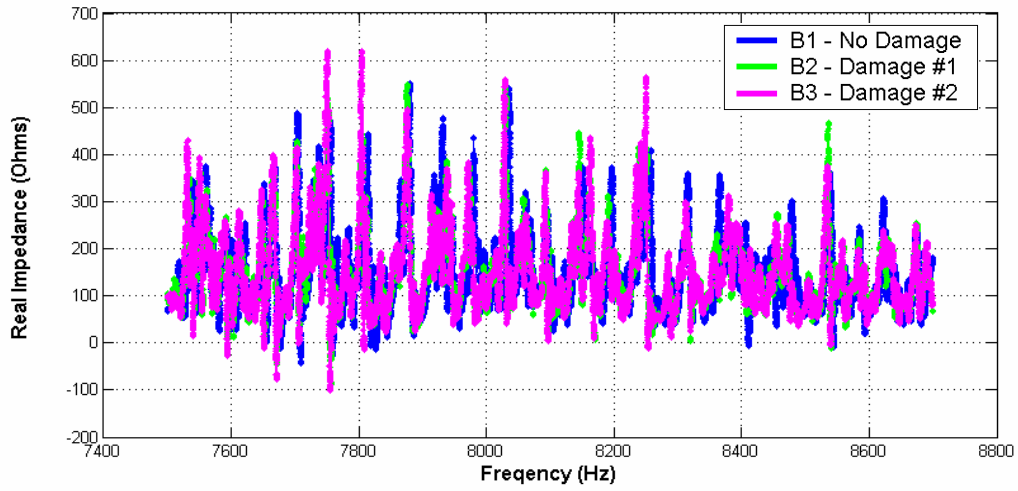


Figure C.25: Plate impedance signatures measured with PZT #3.

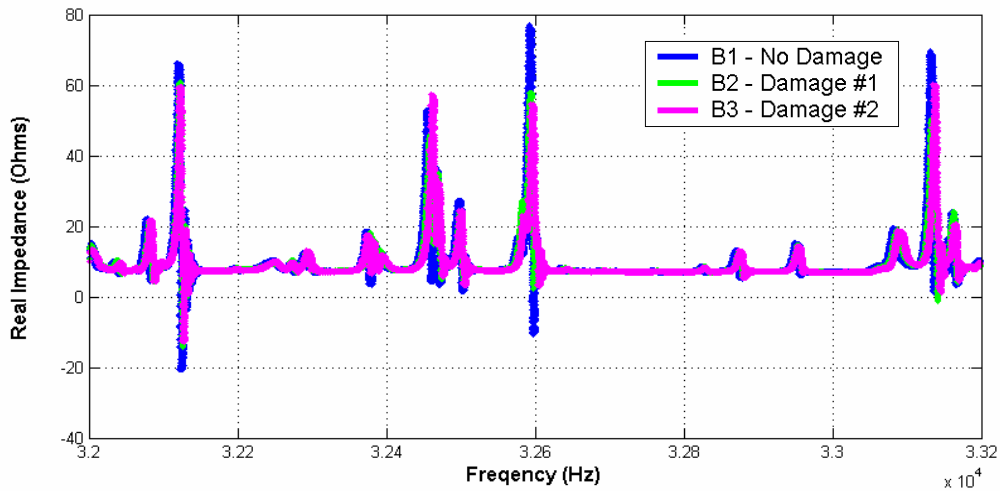


Figure C.26: Plate impedance signatures measured with PZT #3.

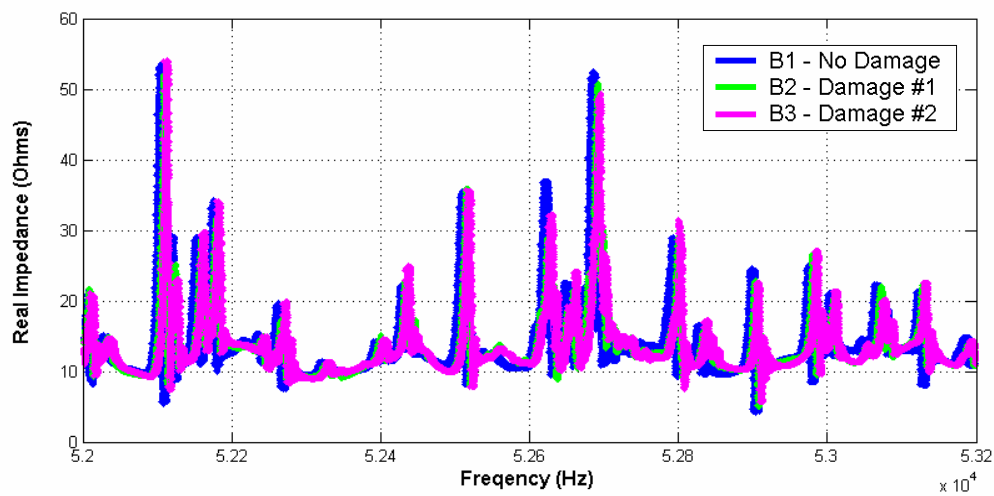


Figure C.27: Plate impedance signatures measured with PZT #3.

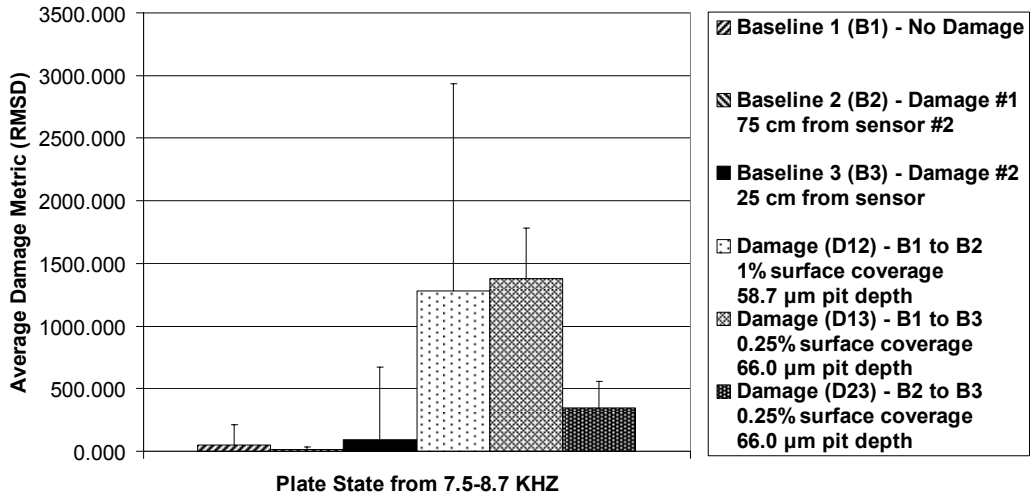


Figure C.28: Plate damage plots for PZT #3.

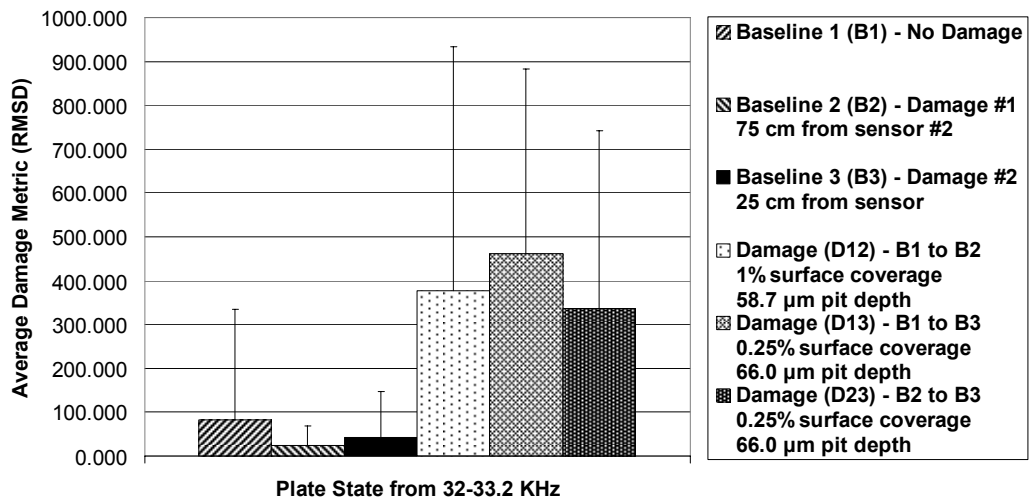


Figure C.29: Plate damage plots for PZT #3.

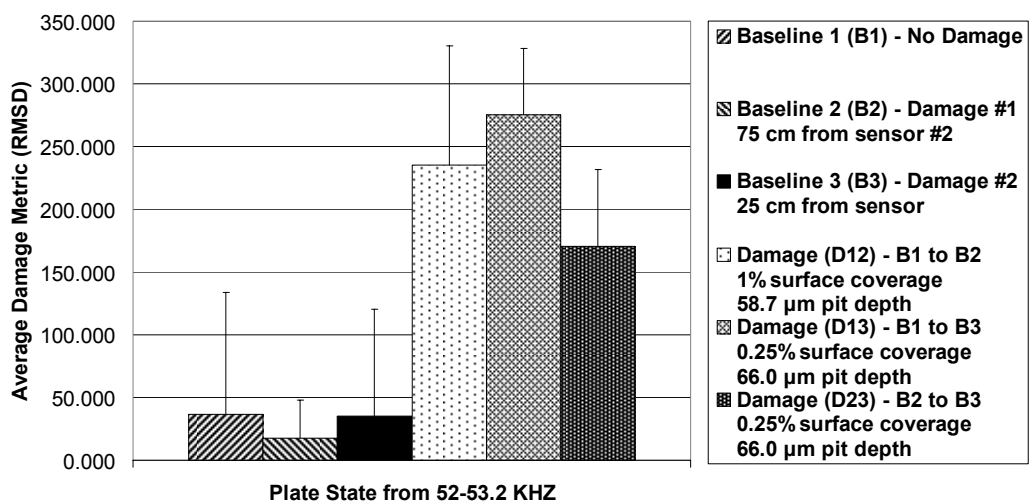


Figure C.30: Plate damage plots for PZT #3.

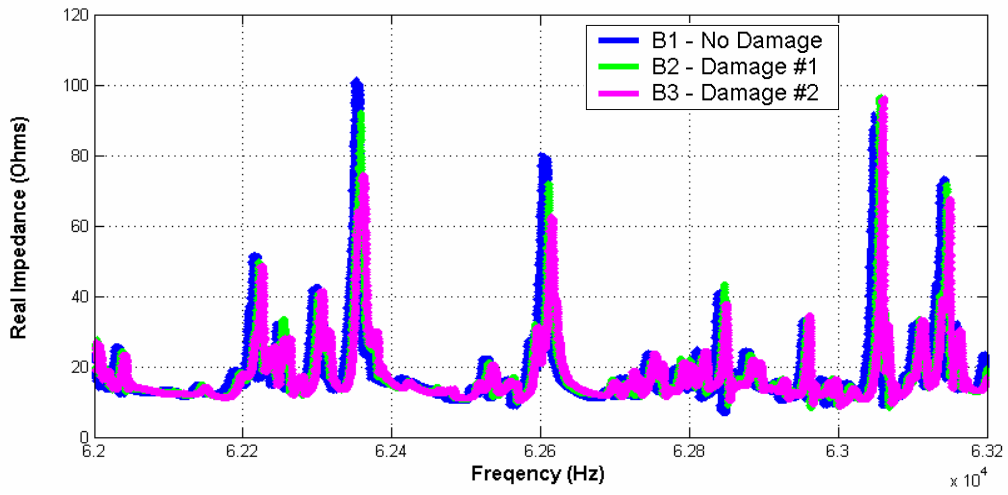


Figure C.31: Plate impedance signatures measured with PZT #3.

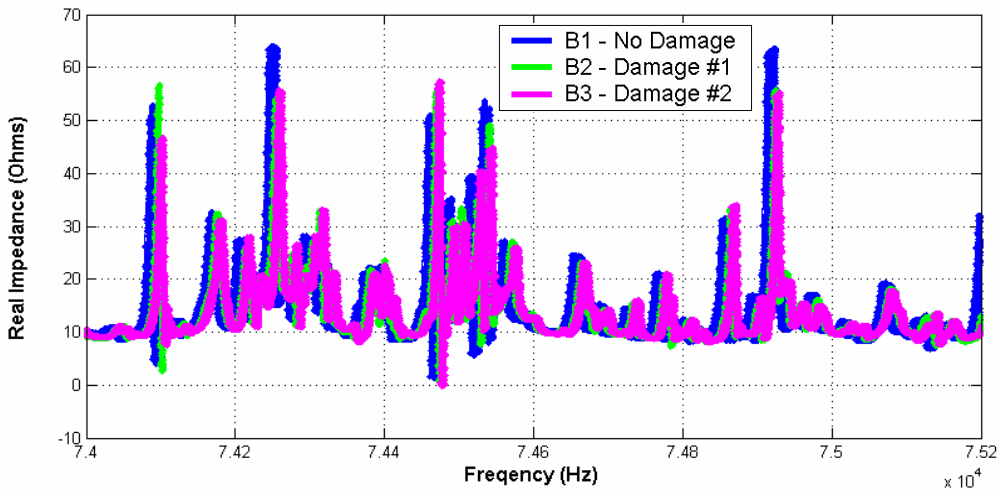


Figure C.32: Plate impedance signatures measured with PZT #3.

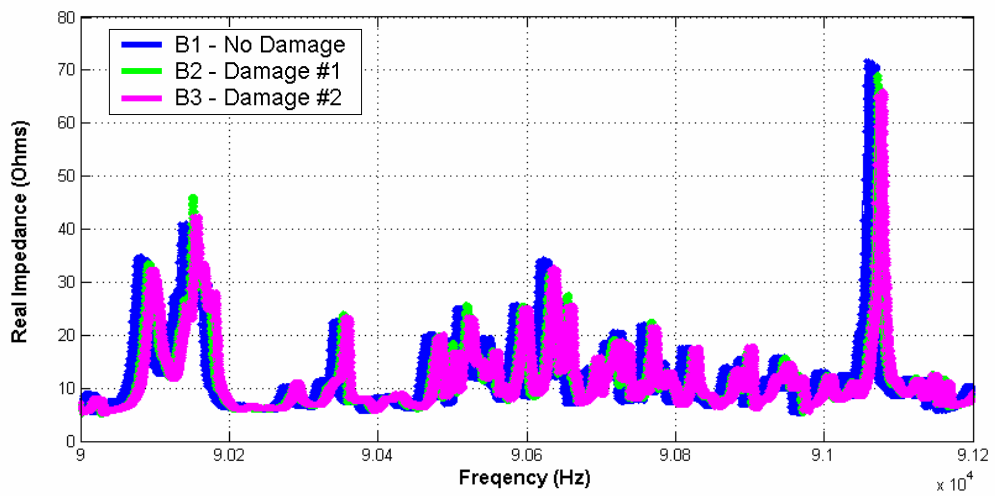


Figure C.33: Plate impedance signatures measured with PZT #3.

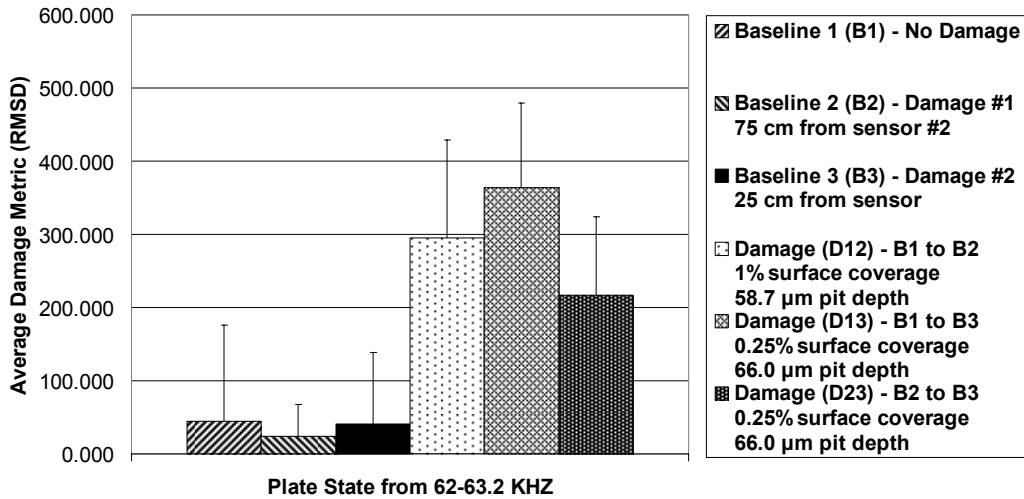


Figure C.34: Plate damage plots for PZT #3.

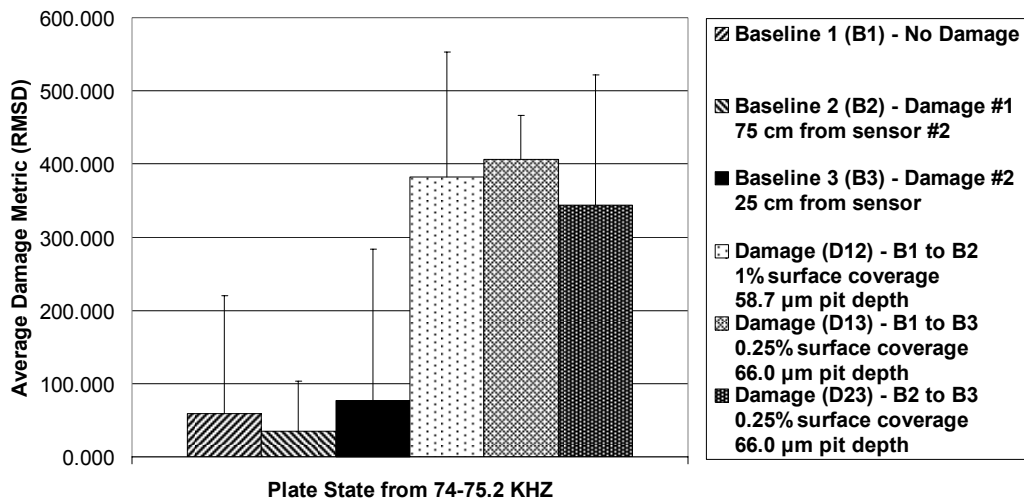


Figure C.35: Plate damage plots for PZT #3.

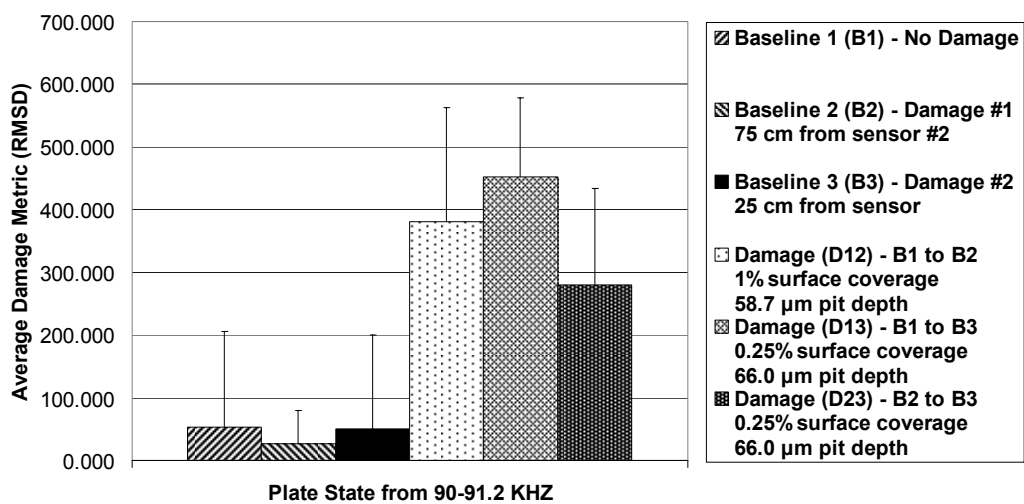


Figure C.36: Plate damage plots for PZT #3.

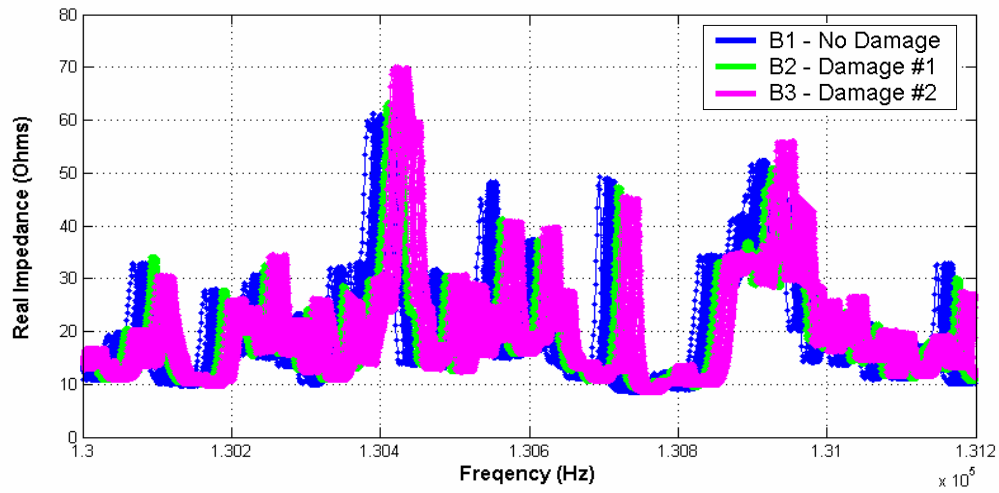


Figure C.37: Plate impedance signatures measured with PZT #3.

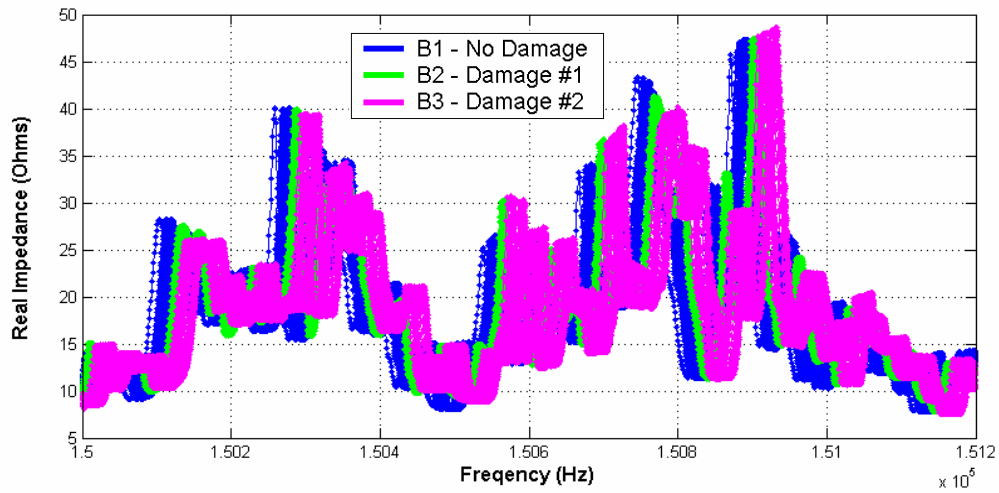


Figure C.38: Plate impedance signatures measured with PZT #3.

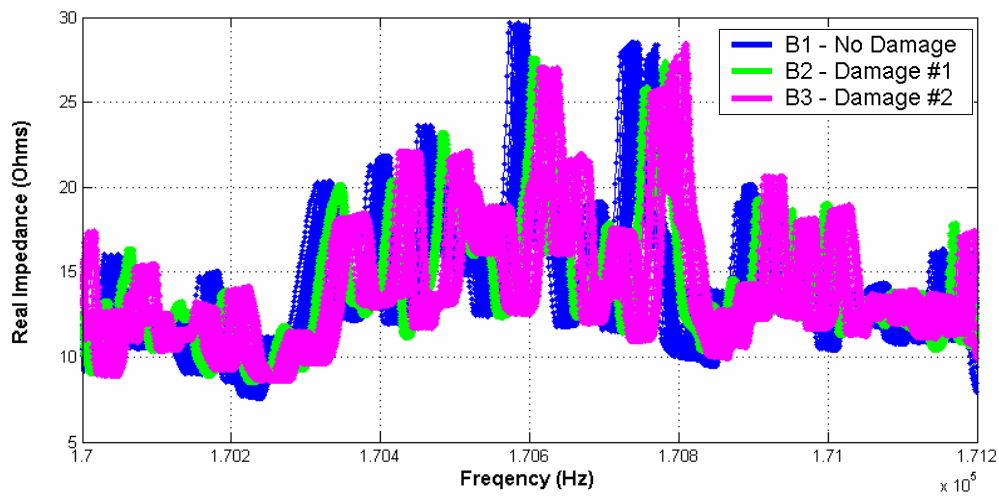


Figure C.39: Plate impedance signatures measured with PZT #3.

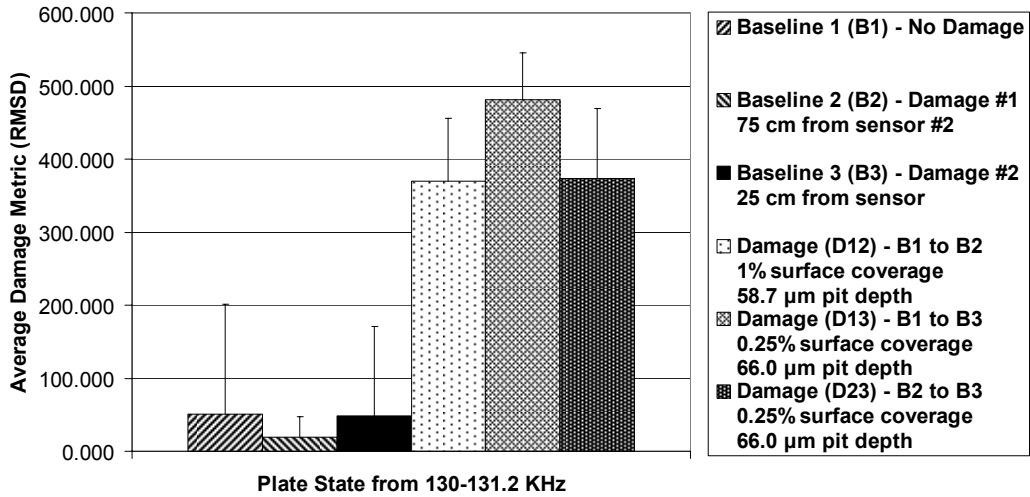


Figure C.40: Plate damage plots for PZT #3.

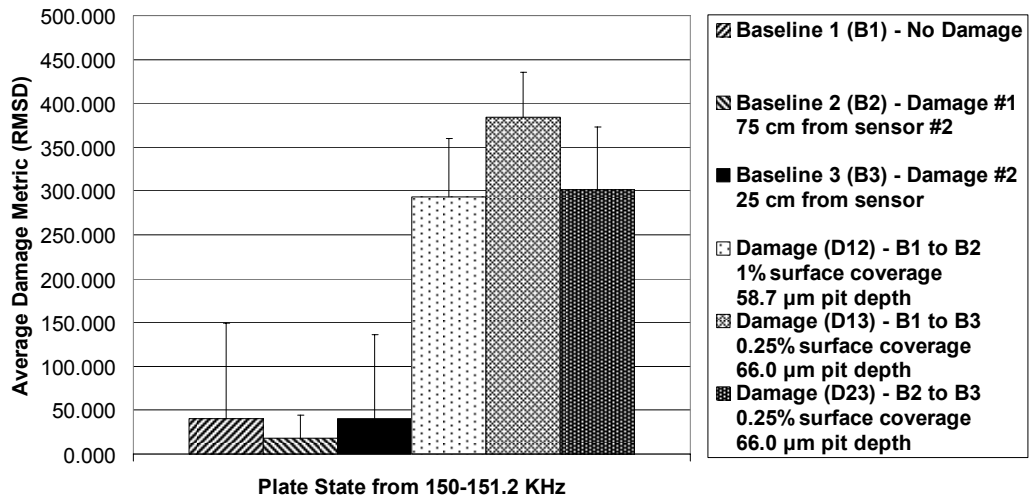


Figure C.41: Plate damage plots for PZT #3.

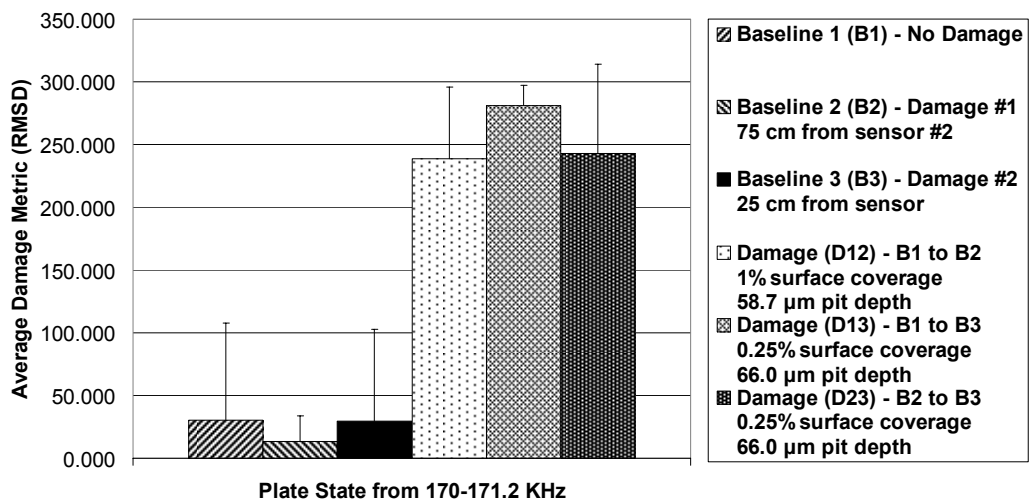


Figure C.42: Plate damage plots for PZT #3.

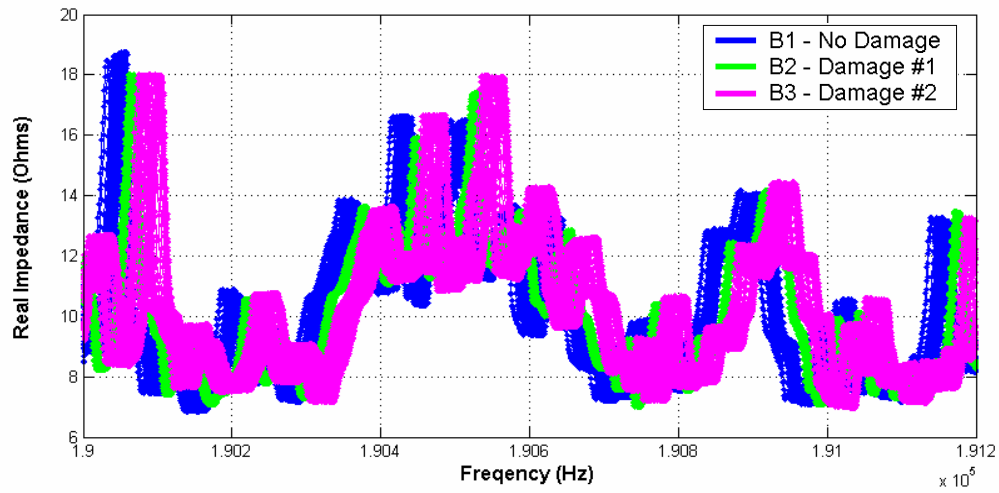


Figure C.43: Plate impedance signatures measured with PZT #3.

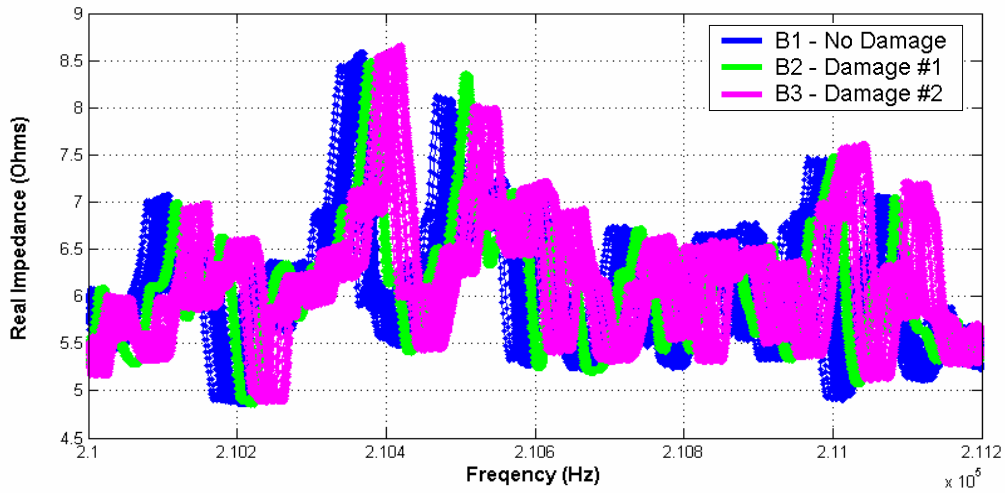


Figure C.44: Plate impedance signatures measured with PZT #3.

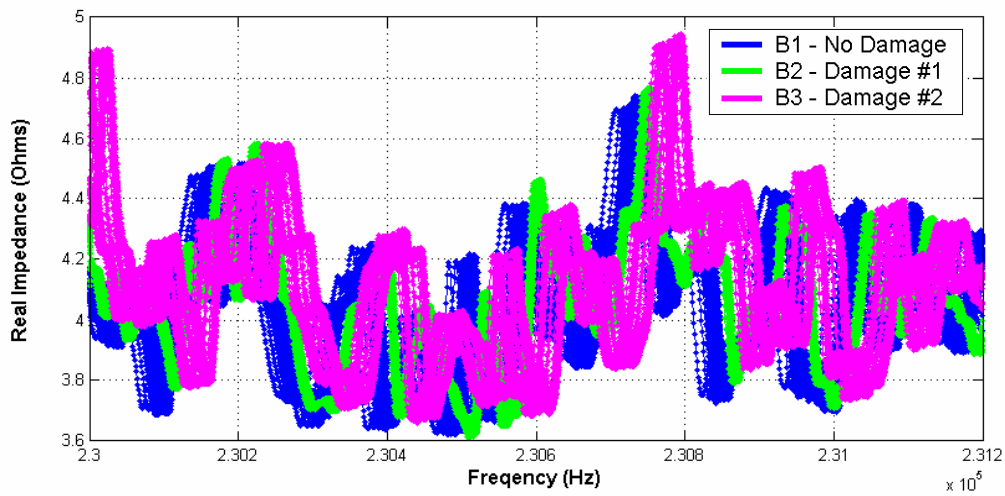


Figure C.45: Plate impedance signatures measured with PZT #3.

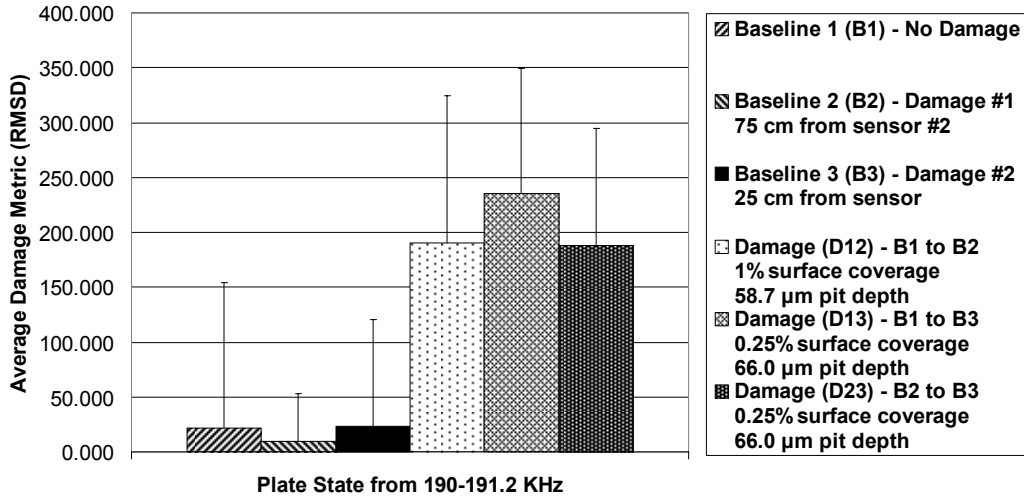


Figure C.46: Plate damage plots for PZT #3.

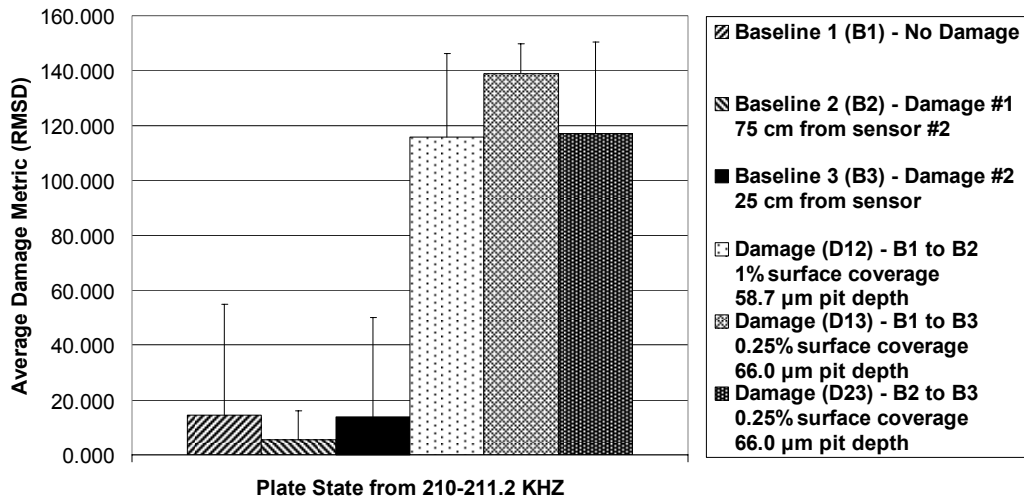


Figure C.47: Plate damage plots for PZT #3.

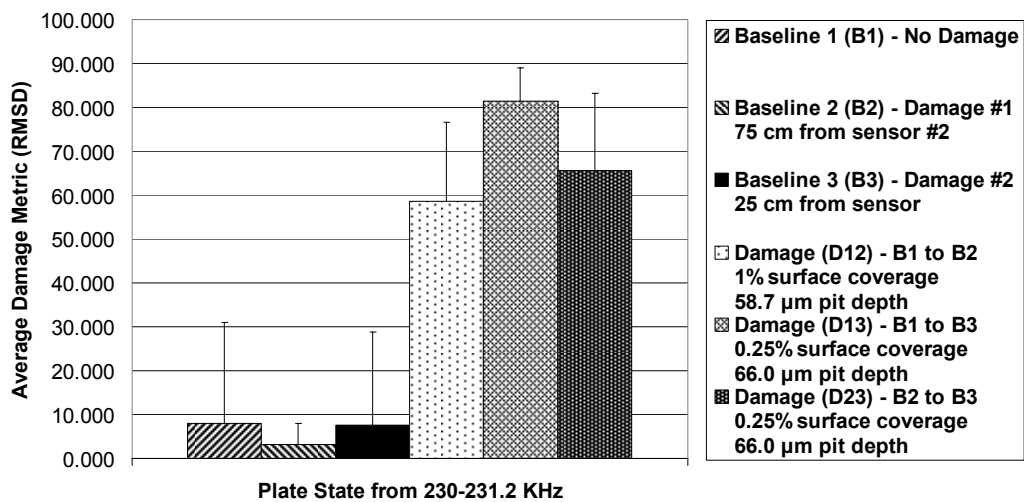


Figure C.48: Plate damage plots for PZT #3.

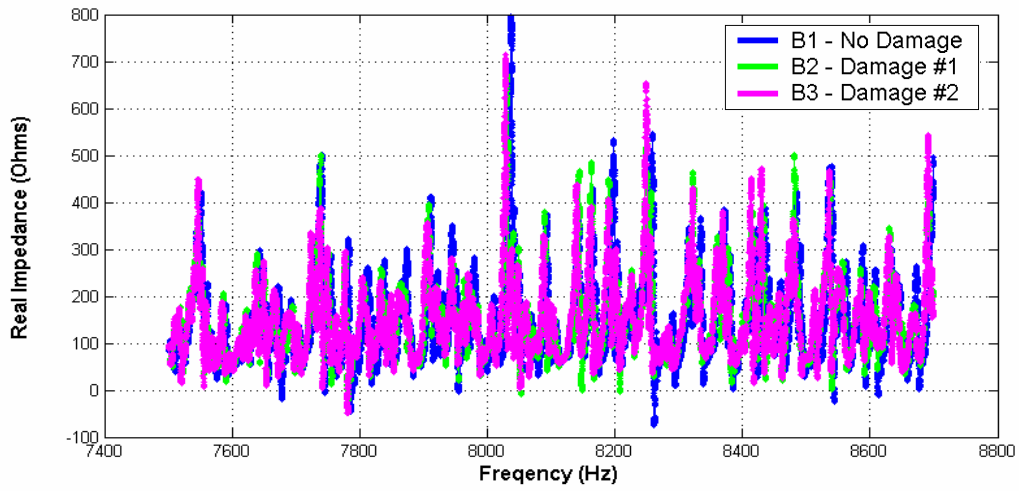


Figure C.49: Plate impedance signatures measured with PZT #4.

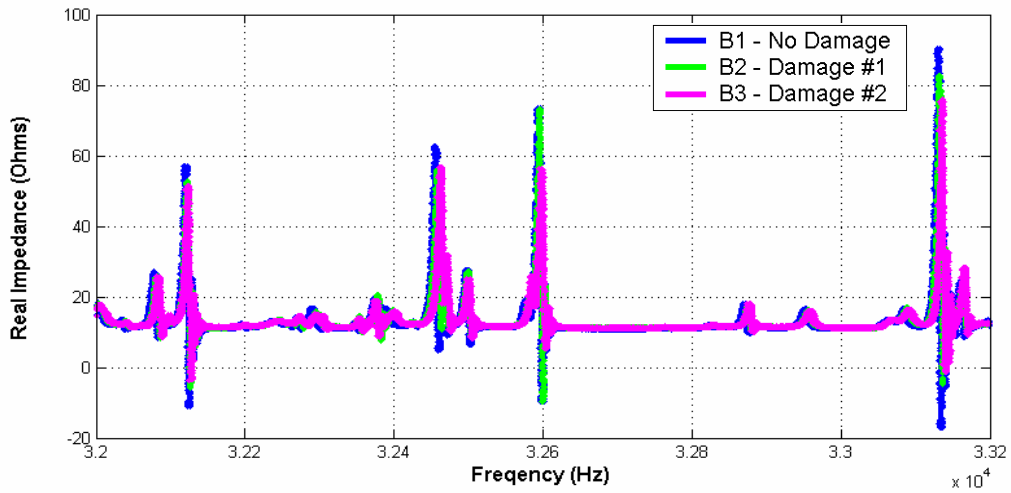


Figure C.50: Plate impedance signatures measured with PZT #4.

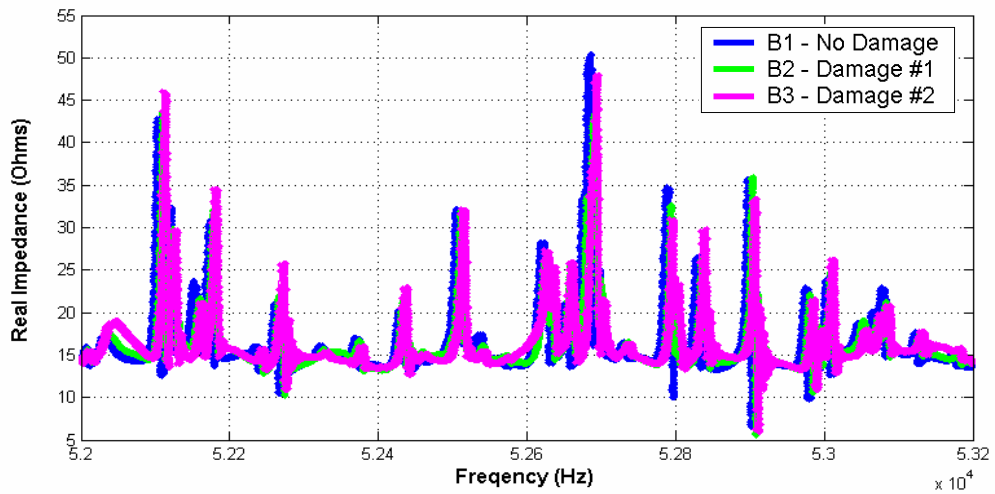


Figure C.51: Plate impedance signatures measured with PZT #4.

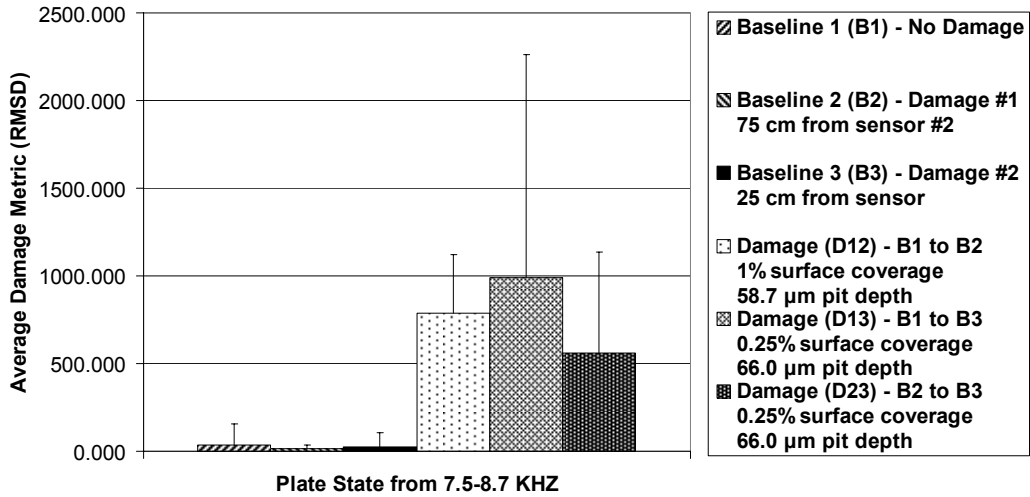


Figure C.52: Plate damage plots for PZT #4.

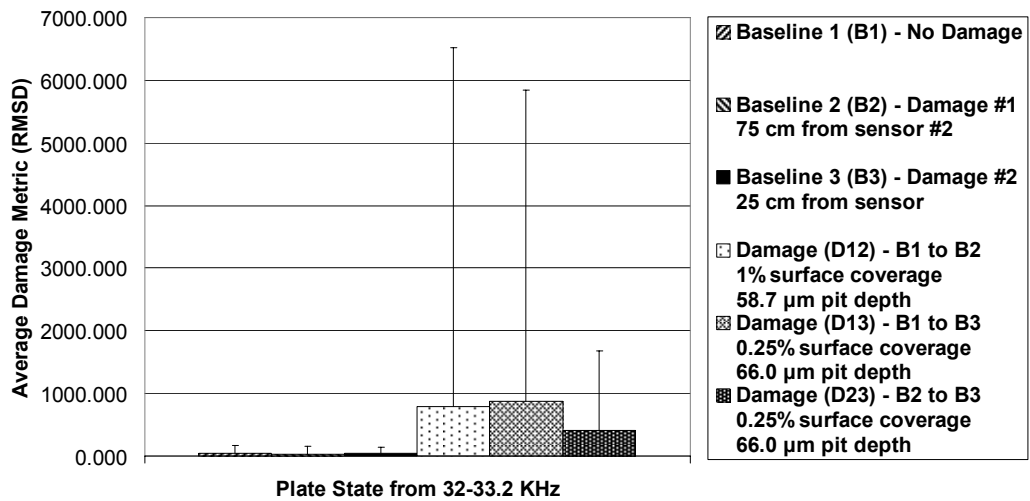


Figure C.53: Plate damage plots for PZT #4.

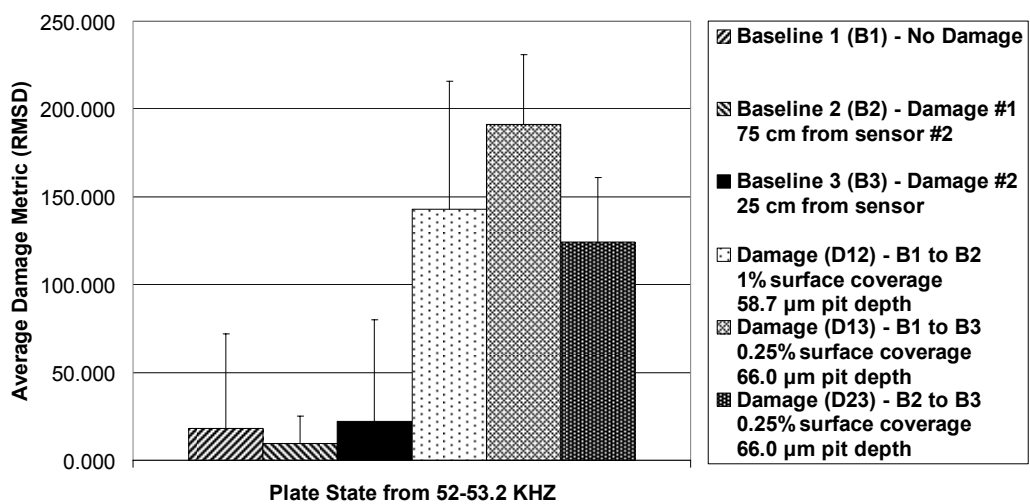


Figure C.54: Plate damage plots for PZT #4.

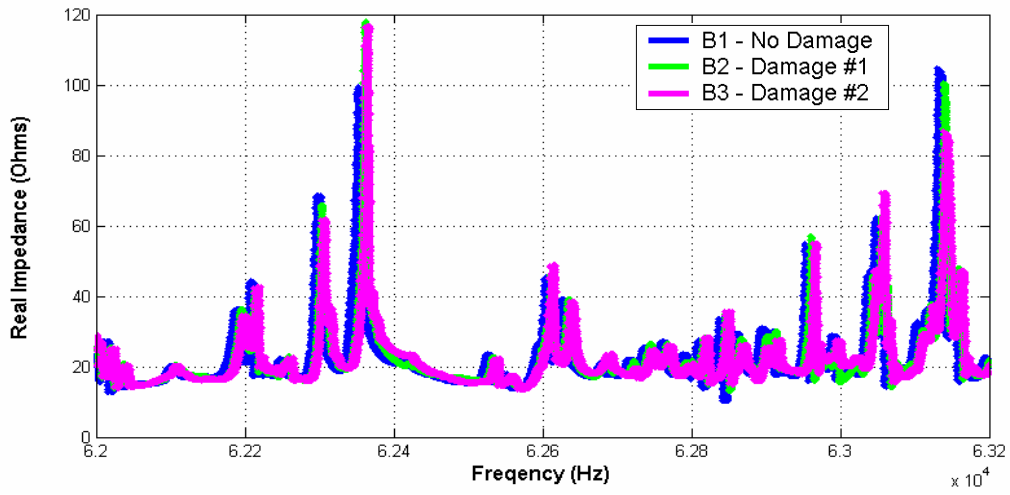


Figure C.55: Plate impedance signatures measured with PZT #4.

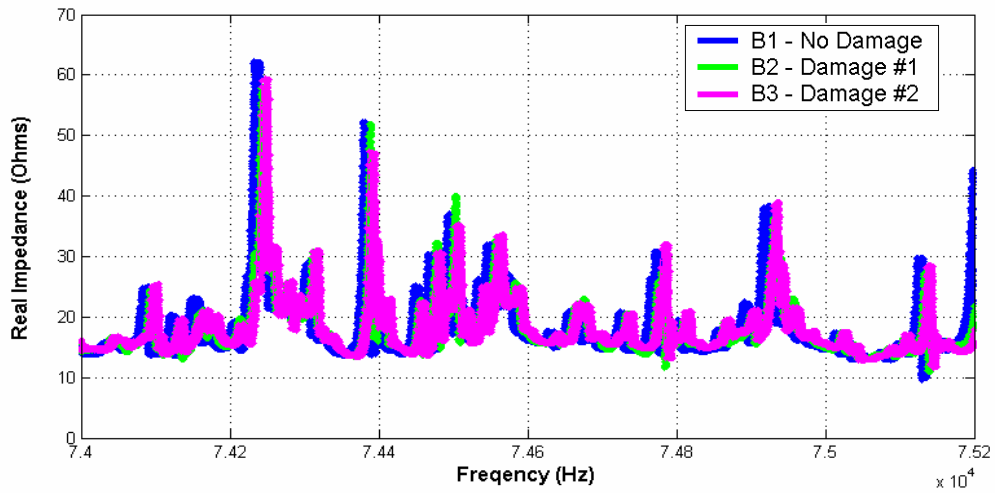


Figure C.56: Plate impedance signatures measured with PZT #4.

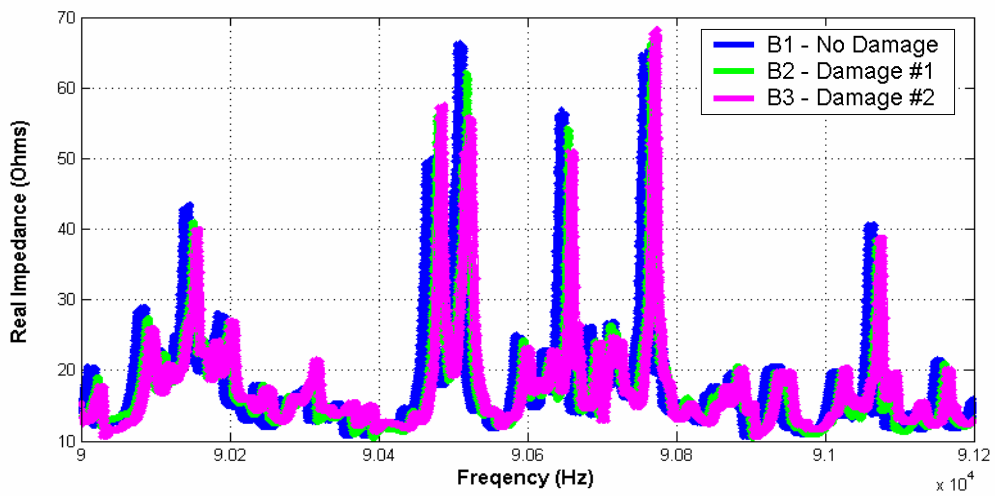


Figure C.57: Plate impedance signatures measured with PZT #4.

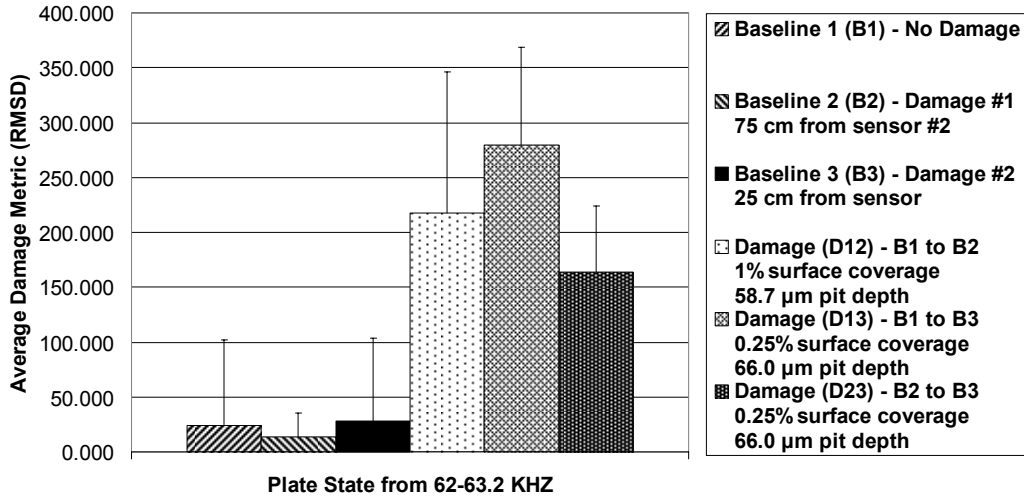


Figure C.58: Plate damage plots for PZT #4.

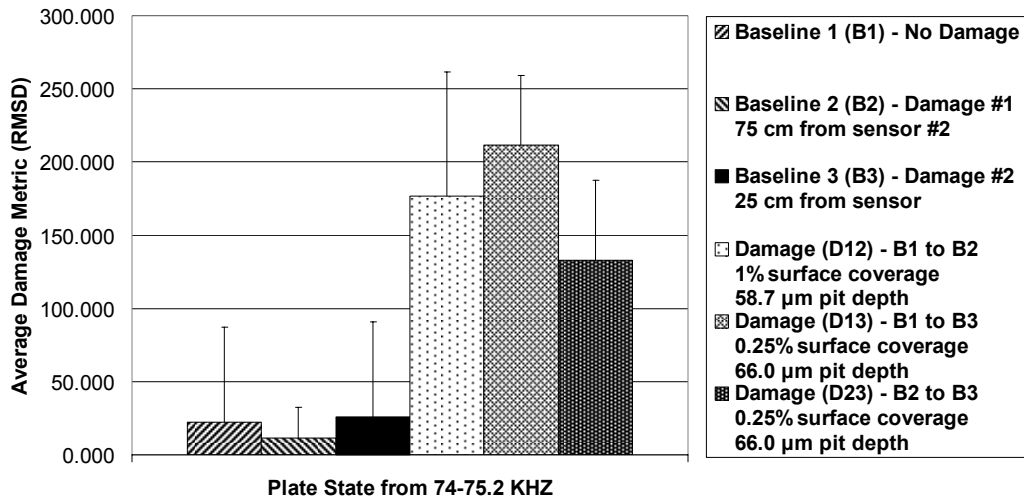


Figure C.59: Plate damage plots for PZT #4.

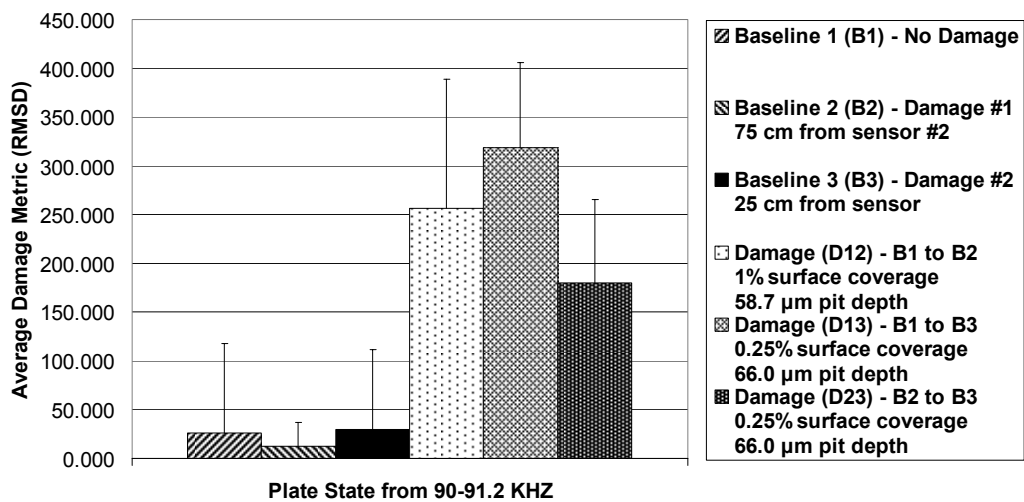


Figure C.60: Plate damage plots for PZT #4.

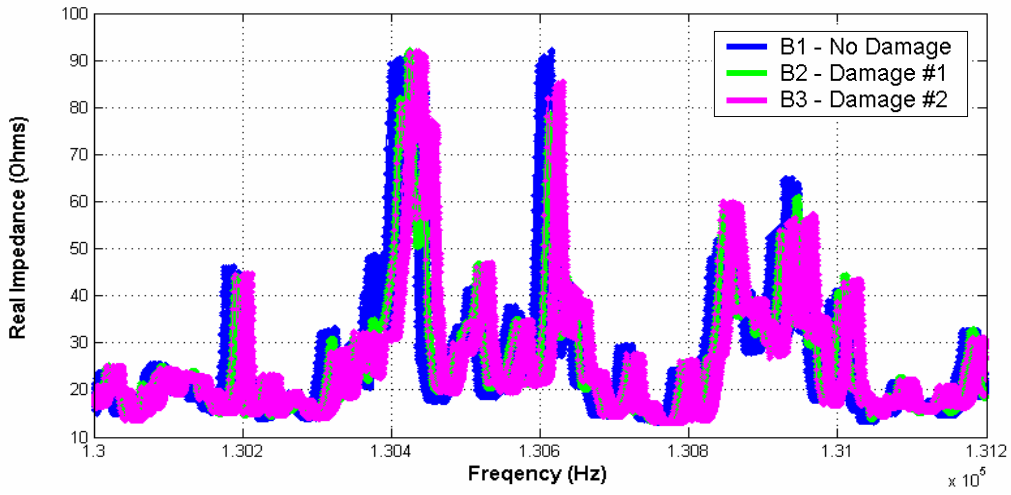


Figure C.61: Plate impedance signatures measured with PZT #4.

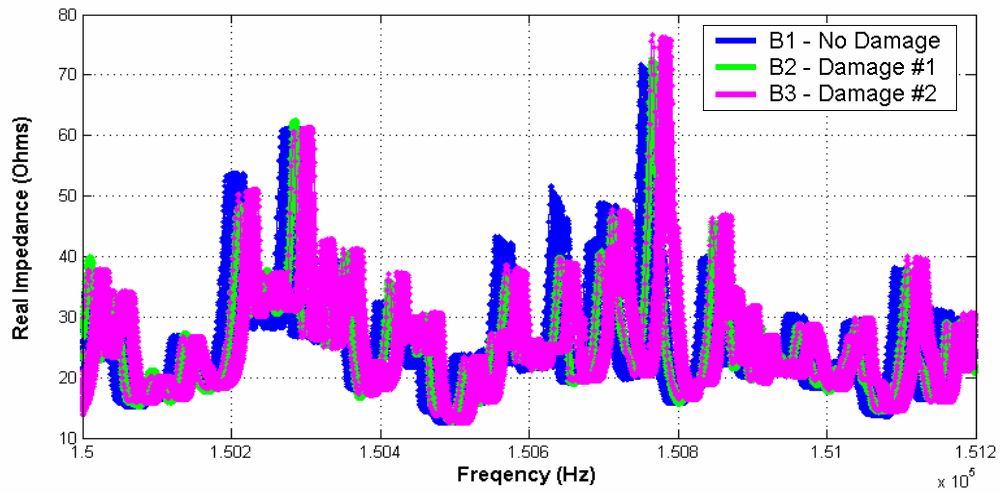


Figure C.62: Plate impedance signatures measured with PZT #4.

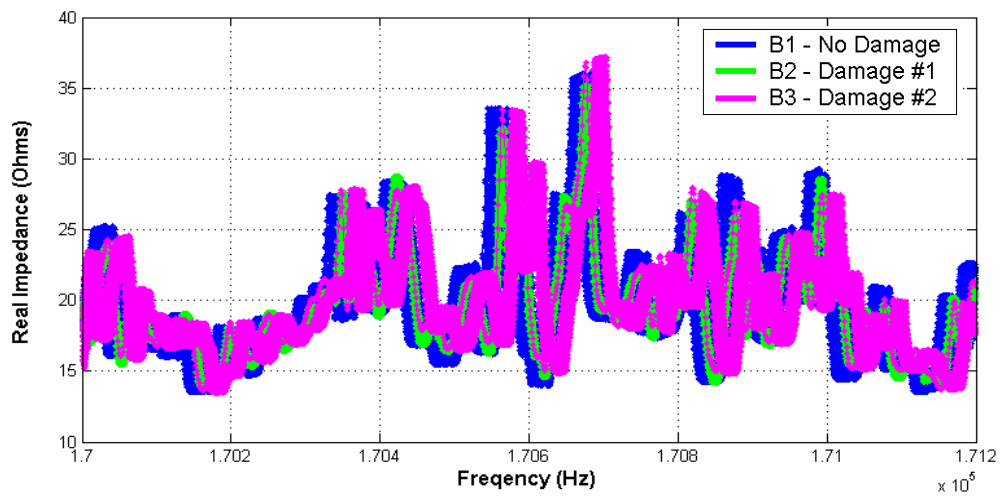


Figure C.63: Plate impedance signatures measured with PZT #4.

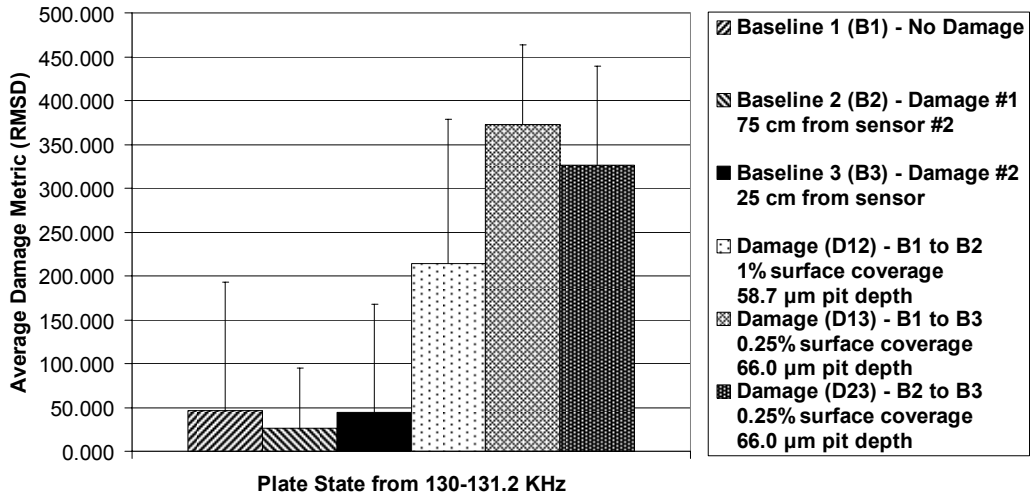


Figure C.64: Plate damage plots for PZT #4.

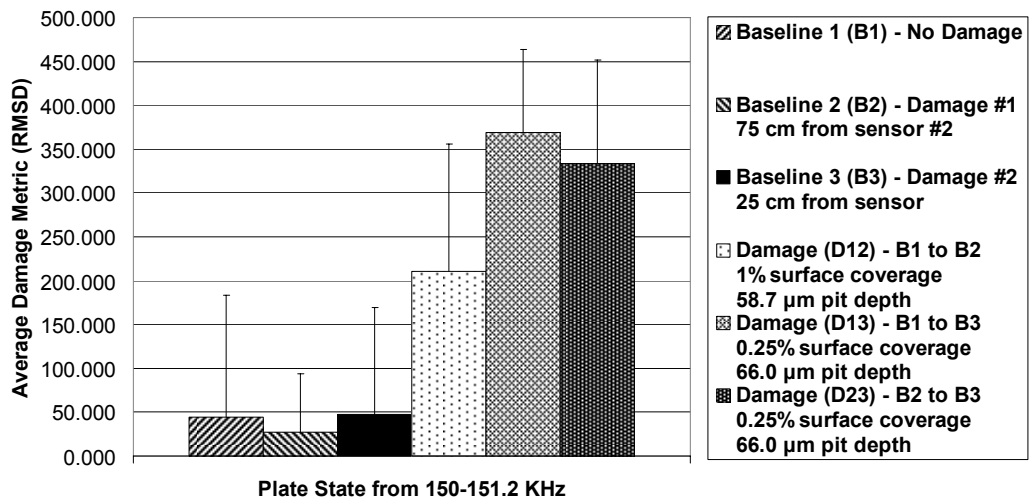


Figure C.65: Plate damage plots for PZT #4.

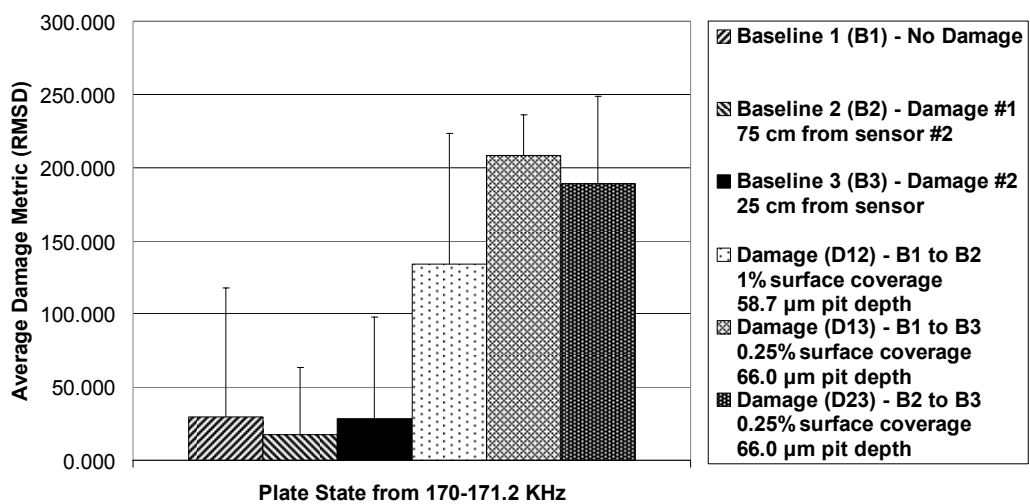


Figure C.66: Plate damage plots for PZT #4.

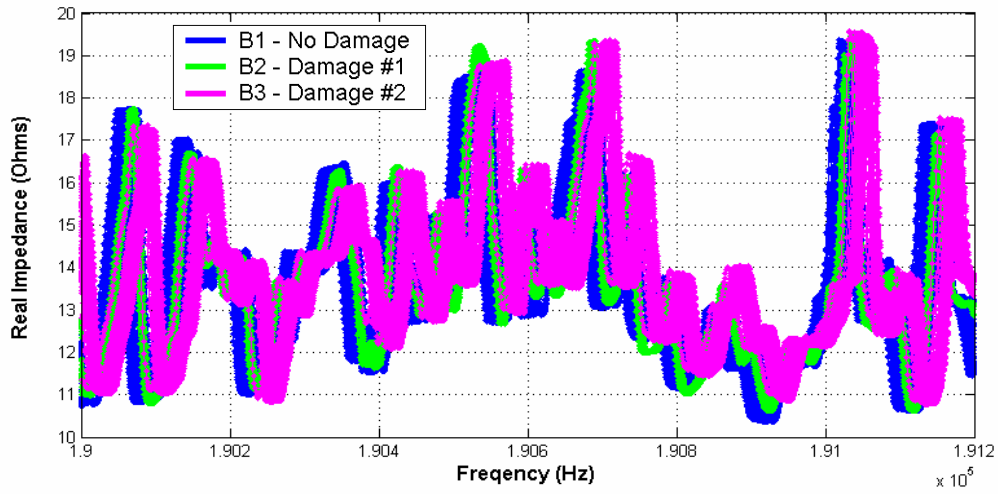


Figure C.67: Plate impedance signatures measured with PZT #4.

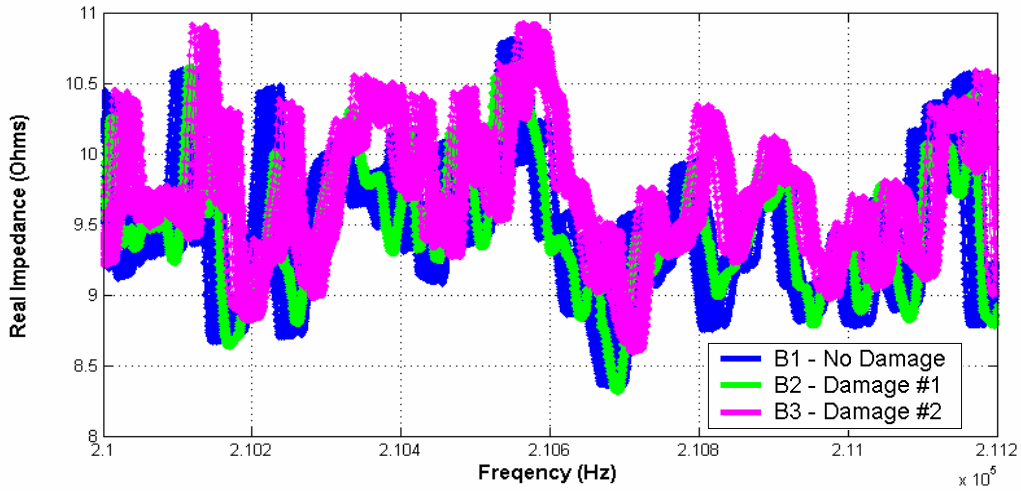


Figure C.68: Plate impedance signatures measured with PZT #4.

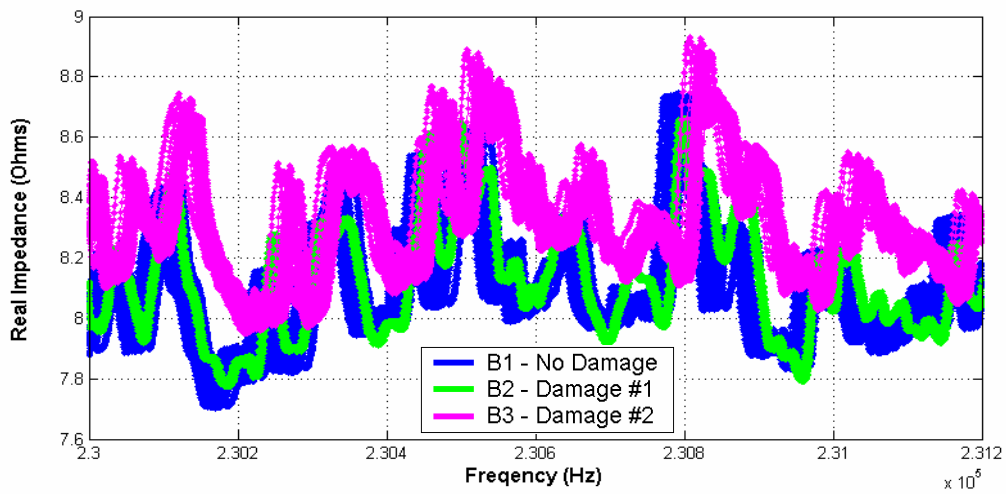


Figure C.69: Plate impedance signatures measured with PZT #4.

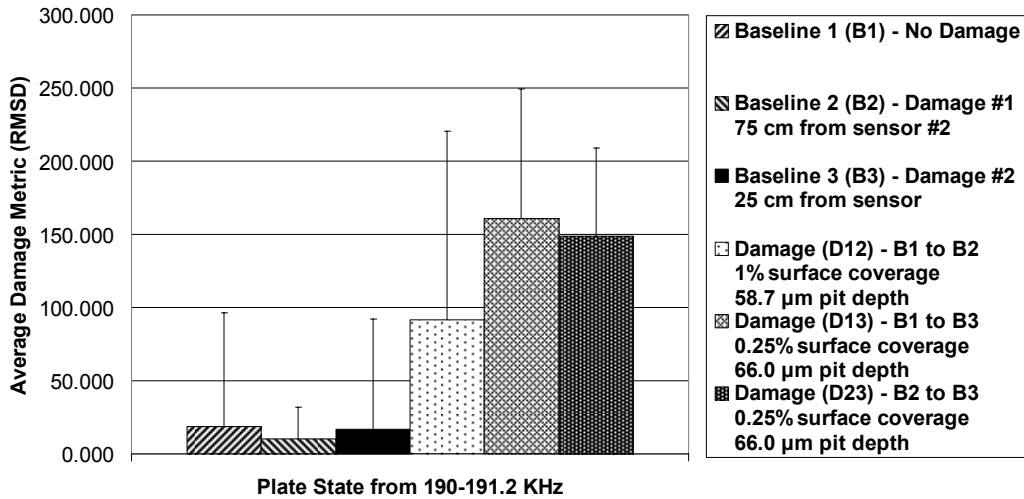


Figure C.70: Plate damage plots for PZT #4.

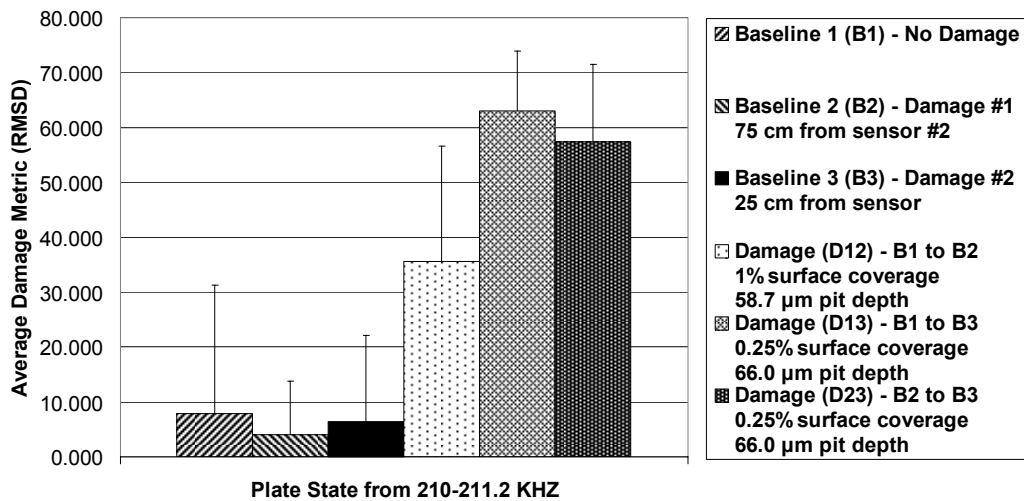


Figure C.71: Plate damage plots for PZT #4.

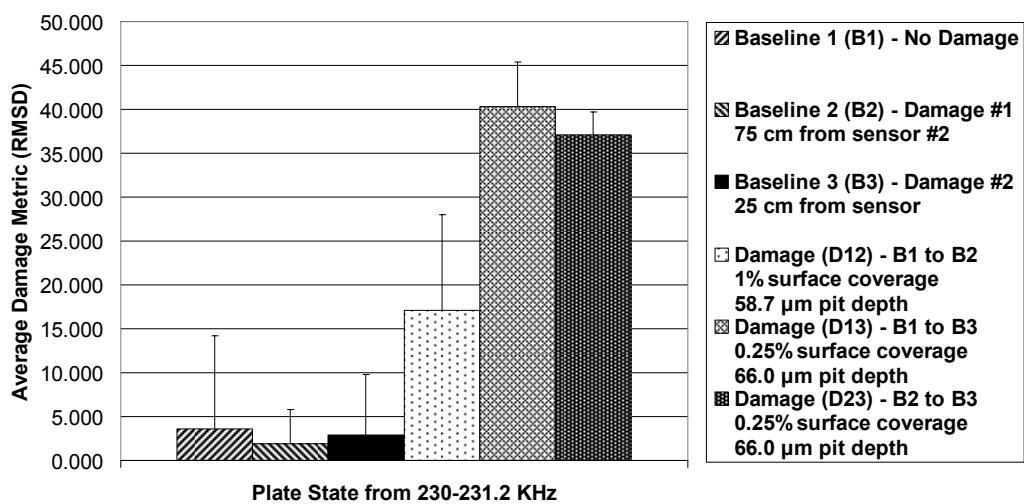


Figure C.72: Plate damage plots for PZT #4.

Appendix D

Sensor Corrosion Impedance and Damage Metric Plots

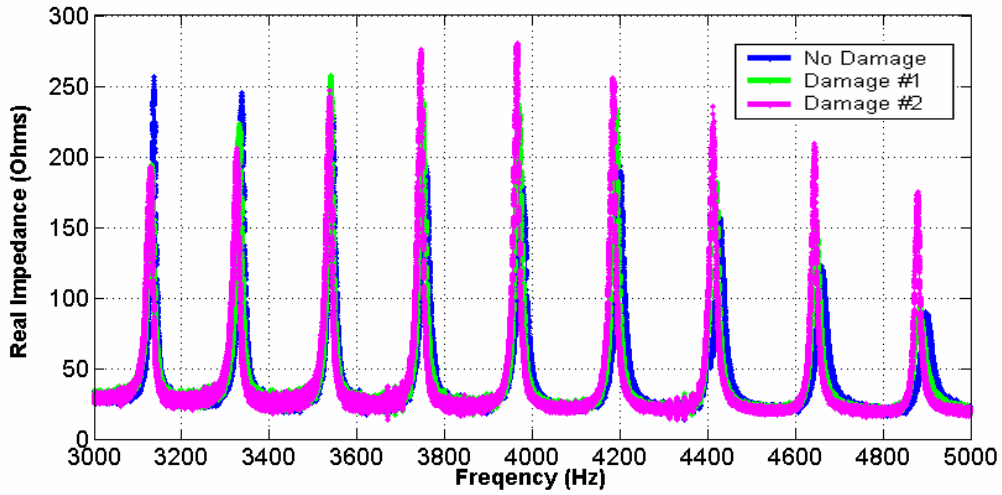


Figure D.1: Impedance signatures for MFC D₃₁ from 3-5 kHz.

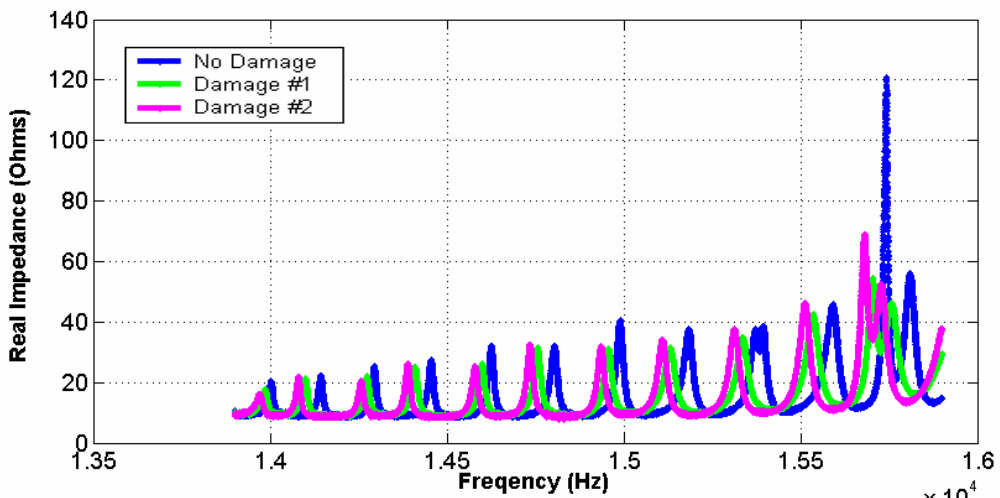


Figure D.2: Impedance signatures for MFC D₃₁ from 13.9-15.9 kHz.

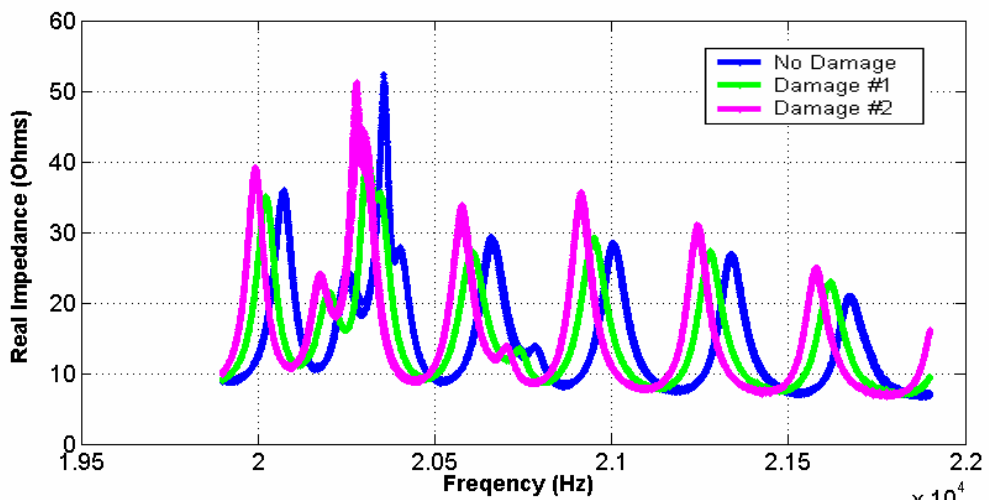


Figure D.3: Impedance signatures for MFC D₃₁ from 19.9-21.9 kHz.

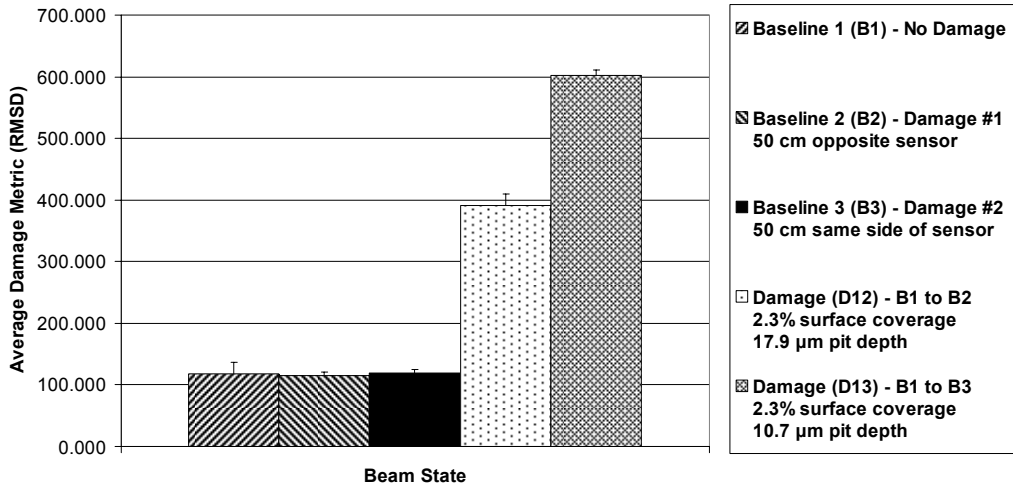


Figure D.4: Damage metric plots for MFC D₃₁ from 3-5 kHz.

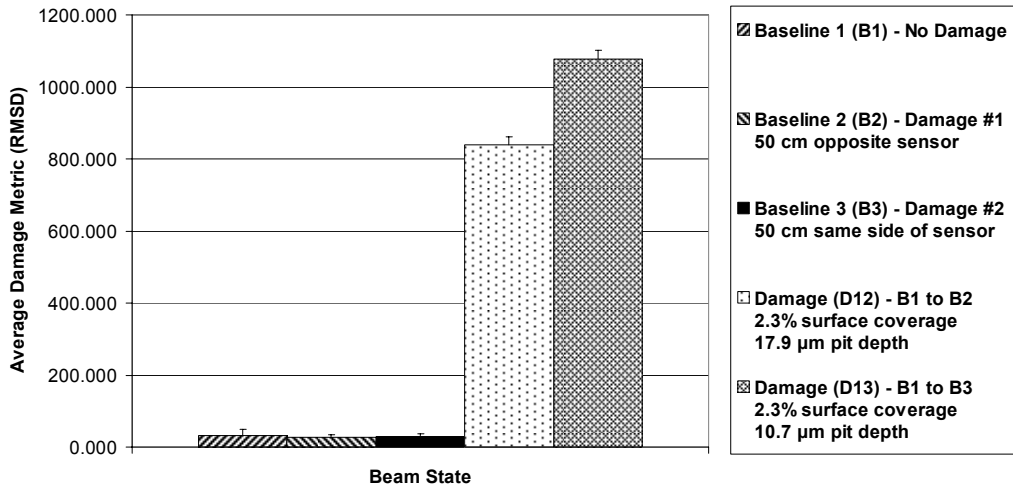


Figure D.5: Damage metric plots for MFC D₃₁ from 13.9-15.9 kHz.

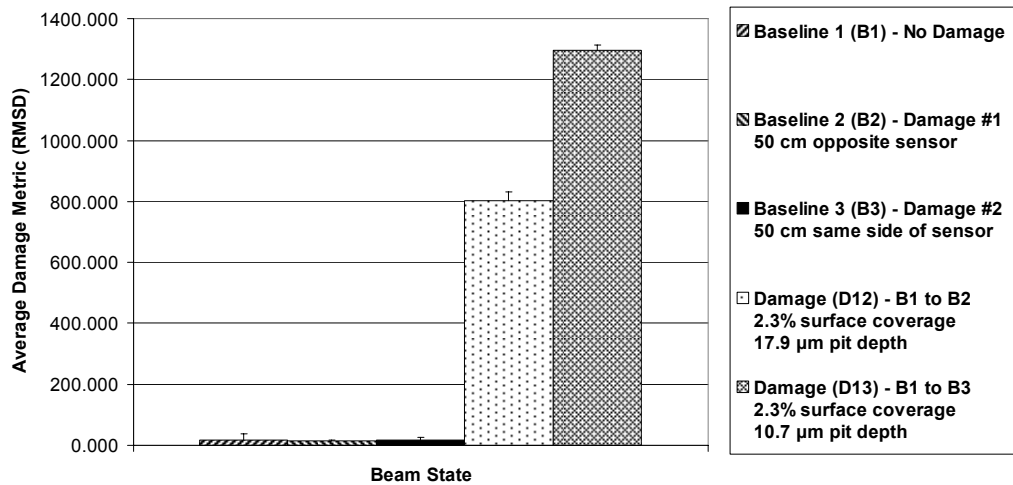


Figure D.6: Damage metric plots for MFC D₃₁ from 19.9-21.9 kHz.

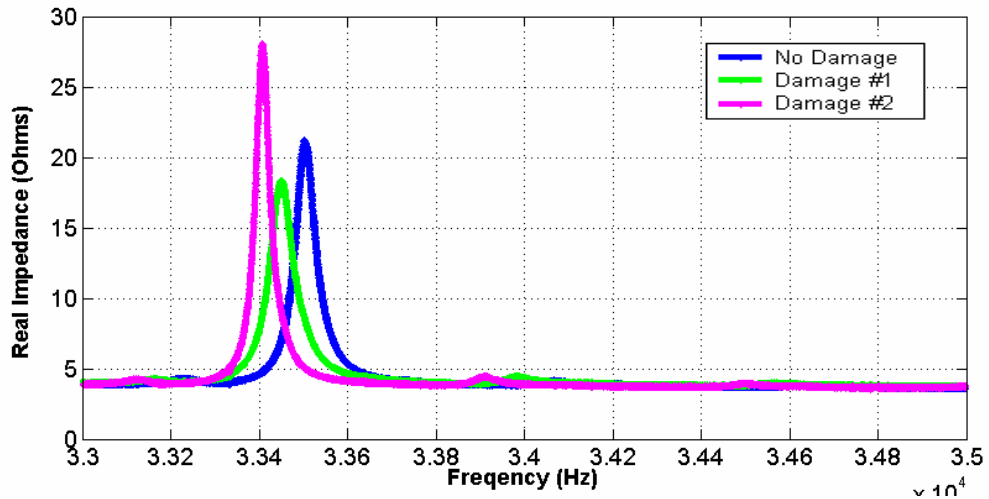


Figure D.7: Impedance signatures for MFC D₃₁ from 33-35 kHz.

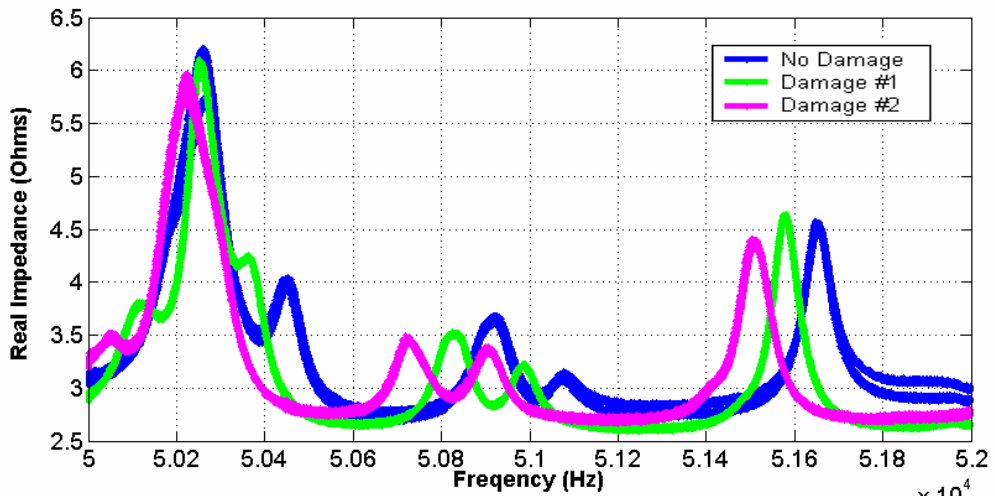


Figure D.8: Impedance signatures for MFC D₃₁ from 50-52 kHz.

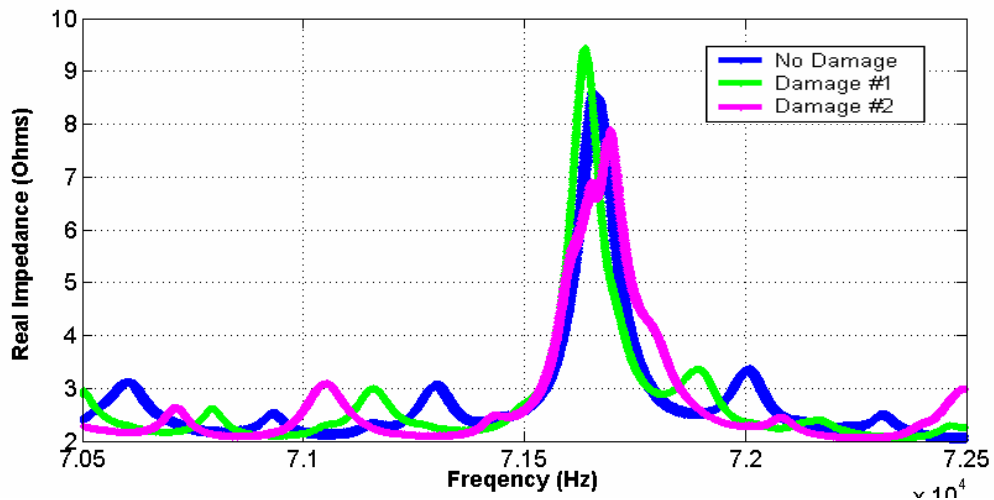


Figure D.9: Impedance signatures for MFC D₃₁ from 72.5-74.5 kHz.

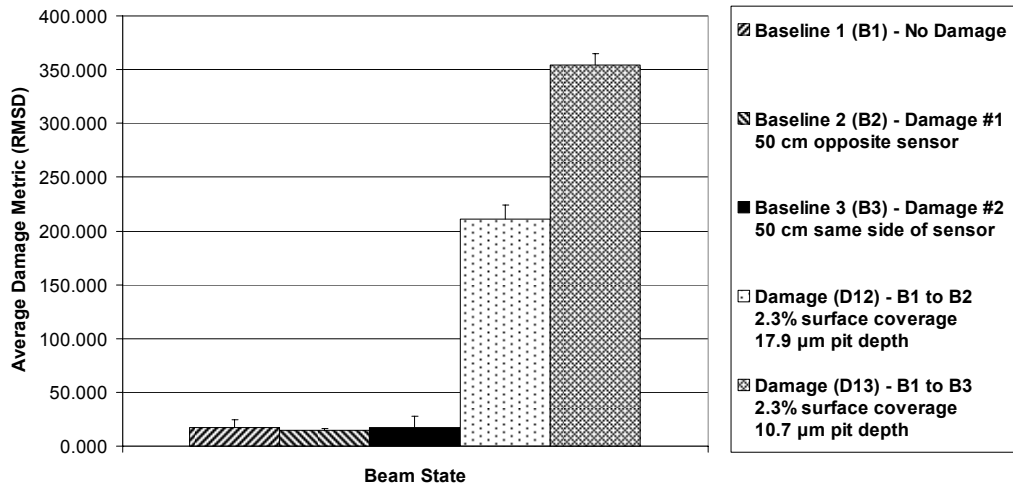


Figure D.10: Damage metric plots for MFC D₃₁ from 33-35 kHz.

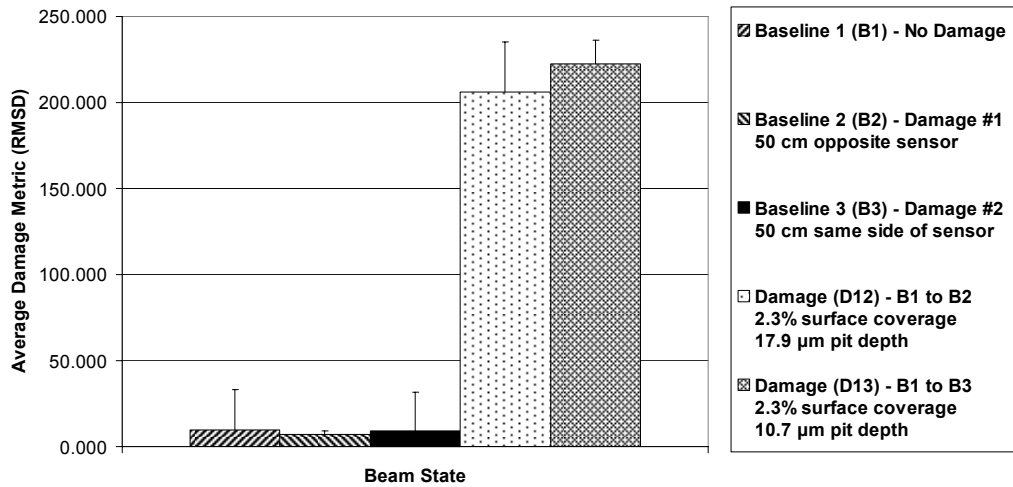


Figure D.11: Damage metric plots for MFC D₃₁ from 52-54 kHz.

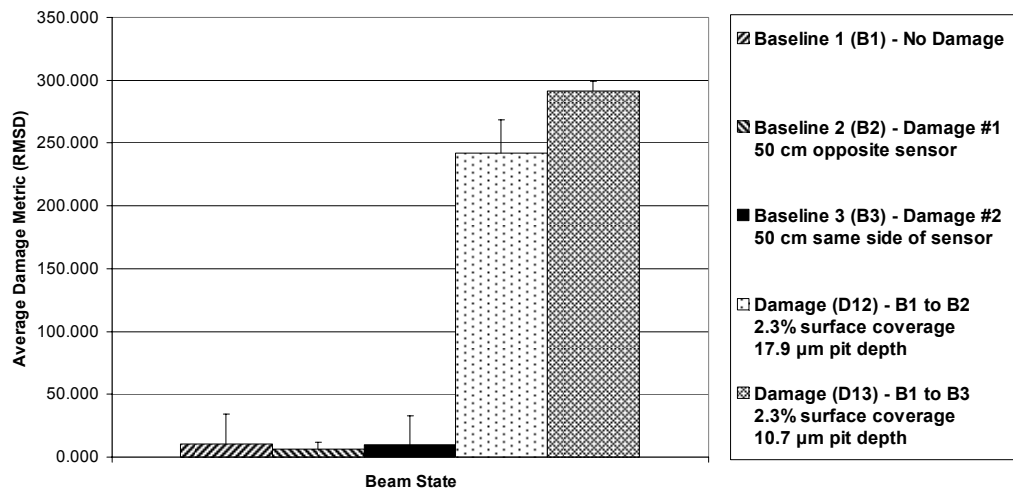


Figure D.12: Damage metric plots for MFC D₃₁ from 72.5-74.5 kHz.

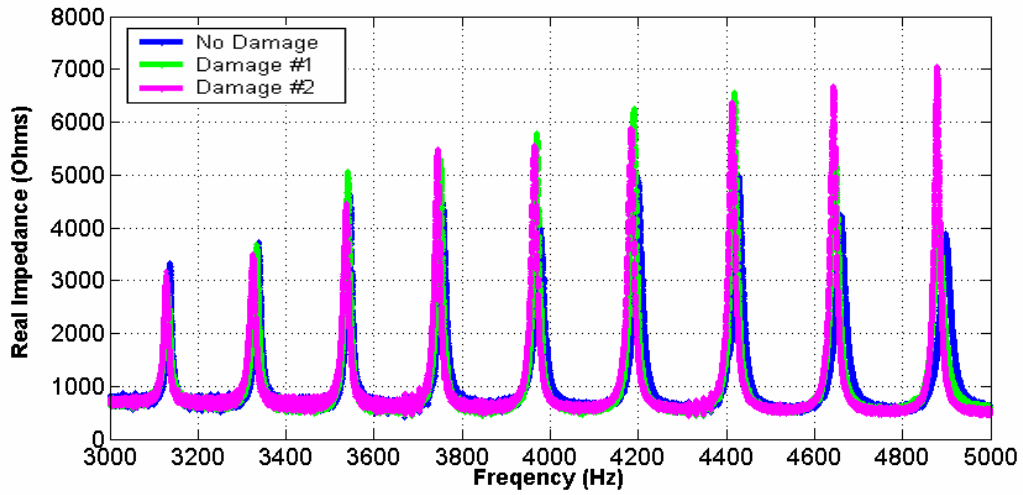


Figure D.13: Impedance signatures for MFC D₃₃ from 3-5 kHz.

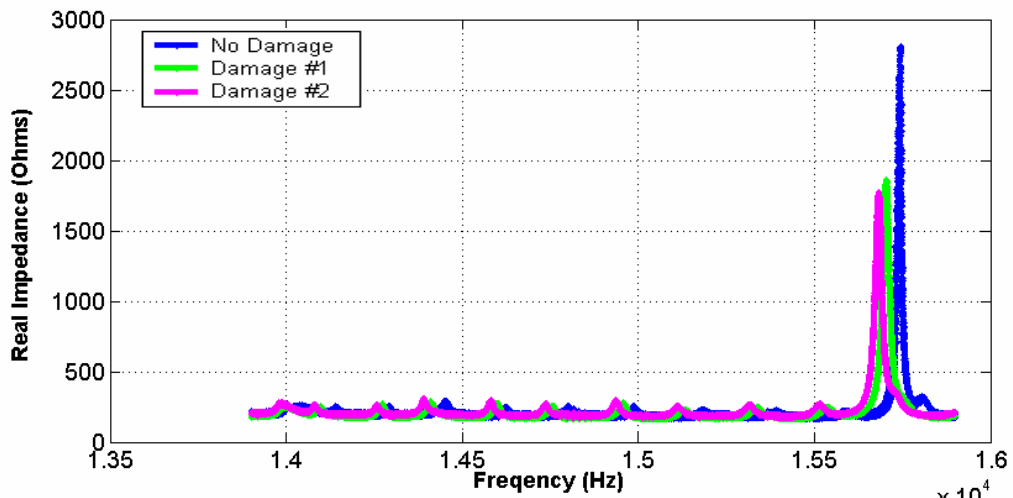


Figure D.14: Impedance signatures for MFC D₃₃ from 13.9-15.9 kHz.

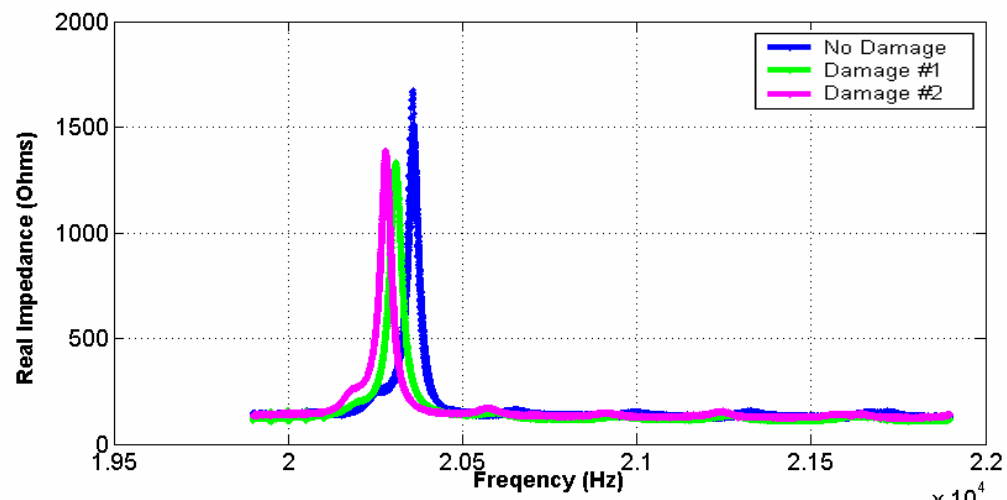


Figure D.15: Impedance signatures for MFC D₃₃ from 19.9-21.9 kHz.

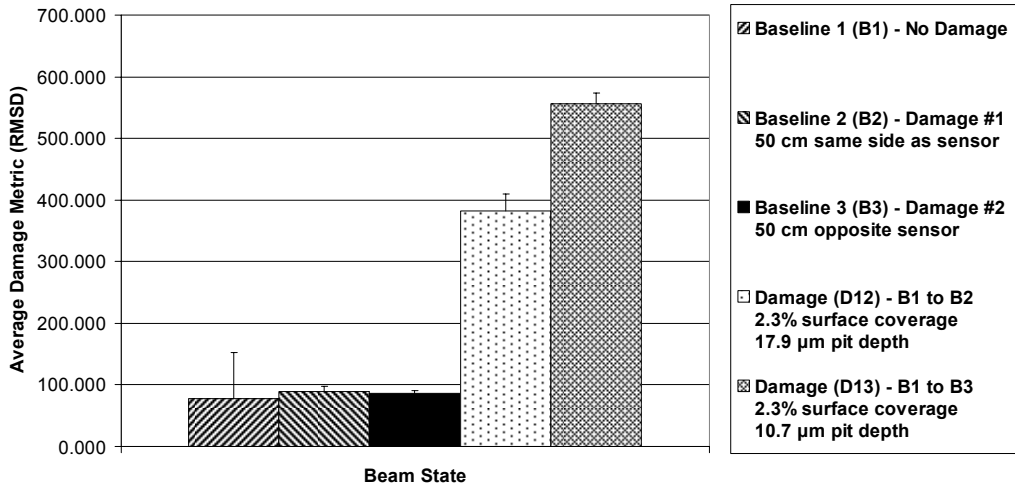


Figure D.16: Damage metric plots for MFC D₃₃ from 3-5 kHz.

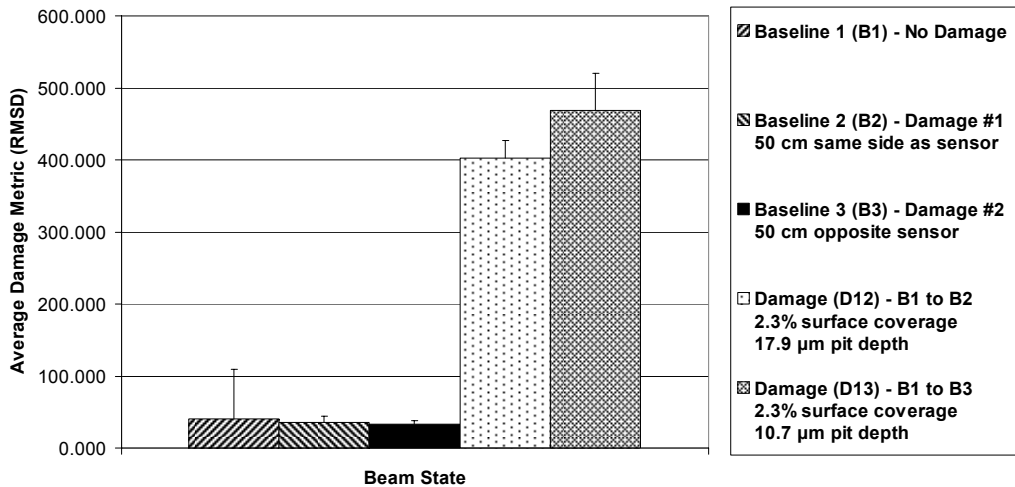


Figure D.17: Damage metric plots for MFC D₃₃ from 13.9-15.9 kHz.

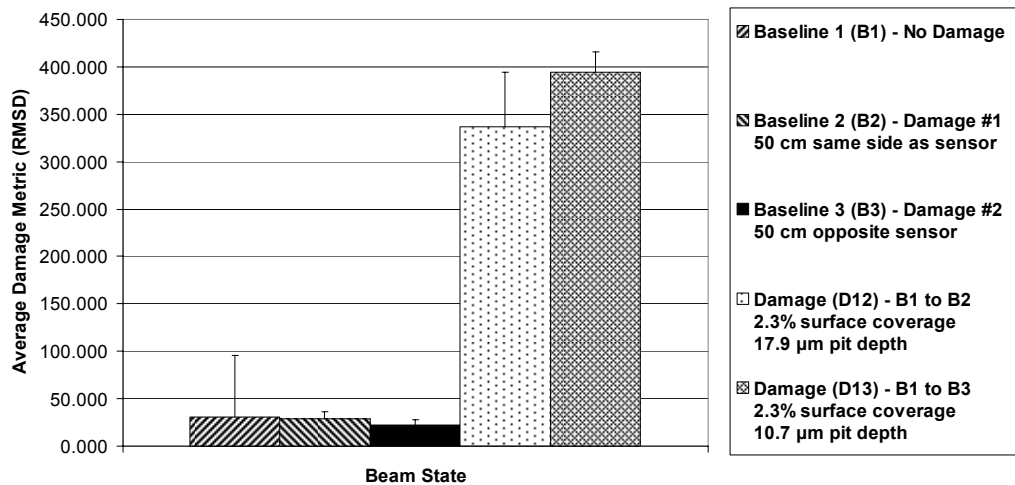


Figure D.18: Damage metric plots for MFC D₃₃ from 19.9-21.9 kHz.

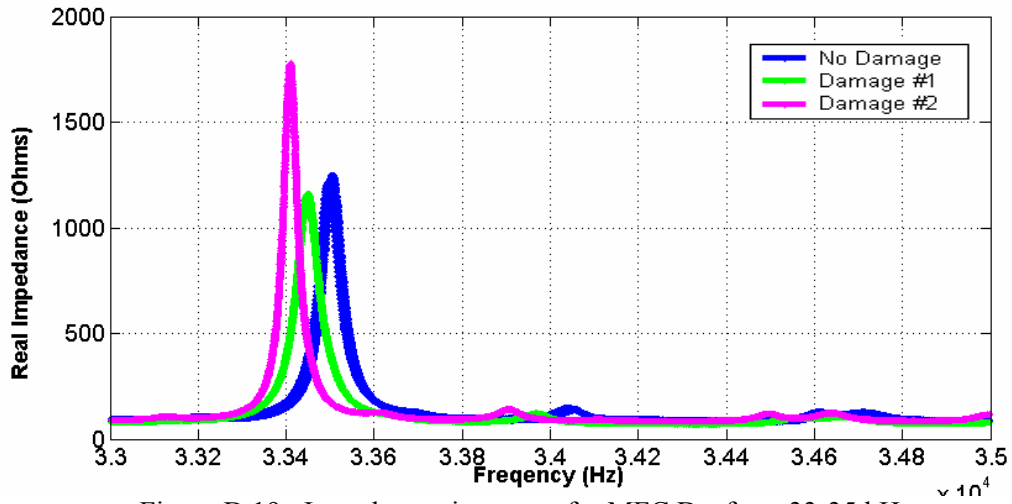


Figure D.19: Impedance signatures for MFC D₃₃ from 33-35 kHz.

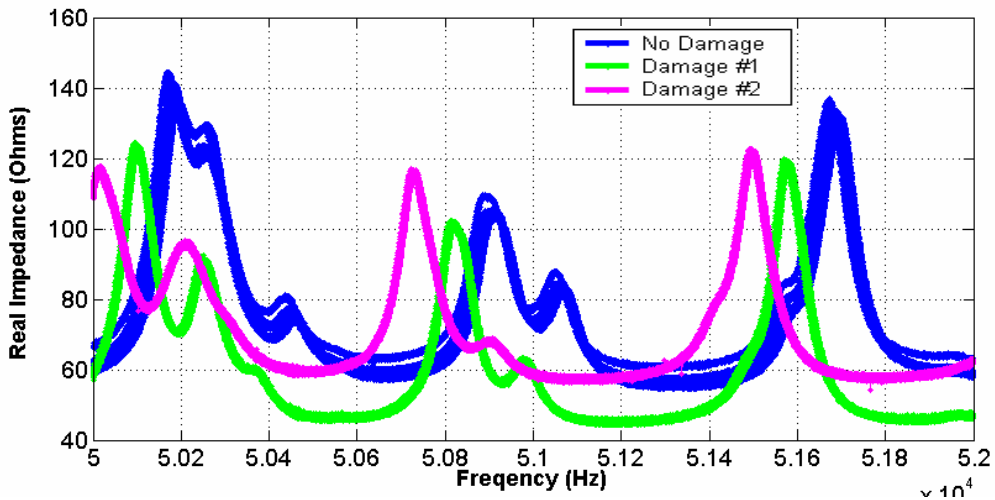


Figure D.20: Impedance signatures for MFC D₃₃ from 50-52 kHz.

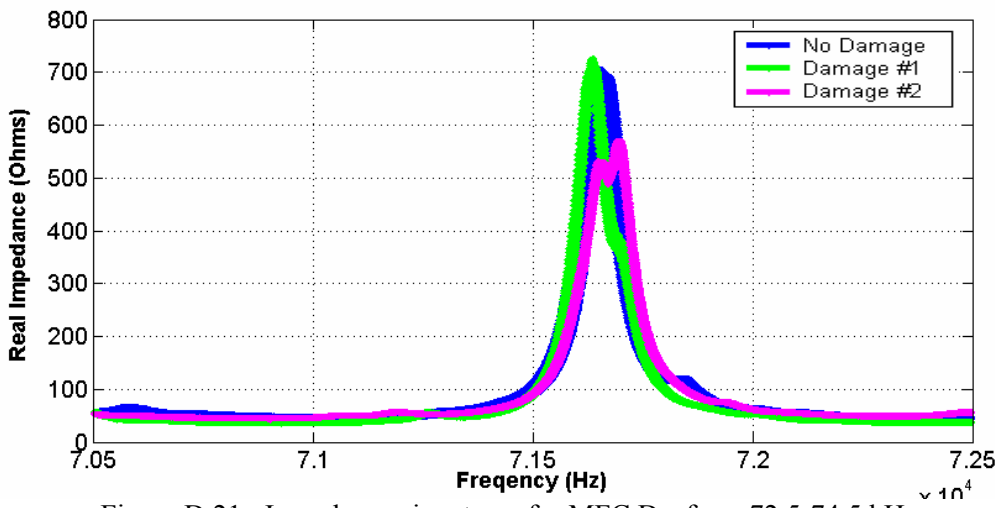


Figure D.21: Impedance signatures for MFC D₃₃ from 72.5-74.5 kHz.

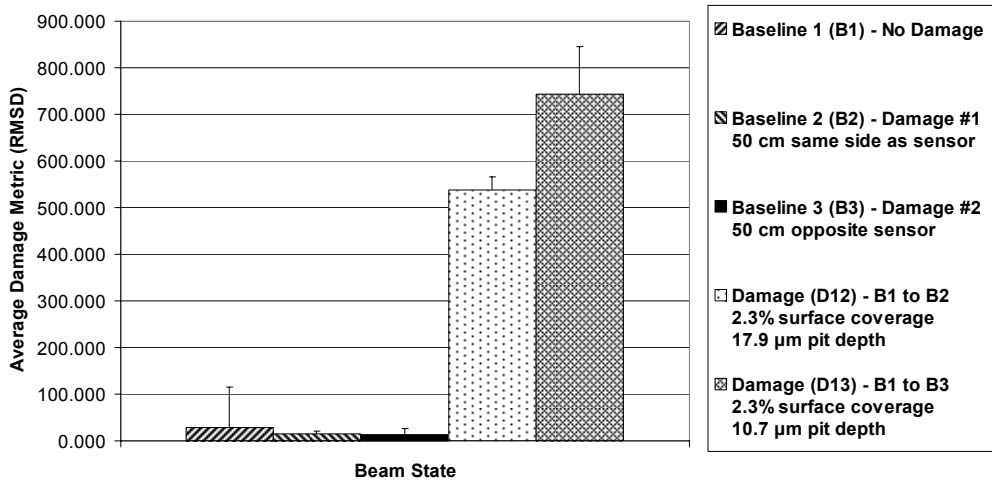


Figure D.22: Damage metric plots for MFC D₃₃ from 33-35 kHz.

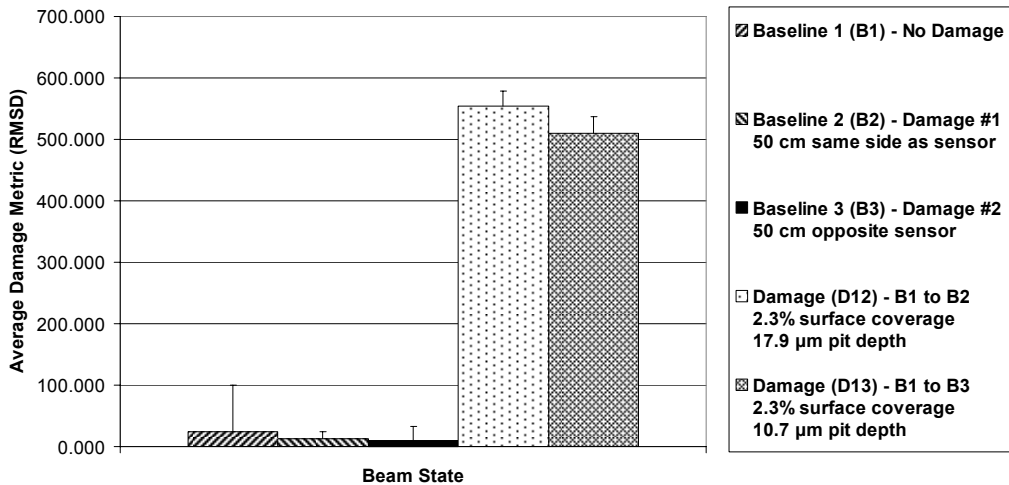


Figure D.23: Damage metric plots for MFC D₃₃ from 50-52 kHz.

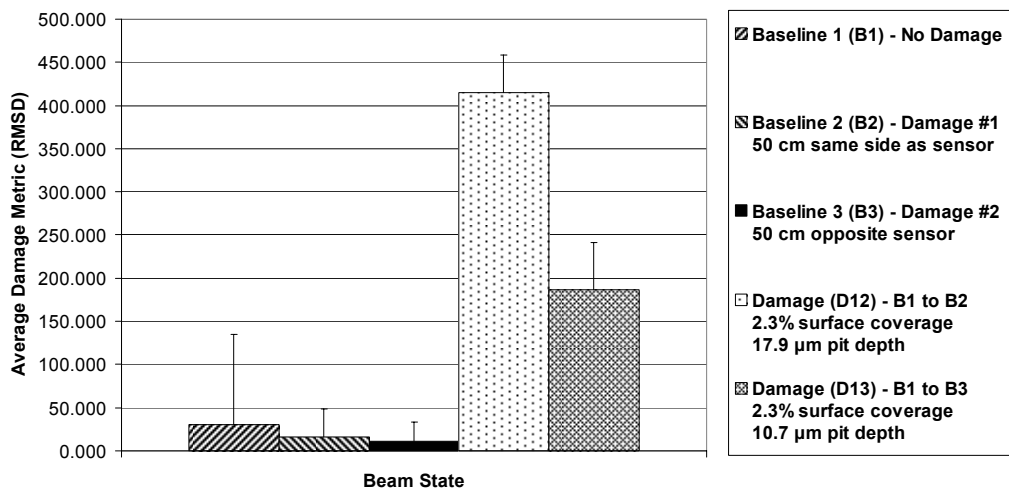


Figure D.24: Damage metric plots for MFC D₃₃ from 72.5-74.5 kHz.

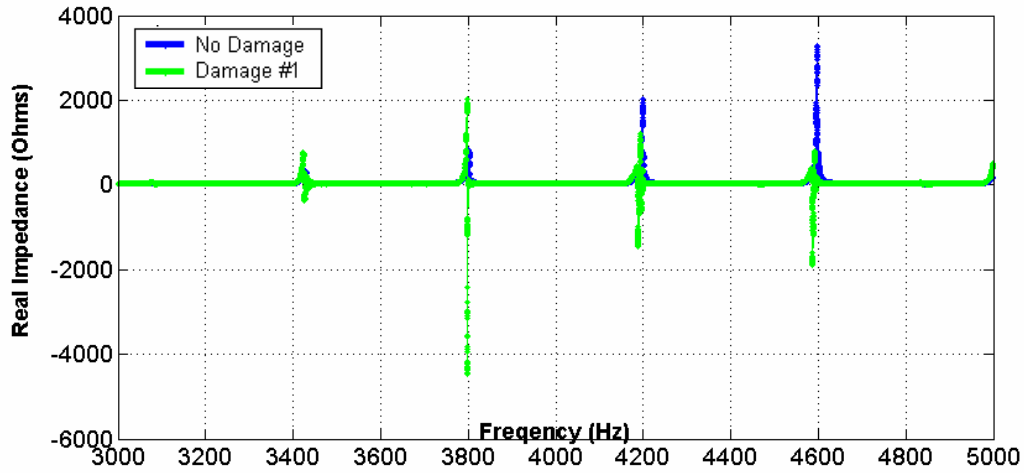


Figure D.25: Impedance signatures for PZT A4 from 3-5 kHz.

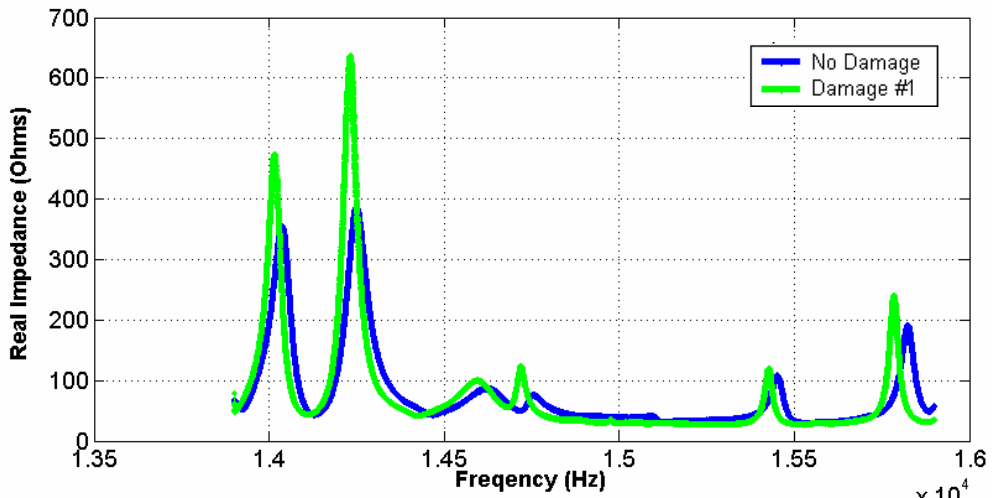


Figure D.26: Impedance signatures for PZT A4 from 13.9-15.9 kHz.

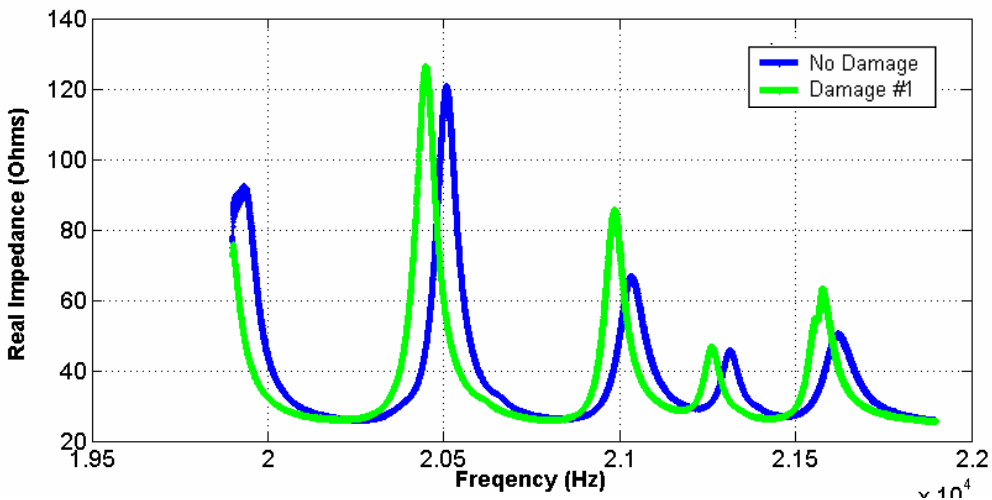


Figure D.27: Impedance signatures for PZT A4 from 19.9-21.9 kHz.

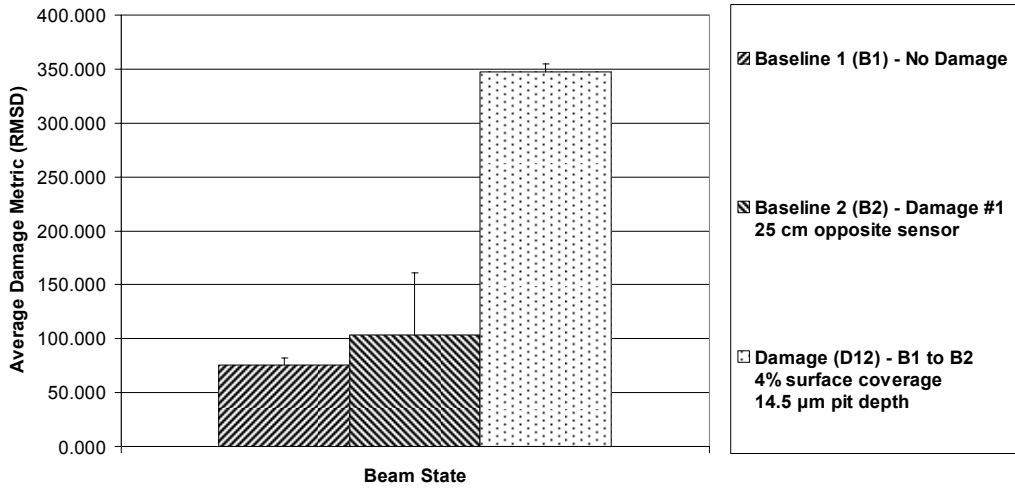


Figure D.28: Damage metric plots for PZT A4 from 3-5 kHz.

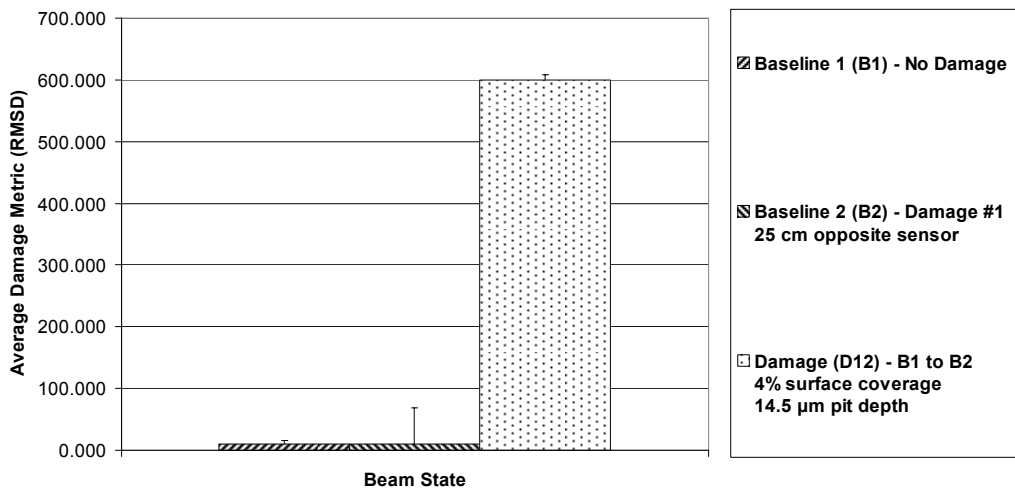


Figure D.29: Damage metric plots for PZT A4 from 13.9-15.9 kHz.

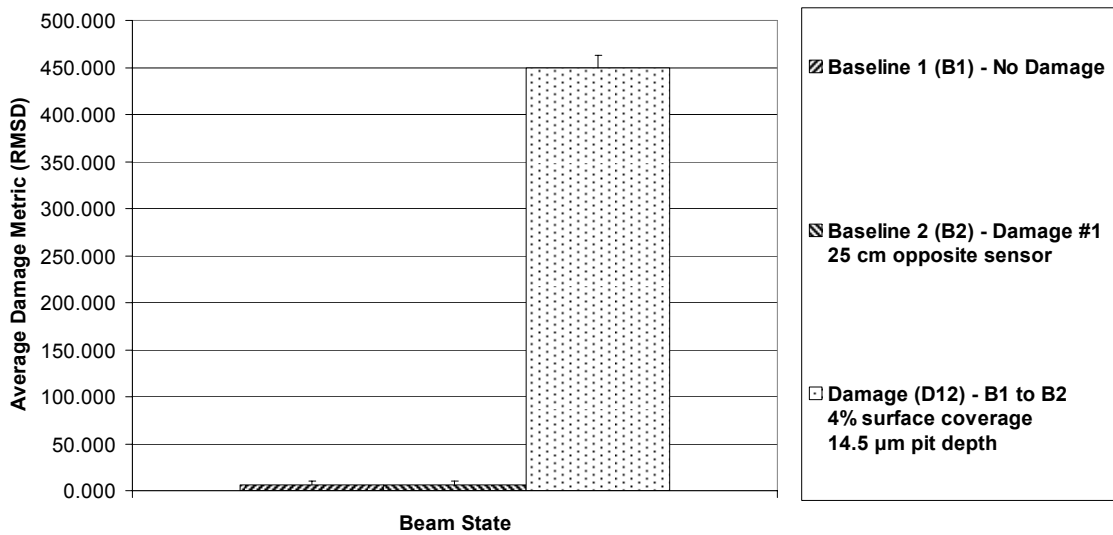


Figure D.30: Damage metric plots for PZT A4 from 19.9-21.9 kHz.

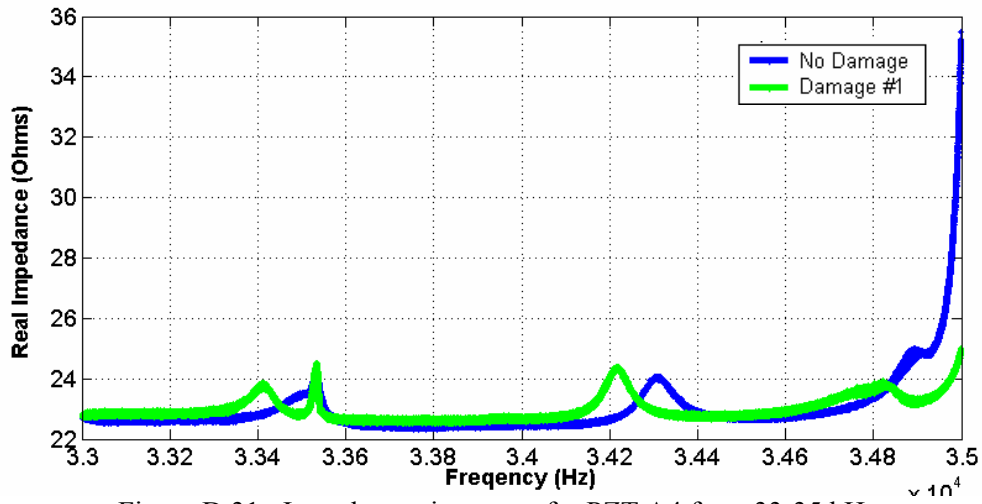


Figure D.31: Impedance signatures for PZT A4 from 33-35 kHz.

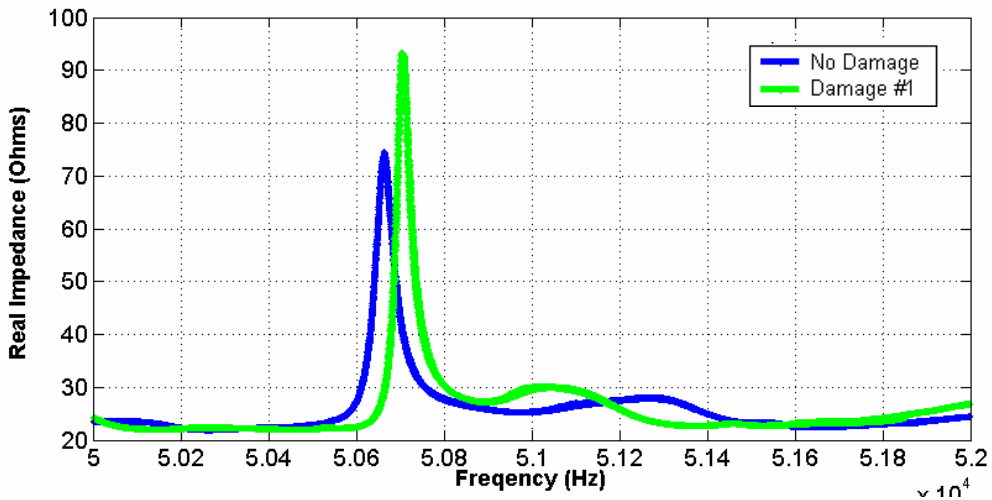


Figure D.32: Impedance signatures for PZT A4 from 50-52 kHz.

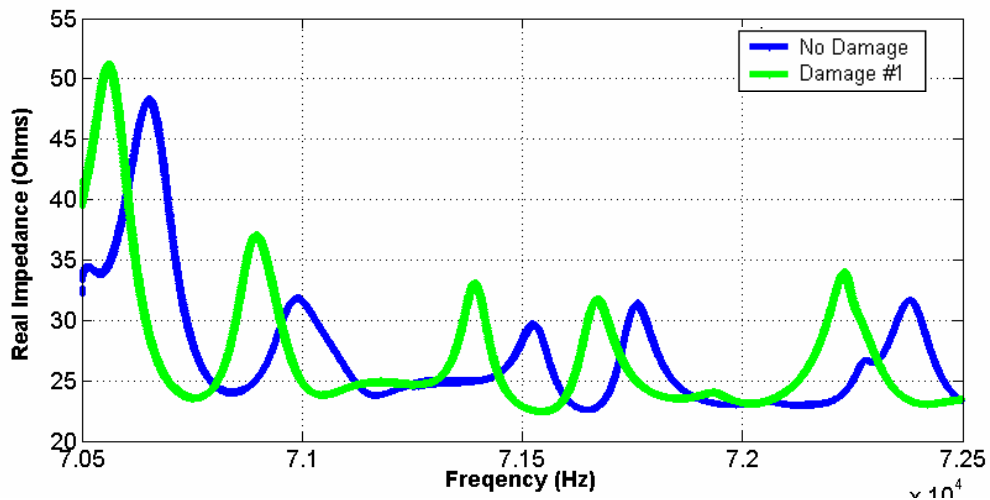


Figure D.33: Impedance signatures for PZT A4 from 72.5-74.5 kHz.

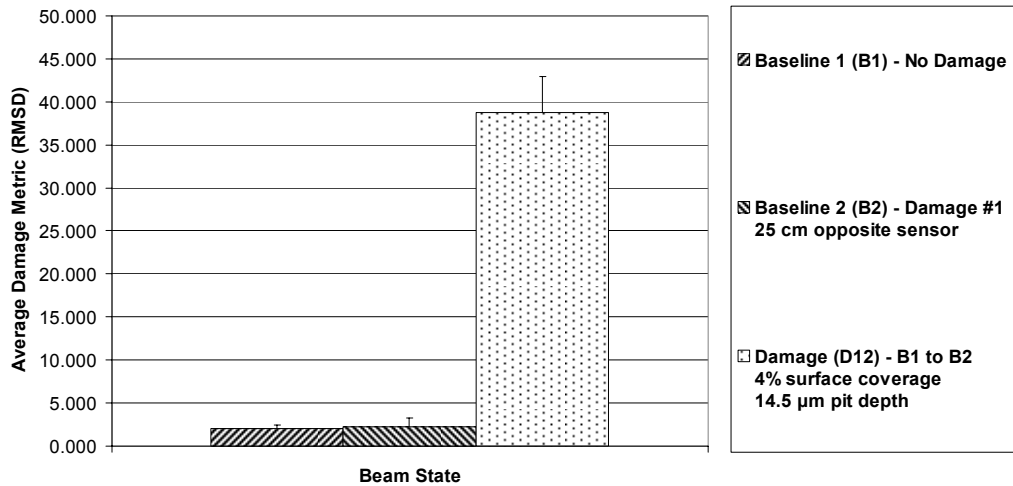


Figure D.34: Damage metric plots for PZT A4 from 33-35 kHz.

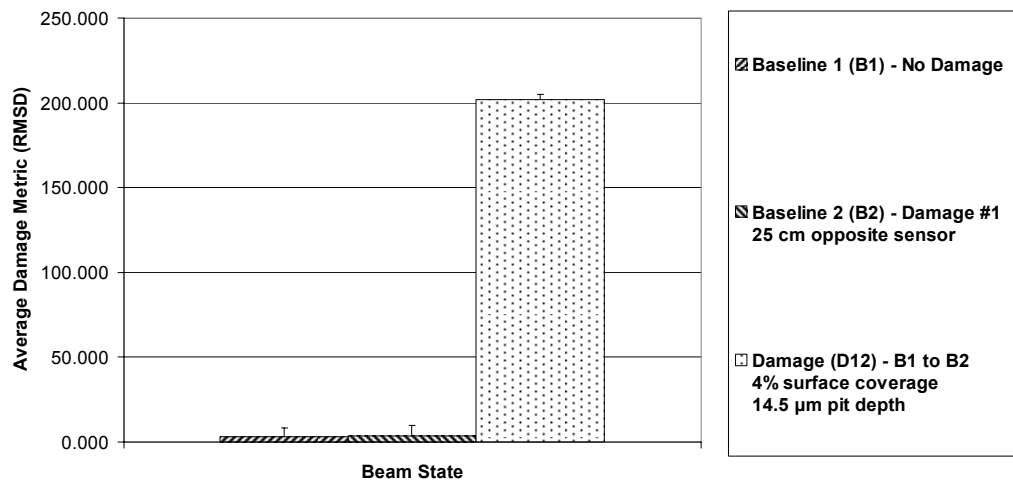


Figure D.35: Damage metric plots for PZT A4 from 50-52 kHz.

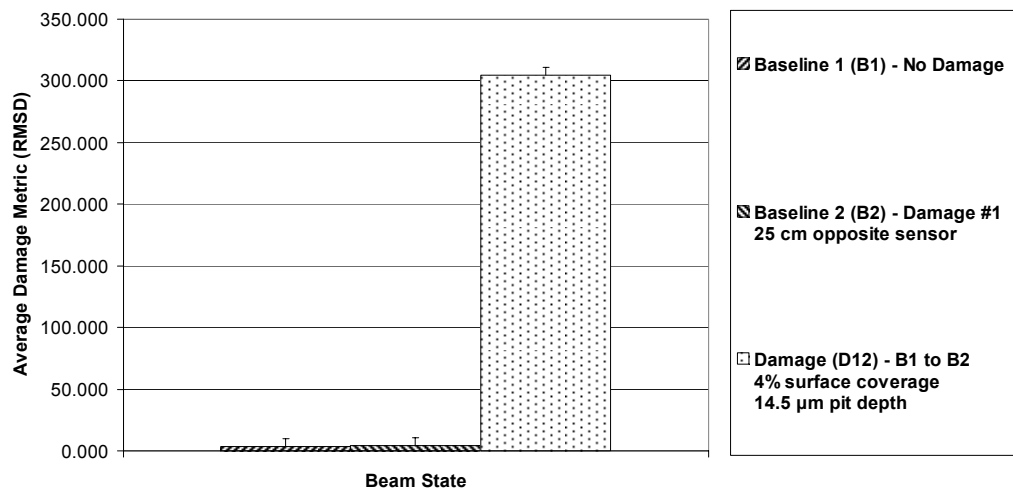


Figure D.36: Damage metric plots for PZT A4 from 72.5-74.5 kHz.

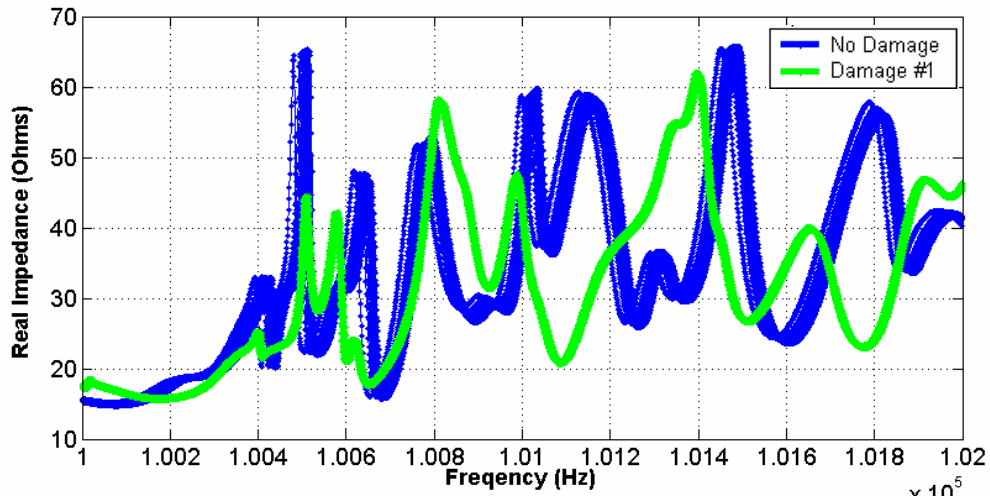


Figure D.37: Impedance signatures for PZT A4 from 100-102 kHz.

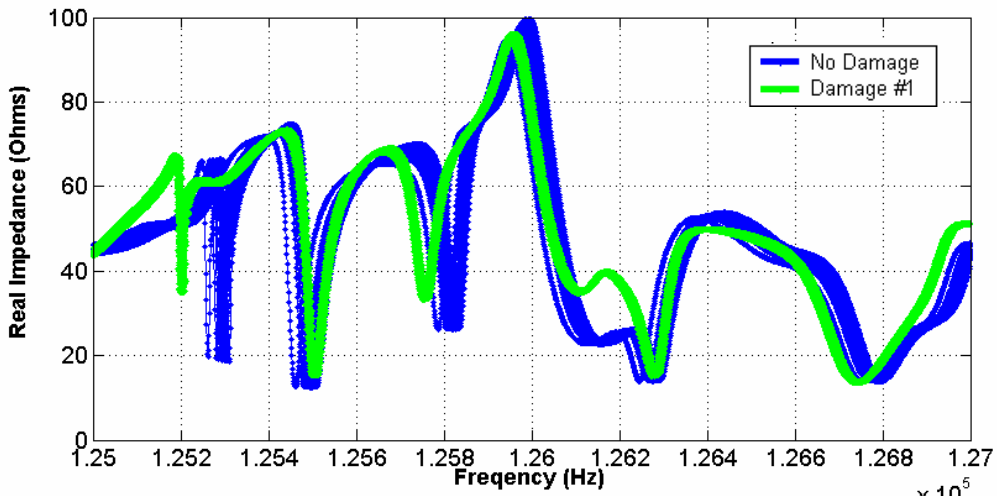


Figure D.38: Impedance signatures for PZT A4 from 125-127 kHz.

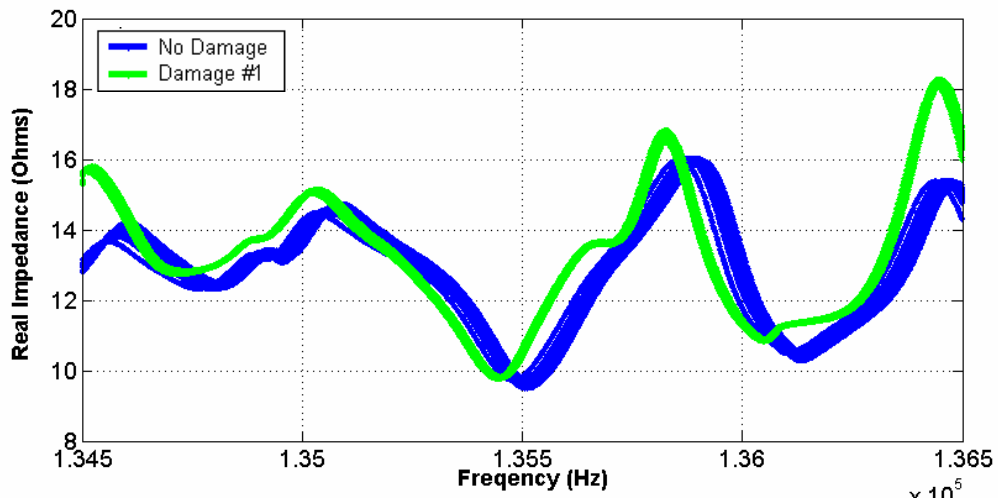


Figure D.39: Impedance signatures for PZT A4 from 134.5-136.5 kHz.

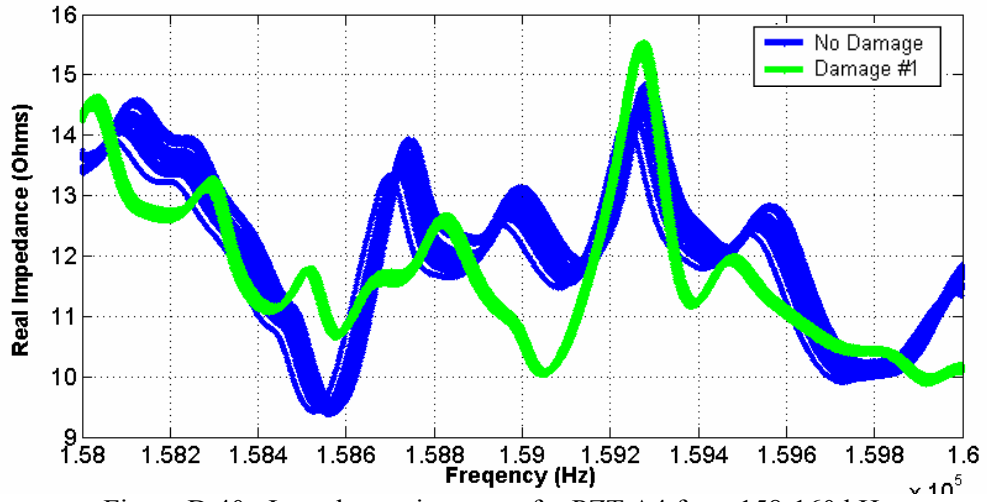


Figure D.40: Impedance signatures for PZT A4 from 158-160 kHz.

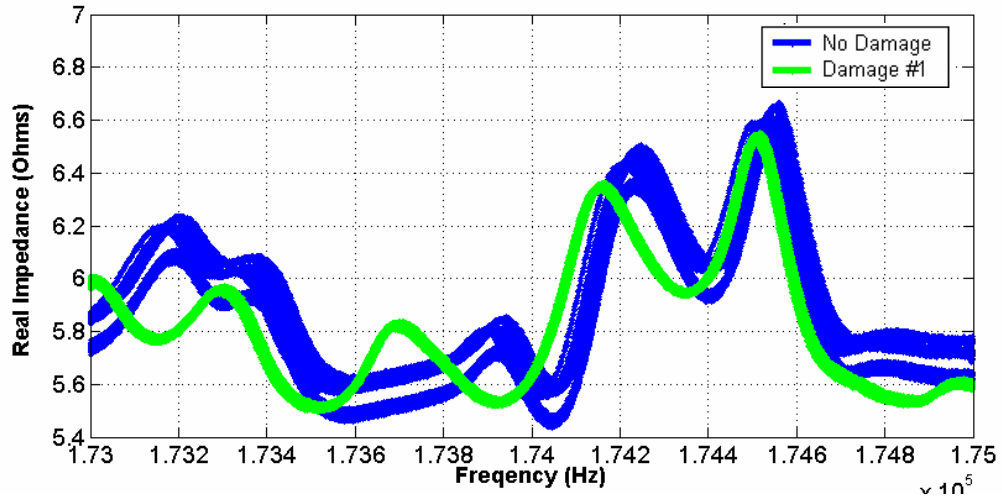


Figure D.41: Impedance signatures for PZT A4 from 173-175 kHz.

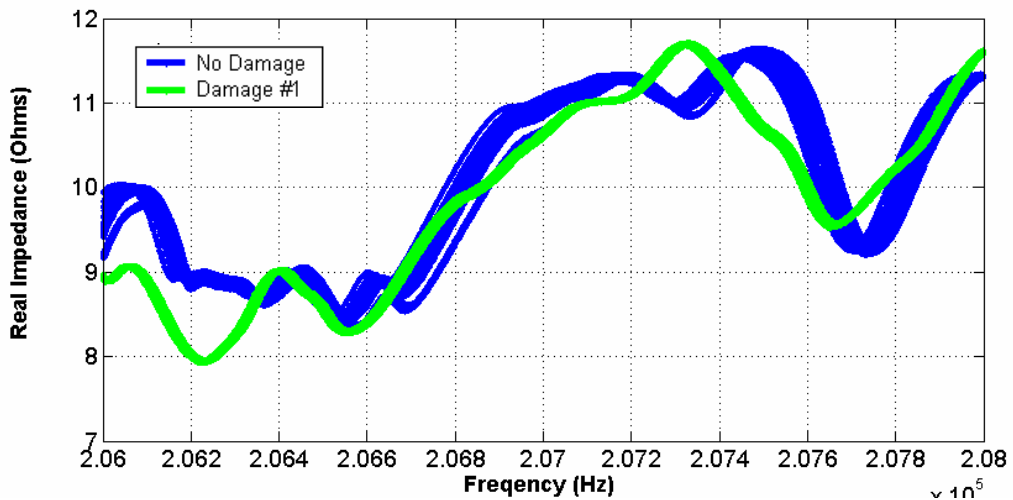


Figure D.42: Impedance signatures for PZT A4 from 206-208 kHz.

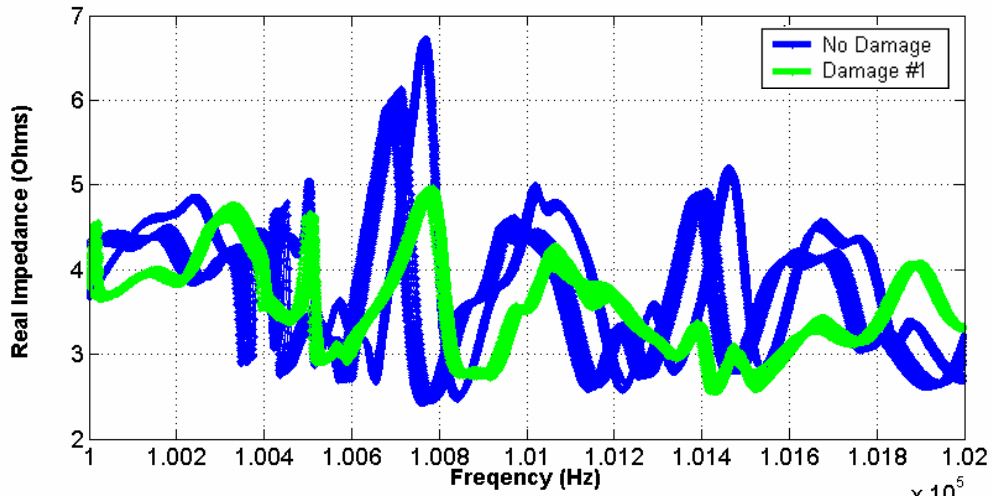


Figure D.43: Impedance signatures for MFC D₃₁ from 100-102 kHz.

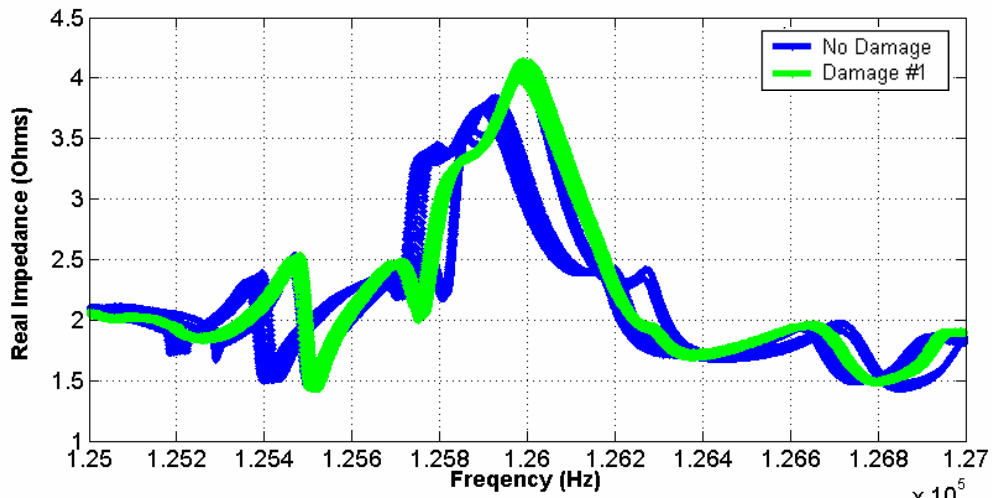


Figure D.44: Impedance signatures for MFC D₃₁ from 125-127 kHz.

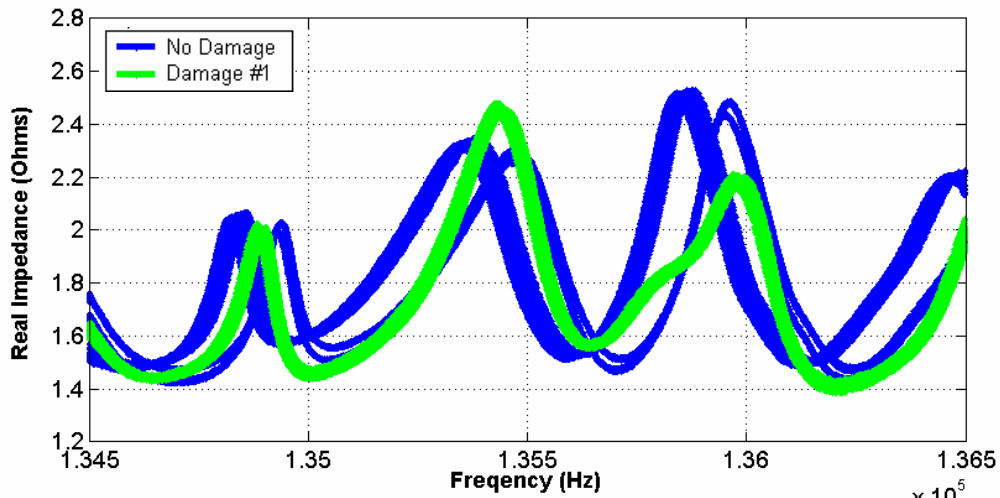


Figure D.45: Impedance signatures for MFC D₃₁ from 134.5-136.5 kHz.

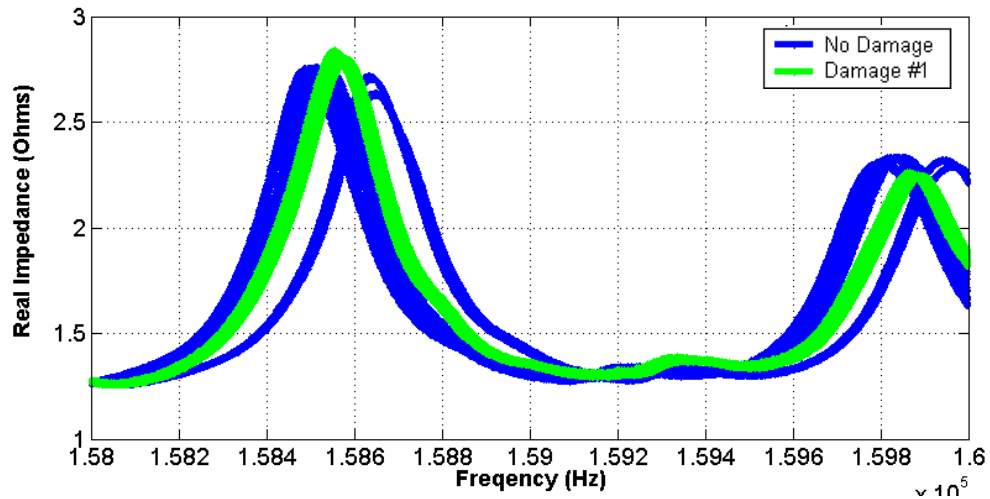


Figure D.46: Impedance signatures for MFC D₃₁ from 158-160 kHz.

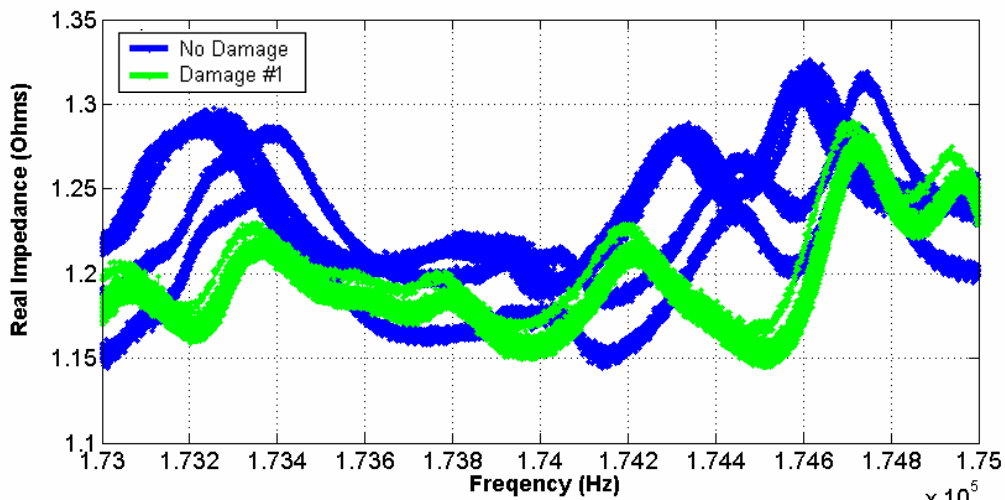


Figure D.47: Impedance signatures for MFC D₃₁ from 173-175 kHz.

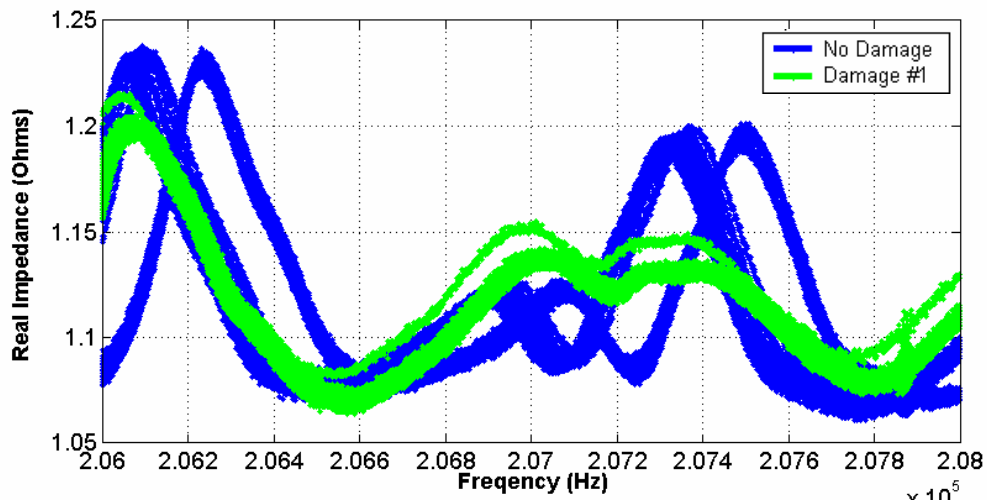


Figure D.48: Impedance signatures for MFC D₃₁ from 206-208 kHz.

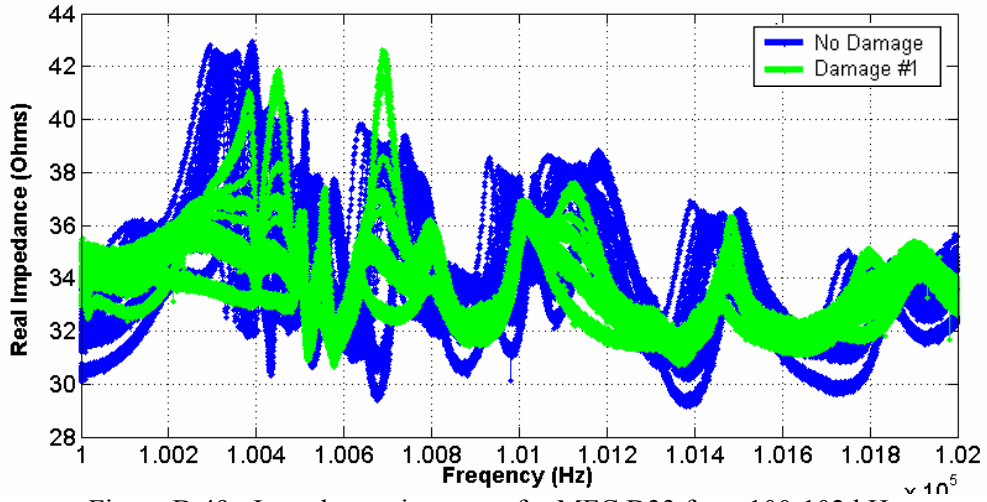


Figure D.49: Impedance signatures for MFC D33 from 100-102 kHz.

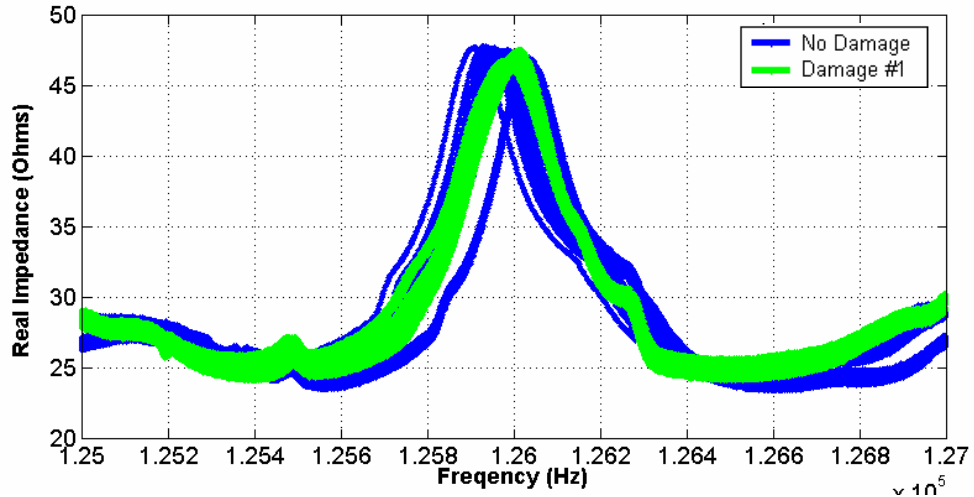


Figure D.50: Impedance signatures for MFC D33 from 125-127 kHz.

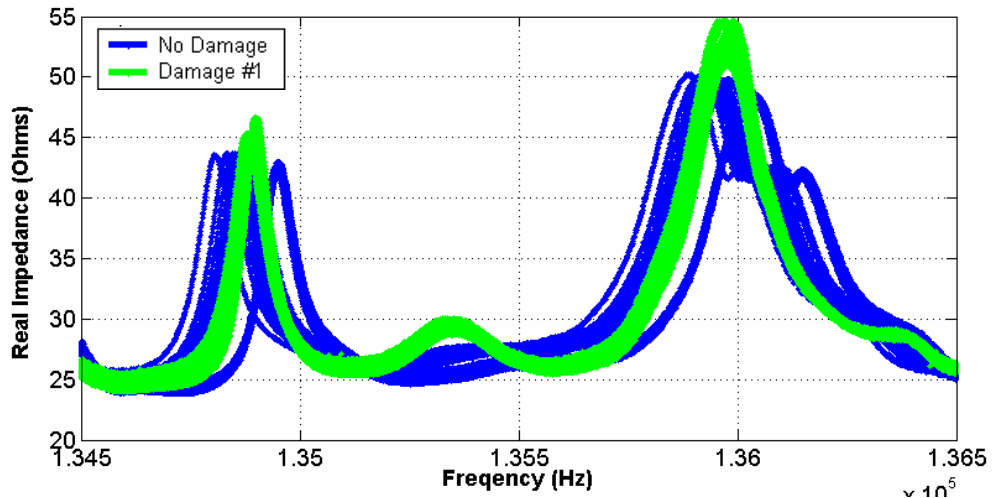


Figure D.51: Impedance signatures for MFC D33 from 134.5-136.5 kHz.

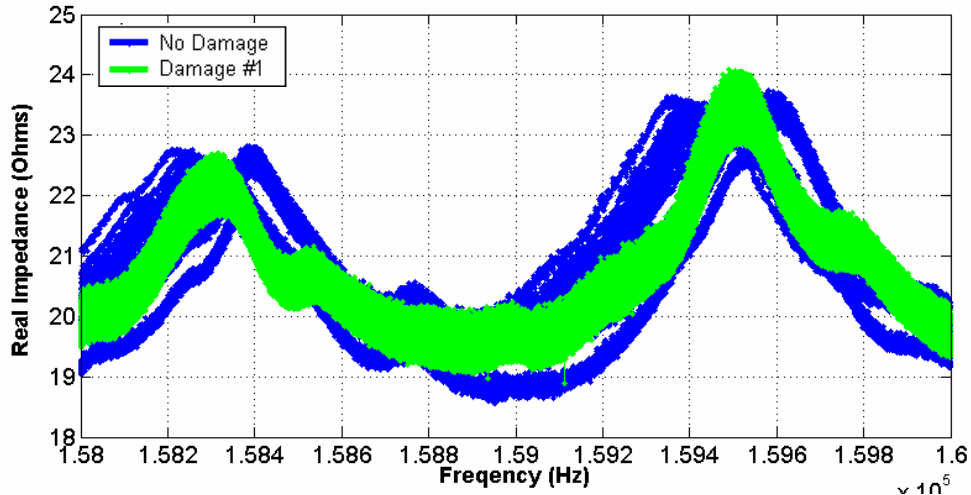


Figure D.52: Impedance signatures for MFC D33 from 158-160 kHz.

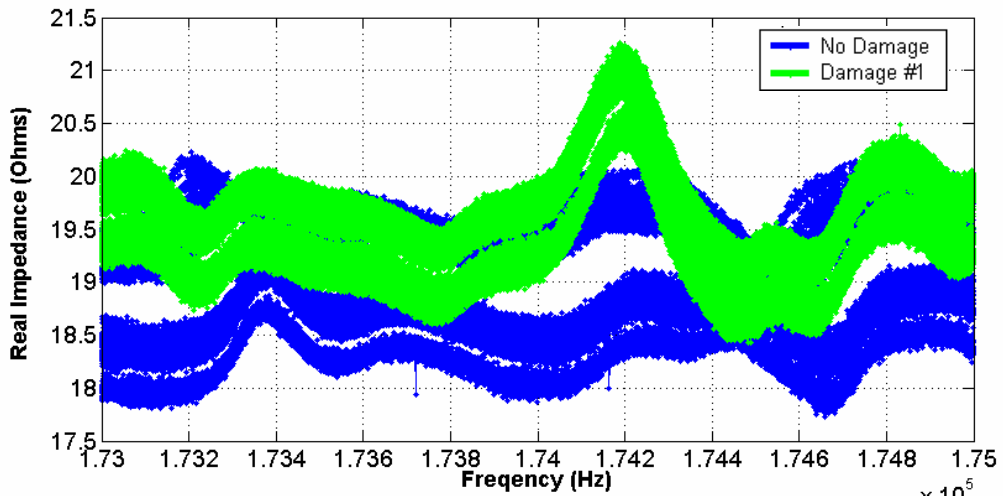


Figure D.53: Impedance signatures for MFC D33 from 173-175-127 kHz.

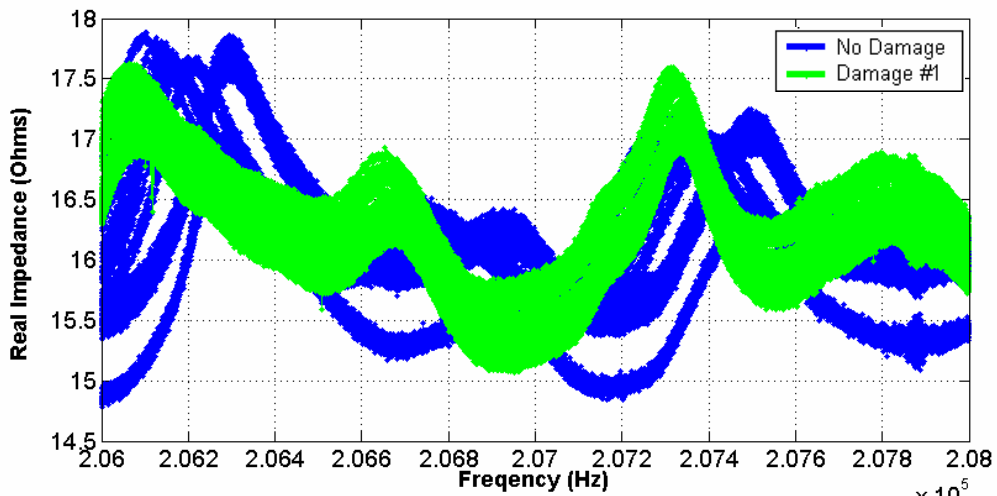


Figure D.54: Impedance signatures for MFC D33 from 206-208 kHz.

Vita

Eddie Simmers was born on April 14, 1974 to parents Eddie and Julia Simmers in Radford, Virginia. In 1992, he graduated from Pulaski County High School and the Southwest Virginia Governor's School. Later that same year he enrolled at Emory & Henry College to pursue a Bachelors degree in Physics and Mathematics. During those five years he was awarded a Professional License to teach Secondary Education in the state of Virginia. For the next five years he taught physics and mathematics at Fork Union Military Academy and Northside High School. At nights and during the summer he took engineering classes at local community colleges in preparation for a return to college in the future.

In the summer of 2001, Eddie enrolled in the B.S. engineering program at Virginia Tech. In 2003, he was accepted into the Dynamics Summer School at Los Alamos National Laboratory by Dr. Chuck Farrar, and he completed his first research in the structural health monitoring field while working with Dr. Gyuhae Park. At the end of the summer, Dr. Daniel Inman hired him as an undergraduate research assistant at the Center for Intelligent Materials System and Structures to conduct power harvesting experiments. He completed his B.S. in Mechanical Engineering, and was accepted into the Masters of Mechanical Engineering program. In the spring of 2004, the National Science Foundation awarded him an Honorable Mention in the Graduate Fellowship awards. The National Physical Science Consortium awarded him a graduate fellowship, and Los Alamos National Laboratory served as his sponsor. Over the past year he completed his thesis topic and Masters coursework and will graduate in May 2005. In June, he will begin working as a Rotating Machinery Analysis Engineer in the Reliability department of Eastman Chemical Company in Kingsport, Tennessee.

Address: 1011 Maple Leaf Drive
Jonesborough, TN 37569